Title
Characterization, Modeling, and Energy Harvesting of Phase Transformations in Ferroelectric Materials

Author
Dong, Wen

Publication Date
2015

Peer reviewed|Thesis/dissertation

UNIVERSITY OF CALIFORNIA

LOS ANGELES

Characterization, Modeling, and Energy Harvesting of Phase Transformations in Ferroelectric Materials

A dissertation submitted in partial satisfaction

of the requirements for the degree of

Doctor of Philosophy in Mechanical Engineering

By

Wenda Dong

2015

ABSTRACT OF THE DISSERTATION

Characterization, Modeling, and Energy Harvesting of Phase Transformations in Ferroelectric Materials

By

Wenda Dong

Doctor of Philosophy in Mechanical Engineering

University of California, Los Angeles, 2015

Professor Christopher S. Lynch, Chair

Solid state phase transformations can be induced through mechanical, electrical, and thermal loading in ferroelectric materials that are compositionally close to morphotropic phase boundaries. Large changes in strain, polarization, compliance, permittivity, and coupling properties are typically observed across the phase transformation regions and are phenomena of interest for energy harvesting and transduction applications where increased coupling behavior is desired.

This work characterized and modeled solid state phase transformations in ferroelectric materials and assessed the potential of phase transforming materials for energy harvesting applications. Two types of phase transformations were studied. The first type was ferroelectric rhombohedral to ferroelectric orthorhombic observed in lead indium niobate lead magnesium niobate lead titanate (PIN-PMN-PT) and driven by deviatoric stress, temperature, and electric field. The second type of phase transformation is ferroelectric to antiferroelectric observed in lead zirconate titanate (PZT) and driven by pressure, temperature, and electric field.

Experimental characterizations of the phase transformations were conducted in both PIN-PMN-PT and PZT in order to understand the thermodynamic characteristics of the phase transformations and map out the phase stability of both materials. The ferroelectric materials were characterized under combinations of stress, electric field, and temperature.

Material models of phase transforming materials were developed using a thermodynamic based variant switching technique and thermodynamic observations of the phase transformations. These models replicate the phase transformation behavior of PIN-PMN-PT and PZT under mechanical and electrical loading conditions. The switching model worked in conjunction with linear piezoelectric equations as ferroelectric/ferroelastic constitutive equations within a finite element framework that solved the mechanical and electrical field equations. This paves the way for future modeling work of devices that incorporate phase transforming ferroelectrics.

Studies on the energy harvesting capabilities of PIN-PMN-PT were conducted to gauge its potential as an energy harvesting material. Using the phase stability data collected in the characterization studies, an ideal energy harvesting cycle was designed and explored to ascertain the maximum energy harvesting density per cycle. The energy harvesting characteristics under non-ideal sinusoidal stress and constant electric load impedance were also investigated. Energy harvesting performance due to changes in loading frequency and electrical load impedance was reported.

The dissertation of Wenda Dong is approved.

Gregory P. Carman

Laurent Pilon

Ertugrul Taciroglu

Christopher S. Lynch, Committee Chair

University of California, Los Angeles

2015

TABLE OF CONTENTS

LIST OF FIGURES

LIST OF TABLES

VITA

2008	B.S. (Mechanical Engineering and Materials Science and Engineering), UC Berkeley, Berkeley, California
2009-2015	Graduate Student Researcher, UCLA. Researched projects including: Characterization of load-driven ferroelectric phase transformations, modeling of domain structures, modeling of ferroelectric materials and devices, energy harvesting using ferroelectric phase transformations.
2010-2012	Naval Research Enterprise Internship Program, NUWC-Newport, Newport, Rhode Island
2011-2015	Teaching Assistant UCLA. Mechanical Engineering, MSOL, and Physics departments. Taught classes on composite theory, statics, aircraft structures, and physics laboratory.
2012	M.S. (Mechanical Engineering), UCLA, Los Angeles, California

PUBLICATIONS, PRESENTATIONS, AND PATENTS

Publications

W. D. Dong et al., "Pressure, Temperature, and Electric Field Dependence of Phase Transformations in Niobium Modified 95/5 Lead Zirconate Titanate," Journal of Applied Physics (submitted 2015)

W. D. Dong et al., "Ideal energy harvesting cycle using a phase transformation in ferroelectric crystals," Smart Materials and Structures, 23(12), (2014).

W. D. Dong et al., “Energy harvesting using the FER-FEO phase transformation in [011] cut single crystal PIN-PMN-PT,” Journal of Intelligent Material Systems and Structures, 25(14), (2014)

W. D. Dong, D. M. Pisani, and C. S. Lynch, “A finite element based phase field model for ferroelectric domain evolution,” Smart Materials and Structures, 21(9), (2012).

W. D. Dong et al., “Stress dependence of thermally driven pyroelectric charge release during FER-FEO phase transformations in [011] cut relaxor ferroelectric crystals,” Applied Physics Letters, 100(26), (2012).

W. D. Dong et al., “Giant electro-mechanical energy conversion in [011] cut ferroelectric single crystals,” Applied Physics Letters, 100(4), (2012).

P. Zhao, S. Goljahi, W. Dong et al., “The strength of PIN-PMN-PT single crystals under bending with a longitudinal electric field,” Smart Materials & Structures, 20(5), (2011).

M. B. Rauls, W. Dong, J. E. Huber et al., “The effect of temperature on the large field electromechanical response of relaxor ferroelectric 8/65/35 PLZT,” Acta Materialia, 59(7), 2713-2722 (2011).

Presentations

W. D. Dong, P. Finkel, and C. S. Lynch, “Mechanical and thermal energy transduction utilizing phase transformations in 32 mode relaxor-ferroelectric single crystals," Proc. SPIE Smart Structures and Non-Destructive Evaluation 2013 (2013).

W. D. Dong, D. M. Pisani, and C. S. Lynch, “A Discrete Phase Model for Ferroelectric Domain Evolution," Proc. ASME SMASIS 2011, SMASIS2011-5061 403-410 (2011).

W. D. Dong, P. Finkel, A. Amin, and C. S. Lynch, “Mechanical energy harvesting utilizing phase transition in 32 mode relaxor-ferroelectric PIN-PMN-PT single crystals," Proc. SPIE 8343, Industrial and Commercial Applications of Smart Structures Technologies 2012, 834308 (2012).

W. Dong, D. Pisani, and C. S. Lynch, “Discrete Phase Model of Domain Walls in Ferroelectric Crystals,” Proc. SPIE 7978, Behavior and Mechanics of Multifunctional Materials and Composites 2011, 797804 (2011).

W. Dong and C. S. Lynch, “An examination of the structure and the gradient terms used in phase field modeling,” Proc. SPIE 7644, Behavior and Mechanics of Multifunctional Materials and Composites 2010, 764405 (2010).

P. Finkel, W. Dong, C. S. Lynch, and A. Amin, “Giant Electro-Mechanical Energy Conversion in [011] cut Relaxor Ferroelectric Single Crystals," Bulletin of the American Physical Society 57 (2012).

P. Finkel, A. Amin, and W. Dong “Spontaneous ferroelectric-ferroelectric phase transitions and giant electro-mechanical energy conversion in [011] cut relaxor ferroelectric crystals," Bulletin of the American Physical Society 58 (2013).

Patents

US Patent Application Ser. No. 13/053,577 “Energy Harvesting Utilizing Stress Induced Phase Transformation in Ferroelectric Piezocrystals.”

CHAPTER 1

INTRODUCTION

1.1 Motivation

Active materials are a class of materials in which one or more properties can be altered in a controlled manner through the application of external stimuli that can be mechanical, electrical, magnetic, or thermal. Active materials typically respond to at least two different sources of stimuli and are used in applications where the coupling or transduction between two physical properties is desired. Active materials include ferroelectric, ferromagnetic, and shape-memory alloys. The material class of interest in this work is crystalline ferroelectric where there exists a strong coupling of mechanical and electrical properties. In addition to possessing piezoelectric properties, where electric fields leads to mechanical deformation and stresses lead to electric displacement change, ferroelectrics also retain a spontaneous electrical polarization and an associated spontaneous strain. Each solid state phase of the ferroelectric material possesses one or more variant(s) where each variant has a unique spontaneous polarization direction and associated spontaneous strain. Under sufficiently large electric fields or stresses, the variant can be driven to another variant in the same phase or to a variant in another phase. The mechanism is domain wall or phase boundary motion. Domain wall motion makes an extrinsic contribution to piezoelectricity whereas deformation of the crystal structure contributes an intrinsic effect. Therefore, extrinsic effects offers increased electrical-mechanical coupling behavior over the intrinsic piezoelectric behavior. The scope of application for ferroelectric materials includes energy transduction, actuation, sensing, and energy harvesting[1-2]. Much of this work is focused on using phase transformations in ferroelectrics for energy harvesting.

While ferroelectric ceramic and single crystal devices are widely used as both monolithic and structured composite materials in devices, they are typically employed for their linear piezoelectric characteristics. Therefore, significant research has gone into characterizing the class's piezoelectric properties and linear loading characteristics. Traditional applications such as sonar and ultrasonic transducers valued the linear nature of the piezoelectric operating region due to the ease of device calibration. However, operation in the highly non-linear and hysteretic phase transformation or polarization reorientation regime offers significantly increased electromechanical coupling and energy transduction properties. In ferroelectric materials, phase transformations are typically identified through changes, jumps, or hysteresis in material properties. Common material properties used to indicate phase transformations include lattice parameters, strain, electric polarization, and dielectric constant. Figure 1-1 illustrates the hysteresis and jump type discontinuities of unit cell parameters, electric polarization, and dielectric constants across phase transformations in thermally excited barium titanate.

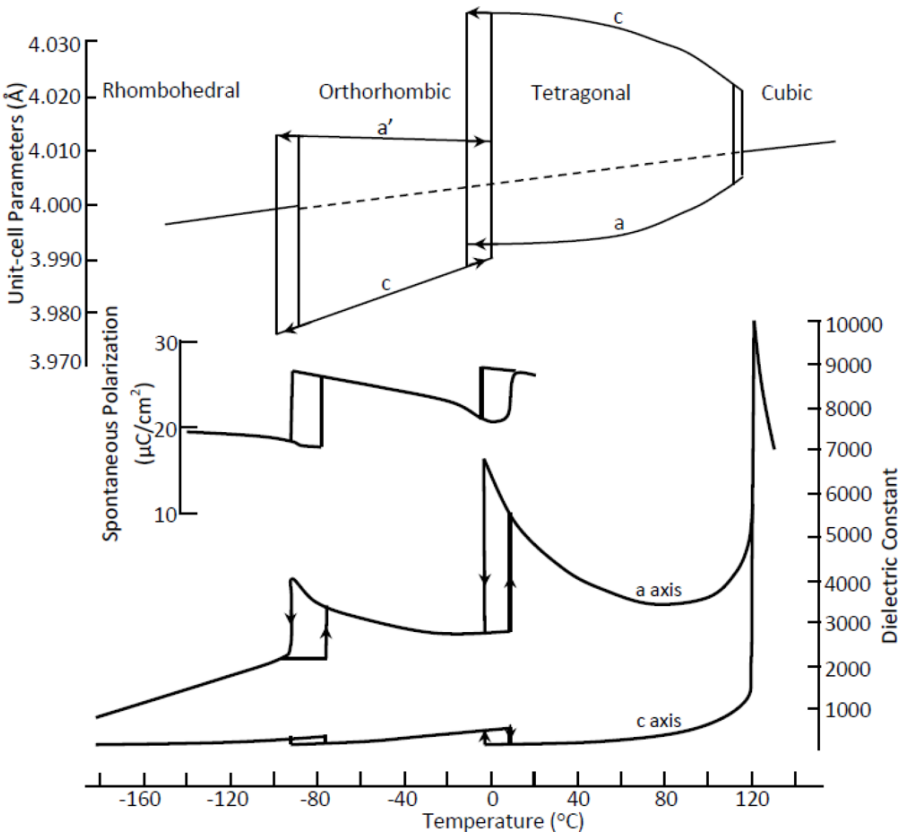

Figure 1-1 Phase transformations in barium titanate driven by temperature. Phase transformations are indicated by jump type discontinuities and hysteresis in unit cell parameters, spontaneous polarization and dielectric constant. Reproduced from Aksel [3].

Two types of solid state ferroelectric phase transformations are of interest in this work. The first is a ferroelectric rhombohedral (FE_R) to ferroelectric orthorhombic (FE_O) phase transformation that occurs in single crystal relaxor ferroelectrics. The second is a ferroelectric (FE) to antiferroelectric (AF) phase transformation that occurs in polycrystalline 95/5 lead zirconate titanate. Phase transformations in these types of materials result in significant change in the internal spontaneous polarization and strain. Across phase transformations, electric displacement and strain exhibit significant nonlinearity under stress, electric field, or temperature loading. In order to fully utilize the enhanced electromechanical coupling effects of phase

transforming ferroelectric materials in a repeatable manner, the driving forces must be large enough to fully drive the phase transformation.

While stress, electric field, and temperature driven phase transformations are well known in ferroelectric materials, significant work in the area has been focused on avoiding non-linear effects of domain wall motion and phase transformations in ferroelectric materials, especially in the case of single crystal relaxor ferroelectrics. This work addresses the characteristics of the non-linear phase transformations, the mechanisms behind the phase transformations, and their applicability to energy harvesting applications. This dissertation addresses three major topics:

1. A characterization of electrical, mechanical, and thermal behavior of phase transformations under combinations of stress, electric field, and temperature loading.
2. Development and testing of ideal and non-ideal energy harvesting cycles using phase transforming ferroelectric materials. This addresses the theoretical limitations of the material's energy harvesting performance as well as its performance changes due to frequency and electric load.
3. Development of an energy based micromechanics material model that is capable of capturing nonlinearity of the phase transformation.

1.2 Background

1.2.1 History of 95/5 PZT

The first type of phase transformation characterized occurs in ceramic niobium modified lead zirconate-lead titante, $Pb_{0.99}Nb_x(Zr_{0.95}Ti_{0.05})_{1-x}O_3$ (PZT 95/5-xNb). A binary solid state solution of lead zirconate (PZ) and lead titanate (PT), PZT ceramics was first discovered in 1952 as a multi-phased ferroelectric material [4] however its application as a piezoelectric was not fully realized until 1954 [5-7]. PZT 95/5 has a 95% PZ and 5% PT composition. Doped with a small amount of niobium (x~2%), PZT 95/5-2Nb is a composition of PZT that has found applications in impact generated pulse power devices due to its ability to undergo a ferroelectric (FE) to antiferroelectric (AF) phase transformation [8-17] and has potential application in actuation and energy harvesting. Pressure can force the ceramic into the AF phase as the AF phase has a volume reduction over the FE phase. In poled specimens, the FE – AF phase transformation is accompanied by a release of the electrode charge that was terminating the normal component of remnant polarization. This work addresses bipolar large electric response and the phase stability of the FE and AF phases as a function of stress, electric field, and temperature. The resulting insight into the large bipolar electric response and phase diagram parameters is useful for material selection and device design.

Considerable past work has been conducted to map out the composition – temperature phase diagram of lead zirconate (PZ) and lead titanate (PT) solid solutions [4-5, 18-19]. Five major phases were discovered for the PZT solid solution below the Curie temperature above which a paraelectric cubic phase, P_C, exists. A ferroelectric tetragonal phase (FE_T) exists at high PT values (~48 to 100%). An antiferroelectric orthorhombic (AF_O) phase exists at low PT (0 to

~5%) and is separated from the P_C phase by a small antiferroelectric tetragonal phase (AF_T) [4]. The region between the AF_O and FE_T phases is ferroelectric rhombohedral (FE_R) [18], with a low temperature FE_{R1} and a high temperature FE_{R2} phase [20-21]; the FE_{R1} phase has a superstructure and higher remnant polarization [22-24].

The composition of 95% PZ and 5% PT is of considerable interest as it lies on the phase boundary between the AF and FE_R phases where the phase stability of the AF and FE phases is significantly weakened. The vertical dashed line in Figure 1-2.a indicates the 95/5 PZT composition. This composition is very near the FE – AF phase boundary at room temperature. As the temperature is increased, the 95/5 PZT changes from the low temperature FE_{R1} to the high temperature FE_{R2}. Figure 1-2.b shows the temperature – pressure phase diagram for 95/5-2Nb PZT developed by Fritz and Keck [24] and shows four distinct phases: FE_{R1}, FE_{R2}, AF_O, and AF_T. At low pressures, 95/5 PZT is FE_{R1} at low temperature and the FE_{R2} at high temperature. At high pressures, the material is AF_O at low temperature and AF_T at high temperature. Fritz and Keck's investigation also noted a slight temperature dependence of the FE to AF phase transformation pressure where increases in temperature helped to stabilize the FE phases and increased the transformation pressure.

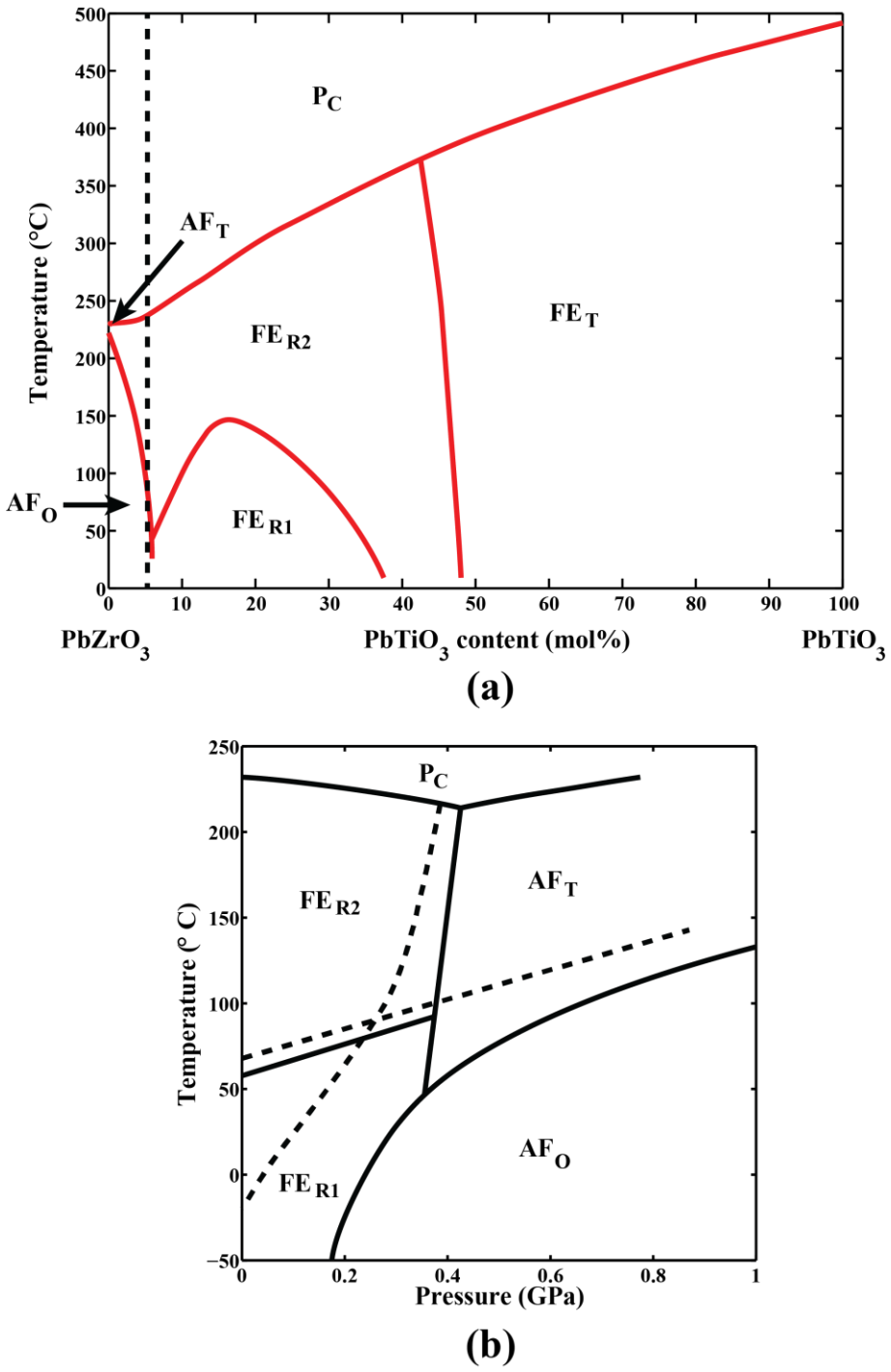

Figure 1-2. a) Composition – temperature phase diagram of PZT with a black dashed line showing the location of the 95/5 composition (adapted from Jaffe, Cook, and Jaffe [25]) and b). Temperature – pressure phase diagram of 95/5-2Nb PZT adapted from Fritz [24] with the solid lines indicating the forward transformation and the dashed lines indicating the reverse transformation.

Research on phase transformations in 95/5 PZT has been ongoing since the 1960s. Materials with compositions near the AF – FE phase boundaries were shown to be susceptible to phase transformations under applied loads of temperature, pressure, and electric field as the energy barrier separating the two phases is lessened. Electric field and temperature were shown to stabilize the FE phases over the AF phases [22-24, 26]. Pressure [22, 24] was shown to stabilize the AF phases over the FE phases. Berlincourt et el. [22] developed phase diagrams for AF phase lead zirconate with increasing content of lead titanate and also discussed the effects of substitution of small amounts of Sn^{+4} for Ti^{+4}, the substitution of La^{+3} for Pb^{+2}, and the effect of Nb^{+5} for Zr^{+4} and Ti^{+4}. The donor dopants affected resistivity, coercive fields, and phase stability with Nb favoring the FE phase and La favoring the AF phase. Berlincourt developed phase diagrams by measuring changes in dielectric permittivity. Phase diagrams for the AF – FE phase transformation have been explored for temperature-electric field [23], pressure-electric field [22], and temperature-pressure [24] loading conditions. Temperature – electric field phase stability plots were created by observing bipolar electric displacement-electric field curves at various temperatures [23]. Phase stability diagrams of electric field – pressure [22] and temperature – pressure [24] have been generated from measurements of the permittivity and tanδ at various pressure and electric field or pressure and temperature combinations. The effects of semi-uniaxial stress on the behavior of bipolar electric displacement – electric field loops have also been reported [27].

1.2.2 History of [011] Cut and Poled Single Crystal Relaxor Ferroelectrics

Certain ferroelectric solid state solutions, for example PZT that is subject to partial substitution by certain dopants (e.g. lanthanum, indium, niobium, magnesium), fall into a category known as relaxor ferroelectrics, characterized by wide peaks in the temperature dependence of the dielectric permittivity [28]. In addition some relaxor ferroelectrics can be grown as single crystals giving them remarkable dielectric and piezoelectric properties.

Single crystal relaxor ferroelectrics have been developed for sensing and transduction applications and are now showing considerable promise for energy harvesting applications due to their exceptional electromechanical properties. Relaxor single crystal properties were reported by Kuwata et al. [29-30] for lead zinc niobate lead titanate $(1-x)PbZn_{1/3}Nb_{2/3}O_3 - xPbTiO_3$ (PZN-PT) and by Shrout et al. [31] for lead magnesium niobate lead titanate $(1-x)PbMg_{1/3}Nb_{2/3}O_3 - xPbTiO_3$ (PMN-PT) and by Yamashita and Shimanuki [32] for $(1-x)PbSc_{1/2}Nb_{1/2}O_3 - xPbTiO_3$ (PSN-PT).

The phase diagram for PMN-PT is shown in Figure 1-3.a with the corresponding spontaneous electric polarization directions of each phase shown in Figure 1-3.b. Below the Curie temperature, the temperature – pressure phase diagram for these relaxor-PT ferroelectrics typically comprise of a ferroelectric tetragonal phase (FE_T) at high PT concentrations and a ferroelectric rhombohedral phase (FE_R) at low PT concentrations. The FE_T and FE_R phases are separated by a morphotropic phase boundary (MPB) [33]. Studies have shown the existence of monoclinic (FE_M) and orthorhombic (FE_O) phases within the MPB that act as intermediate phases between the FE_T and FE_R end members [34-37].

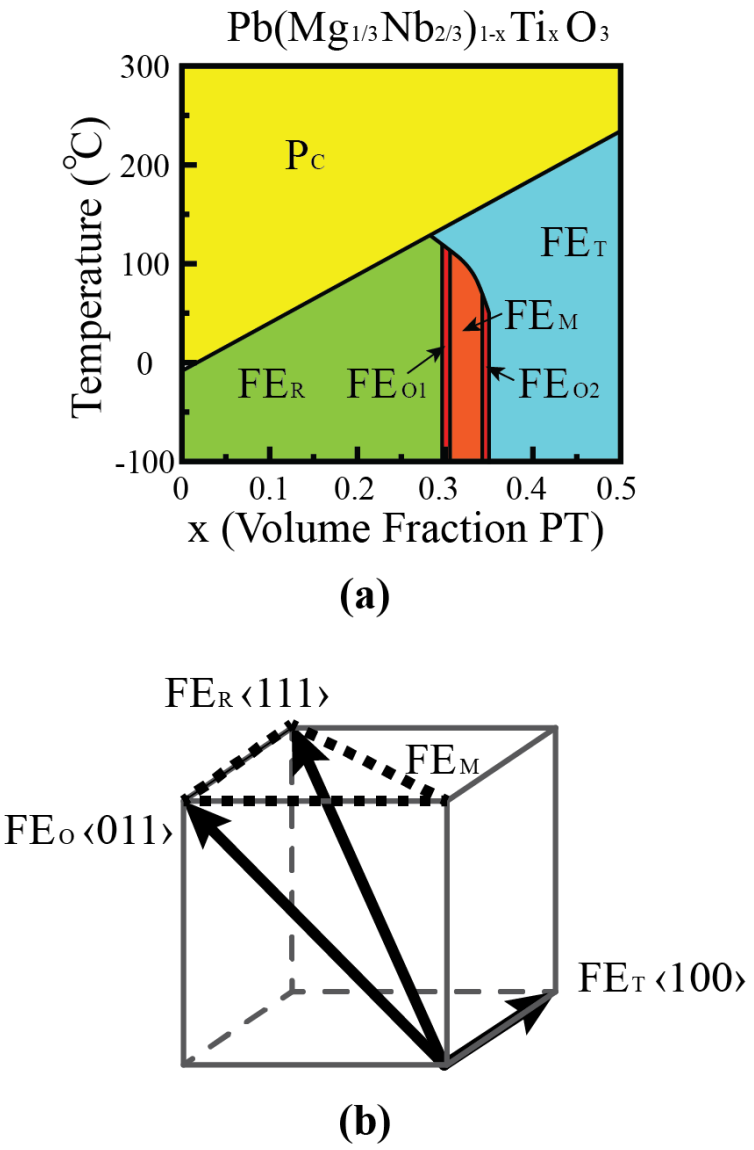

Figure 1-3. a) Temperature – composition phase diagram of PMN-PT reproduced from Guo et al. 2003 [33]. b) Families of crystallographic directions for electrical polarization orientations of different phases.

The compositions of interest that show the greatest electromechanical properties are FE_R with PT concentrations close to the MPB [35, 38]. Proximity to the MPB weakens the stability of the FE_R phase and allows for greater polarization rotation and increased electromechanical coupling properties within the material. Additionally, under certain combinations of applied

electric field, stress, and temperature; these materials can be driven into the neighboring FE_O, FE_M, or FE_T phases [39-43]. Materials where these stimuli driven phase transformations have been demonstrated include PZN-xPT [29-30], PMN-xPT [31, 44] , and yPIN-(1-x-y)PMN-xPT [45-49]. In PMN-PT and PIN-PMN-PT, the PT composition is typically 27-33%. Note the phase diagram for PIN-PMN-PT is nearly identical to that of PMN-PT.

One of the field driven phase transformations from FE_R to FE_O occurs in the [011] cut and poled configuration. Miller indices are cubic referenced. Figure 1-4 defines the rhombohedral variants, the orthorhombic variants, the [011] crystal cut, and the stress and electric field driven FE_R to FE_O phase transformation. The FE_R phase has eight crystal variants where the polarization vector can point toward any one of the corners of the unit cell, the $\langle 111 \rangle$ directions in a cubic referenced coordinate system, as shown in Figure 1-4.a. The spontaneous strain for each variant is an elongation in the spontaneous polarization direction and a contraction perpendicular to this direction. The FE_O phase has twelve crystal variants with the polarization pointing toward any one of the edges of the unit cell, the $\langle 011 \rangle$ directions, as shown in Figure 1-4.b. As with the FE_R variants, the FE_O variants also possess spontaneous strain with elongation in the polarization direction and transverse contraction. The $[011]$cut indicates bars or plates cut from the cubic oriented crystal with faces oriented in the $[011]$, $[0\bar{1}1]$, and $[100]$ directions and electrodes on the faces perpendicular to $[011]$ as shown in Figure 1-4.c. This enables application of electric field in the $[011]$ direction and compressive stress in the $[100]$ direction. When the electric field is above the coercive field but below the transformation field, the material possesses volume average polarization in the $[011]$ direction. This results in a domain

engineered two FE_R variant state with the polarization of the two variants lying in the $[111]$ and $[\bar{1}11]$ directions [50-53] as shown schematically in Figure 1-4.d. The resulting polarization and strain are the volume average response of the two variant system. The resulting linear piezoelectric behavior is a positive d_{33} (x_3 in the $[011]$ direction), a negative d_{32} (x_2 in the $[100]$ direction), and a positive d_{31} (x_1 in the $[0\bar{1}1]$ direction). When the electric field is sufficiently large, the crystal will undergo a transformation from the two-variant FE_R state to a single-variant FE_O state that is polarized in the $[011]$ direction. The phase transformation is accompanied by large strain and polarization changes [54-55]. In the [011] cut and poled crystals, the FE_R - FE_O phase transformation can also be driven by a compressive uniaxial stress in the $[100]$ direction. The crystal contracts in the $[100]$ direction during the transformation and thus compressive stress does positive work during the transformation. The FE_R to FE_O phase transformation driven by stress and electric field has been characterized for binary PMN-PT [54-56], PZN-PT [57-59], and ternary PIN-PMN-PT [60-63]. FE_R compositions with higher PT content (closer to the MPB) have been found to exhibit higher electromechanical coupling behavior and lower critical electric field and stress loading are required to induce the phase transformation [64-65].

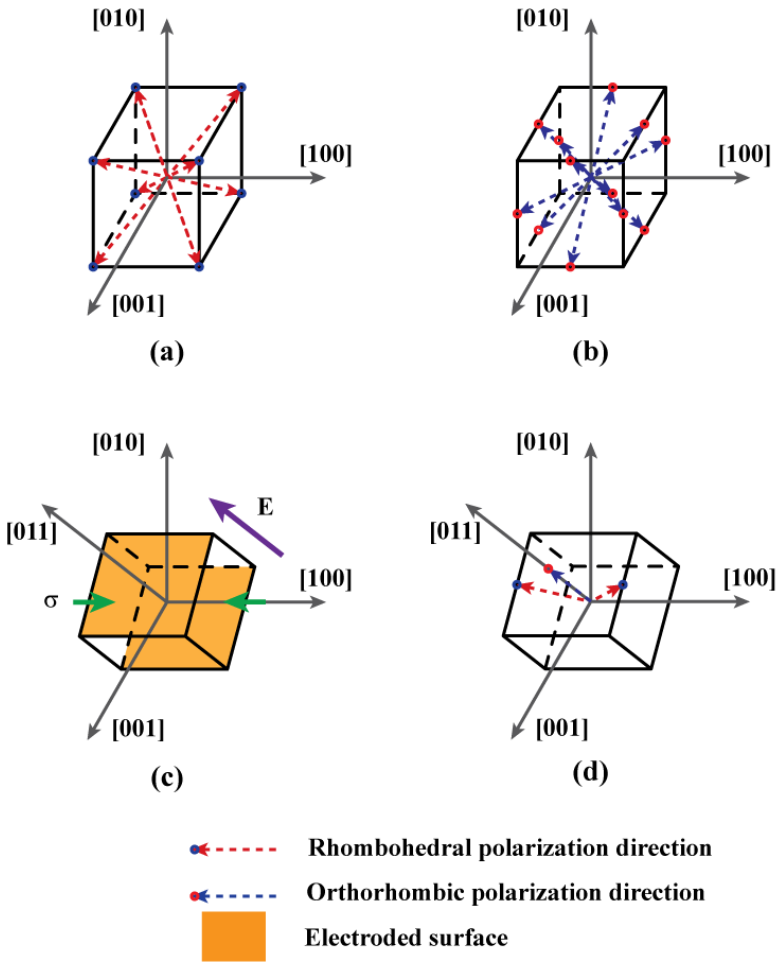

Figure 1-4. The [011] crystal cut and the FE_R to FE_O phase transformation showing a) the polarization directions of the FE_R crystal variants, b) the polarization directions of the FE_O crystal variants, c) the [011] crystal cut with the components of applied electric field and stress that drive the transformation, and d) the two variant FE_R phase that transforms to the single variant FE_O phase in a poled [011] cut crystal.

The material of interest for this study of single crystal relaxor ferroelectrics is PIN-PMN-PT. PMN-xPT and PZN-xPT have a Curie point around 100ºC, limiting their application to temperature ranges below this level. PIN-PMN-PT compositions display similarly large

piezoelectric coefficients and also display increased Curie temperatures and coercive fields, enabling them to be used in a broader range of environments. This makes PIN-PMN-PT more attractive as a robust material for transduction and energy harvesting applications.

1.2.3 History of Micromechanics Modeling

The finite element method (FEM) has been used to model both linear piezoelectric and non-linear hysteretic ferroelectric behavior. Allik and Hughes paved the way with the first piezoelectric finite element model in 1970 with a finite element formulation that used tetrahedral elements and scalar electric potential [66]. Allik and Hughes' work has since been widely adapted and linear piezoelectric finite element codes are now commercially available for use with a variety of element types and interpolation shape functions [67].

Non-linear hysteretic ferroelectric codes tend to exist only as specialized codes used by researchers in the area of ferroelectric modeling. A quadratic electrostrictive constitutive law without hysteresis was implemented by Hom [68] that also addressed the electrode edge field concentration effect. One of the most common methods of capturing the behavior of ferroelectric materials is to use linear piezoelectric finite element code that calls on a material model to calculate the ferroelectric and ferroelastic effects. Micromechanics based material models are used for material models at length scales where domain structure level effects can be neglected in favor of a volume average response. The micromechanics approach states that there are spontaneous polarizations and strains for each ferroelectric variant and assumes changes from one variant to another follows a Preisach type hysteresis [69]. A free energy criterion is typically

employed to determine switching behavior. Hwang et al. [69] and Chen and Lynch [70] used a micromechanics model within a finite element framework to capture the hysteretic ferroelectric and ferroelastic switching behavior and modeled crack tip field concentrations in ferroelectric materials. Similarly, Fang et al. [71-73] developed a micromechanics FEM to address defect effects in ferroelectrics. Kamlah [74-76] has also modeled ferroelectric materials using finite elements with a material model centered on reversible and irreversible polarization and strain. The first electromechanical finite element formulations used a scalar potential (voltage) to model the electrical degree of freedom in the finite element code. Landis [77] proposed using vector potential theory to account for the instabilities that could arise using the Allik and Hughes formulation.

Micromechanics has been employed in the modeling of both single crystal relaxor ferroelectrics and ceramic ferroelectrics [78]. Hwang et al. [69] used variant switching micromechanics material model to simulate the stress and bipolar electric field driven strain and polarization curves in a single PLZT grain. This method was then used to simulate ceramic PLZT by taking the volume average behavior of many randomly oriented and super positioned grains [79-80]. Methods using micromechanics were developed to model several types of single crystal relaxor ferroelectrics [81]. Liu and Lynch [82-84] modeled the sharp $FE_R - FE_O$ phase transformation in domain engineered PZN-4.5PT. Webber et al. [44, 85-87] adapted the method to model the gradual $FE_R - FE_O$ phase transformation in PMN-32PT by using a Gaussian distribution of the phase transformation criteria. Webber [85] also used a FEM micromechanics model to simulate uniaxial effects on bipolar strain and electric polarization. Jayabal et al. [88] used a similar micromechanics model to investigate the multi-axial loading effects on ferroelectric barium titanate single crystals and ceramics. Gallagher et al. [89] used a variation

of Webber's micromechanics model to simulate FE_R – FE_O phase transformation in PIN-PMN-PT single crystals using free energy criteria based on positive work on the material using the strain and polarization change during a phase transformation. Micromechanics methods have also been adapted to model the effects of domain wall motion hysteresis and the FE – AF phase transformation in PZT. Robbins et al. [90] used an extended finite element method to model pressure induced phase transformation and porosity effects in 95/5 PZT. Lange et al. [91] employed a micromechanically inspired discrete variant switching on the unit cell level and continuous evolution of inelastic fields on the domain wall level to model ferroelectric and ferroelastic hysteretic behavior in FE_T PZT.

Several phenomenological material models have also been developed for modeling ferroelectricity. Ghandi and Hagood [92] developed a phenomenological nonlinear constitutive model in finite elements that models variant switching in PZT. Montgomery and Zeuch [93] developed a nonlinear phenomenological model for pressure driven FE – AF phase transformations in porous 95/5 PZT. Tan et al. [94] used experimental data to create a phenomenological electric polarization vs. electric field model for uniaxially compressed and laterally confined 95/5 PZT where unipolar electric field was a cubic function electric polarization and a linear function of stress.

1.2.4 History of Phase Field Modeling

Phase field theory is a technique that allows the modeling of domain-domain evolution and interactions on a length-scale down from the micromechanics model. Phase field theory uses thermodynamic arguments to describe driving forces for the temporal evolution of material microstructures. Phase field theory was used in the 1980s by Fix and Langer in order to study pattern formation in crystal growth [95-97]. The application of phase field theory to ferroelectrics was initiated mainly by Nambu and Sagala who adapted Onuki's method to ferroelectric materials [98-99]. Onuki used a time-dependent Ginzburg-Landau method (TDGL) to compute the microstructure evolution of phase separating alloys. Where Onuki had used elastic effects to drive TDGL in the separating alloys simulation, Nambu and Sagala used instead Landau-Devonshire theory in their TDGL to model ferroelectric microstructure evolution. Landau-Devonshire theory was initially developed by Devonshire in the 1950s, as a phenomenological technique to capture the nonlinearity in the behavior of ferroelectrics [100]. Devonshire proposed a description of ferroelectric behavior using free energy surfaces with polarization as an order parameter. Figure 1-5 shows the free energy function (G) of a FE_T phase material in 2-dimensional $P_1 - P_2$ space. Energy minimums (wells) in the free energy function were used to describe the spontaneous polarization and for a FE_T material these energy wells lie in the $\langle 100 \rangle$ directions.

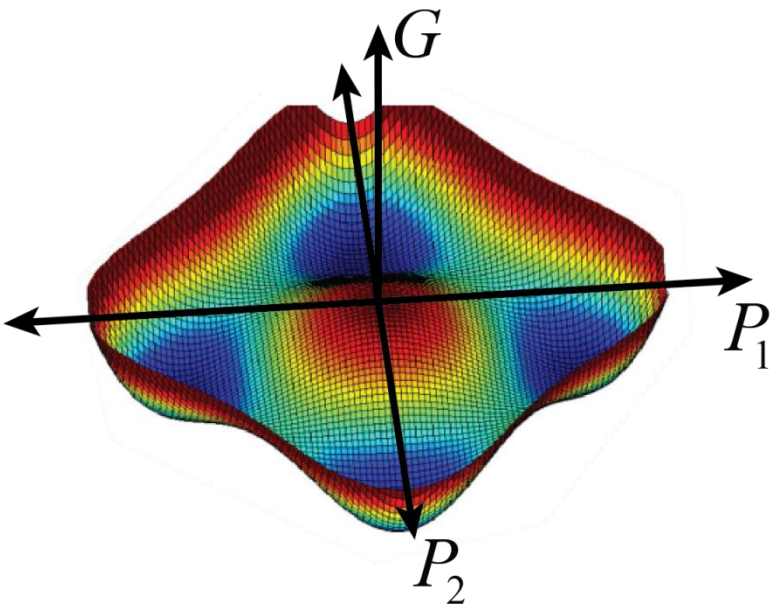

Figure 1-5. 2-dimensional free energy function G of FE_T material in $P_1 - P_2$ space with energy wells in the $\langle 100 \rangle$ directions.

Devonshire theory has since been further augmented by numerous groups such as Barsch, Cross, and Rossetti [101-102]. There is currently growing momentum in the field to tie Devonshire theory to temperature and composition phase behavior as well as describing Devonshire theory with first principles calculations through the use of density functional theory [103-105]. Cao and Cross added phenomenologically correct elastic and polarization gradient energy density terms to the free energy density equation in order to account for domain wall width of perovskite twinning structures [106]. Hu and Chen demonstrated that long range electrostatic and non local elastic interactions were required to achieve correct head to tail dipole-dipole solutions [107-108]. Shen and Chen introduced a spectral method for solving microstructure evolution in Fourier space using the semi-explicit Fourier-spectral method and

showed evolving in Fourier space allowed for a greater rate of convergence [109]. Adaptation of phase field modeling for thin film applications was conducted by Li and Chen [110]. Wang et al. [111] created macroscopic polarization-electric field and strain-electric field hysteresis loops using phase field models [111]. Su and Landis [112] used a finite element formulation to study the electromechanical domain wall pinning strength of line charges. Wang, Kamlah and Zhang [113] used long range electrostatic and elastic energy density terms in the free energy formulation to account for vortex structures in ferroelectric materials at the nanoscale. Wang and Kamlah [114-115] presented a model using Landau-Devonshire theory within a finite element codes in order to model physical defect behavior in single domain ferroelectric materials.

Finite element based phase field method has been adapted to solve phase transformation problems. Young et al. [116] adapted a phase field model to model the FE – AF phase transformation and energy storage capabilities of antiferroelectric capacitors. The model uses the two sub-lattice approach first proposed by Kittel [117] and further developed by Cross [118] and Uchino [119-120]. The FE_R – FE_O phase transformation in single crystal relaxor ferrelectrics can also be modeled using phase field. Zhang [121] outlined the anisotropic free energy as a function of polarization direction in domain engineered relaxor ferroelectric crystals.

1.2.5 History of Energy Harvesting

A significant amount of work has been done on mechanical to electrical energy transduction through the use of linear piezoelectric materials in vibratory systems and broadband

responses[122-124], composite structures[123, 125], or nanoscale systems [126]. However, the use of non-linear phase transformations for mechanical to electrical energy conversion remains largely unexplored.

One of the first studies to explore the energy conversion characteristics of phase transformations in ferroelectric materials was by Olsen et al. who developed a pyroelectric energy harvesting cycle based on the Ericsson cycle that was demonstrated on ferroelectric ceramic and ferroelectric polymer. Tin doped lead zirconate titanate (PSnZT) [127-128] and polyinylidene fluoride-trifluoroethylene copolymers (P(VDF-TrFE)) [129-130] were driven between the ferroelectric phase and the paraelectric phase by cycling between a high temperature and a low temperature under specified electric field loads. Limitations on the Olsen cycle include limited cycling frequency that is constrained by the heat transfer rate between the hot and cold temperature reservoirs and the need for actively applied electric fields.

Significant work has gone into on improving the Olsen cycle in ferroelectric polymers and relaxor single crystals. Studies of the Olsen cycle using P(VDF-TrFE) have yielded energy densities ranging from 15kJ m^{-3} per cycle to 279kJm^{-3} per cycle [131-134] depending on polymer dimensions, temperature range, and electric field range. Significant work has gone into improving Olsen cycle performance in single crystal relaxor ferroelectrics. Sebald et al. outlined electrocaloric and pyroelectric properties for PMN-PT [135-136] and demonstrated an electrical-thermal Ericsson cycle in non-phase transforming PMN-PT [137-138]. Olsen cycles over phase transformations in single crystal relaxor ferroelectrics were demonstrated by Guyomar, Kandilian, McKinley, Zhu and others for PMN-PT [139-141] and PZN-PT [142-144]. Electric analogs of the Sterling [143] and Carnot cycles[145] have also been demonstrated in PZN-PT.

Mechanically driven analogs of the Olsen cycle have been proposed by Patel et al. [146] for stress driven FE – AF phase transformations in niobium and tin doped PZT.

1.3 Contributions

The following describes the contributions of this dissertation in advancing the technology of phase transforming ferroelectric single crystal and ceramic materials material for applications in transduction and energy harvesting:

- FE – AF phase transformation in ceramic 95/5-2Nb PZT was characterized and shown to have phase transformation criterion that is linearly dependent on pressure and electric field. The electric field – pressure phase diagram at each temperature was could be mapped with as few as two independent measurements.
- A 3-dimensional phase diagram was created for the FE – AF phase diagram in pressure (0 to 500MPa), temperature (25 to 125°C), and electric field (0 to $\pm 6 MVm^{-1}$).
- FE_R – FE_O phase transformation in domain engineered cut and poled PIN-PMN-PT was characterized and shown to have phase transformation criterion that is linearly dependent on stress, electric field, and temperature. The phase diagram in stress, electric field, and temperature could thus be characterized using as few as three independent measurements.
- A generalized micromechanics material model was developed to model variant switching and phase transformation. The material model was developed using a generalized approach that is capable of modeling both the AF – FE and FE_R – FE_O phase transformations. The model describes non-linear constitutive behavior as a combination of linear constitutive and nonlinear spontaneous polarization and strain. A finite element

frame work was used to solve the field equations for the constitutive material. A discussion on how experimental values relate to model parameters was presented.

- The energy harvesting characteristics of single crystal relaxor ferroelectric PIN-PMN-PT was assessed. First, specimens were loaded under an ideal energy harvesting cycle, similar to the reverse-Brayton cycle, to assess the maximum possible energy harvesting characteristics of the material. Second, specimens were loaded under sinusoidal stress loading cycles and the energy harvesting characteristics of PIN-PMN-PT was assessed under changes of load frequency and electric load impedance.

1.4 Dissertation Overview

The following describes each chapter and serves as an overview of the dissertation.

Chapter 2: The FE – AF phase transformation in near 95/5-2Nb PZT ceramic ferroelectric material was explored under loading of pressure, bipolar electric field, and temperature combinations. Electrodes were attached to surfaces of 95/5-2Nb plates and placed inside a high pressure chamber with a built in PID controlled heating element in order to subject specimens to pressure and temperature combinations. A Sawyer-Tower circuit and high voltage amplifier was connected in line with the specimen in order to load the specimen with a large bipolar electric field and capture the electric displacement response. Monoplex® DOS was used as the working fluid, heating fluid, and insulating fluid within the pressure chamber. At fixed combinations of pressure and temperature, specimens were electrically loaded with a large biaxial electric field and the corresponding electric displacement was captured to determine the material phase. Increasing pressure was shown to stabilize the AF phase and destabilize FE

phase. Electric field was shown to stabilize the FE phase and destabilize the AF phase. Temperature was shown to slightly stabilize the FE phase over the AF phase. The phase transformation criterion for FE to AF and AF to FE were shown to be linear functions of stress and electric field and non-linear functions of temperature. Electric field – pressure phase diagrams were created at different temperatures for the FE – AF phase transformation. The characteristics of the phase diagram indicated three types of FE – AF phase transformations occurring over the temperature range tested. The linear dependence of the phase transformation criterion allowed for the development of simplified and streamlined material characterization techniques.

Chapter 3: The FE_R – FE_O phase transformation in near MPB FE_R composition PIN-PMN-PT single crystal relaxor ferroelectric material was explored under stimulation of stress, electric field, and temperature combinations. Near MPB composition PIN-PMN-PT single crystals (30-32% PT) were cut and electrically poled in the $[011]$ direction such that compressive stress can be applied on $[100]$ faces and electric field can be applied in the $[011]$ direction using a load frame and high voltage amplifier. Strain gauges were attached and a Sawyer-Tower circuit was connected in line with the electrical system such that strain in the $[100]$ direction and electric displacement in the $[011]$ direction could be captured. Specimens were submerged in an electrically insulating Fluorinert™ fluid with a PID controlled heating element such that temperature could be applied and monitored. The material was loaded in combinations of stress, electric field, and temperature from the FE_R phase across a phase transformation to the FE_O phase. Stress, electric field, and temperature were shown to contribute towards the destabilization of the FE_R phase and stability of the FE_O phase. Stress, electric field, and

temperature phase diagrams were created for the FE_R – FE_O phase transformation. The phase transformation criterion for FE_R to FE_O and FE_O to FE_R were shown to be linear functions of stress, electric field, and temperature. The linear dependence of the phase transformation criterion allowed for the development of simplified and streamlined material characterization techniques.

Chapter 4: The energy harvesting characteristics and performance of PIN-PMN-PT was explored by loading a specimen through an idealized energy harvesting thermodynamic cycle. This idealized energy harvesting thermodynamic cycle was modeled after the reverse-Brayton cycle where pressure, volume, temperature, and entropy are replaced by uniaxial stress, strain, electric field, and electric displacement. The thermodynamic cycle consisted of four steps: 1) Isocharge (constant electric displacement) compression. 2) Isostress electric displacement change to minimize electric field. 3) Isocharge decompression. 4) Isostress electric displacement change to minimize electric field. In theory, the ideal cycle generates the greatest electrical energy density per cycle per over a given operating stress range independent of excitation frequency or electric load impedance values. The cycle was implemented over various stress excitation ranges across phase transformation regions. Input mechanical and output electrical energy densities per cycle are compared. A 66% conversion rate of mechanical to electrical energy was achieved for mechanical energy in surplus of the overhead cost of driving the phase transformation at low applied stress intervals. At high stress intervals further electrical energy loss occurred due to internal electrical leakage across the specimen.

Chapter 5: The electrical load and frequency dependence of non ideal energy harvesting cycles in PIN-PMN-PT are explored. Cyclic mechanical stress loading of ~5MPa was applied

across the phase transformation hysteretic region. Size of the mechanical hysteresis (input mechanical energy) was shown to increase as electrical load impedance was increased. The corresponding increase in input mechanical energy saw a 66% conversion to output electrical energy. The same material was excited over the same stress amplitude over a linear piezoelectric region in the FE_R phase. The energy density of the phase transformation region was on average 27 times, with a maximum of 108 times, greater than that of the linear piezoelectric region. An electromagnetic shaker and a prestress fixture was used in conjunction to supply a prestress and a variable frequency cyclic stress onto the specimen to measure the frequency and electrical load impedance dependence of the energy harvesting characteristics. The result showed the energy density per cycle scaled linearly with electric load impedance and linearly with frequency. The power density scaled linearly with electric load impedance and quadratically with frequency. This was verified with a simple electrical model of the specimen and electric load impedance. Under pure tone mechanical actuation, the model predicts an optimum electric load impedance value for a given drive frequency.

Chapter 6: A non-linear ferroelectric material model was developed to simulate the FE_R – FE_O phase transformation in PIN-PMN-PT and the FE – AF phase transformation in 95/5-2Nb PZT on a length scale where domain-domain interactions can be ignored and material properties are represented by a volume average behavior of many superimposed single-crystal single-domain grains where each grain has a phase variant value that can switch independently of all other grains. The ferroelectric material model was developed to improve upon linear piezoelectric models by incorporating ferroelectric and ferroelastic phenomena. The switching model with linear piezoelectric constitutive behavior creates a nonlinear ferroelectric constitutive model for the finite element frame work to solve the field equations. The phase/variant

switching model uses energy based switching criteria to determine if changes are required in phase-variant of the material.

Chapter 7: A phase field model was developed using a finite element framework to model domain-domain interactions. A material model solves for updates to the local spontaneous polarization and strain using the Time – Dependent Landau – Ginzburg equation and Landau – Devonshire type multi-well potential energy functions. The material model worked in conjunction with a linear piezoelectric finite element model to solve for local stresses and electric fields that change the shape of the Landau – Devonshire free energy landscape. The effect of this iterative exchange leads to a free energy minimization that determines the domain structure of the simulated material. The effect of geometry and free energy function terms on the domain structure and 90 and 180 domain wall behavior is discussed. A physical description of the gradient energy term in Landau-Devonshire theory was presented. Potential uses of the finite element based phase field models include the exploration of phase transformations on domain – domain interactions and domain/phase boundaries. Methods to implement FE – FE and FE – AF phase transformations in phase field models were presented.

CHAPTER 2

PRESSURE, TEMPERATURE, AND ELECTRIC FIELD DEPENDENCE OF PHASE TRANSFORMATIONS IN NB MODIFIED 95/5 LEAD ZIRCONATE TITANATE

The motivation for this chapter was to gain insight into the FE – AF phase transformation in ceramic niobium modified lead zirconate-lead titante, $Pb_{0.99}Nb_x(Zr_{0.95}Ti_{0.05})_{1-x}O_3$ (PZT 95/5-xNb) under combined temperature, pressure, and electric field loading. Ceramic niobium modified 95/5 lead zirconate-lead titanate (PZT) undergoes a pressure induced ferroelectric to antiferroelectric phase transformation accompanied by an elimination of polarization and a volume reduction. Electric field and temperature drive the reverse transformation from the antiferroelectric to ferroelectric phase. The phase transformation was monitored under pressure, temperature, and electric field loading. Pressures and temperatures were varied in discrete steps from 0MPa to 500MPa and 25°C to 125°C respectively. Cyclic bipolar electric fields were applied with peak amplitudes of up to $6MVm^{-1}$ at each pressure and temperature combination. The resulting electric displacement – electric field hysteresis loops were open "D" shaped at low pressure, characteristic of soft ferroelectric PZT. Just below the phase transformation pressure, the hysteresis loops took on an "S" shape, which separated into a double hysteresis loop above the phase transformation pressure. Far above the phase transformation pressure, when the applied electric field is insufficient to drive an antiferroelectric to ferroelectric phase transformation, the hysteresis loops collapse to linear dielectric behavior. Phase stability maps were generated from the experimental data at each of the temperature steps and used to form a three dimensional pressure – temperature – electric field phase diagram.

2.1 Experimental Approach

2.1.1 Specimen Preparation

Low porosity 95/5-2Nb PZT specimens were obtained from TRS Technologies, Inc. and were prepared by a solid oxide route. The constituent oxides were batched in stoichiometric proportions after adjusting for ignition losses and vibratory milled with stabilized zirconia media for 16 hours in an aqueous slurry. Proper particle size reduction and thorough mixing were ensured by using a dispersant (Tamol) and controlling the pH with ammonia additions. After milling, the slurries were dried and then ground to 80-mesh. The sieved powders were then calcined at various temperatures in alumina crucibles to achieve a homogeneous perovskite-structure. X-ray diffraction was used to determine the phase-purity of the final product. Ceramics of each composition were fabricated by adding a polymer binder (Rhoplex HA-8) and then uniaxially pressing pellets. A high-pressure cold isostatic press (CIP) was used to enhance the density. The pellets were then sintered (densified) at ~1150 ^{o}C for 1-3 hours. The atmosphere during sintering was maintained using a source powder containing excess lead. After sintering, specimens were cut and polished to dimensions of 0.25×10×10 mm^3. Fired-on silver electrodes (DuPont 7095) were applied in preparation for poling and dielectric measurements. The parts were poled with an electric field of 20 kV/cm applied across the 0.25 mm thickness at a rate of ±250 V/min for 3min at 65 ^{o}C. Capacitance, dielectric loss, and remnant polarization were measured to verify the quality of the material. Wires were attached to the electroded surfaces using silver epoxy and the entire specimen was coated with pliable non-conductive Duralco™ 4525-IP epoxy and wrapped with a layer of Teflon® tape.

2.1.2 Experimental Arrangement

A diagram of the experimental arrangement is shown in Figure 2-1. A cylindrical high-pressure chamber with internal dimensions of 1-inch diameter and 3.5-inch depth was used to subject specimens to pressure. Pressure was provided by a high-pressure pump capable of delivering pressures of up to 1.5GPa. Electric field was applied using a signal generator in conjunction with a high-voltage amplifier. The output of the amplifier was fed into the pressure chamber across the specimen and out of the pressure chamber using specially designed electrical feed-throughs. The electrical return path for the power supply was connected to a large "read" capacitor (9.5μF) outside the pressure chamber to form a Sawyer-Tower circuit. The read capacitor was connected to a high input impedance electrometer to monitor the electric displacement. The input impedance of the electrometer was sufficiently high that the voltage on the "read" capacitor could be monitored without draining the charge and altering the electric displacement measurement. Additional electrical feed-throughs connected a Type J iron-constantan thermocouple. The chamber temperature was controlled using a PID controller connected to heating elements within the pressure chamber. The chamber was filled with Monoplex® DOS, which acts as an electrical insulator, working fluid, and heat transfer fluid.

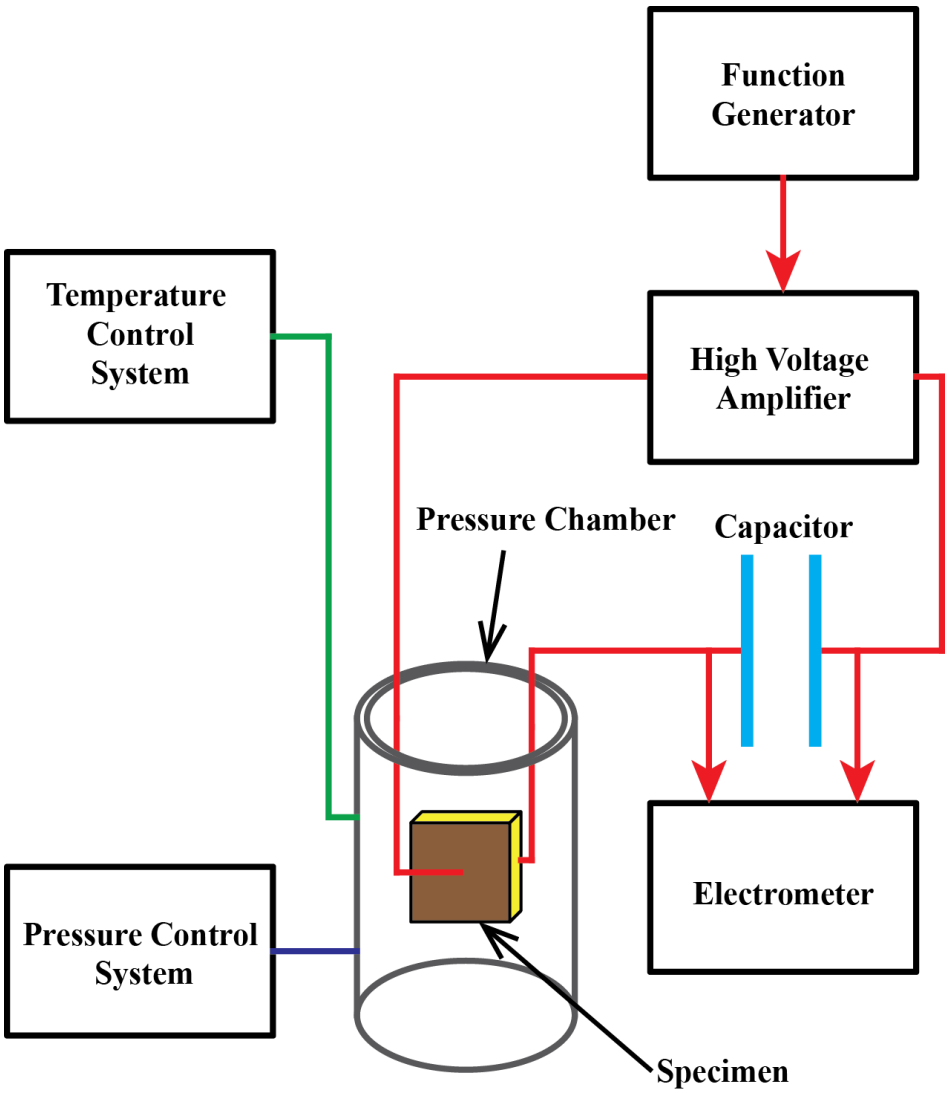

Figure 2-1. Experimental setup for pressure, temperature, and electric field loading. Sawyer – Tower circuit was used to capture electric displacement behavior.

2.1.3 Experimental Methodology

The specimens were subjected to the combinations of pressure, electric field, and temperature shown in Table 2-1. The temperatures were held fixed at 25ºC, 50ºC, 75ºC, 100ºC, and 125ºC. At each temperature, pressure was increased from 0MPa to 500MPa and back down to 0MPa in increments of approximately 25MPa. At each pressure and temperature combination, bipolar electric field loading was applied to specimens in the form of a triangle wave with a frequency of 2Hz and peak amplitude of $6MVm^{-1}$ for 25ºC and $5MVm^{-1}$ for 50ºC, 75ºC, 100ºC, and 125ºC. Electric fields greater than $6MVm^{-1}$ were not used in order to avoid dielectric breakdown. In low porosity 95/5 PZT break down occurs at electric fields around 6.8-7.5MVm^{-1} [147].

Table 2-1. Temperature, pressure and electric field loading conditions

Temperature (°C)	**Pressure Range (MPa) (~25 MPa increments)**	**Electric Field Peak Amplitude (MVm^{-1})**
25	0-500	6
50	0-500	5
75	0-500	5
100	0-500	5
125	0-500	5

2.2 Results

Electric displacement – electric field, D – E, curves are shown in Figure 2-2 for select temperature and pressure loading steps. Figures 2.2a and 2.2b show the same data in 2-dimensions and 3-dimensions respectively. At pressures to just below the phase transformation pressure, the shape of the D – E hysteresis curves take on a characteristic "D" shaped single loop typical of the FE phase because the FE phase retains remnant polarization that is only reoriented when electric field reaches the coercive field. In this work, a depolarizing field is defined as an electric field that is applied in the opposite direction of the material polarization. As pressure is increased, the energetic stability of the FE phase is weakened. After a certain pressure threshold is reached, depolarizing fields smaller than the FE phase coercive electric field will destabilize the FE phase and drive the material into the AF phase. Further increasing the electric field drives the material back to the FE phase. This causes the D – E hysteresis loops to take on an "S" shape prior to full separation into double loops and, after sufficient pressure is reached, to take on the double loop shape. In the double loop regime, a non-hysteretic AF region occurs between the two separated hysteresis loops. When the pressure is further increased such that the applied electric field is insufficient to drive the AF to FE transformation, the D – E curve takes on a non-hysteretic dielectric behavior.

Increasing temperature results in significant changes in the pressure dependent D – E loop behavior. Under low stress conditions, the FE phase D – E behavior experiences a noticeable drop in coercive field and remnant polarization as temperature increases. At zero pressure, a comparison of the 25°C to 125°C D – E loops shows the coercive field and remnant electric displacement values change from $1.8 MVm^{-1}$ to $1.0 MVm^{-1}$ and $0.33 Cm^{-2}$ to $0.29 Cm^{-2}$

respectively. Furthermore, the width of the FE – AF phase transformation hysteresis decreases as temperature increases. At 25°C, the applied electric field range of ±6MVm^{-1} is barely able to capture the full double loop behavior without a significant non-hysteretic AF zone. At 125°C, the FE – AF hysteresis is much narrower and the applied ±5MVm^{-1} is able to capture the entire double loop behavior with a significant non-hysteretic AF zone. The threshold pressure for the FE – AF transformation is also observed to increase with temperature. At 25°C, the D – E loop first displays a fully separated double loop behavior and has a non-hysteretic AF phase at 325MPa. At 125°C, the same double loop behavior with non-hysteretic AF phase requires 380MPa.

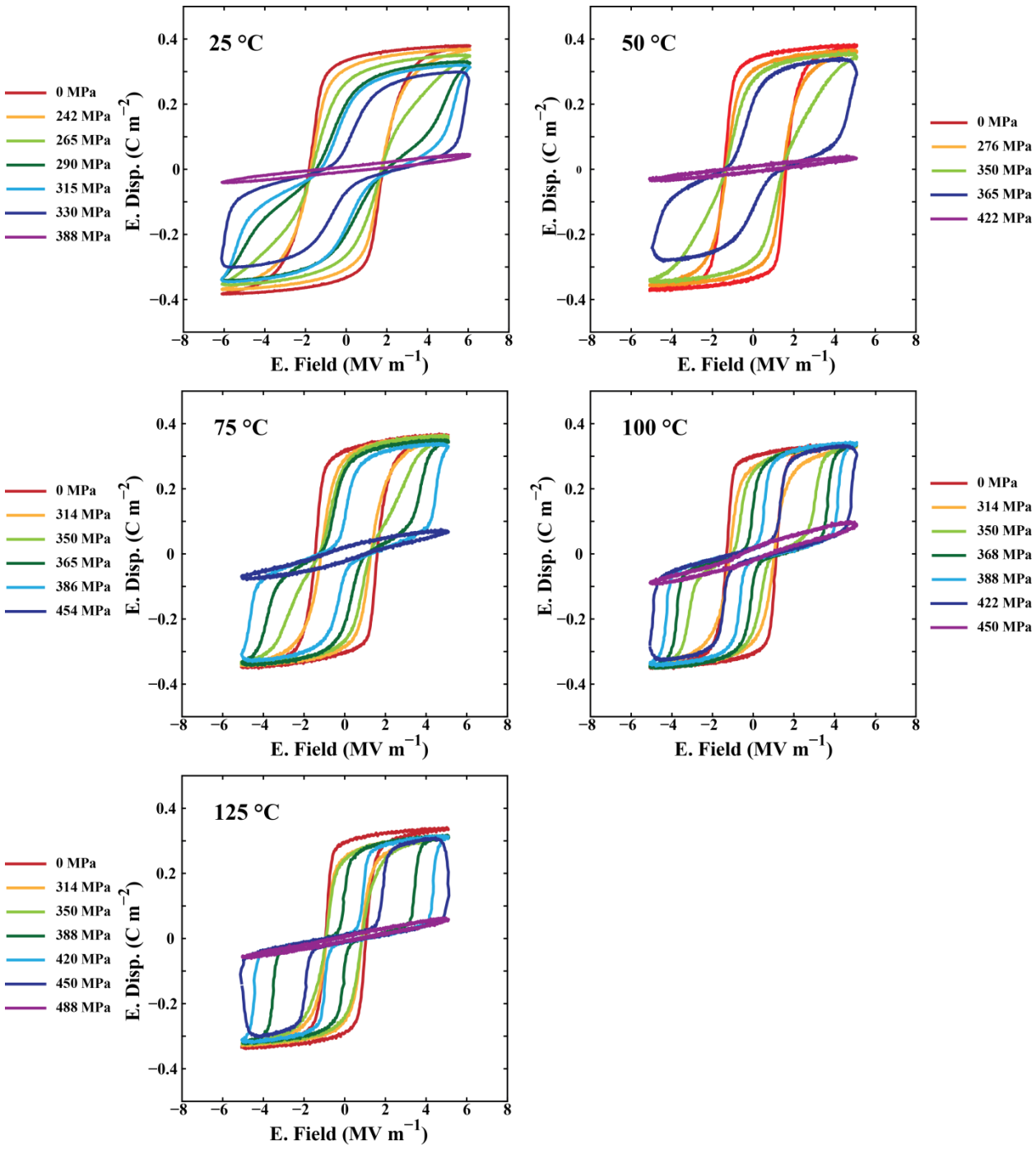
25 °C
0 MPa
242 MPa
265 MPa
290 MPa
315 MPa
330 MPa
388 MPa
50 °C
0 MPa
276 MPa
350 MPa
365 MPa
422 MPa
75 °C
0 MPa
314 MPa
350 MPa
365 MPa
386 MPa
454 MPa
100 °C
0 MPa
314 MPa
350 MPa
368 MPa
388 MPa
422 MPa
450 MPa
125 °C
0 MPa
314 MPa
350 MPa
388 MPa
420 MPa
450 MPa
488 MPa
E. Disp. (C m−2)
E. Field (MV m−1)

(a)

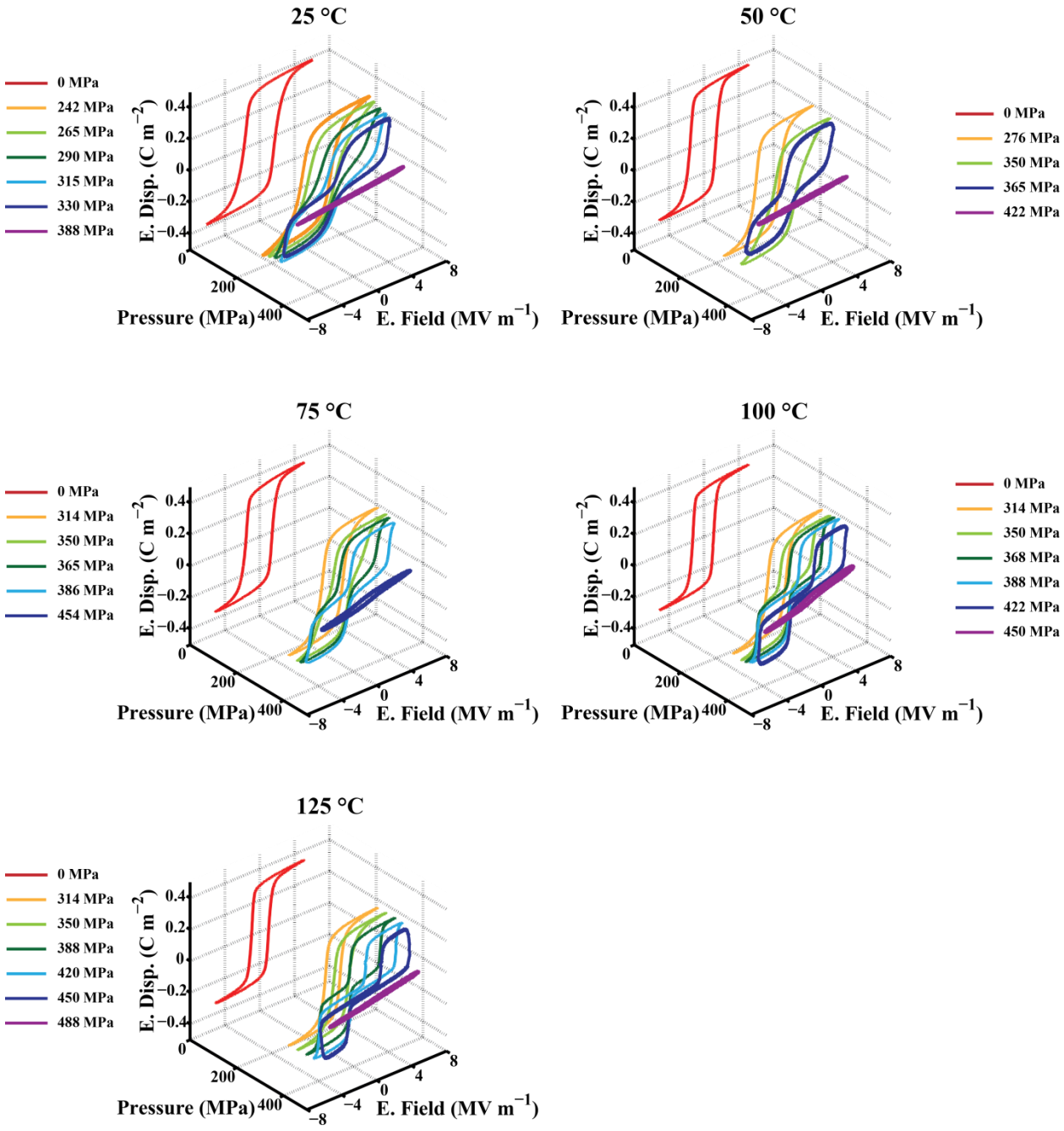

(b)

Figure 2-2. a) Two dimensional and b) three dimensional plots of select bipolar electric displacement – electric field loops at pressure and temperatures steps.

2.3 Discussion

The saturation polarization value of FE 95/5 PZT is approximately 0.4 Cm^{-2}, therefore electric displacement values of 0.1 Cm^{-2}, 0.2 Cm^{-2}, and 0.3 Cm^{-2} were used as indicators of the material reaching 25%, 50%, and 75% of the saturation value of the poled FE phase. On the polarizing branch of the electric field cycle, the field values corresponding to 0.2 Cm^{-2} and 0.3 Cm^{-2} were determined for each loop, and on the depolarizing branch, the field values corresponding to 0.2 Cm^{-2} and 0.1 Cm^{-2} were determined as shown in Figure 2-3. Contour curves were created using data from D – E loops measured at each temperature. This is shown in Figure 2-3 for the 25°C measurements. These four critical field values were plotted as a function of pressure in Figure 2-3.a. The resulting plot gives a clear indication of the phase transformation. The critical field values vs. pressure lines abruptly change slope at the phase transformation. The four critical field values for all that correspond to electric displacement values of 0.1Cm^{-2}, 0.2Cm^{-2}, 0.2Cm^{-2}, and 0.3 Cm^{-2} for all temperatures are shown in appendix B.

Methods in previous studies used to determine phase boundaries relied on peaks in dielectric and tanδ response as indicators of phase transition points [22, 24]. Peaks in dielectric and tanδ response correspond to roughly 50% FE volume fraction, but do not indicate the sharpness of the phase transformation, where a sharp transformation is defined to occur over a small range of pressure. The critical electric field vs. pressure curves corresponding to the four electric displacement values help to clearly illustrate the sharpness of phase transformations in 95/5 PZT. The 25% and 75% FE curves close to the 50% FE curves indicate a sharp transition that occurs over a small electric field or pressure range; and conversely, contour curves further

apart indicate a more gradual phase transformation where the phase transformation occurs over a large electric field or pressure range.

In Figure 2-3.a, two distinct regions exist on the critical electric field vs. pressure plots. An FE region occurs at low pressures and is characterized by contour lines that vary little in electric field as pressure is increased and remain mostly parallel to the pressure axis. During this stage, the contour lines outline the coercive fields of the top half of the "D" shaped bipolar FE – FE hysteresis. A significant bend in the contour curves can be observed at higher pressures after which an AF region is distinguished. During this stage, the contour lines outline the coercive fields of the top half of the "S" and double loop hysteresis curves. This marks a region where increasing pressures require increasing electric fields to stabilize the FE phase and the contour lines outline the coercive fields of the FE – AF hysteresis.

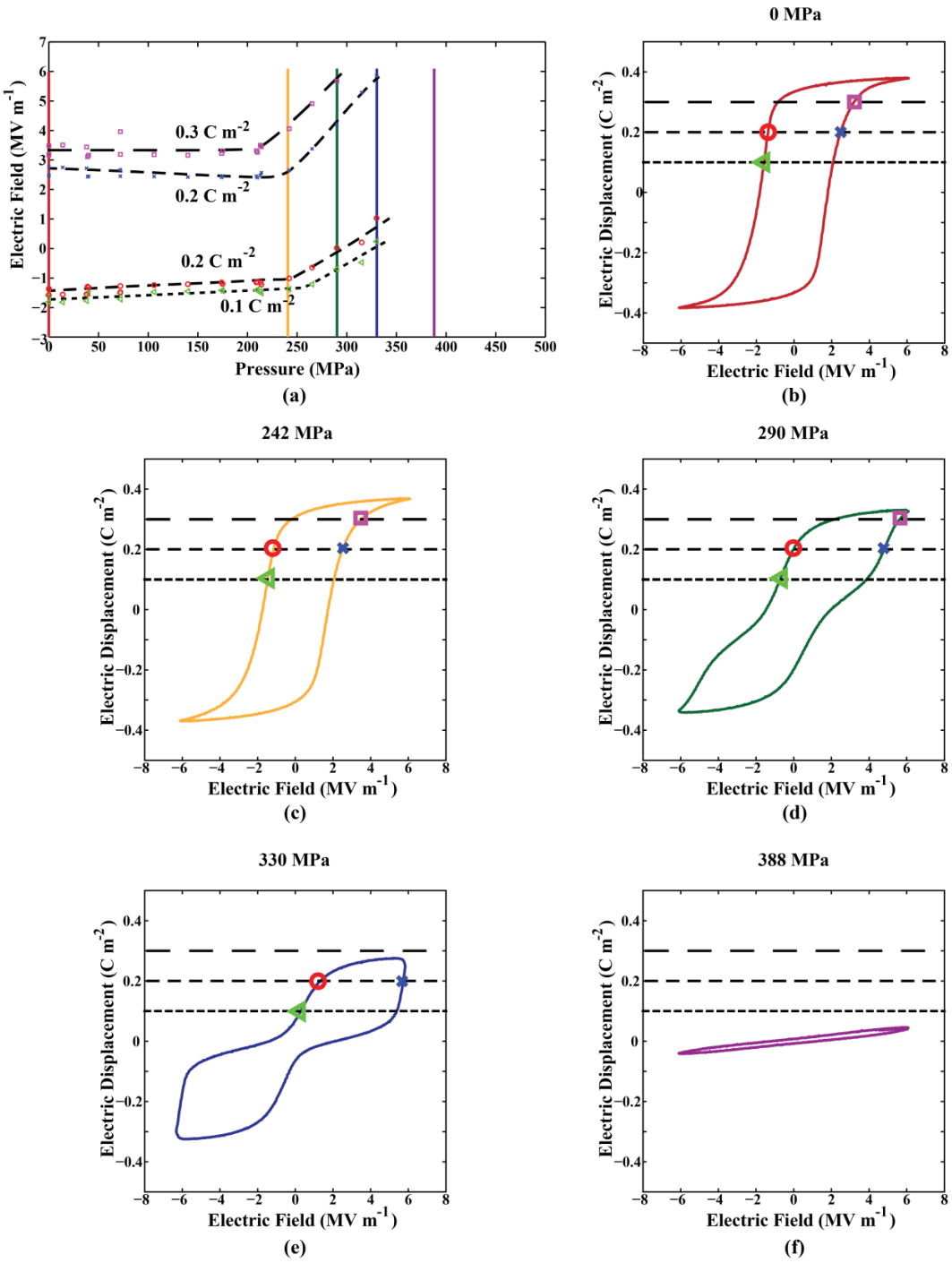

Figure 2-3. a) Electric displacement contour curves for the using D – E loop data at 25°C. Contour curves are created for values of 0.1 Cm^{-2}, 0.2 Cm^{-2}, and 0.3 Cm^{-2} which correspond to as 25%, 50%, and 75% electric poling saturation of the ferroelectric state. 0.2 Cm^{-2} and 0.3 Cm^{-2} curves are shown for the positive loading segment of the electric field and 0.1 Cm^{-2} and 0.2 Cm^{-2} curves are shown for the negative loading segment of the electric field. Examples are shown with D – E loops for pressures of b) 0 MPa, c) 242 MPa, d) 290 MPa, e) 330 MPa, and f) 388 MPa.

The electric field and pressure FE – AF phase diagrams shown in Figure 2-4 were created by mirroring the critical field vs. pressure plots across the zero electric field axis. The phase diagrams are symmetric in electric field. Four regions in the pressure – electric field domain are defined at each temperature: non-hysteretic FE, non-hysteretic AF, hysteretic FE – FE, and hysteretic FE – AF. The low pressure region between the 0.3 Cm^{-2} and mirrored 0.3 Cm^{-2} curves represents the hysteretic FE – FE area (blue and white hash) and the region with electric field magnitudes in excess of these curves represents the fully poled FE region (solid blue). At high pressures, 0.3 Cm^{-2} and 0.1 Cm^{-2} curves represent the AF to FE and FE to AF phase transformation field values. Between the 0.3 Cm^{-2} and 0.1 Cm^{-2} curves is the AF – FE hysteretic region (solid purple) and the boundary for this region can be found by extrapolating the high pressure 0.3 Cm^{-2} curve back to the zero electric field axis. The high pressure region between the 0.1 Cm^{-2} and mirrored 0.1 Cm^{-2} curves represents the non-hysteretic AF phase (solid red).

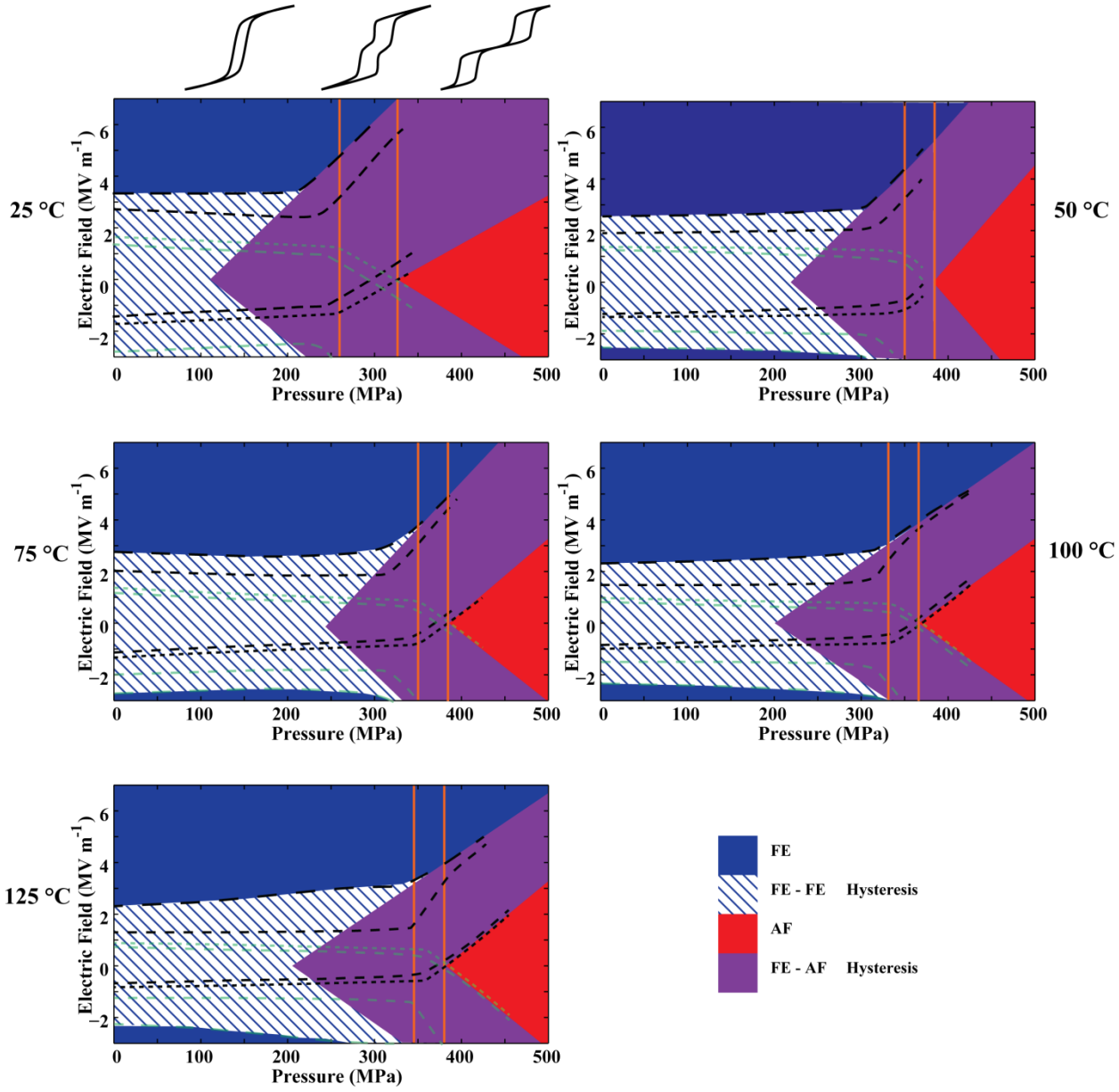

Figure 2-4. FE – AF phase diagrams for 25°C, 50°C, 75°C, 100°C, and 125°C constructed using electric displacement contour diagrams. Four major regions are shown: non-hysteretic FE, non-hysteretic AF, hysteretic FE – FE, and hysteretic FE – AF. Three D – E loop behavior experiences three characteristic zones as pressure is increased: "D" shaped hysteresis, "S" shaped hysteresis, and double-loop hysteresis.

Three distinct pressure zones appear as pressure is increased corresponding to the "D," "S," and double-loop hysteresis loops occurring at low, intermediate, and high pressure respectively. These zones are illustrated in the phase stability plots of Figure 2-4 where they are separated by orange vertical lines. For materials that start out in the FE phase, the "D" shaped hysteresis zone begins at zero pressure and ends at the pressure where the 0.1 Cm^{-2} curve changes in slope. This region is characterized by a FE polarization reorientation hysteretic behavior caused by domain wall motion at low electric fields and a non-hysteretic saturated FE region at high electric field values electric field values. The "S" shaped hysteresis zone begins at the pressure where the 0.1 Cm^{-2} curve changes slope and ends at the intersection of the 0.1 Cm^{-2} and mirrored 0.1 Cm^{-2} curves. In this region the hysteretic region is comprised of a mixture of FE polarization reorientation and FE – AF phase transformation. The intersection of the 0.1 Cm^{-2} and mirrored 0.1 Cm^{-2} indicate the pressure at which the material is no longer ferroelectric in the absence of electric field. This is when the non-hysteretic AF phase begins and the double loop hysteresis loops fully separate. In this high pressure AF phase region, the full double loop behavior is absent if the electric field applied does not cross from the red AF region into the blue FE region. Thus the full double loop behavior, for the applied electric field magnitudes, is only observed for temperatures above 75 °C.

The characteristics of the 25°C, 50°C, 75°C, 100°C, and 125°C phase transformations fall into three main groupings: [25°C]; [50°C and 75°C]; and [100°C and 125°C]. These groupings correspond to the FE_{R1}-AF_O, FE_{R1}-AF_T, FE_{R2}-AF_T phase transformations respectively. The pressure loading paths at constant temperature and corresponding phase transformation type are illustrated in Figure 2-5. Looking at the phase stability plots in Figure 2-4, the FE_{R1}-AF_O phase diagram at 25°C is distinguished from the FE_{R1}-AF_T and FE_{R2}-AF_T phase diagrams most

prominently by a smaller zero electric field FE to AF phase transformation pressure. The zero electric field FE to AF phase transformation pressure for FE_{R1}-AF_O occurs at 325MPa while for the same FE to AF transformation, the transformation pressure occurs close to 380MPa for the FE_{R1}-AF_T and FE_{R2}-AF_T transformations. This is in agreement with the phase diagram reported by Fitz and Keck [24] shown in Figure 2-5 where the FE – AF_O transformation pressure is significantly more temperature dependent than the FE – AF_T transformation pressures. From Figure 2-4, the FE_{R1}-AF_O phase boundary is also differentiated from the FE_{R1}-AF_T and FE_{R2}-AF_T phase boundaries by its extremely wide critical electric field hysteresis and non-parallel forward FE to AF phase transformation field curve and reverse AF to FE phase transformation field curves. The non-constant width of the phase transformation hysteretic region implies the energy barrier for transformation does not remain constant as pressure and electric field are increased. The large electric field hysteresis of the phase transformation implies a much larger energy barrier associated with both the forward and reverse transformations.

Figure 2-4 also contrasts the difference between the FE_{R1}-AF_T and FE_{R2}-AF_T phase diagrams. While the two share similar zero electric field FE to AF phase transformation pressures and exhibit fairly parallel forward and reverse phase boundary curves, the two types of phase diagrams can be discriminated by the slope of the phase boundary curves. The forward and reverse phase boundary curves for the FE_{R1}-AF_T have a greater slope than the FE_{R2}-AF_T curves. This implies that the FE_{R1}-AF_T phase transformation has wider phase transformation hysteresis and the threshold electric fields are more sensitive to changes in pressure than the FE_{R2}-AF_T phase transformation threshold electric fields.

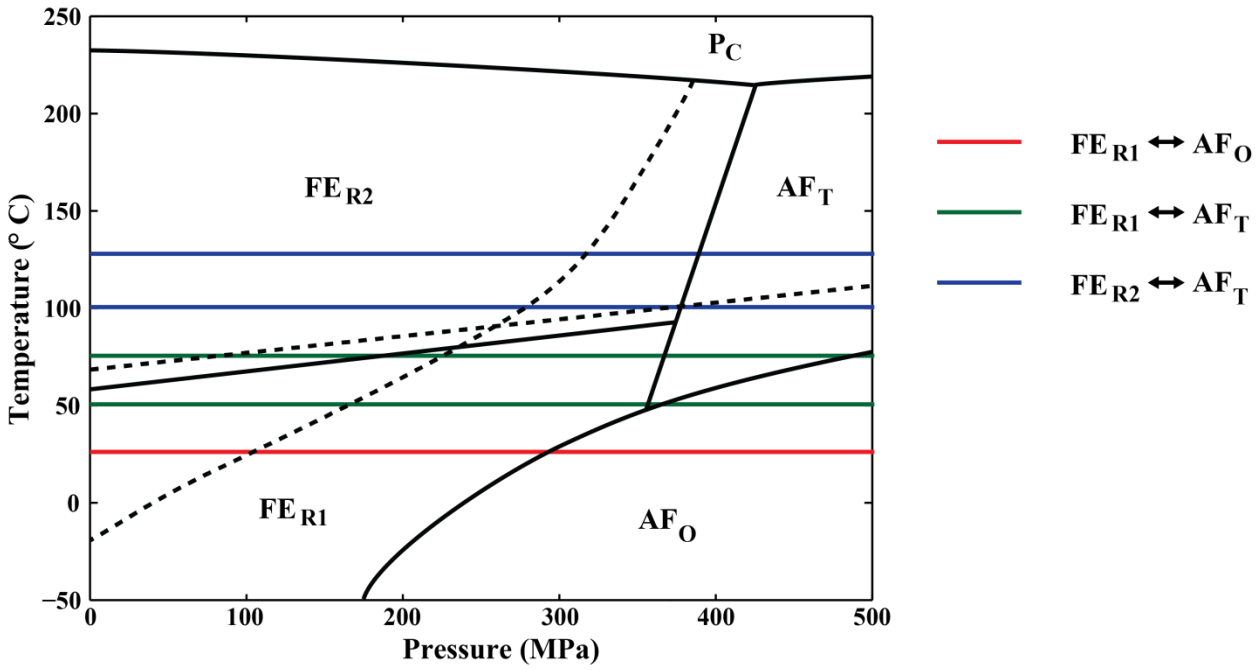

Figure 2-5. Pressure and temperature loading paths of the 95/5 PZT specimen. Red, green, and blue paths correspond to FE_{R1}-AF_O, FE_{R1}-AF_T, and FE_{R2}-AF_T phase transformations respectively.

The phase stability plots constructed in Figure 2-4 extend the temperature – pressure phase diagram work by Fritz and Keck [24] such that the phase diagram of 95/5 PZT is mapped with an additional axis, electric field, to produce a temperature – pressure – electric field phase diagram as shown in Figure 2-6.a. The material transforms from the FE phase into the AF phase when the pressure – electric field – temperature combination crosses the FE to AF phase transformation criteria surface (outlined in red). Starting in the AF phase, the material transforms back into the FE phase when the pressure – electric field – temperature combination cross the AF to FE phase transformation criteria surface (outlined in blue). Grey lines indicate the intersection of the FE – AF hysteretic region with the figure axis limits.

While the zero electric field FE to AF phase transformation pressure is experimentally measurable by finding the critical pressure where the "S" shaped hysteresis changes into the double loop hysteresis, the reverse zero electric field AF to FE phase transformation pressure cannot be found experimentally by measuring electric displacement because in the absence of electric field 95/5 PZT will revert from a AF phase to unpoled FE phase as it crosses the AF to FE transformation pressure. The AF and unpoled FE phases are indistinguishable when measuring only electric displacement. Instead, the zero electric field AF to FE phase transformation pressure is calculated by extrapolating the AF to FE critical electric field curve to the pressure axis intercept as shown in Figure 2-4. In Figure 2-6.a, phase transformation criteria curves backed by experimental data are bold and extrapolated curves are slim. On the zero electric field plane, Figure 2-6.a compares the zero electric field FE to AF and the AF to FE transformation pressures calculated from the experimental data in this study with that reported in the Fritz and Keck study [24]. The zero electric field FE to AF transformation pressures are collected in this study are mostly agreeable to those from the FE to AF phase boundaries identified in the Fritz and Keck study. A small but noticeable difference is that the FE to AF phase boundary found in this study suggests that the FE to AF_T phase transformation pressure from 50°C to 125°C is comparatively temperature independent. There is greater deviation for the extrapolated AF to FE phase boundary compared to that reported by Fritz and Keck. This can be explained by the inaccuracies of the extrapolation assumption, which assumes a linear AF to FE phase boundary which is less reliable than the dielectric measurements used by Fritz and Keck.

The mapping of the 3-dimensional FE – AF phase transformation criteria allows the creation of phase diagrams at operating electric fields of devices. In pulse power applications,

electric fields can reach magnitudes close to that of break down fields and knowledge of high field electrical effects on phase transformations is critical. Figure 2-6.b shows the FE – AF hysteresis at an electric field of $5MVm^{-1}$ created by taking a slice of the phase transformation region in Figure 2-6.a at $5MV^{-1}$. In this case, the FE to AF curve is extrapolated and the AF to FE curve is experimentally measured. At $5MVm^{-1}$, the FE – AF hysteresis is shifted right by approximately 200MPa. This is consistent with expected results as the electrical AF phase energy destabilization is given by the product of the electric field with the electric displacement change from AF to FE phase and requires the counter balance of mechanical AF phase energy stabilization given by the product of the phase transformation critical pressure shift and the volumetric strain change of the AF to FE phase transformation. With the AF to FE electric displacement change of $0.35Cm^{-2}$ at an electric field of $5MVm^{-1}$ and the volumetric strain change of the AF to FE of 0.8% at a pressure change of 200MPa, the electrical destabilization is $1.75MJm^{-3}$, which is approximately on par with the mechanical stabilization of $1.6MJm^{-3}$.

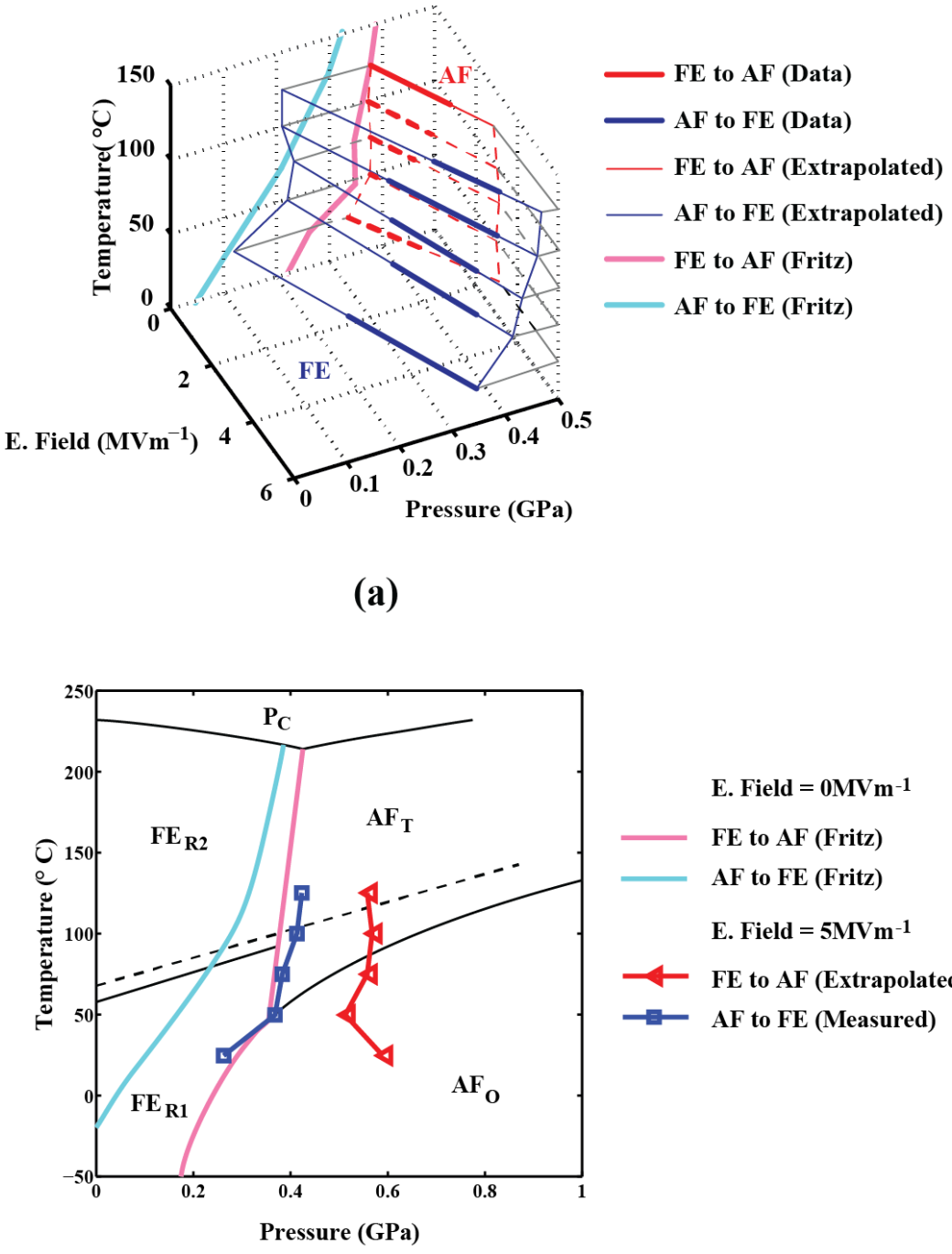

Figure 2-6. a) 3-D phase diagram of the FE – AF phase transformation in 95/5 PZT shown for drive parameters of electric field and temperature. Additional comparison of the critical phase transformation parameters with earlier work on the pressure-temperature phase diagram mapped by Fritz and Keck[24]. b) Shift in the FE – AF hysteretic region at 5MVm^{-1} compared to the 0MVm^{-1} hysteresis from the Fritz and Keck study.

2.4 Concluding Remarks

The polarization of the 95/5 PZT was recorded under cyclic bipolar electric field and combinations of static pressure and temperature. Evidence for FE – AF phase transformation of the ceramic under electric field and pressure loading was measured. Select contour curve maps of the electric displacement were created to assist in the mapping of electric field and pressure phase diagrams at different temperatures and the sharpness and saturation characteristics of D – E loops at each phase was shown. The phase transformation criterion for both the forward FE to AF and reverse AF to FE phase transformations are observed to be linear equations of applied electric field and pressure. Increasing pressures are observed to stabilize the AF phase and are counteracted by increasing electric fields that stabilize the FE phase. From 25°C to 125°C, three distinguishable types of phase diagrams are observed and can be attributed to the $FE_{R1} - AF_O$, $FE_{R1} - AF_T$, and $FE_{R2} - AF_T$ phase transformations when their pressure and temperature loading paths are compared to the pressure-temperature phase diagram explored by Fritz and Keck. The linearity of the phase transformation criterion curves greatly simplifies the phase diagram characterization process of the material. D – E loops conducted at two pressures are sufficient to determine the slope of the phase transformation criterion curve. It is therefore possible to reduce the number of experimental measurements required to capture the behavior of the electric displacement contour curves and, as a consequence, the phase diagram. Shown in Figure 2-7, the contour curves for each type of hysteresis, at a particular temperature, can be captured using D – E loop measurements conducted at two pressures. This result in a requirement of four total distinct pressure D – E loops to capture both the FE – FE and FE – AF hysteresis, and two distinct pressure D – E loops to map the FE – AF hysteresis; substantially reducing the experiments and tests required to map the electric field-pressure phase diagram.

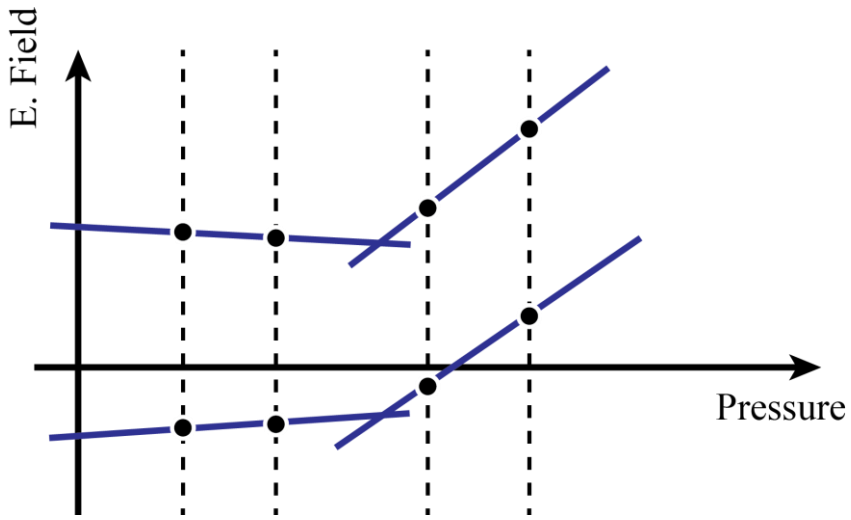

Figure 2-7. Characterization of the electric displacement contour plot in 95/5 PZT using four pressure measurements. Two low pressure D – E loops are required to map the FE – FE hysteresis and two high pressure D – E loops are required to map the FE – AF hysteresis.

These results are important to material development for applications such as ferroelectric pulse power. A critical result is that a field of 5MV/m shifts the transformation pressure by 200MPa. This shift is linear in the range tested and suggests that if high voltage devices are designed, the resulting electric field across the ferroelectric element will interact with the transformation pressure. Higher pressure will be required to drive the FE-AF transformation to obtain higher voltages.

CHAPTER 3

CHARACTERIZATION OF THE FE_R – FE_O PHASE TRANSFORMATION IN PIN-PMN-PT

This chapter addresses the electrical, mechanical, and thermal characterization of the FE_R - FE_O phase transformations in single crystal relaxor ferroelectric PIN-PMN-PT crystals. The results have been published in Dong et al. [61-62]. Mechanical, electrical, and thermal load driven phase transformations were performed that shed light on the electrical – mechanical and thermal – mechanical phase transformation characteristics and energy transduction capabilities of the material. The FE_R – FE_O phase transformation and phase stability data aids in the design of future phase transformation energy harvesting work.

The choice of material in this study stems from the recent developments of ternary composition relaxor ferroelectrics. Ternary solid solutions like PIN-PMN-PT were developed to improve upon binary solutions like PMN-PT and PZN-PT by increasing Curie temperatures, coercive fields, and thermodynamic phase stability while still exhibiting large electromechanical coupling properties [148-149]. Despite increases in thermodynamic phase stability, PIN-PMN-PT is still capable of load driven FE – FE phase transformations similar to that found in PZN-PT and PMN-PT. Finkel et al [60, 150] reported elastic hysteretic behavior associated the with the FE_R to FE_O phase transition in PIN-PMN-PT and showed that PT concentrations close to the MPB composition resulted in sharp strain and polarization jumps during the phase transition. The increased thermal stability and sharp phase transformation properties make PIN-PMN-PT an ideal candidate for mechanical energy harvesting.

While there have been numerous characterizations of phase transformations in PMN-PT and PZN-PT, there have been few in depth studies on phase stability and the phase transformation strain – stress and electric displacement – electric field hysteresis characteristics of PIN-PMN-PT. In this study, $[011]$ cut and poled near MPB composition FE_R phase single crystal PIN-PMN-PT specimens were subject to combinations of uniaxial stress, electric field, and temperature loads through the FE_R – FE_O phase transformation. Strain and electric displacement data were characterized. The electric field dependence of stress driven phase transformation, the stress dependence of electric field driven phase transformation, and the stress dependence of temperature driven phase transformation are reported in this study. The results indicate the phase transformation criteria have a strong linear dependence on stress, electric field, and temperature loads. Phase transformations are indicated in the material by large jumps in polarization and strain and demonstrate large nonlinear electrical – mechanical coupling across the phase transformation hysteresis. These phenomena suggest the FE_R – FE_O phase transformation has potential in towards energy harvesting and thermal sensing applications.

3.1 Experimental Arrangement

3.1.1 Materials and Specimen Preparation

PIN-PMN-PT single crystal specimens grown by the Bridgeman method were provided by HC Materials Inc. The crystals had PT concentrations that place them on the FE_R side of a FE_R – FE_O phase boundary (PT concentrations at 30-32%). Shown in Figure 3-1, the specimens were prepared in the [011] cut and electrically poled configuration. Miller indices are referenced in the cubic configuration. Specimens were cut to bars of dimensions $4\times4\times12mm^3$ with the $4\times4mm^2$ faces cut in the [100] and $[\bar{1}00]$ directions and the $4\times12mm^2$ faces in the [011], $[0\bar{1}\bar{1}]$, $[0\bar{1}1]$, and $[01\bar{1}]$ directions. Gold (Au) electrodes were sputtered onto the [011] and $[0\bar{1}\bar{1}]$ surfaces and the specimens were poled along the [011] direction (d_{32} mode crystals). The specimens were cleaned in an ultrasonic cleaner and dehumidified overnight in a 30°C oven.

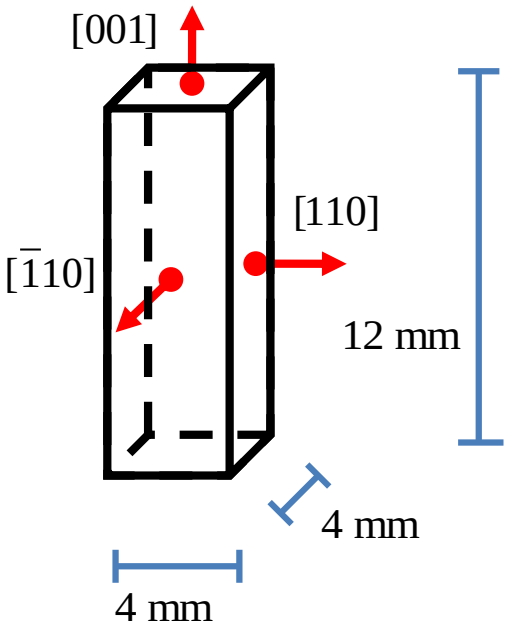

Figure 3-1. Dimensions and crystallographic orientation of PIN-PMN-PT specimens.

3.1.2 Experimental Procedure

The electrical, mechanical, and thermal driving forces for FE_R – FE_O phase transformations were characterized by subjecting [011] cut and poled PIN-PMN-PT single crystals to combinations of stress, electric field, and temperature loading. Stress, strain, electric field, and electric displacement, and temperature are defined as σ, ε, E, D, and T respectively. A coordinate system was introduced with the x_2 axis parallel to the [100] direction and the x_3 axis parallel to the [011] direction as shown in Figure 3-2. The applied loads were σ_{22}, E_3, and T and measured properties were ε_{22}, and D_3 where subscripts refer to directional indices. The orientation of these quantities relative to the crystallographic geometry is shown in Figure 3-2.

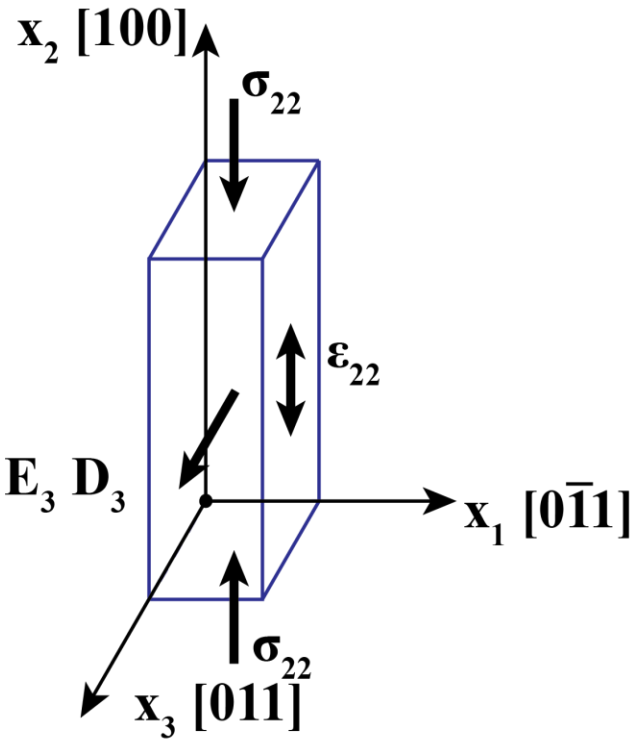

Figure 3-2. The introduced coordinate system relative to the [011] crystal cut. Direction of applied loads and measured parameters are shown.

The characterization experimental technique was similar to that described by McLaughlin and Lynch [55-56], which used the stress dependent electromechanical characterization system (SDECS) located at NUWC Newport. Insulated alumina ceramic end caps were attached to the $4\times4mm^2$ faces of single crystal specimens. The end caps were designed to work with an alignment fixture that had a double ball joint system to shield specimens from bending moments leaving only uniaxial stress loading. In experiments performed at room temperature (20°C), uniaxial stress (σ_{22}) was applied through the fixture to the [100] and [$\bar{1}$00] surfaces using an Instron load frame. In non-room temperature experiments, a heating and cooling environmental chamber was used to provide temperature control while σ_{22} was provided by a pressurized gas driven load frame through the fixture to the [100] and [$\bar{1}$00] surfaces. Strain gauges were mounted on the [0$\bar{1}$1] and [01$\bar{1}$] faces to measure ε_{22}. Shown in Figure 3-3, a signal generator and high voltage amplifier were used to apply E_3 and a read capacitor of 3μF (over three orders of magnitude greater than the specimen) was placed in series with the specimen to act as a charge integrator forming a Sawyer – Tower circuit [151]. Specimens were submerged in a bath of Fluorinert™ for electrical insulation and thermal homogeneity. The charge across the capacitor is measured using an electrometer and used to calculate D_3.

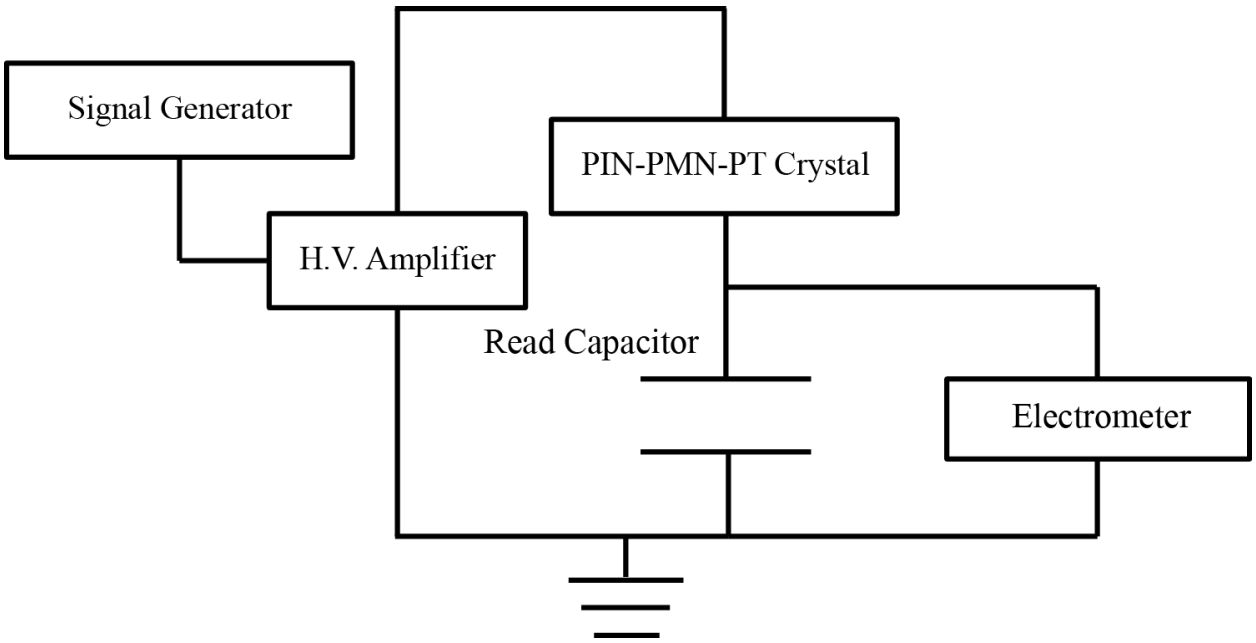

Figure 3-3. Electrical setup in the format of a Sawyer – Tower circuit. Signal generator and high voltage amplifier are used to drive an electric field E_3 across the crystal. An electrometer measures the voltage across a read resistor to measure electric displacement D_3.

The stress, electric field, and temperature loading steps are shown in Table 3-1. Specimens were subjected to three kinds of loading conditions:

1. Constant T at 20°C, constant E_3 at intervals between 0kVm^{-1} and 500kVm^{-1}, and dynamic σ_{22} ramped from 0MPa to -26MPa to 0MPa at a rate of 0.63MPa s^{-1}.
2. Constant T at 20°C, constant σ_{22} at intervals between 0MPa and -26MPa, and dynamic E_3 ramped from 0kVm^{-1} to 500kVm^{-1} to 0km^{-1} at a rate of 200kVm^{-1}s^{-1}.
3. Constant E_3 at 0kVm^{-1} (short circuit), constant σ_{22} at intervals between 0MPa and -20MPa, and dynamic T ramped from 17ºC through the phase transformation temperature and back down to 17ºC at a rate of 2ºC/min from.

In study 3, the temperature driven study, the D_3 and ε_{22} were zeroed at the beginning of each run.

Table 3-1. Stress, electric field, and temperature loading combinations.

Study	σ_{22} **(MPa)**	E_3 **(kVm^{-1})**	T **(°C)**
1	0→-26→0	0, 20, 40, 60, 80, 100, 200, 300, 400, 500	20
2	-17, -19, -21, -23, -25	0→500→0	20
3	-10, -13.3, -16.7, -20	0	17→78→17

3.2 Experimental Results and Discussion

The ε_{22} response of studies 1 and 2 are shown in Figure 3-4. Red curves indicate the stress loading at fixed-electric field data (study 1) and blue curves indicate the electric field at fixed-stress data (study 2). Jump type discontinuities in ε_{22} indicate combined σ_{22} and E_3 conditions for either forward FE_R to FE_O or reverse FE_O to FE_R load induced phase transformations. The higher values of ε_{22} indicate the FE_R phase and lower values of ε_{22} indicate the FE_O phase. The FE_R to FE_O transformation occurs at greater linear σ_{22} and E_3 combinations than the FE_O to FE_R. The jump type discontinuity in ε_{22} occurs when the $[111]$ and $[\bar{1}11]$ FE_R variants snap into a single FE_O variant oriented in the $[011]$. An analogous but mirrored hysteretic behavior

exists in D_3 with a jump discontinuity that increase the electric displacement as the FE_R variants transform into the FE_O variant.

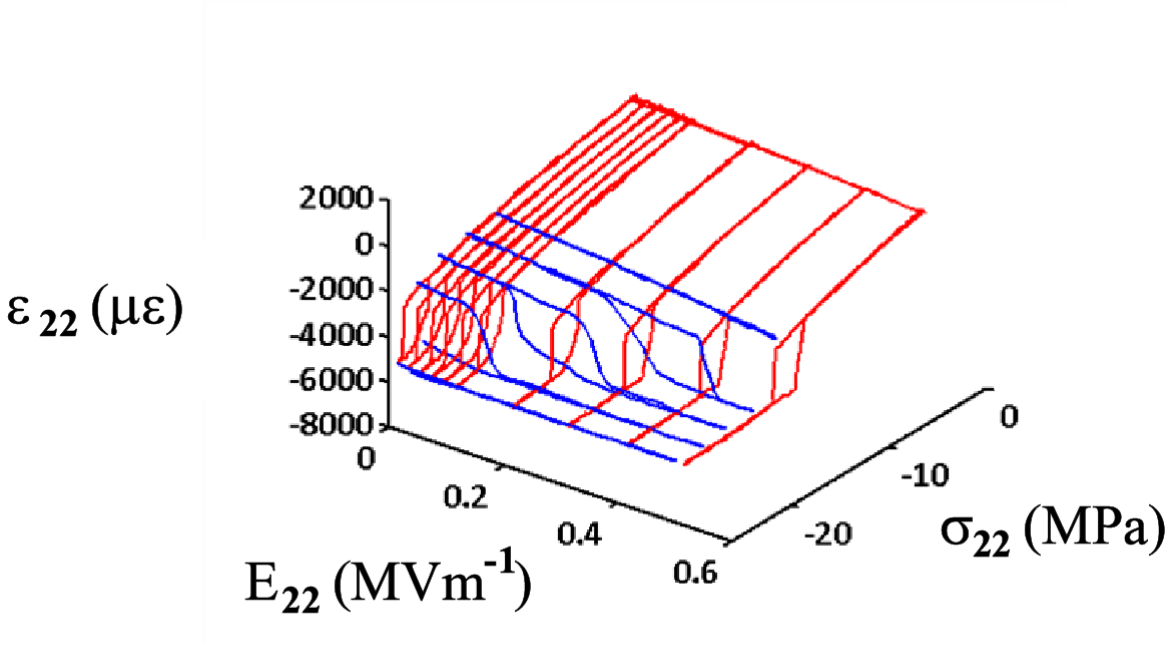

Figure 3-4. Strain **(** ε_{22}) behavior due to loading combinations of uniaxial stress (σ_{22}) and electric field (E_3).

The combinations of stress and electric field that induce the forward and reverse phase transformation are plotted in Figure 3-5. Red circle markers indicate the critical σ_{22} and E_3 combinations for FE_R to FE_O phase transformation and blue triangles indicate critical σ_{22} and E_3 for FE_O to FE_R phase transformation. The region between the FE_R to FE_O and FE_O to FE_R transition is the hysteretic region between the FE_R and FE_O phases. In order to mechanically drive a specimen between the FE_R and FE_O phases, the maximum and minimum excitation

stresses applied must span the hysteretic region at the specified electric field applied. Similarly, in order to electrically drive a specimen between the FE_R and FE_O phases, the maximum and minimum excitation electric fields applied must span the hysteretic region at the specified mechanical stress applied. In PIN-PMN-PT specimens, the width of the hysteretic region appears to remain constant over the range of the measurements, which suggests that the energy barrier between the FE_R and FE_O phases remain nearly constant regardless of applied electrical or mechanical loads. The constant width of the hysteretic region reduces the number of experiments required to characterize a material. The boundaries of the hysteretic region can be linearly interpolated by finding two sets of critical σ_{22} and E_3 for FE_R to FE_O and FE_O to FE_R phase transformation.

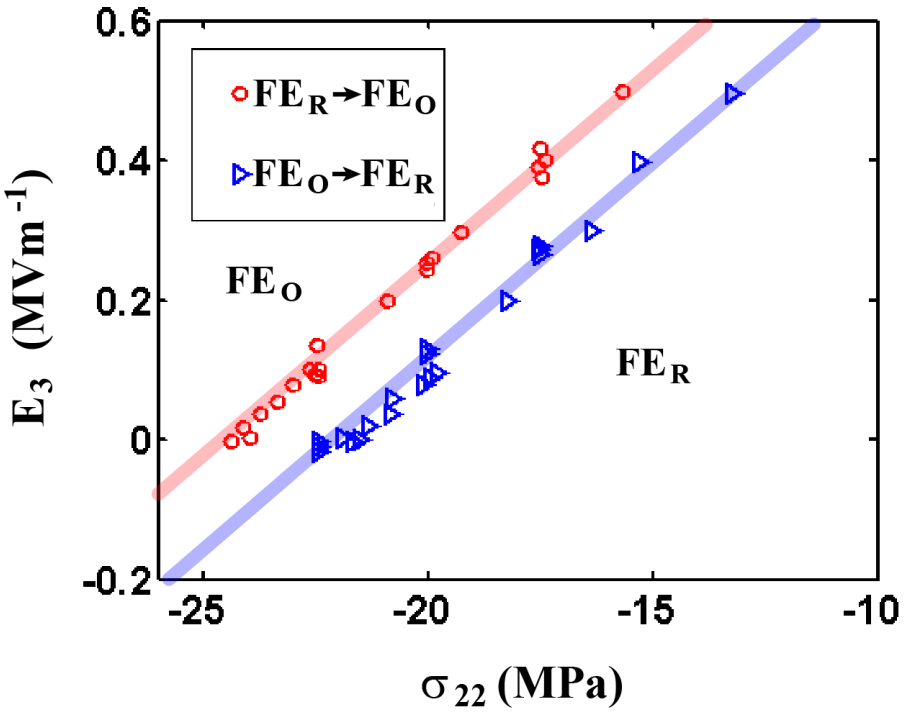

Figure 3-5. Critical σ_{22} and E_3 for FE_R to FE_O and FE_O to FE_R phase transformation.

The ε_{22} and D_3 response of study 3 is shown in Figure 3-6.a and 3-6.b. The D_3 and ε_{22} were zeroed at the beginning of each run. Therefore, measured D_3 and ε_{22} are relative to the electric displacements and strains at the corresponding stress and 17ºC. The first run was conducted at -20MPa and shows open loop behavior outside of the hysteretic region that has been attributed to an incomplete poling of the material during preparation. After the first thermal cycle, the material became fully poled and subsequent tests at other stresses did not show open loop behavior outside of the phase transformation hysteresis. Like in the previous study, jump type discontinuities in ε_{22} and D_3 indicate either forward FE_R to FE_O or reverse FE_O to FE_R load induced phase transformation with the FE_R phase existing at lower temperatures and the FE_O phase existing at higher temperatures. Seen in Figure 3-6, the increases compressive uniaxial stress causes a decrease in the critical temperatures for the FE_R – FE_O phase transformation.

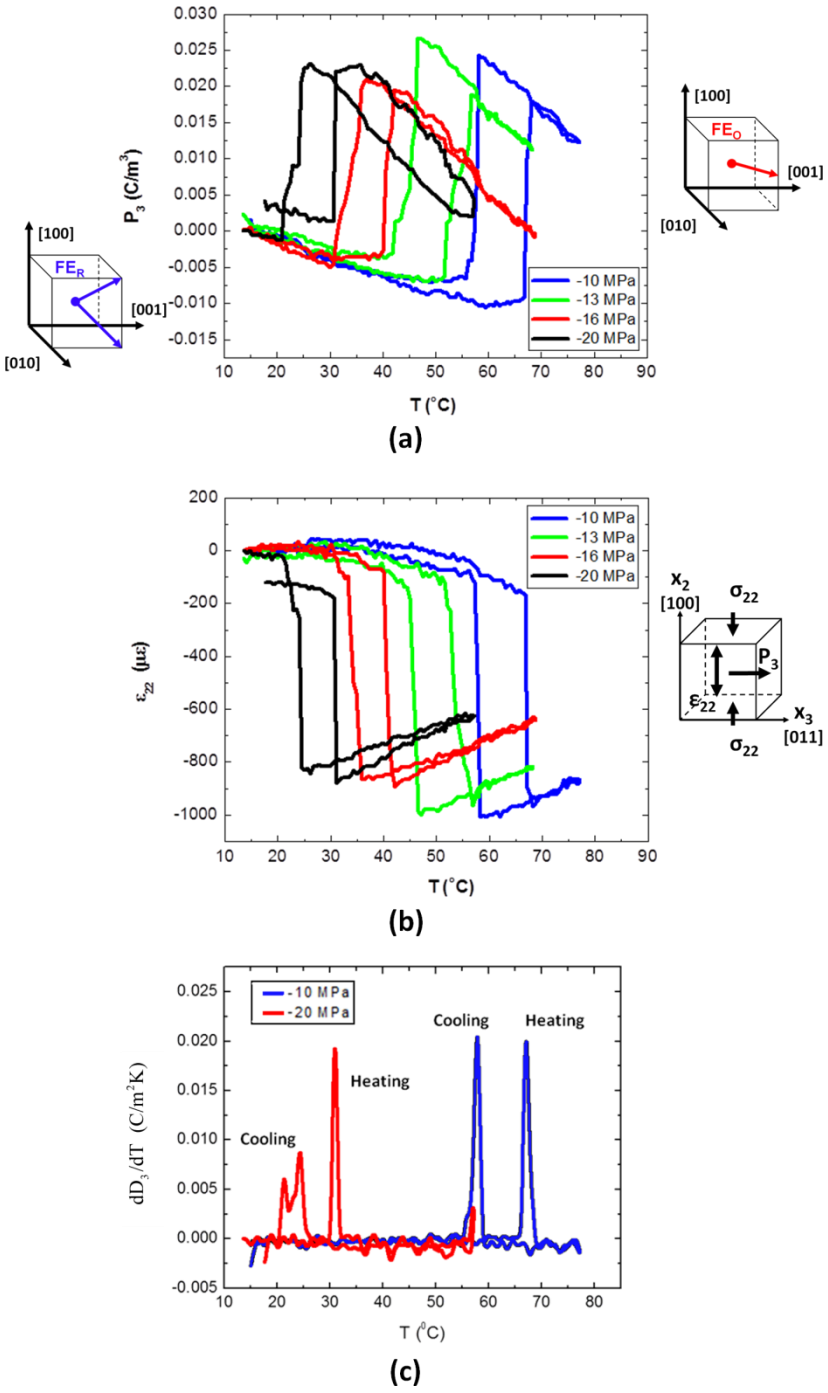

Figure 3-6. a) Temperature driven relative electric displacement response for the FE_R-FE_O phase transformation at different compressive stress values for PIN-PMN-PT. b) Temperature driven relative strain response for the FE_R-FE_O phase transformation at different compressive stress values for PIN-PMN-PT. c) Temperature driven dD_3/dT response for the FE_R-FE_O phase transformation at -10 MPa and -20 MPa.

From the D_3 and ε_{22} versus T behavior in Figure 3-6, a coefficient, m_3, and a thermal expansion coefficient, α_{22}, were determined. Although the exact elastic boundaries acting upon the crystal are uncertain, the m_3 coefficient may be taken as measure of the pyroelectric response of the PIN-PMN-PT single crystal along the poled polarization direction [011]. The α_{22} coefficient measures the thermal expansion of the single crystal in the [100] direction, which is orthogonal to the poled direction [011]. m_3 and α_{22} are components of the vector m_i and tensor α_{ij} respectively where m_i and α_{ij} are anisotropic.

The FE_R – FE_O phase transformation hysteresis was approximated as two regions of linear pyroelectric behavior described by coefficients m_3^R and m_3^O. Superscripts R and O refer to material properties the FE_R and FE_O phases respectively. The linear regions in Figure 3-6.a are separated by an electric displacement jump, ΔD_3, at the phase transformation. The pyroelectric coefficients are negative within each phase and independent of the applied stress, σ_{22}. Near the FE_R-FE_O transformation temperature, m_3^R shows some temperature dependence while m_3^O does not. The phase transformation is sharp and is described in terms of an electric displacement jump. The difference between m_3^R and m_3^O causes $\Delta D_3^{R\to O}$ to be smaller in magnitude than $\Delta D_3^{O\to R}$. The magnitudes of $\Delta D_3^{R\to O}$ and $\Delta D_3^{O\to R}$ decrease as the compressive stress is increased due to piezoelectric effects. The large jump in electric displacement across the phase transformation presents an opportunity for improved thermal energy harvesting as this sudden jump in polarization has the potential to increase the charge generation per cycle over materials that operate in the linear pyroelectric regime.

Looking at the strain vs. temperature response shown in Figure 3-6.b, the slopes of the linear regimes of the FE_R and FE_O phases are the thermal expansion coefficients α_{22}^R and α_{22}^O respectively. The linear regimes are separated by a jump in the strain associated with the phase transformation. Over the small temperature change from the initial temperature to the phase transformation temperature, the material went from expansion to contraction. A single value of α_{22}^R could not be determined due to this nonlinearity. In the FE_O phase, α_2^O is constant and positive. The strain jumps due to the phase transformation, $\Delta\varepsilon_{22}^{R\to O}$ and $\Delta\varepsilon_{22}^{O\to R}$, behave similarly to the polarization jumps $\Delta D_3^{R\to O}$ and $\Delta D_3^{O\to R}$ seen in Figure 1a; the magnitude of the jumps decrease as the compressive stress is increased due linear elasticity and the magnitude of $\Delta\varepsilon_{22}^{R\to O}$ is less than that of $\Delta\varepsilon_{22}^{O\to R}$ due to the differences in α_{22}^R and α_{22}^O. The phase transformation properties of the thermal mechanical and thermal electrical properties of the PIN-PMN-PT crystal are tabulated in Table 3-2.

Table 3-2. Thermal mechanical and thermal electrical properties of PIN-PMN-PT about the FE_R – FE_O phase transformation.

σ_{22} (MPa)	$\Delta D_3^{R\to O}$ (Cm^{-2})	$\Delta D_3^{O\to R}$ (Cm^{-2})	m_3^R $(\mu\text{Cm}^{-2}\text{K}^{-1})$	m_3^O $(\mu\text{Cm}^{-2}\text{K}^{-1})$	$\Delta\varepsilon_{22}^{R\to O}$ $(\mu\epsilon)$	$\Delta\varepsilon_{22}^{O\to R}$ $(\mu\epsilon)$	α_{22}^O $(\mu\epsilon\text{K}^{-1})$
–10	0.027	–0.031	–250	–640	–810	910	8.1
–13.3	0.025	–0.030	–270	–710	–845	865	9.4
–16.6	0.022	–0.025	–260	–650	–815	835	8.9
–20	0.021	–0.024	–280	–720	–700	800	8.7

The actual electric displacement behavior at the phase transformations is not an instantaneous jump but a very large change in electric displacement over a very small change in temperature. The sharpness of the electric displacement peaks are shown in Figure 3-6.c where the $\mathrm{d}D_3/\mathrm{d}T$ curves for the -10 MPa and -20 MPa are plotted. The phase transformation causes a large sharp peak in the $\mathrm{d}D_3/\mathrm{d}T$ behavior. There are two peaks in the $\mathrm{d}D_3/\mathrm{d}T$ vs. temperature response for each stress load: one associated with the FE_R-FE_O phase transformation during heating and another with the FE_O-FE_R phase transformation during cooling. The peak values $\mathrm{d}D_3/\mathrm{d}T$ reach upwards of 0.02 C m^{-2} K^{-1} during the phase transformations, which are orders of magnitude greater than linear pyroelectric coefficients. Note that the $\mathrm{d}D_3/\mathrm{d}T$ values are not true pyroelectric coefficients, which describe a linear relationship between polarization and temperature under fixed elastic boundaries. The $\mathrm{d}D_3/\mathrm{d}T$ behavior near the phase transformations is nonlinear, path-dependent, and hysteretic.

As in studies 1 and 2, a phase stability map can be generated based on $\sigma_{22} - T$ loading as shown in Figure 3-7.a. The region between the FE_R-FE_O and FE_O-FE_R transformation criteria outlines the hysteresis between the FE_R and FE_O phases. When combined with the phase diagram shown in Figure 3-5, a three dimensional plot, Figure 3-7.b, can be constructed. In PIN-PMN-PT specimens, the width of the hysteretic region appears to remain constant; indicating the energy barrier between the FE_R and FE_O phases is nearly independent of whether the transformation is thermally, electrically, or mechanically driven within the subjected range of loads. McLaughlin *et al.*[55] performed phase transformation experiments by electrically driving the FE_R-FE_O phase transformation in PMN-32PT single crystals that resulted in similar phase stability plots. This phase stability map enables the design of thermal energy harvesting

devices that can be mechanically or electrically tuned to operate over a broad range of temperatures. The results also indicate that the electrical and thermal loaded phase transformations could be tuned by varying the applied bias stress. Changing the bias σ_{22} from -10MPa to -20MPa reduces the phase transformation temperature from ~63ºC to ~25ºC. This adaptability broadens the range of waste heat sources that can be exploited.

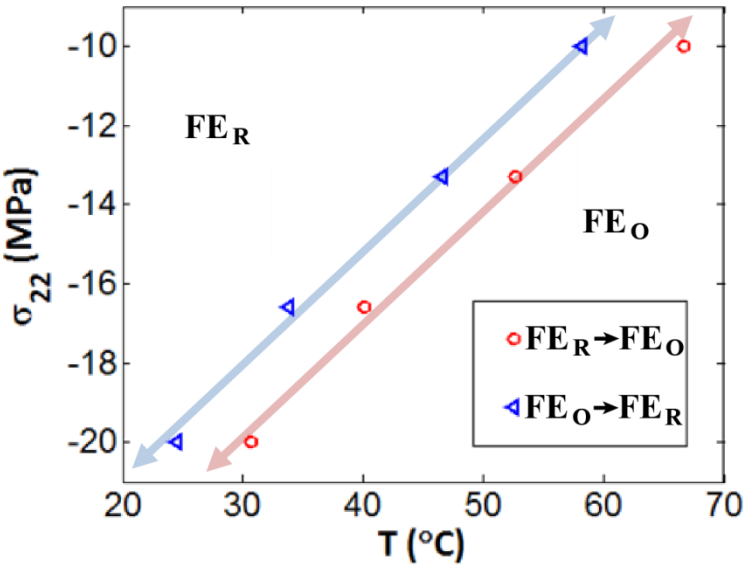

(a)

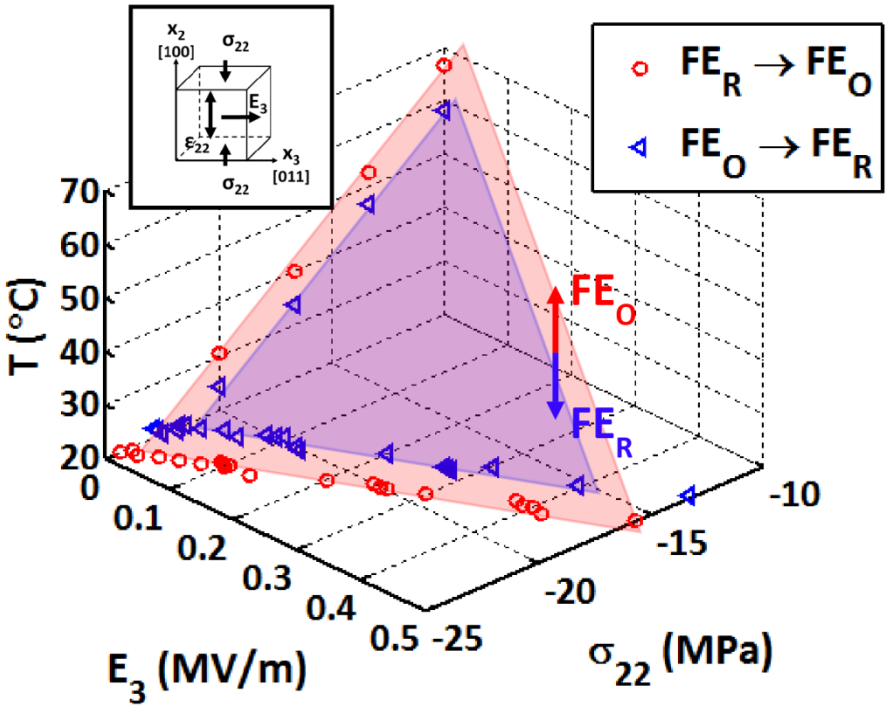

(b)

Figure 3-7. a) Temperature and stress phase stability plot for PIN-PMN-PT showing the phase transformation hysteresis. b) 3-dimensional temperature, stress, and electric field phase stability plot for PIN-PMN-PT showing the phase transformation hysteresis.

3.3 Concluding Remarks

A three dimensional E_3, σ_{22}, and T phase diagram is created for the FE_R – FE_O phase transformation. For the loading ranges applied in this study, the critical loading conditions for the forward and reverse phase transformations form parallel phase transformation surfaces. This indicates the criteria for both and forward and reverse FE_R – FE_O phase transformation are linear combinations of E_3, σ_{22}, and T loads and the energy barrier between the FE_R and FE_O phases remains constant and is independent of loading conditions. This simplifies the characterization of phase transformation behavior in $[011]$ cut and poled PIN-PMN-PT single crystals and opens the way for FE_R – FE_O phase transformation transducer and energy harvester devices.

The study also demonstrated thermally driven FE_R – FE_O phase transformations in relaxor ferroelectric single crystals can be described by two linear pyroelectric regions, associated with the FE_R and FE_O phases respectively separated by a polarization jump at the phase transformation. The polarization jump has the potential to increase the performance of thermal energy harvesters. The phase stability of the material under mechanical, electrical, and thermal loads was discussed. The phase stability diagram enables tuning of thermally driven phase transformations using either compressive uniaxial mechanical bias stress in the [001] direction or electric field bias in the [110] direction. This phenomenon enables a new class of tunable pyroelectric devices with potential application in the field of energy harvesting and thermal sensing.

CHAPTER 4

IDEAL ENERGY HARVESTING CYCLE USING A PHASE TRANSFORMATION IN FERROELECTRIC PIN-PMN-PT RELAXOR SINGLE CRYSTALS

This chapter addresses the demonstration of an ideal mechanical to electrical energy harvesting cycle for ferroelectric materials in $[011]$ cut and poled near-MPB composition FE_R phase $Pb(In_{1/2}Nb_{1/2})O_3$-$Pb(Mg_{1/3}Nb_{2/3})O_3$-$PbTiO_3$ (PIN-PMN-PT) single crystals. The results have been published in Dong et al. [152]. Chapter 1.1.3 covered energy harvesting background information. The highly non-linear and hysteretic load driven FE_R – FE_O phase transformation observed in near-MPB composition FE_R phase relaxor ferroelectrics, described in chapter 3, was selected for energy harvesting due to the increased electrical-mechanical transduction properties across the sharp jump type phase transformation. The FE_R – FE_O phase transformation is advantageous over other types of phase transformations because the crystal cycles between two polarized ferroelectric phases in the absence of applied electric fields, has been shown to withstand 10^6 phase transformation cycles without significant degradation [153], and can be mechanically driven at high frequency (>100Hz).

The ideal ferroelectric mechanical-to-electrical energy harvesting cycle was adapted from the reverse Brayton cycle. Instead of operating between two isobaric and two isentropic processes, the ideal ferroelectric energy harvesting cycle operates between two isostress and two isocharge processes. A $[011]$ cut and poled PIN-PMN-PT single crystal specimen with short circuit uniaxial stress driven phase transformation hysteresis ranging from -18 MPa to -21 MPa was selected for the energy harvesting study. Ideal ferroelectric energy harvesting cycles were run with uniaxial stress ranges spanning the phase transformation. An output electrical energy

density of 6.22 kJ m^{-3} per cycle was demonstrated for a stress loading interval from -14 MPa to -25 MPa and the peak absolute efficiency was measured to be 36% for a stress loading interval of -16.5 to -22.5 MPa. Although electrical output increases with increases in the stress loading interval, charge leakage at high electric fields occurred for large stress intervals. This placed a limit on the maximum energy density achievable.

4.1 Ideal Energy Harvesting Cycle

The work done per unit volume by an applied stress or electric field during the phase transformation is approximately equal to the scalar product of the stress and the transformation strain plus the scalar product of the electric field with the change of transformation electric displacement. The strain and electric displacement change across the phase transformation can range from 1000-2000με and 0.02-0.03Cm^{-2} in PIN-PMN-PT [61-62] depending on composition. The ability of external forces, electric field (E_m) and stress (σ_{ij}), to do positive work on the material while driving the phase transformation is,

$$w^{ext} = \sigma_{ij}\Delta\varepsilon_{ij}^{\alpha\to\beta} + E_m\Delta D_m^{\alpha\to\beta} \tag{4.1}$$

where $\Delta D_m^{\alpha\to\beta}$ and $\Delta\varepsilon_{ij}^{\alpha\to\beta}$ are the components of the strain and electric displacement change when going from FE_R to FE_O. Indices vary from 1 to 3 and repeated indices imply summation. Going to the case of a closed cycle (forward and reverse transformation) and varying stresses and electric fields the terms on the right hand side in Equation (1) are replaced by integrals.

$$w^{ext} = \oint \sigma_{ij}\, d\varepsilon_{ij} + \oint E_m\, dD_m \tag{4.2}$$

The phase transformation can be driven by either stress or electric field. The electrical energy that can be harvested (w^{Elec}) from a single cycle through the phase transformation is given by Equation (4.3),

$$w^{Elec} = \oint \sigma_{ij} d\varepsilon_{ij} - w^{irr,R\leftrightarrow O} \tag{4.3}$$

In a closed loop through the phase transformation, the generated entropy due to irreversibility causes hysteresis. $w^{irr,R\leftrightarrow O}$ is the irreversible work density due to entropy of the phase transformation in a closed cycle. $w^{irr,R\leftrightarrow O}$ can be determined from the area of the stress-strain phase transformation hysteresis loop under short circuit conditions. An integral has been used in Equation (2) because the transformation stress is a function of the electric displacement and the strain.

The ideal energy harvesting cycle is described in Figure 4-1. In the reverse Brayton cycle a four step isobaric, isentropic, isobaric, and isentropic process utilizes mechanical energy to pump heat from a low temperature to a high temperature. Similarly the ideal ferroelectric energy harvesting cycle utilizes a four step constant stress (isostress), constant electric displacement (isocharge), isostress, and isocharge process to drive current through an electrical impedance load.

The ideal ferroelectric energy harvesting cycle operates between a high and a low compressive uniaxial stress, σ_H and σ_L respectively. The range of the applied stresses must span the phase transformation hysteresis and σ_H and σ_L lie on opposite sides of the short circuit stress-strain FE_R-FE_O hysteresis such that loading the material across the full stress range ensures fully saturated phase transformations. In the electric displacement vs. electric field figure, the two dashed orange curves represents the electric displacement – electric field response of the specimen at isostress conditions of σ_H and σ_L. Along path A-B, uniaxial stress is applied from σ_L to σ_H under open-circuit conditions where the polarization changes at constant electric displacement. When the electric displacement is prevented from changing, an electric

field forms that opposes the FE_R to FE_O phase transformation and stabilizes the FE_R phase. As the uniaxial compressive stress is increased, the displacement – electric field ($D-E$) hysteresis curve shifts towards the left. This electric field on the specimen is the electric field shift from the σ_L $D-E$ curve to the σ_H $D-E$ curve. Next, along path B-C, the circuit is closed with stress fixed at σ_H and charge flows across a resistive load changing the electric displacement and decreasing the built up electric field. If the stress is maintained at σ_H, the electric displacement path follows that of the σ_H $D-E$ curve until the electric field is zero. Along path C-D, the mechanical load is decreased to σ_L under open-circuit conditions, again building an electric field that this time opposes the FE_O to FE_R transformation and stabilizes the FE_O phase. Finally, the material is again connected to an electrical load, charge flows, and the electric displacement is allowed to change following the constant σ_L $D-E$ curve and until the electric field is zero, path D-A. The input mechanical energy density, w^{Mech}, for the cycle can be calculated by the path integral of the scalar product of the stress and the strain, Equation (4.4).

$$w^{Mech} = \oint \sigma_{22}\, \mathrm{d}\varepsilon_{22} \tag{4.4}$$

And the output electrical energy density, w^{Elec}, is the negative path integral of the scalar product of the electric field with the electric displacement, Equation 4.

$$w^{Elec} = -\oint E_3\, \mathrm{d}D_3 \tag{4.5}$$

W^{Mech} and W^{Elec} correspond to the area in the stress-strain and electric field-electric displacement cycles respectively. In order to increase the input mechanical energy density and thus the output electrical energy density, the amplitude of the stress excitation can be increased.

In this study the ideal energy harvesting cycle was implemented and its practical limitations were identified. The energy density and efficiency of the cycle using PIN-PMN-PT specimens were determined.

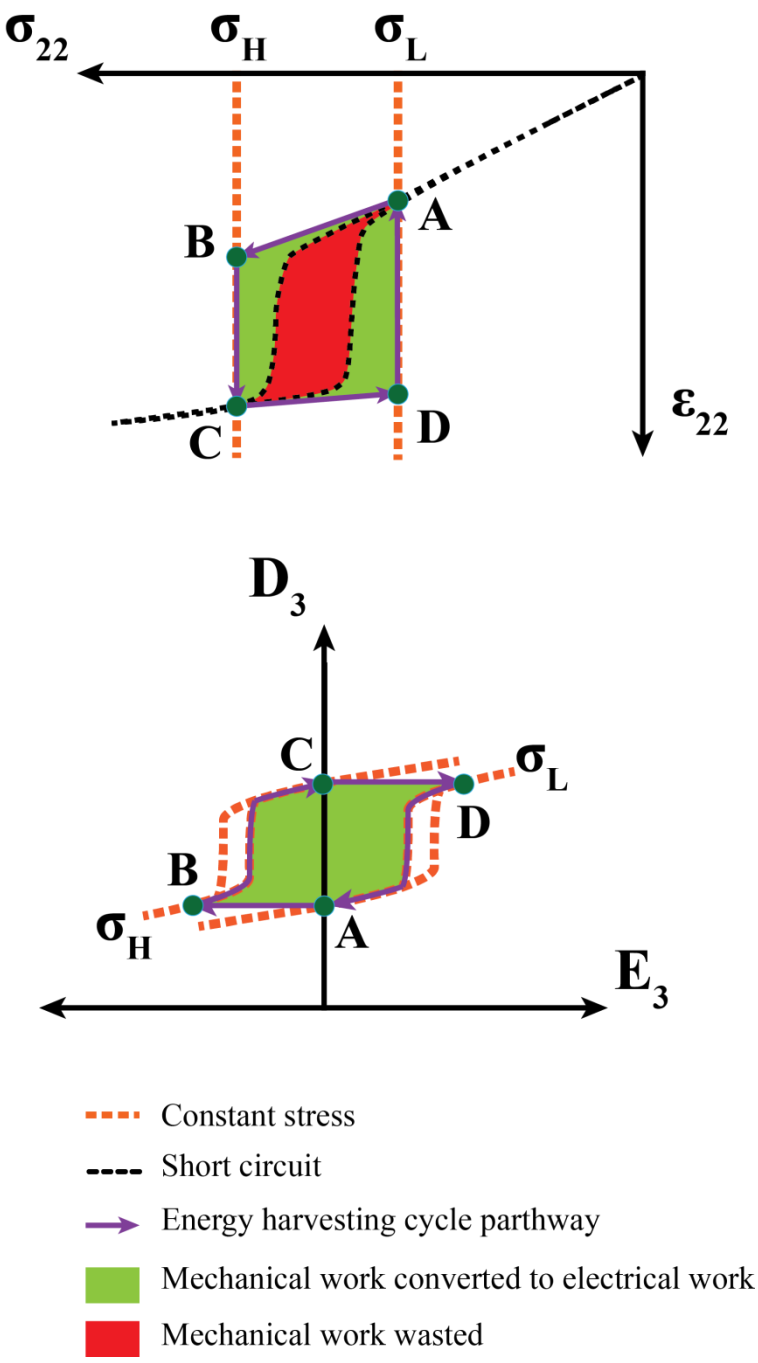

Figure 4-1. An idealized energy harvesting cycle across the phase transformation FE_R-FE_O. σ, ε, E, and D are the stress, strain, electric field and electric displacement respectively. A-B: Open-circuit Isocharge compression from σ_L to σ_H. B-C: charge drain across electric load at isostress σ_H. C-D: Isocharge decompression from σ_H to σ_L. D-A: charge drain across electric load at isostress σ_L.

4.2 Experimental Arrangement

4.2.1 Materials and Specimen Preparation

Specimens of a near MPB FE_R single crystal PIN-PMN-PT composition were provided by H.C. Materials Inc. The crystal cut and the orientation of the applied loads are described in Figure 4-2. The single crystals specimens were prepared by the manufacturer into $[011]$ cut and poled bars with dimensions of $4mm \times 4mm \times 12mm$ with $4mm \times 12mm$ faces normal to the x_1 and x_3 axes, and $4mm \times 4mm$ faces normal to the x_2 axis. The two faces normal to the $[011]$ direction were plated with gold to allow crystal poling and the application of electric field E_3. Strain gauges were mounted on the $[0\bar{1}1]$ faces to measure strain ε_{22} in the $[100]$ direction.

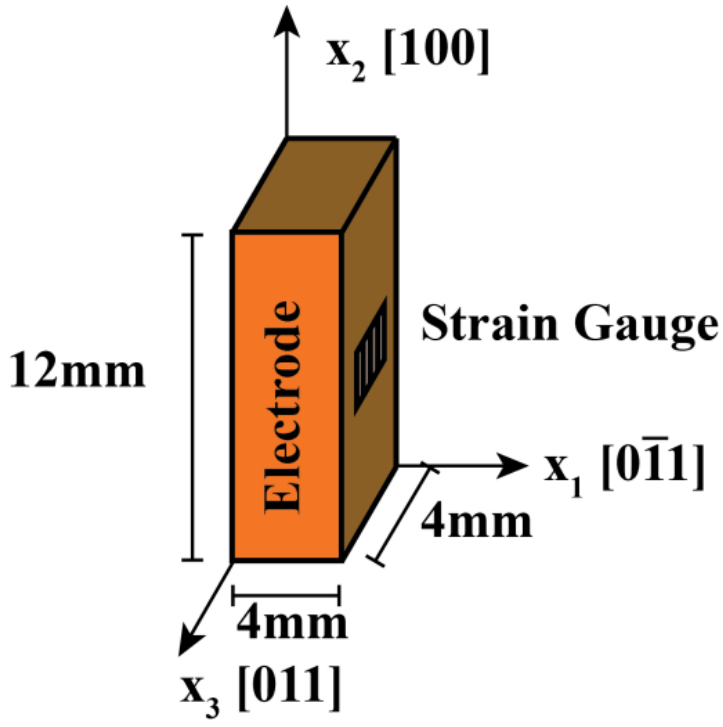

Figure 4-2. Specimen preparation and orientation in the crystal cut. The crystal orientation is defined by the cubic referenced Miller indices and the coordinate system shown.

4.2.2 Experimental Procedure

Compressive stress was applied in the $[100]$ direction and electric field in the $[011]$ direction using a load frame and with a fixture previously described [55-56, 62]. Figure 4-3 shows the electrical layout of the experiment. A knife switch was employed to switch between the open- and closed-circuit conditions. Under closed-circuit conditions, charge across the specimen is bled through two resistors in series with values 50MΩ and 0.5MΩ. The 0.5MΩ resistor is the combined impedance of a 1MΩ resistor in parallel with the 1MΩ input impedance of the scope. The two resistors behave as a 100:1 voltage divider. Both strain and electric potential were recorded using an oscilloscope at a sampling rate of 32.3kHz. The applied stress from the load frame and strain on the specimen were recorded at a sampling frequency of 1kHz.

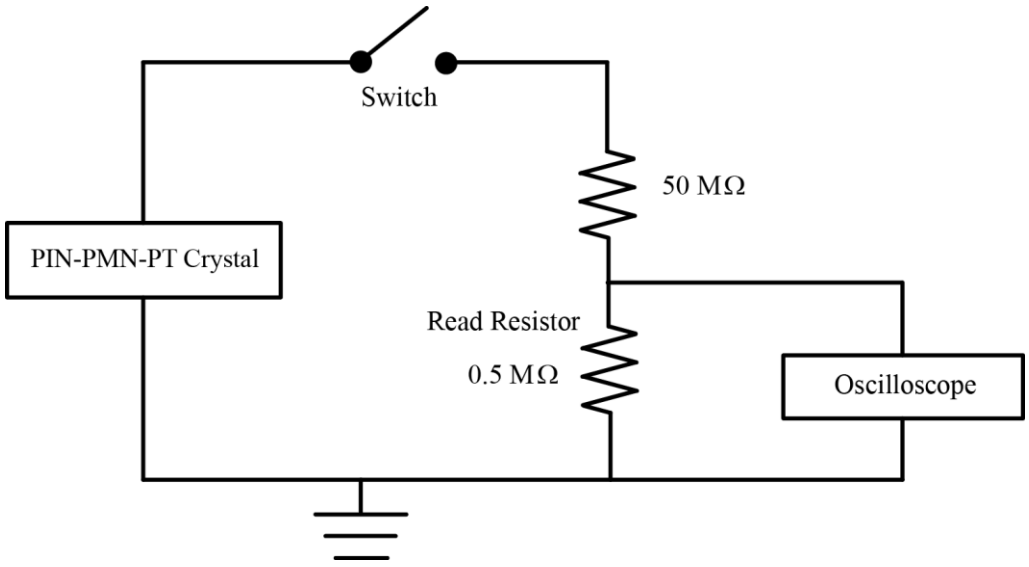

Figure 4-3. Experimental setup of the electrical circuit.

Specimens were compressively pre-loaded under short-circuit conditions to σ_L just less than the short-circuit stress-strain phase transformation threshold. The switch was opened and the stress increased past the short circuit phase transformation threshold to σ_H. The stress was held constant and the switch was closed under fixed stress conditions. Voltage across the read resistor and strain were captured on the oscilloscope. Once the charge was completely drained, the switch was again opened and the specimen unloaded to σ_L. Again, the switch was closed at fixed stress and the electric potential and strain change were monitored. A schematic of the stress verses time profile is shown in Figure 4-4 with the open-circuit stages highlighted in green. The loading rate was 10N/s.

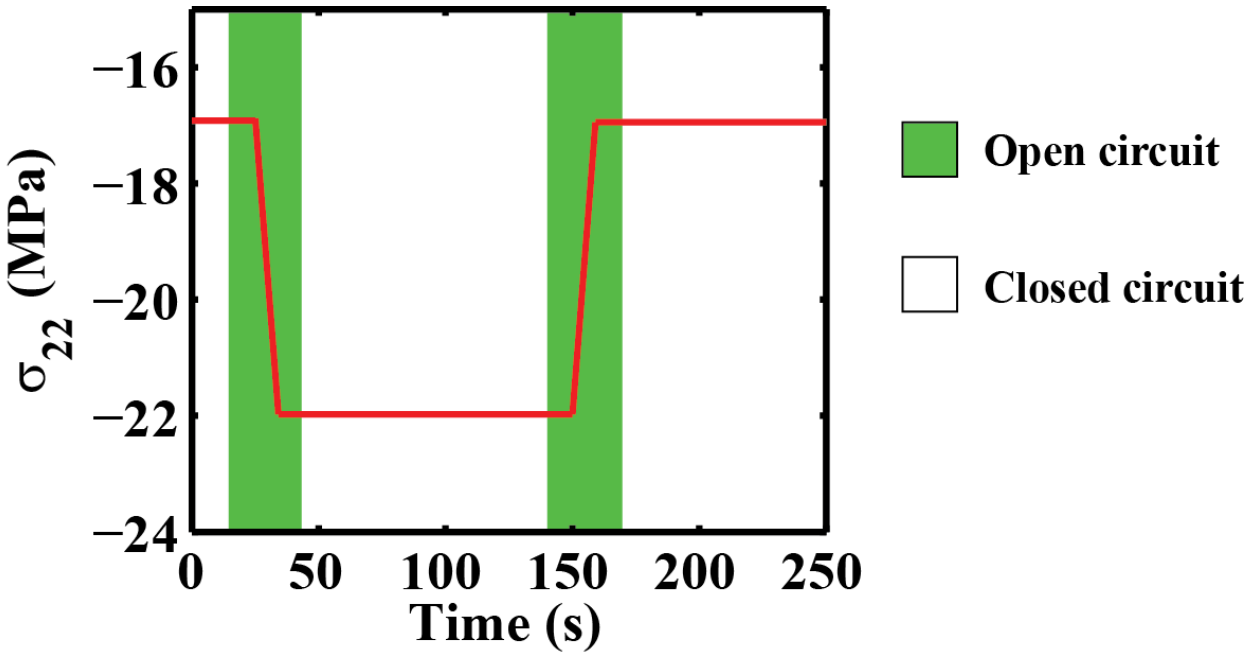

Figure 4-4. Stress profile of energy harvesting cycle with σ_H and σ_L values of -22 and -17 MPa respectively. The open-circuit stage is highlighted in green.

4.3 Experimental Results

When the switch was first closed, the electric field across the crystal was large due to the open circuit mechanical loading. This electric field quickly decayed as charge was drained across the resistor and the electric displacement was allowed to change. The electric field was determined using Equation (4.6)

$$E_3 = \frac{-\phi}{d} \tag{4.6}$$

where ϕ is the electric potential across the specimen as determined from the voltage divider and d is the specimen electrode-to-electrode spacing. The electric displacement change was calculated by integrating the current through the resistor and dividing by the electrode area of the specimen, Equation (4.7).

$$D_3 = \int \frac{\phi}{RA} \mathrm{d}t \tag{4.7}$$

where R is the total resistance of the circuit, A is the electrode area, and t is time.

The stress-strain curves are shown in Figure 4-5.a and the electric field-electric displacement curves are shown in Figure 4-5.b for a cycle under a stress excitation range of -17 to -22 MPa. Under open-circuit conditions, the electric displacement is prevented from changing. This constraint of the electric displacement results in a large electric field that opposes the change in internal polarization of the material. Since the strain is related to the change in internal polarization, this results in a high open-circuit stiffness of the material compared to that of the short circuit FE_R and FE_O phases. The generated electric field also hinders the phase transformation. The application of the open-circuit condition enables an increase in the input

mechanical energy. Because the cycle is closed, the input mechanical energy in excess of the hysteresis of the phase transformation (area inside the loop under short circuit conditions), can be converted to electrical energy. The phase transformation is many times faster than the response time of the load frame that is enforcing constant stress. It is apparent in Figure 4-5.a, that the actual applied mechanical load is not at fixed stress as the load frame takes time to catch-up to the sudden change in strain. This results in less mechanical energy input into the system than predicted. The effect on the electric field and electric displacement are seen in Figure 4-5.b where there is a secondary hump in the electric field caused when the load frame catches up. In Figure 4-5.b, the change in electric displacement is the same for the FE_R to FE_O transformation as the FE_O to FE_R transformation.

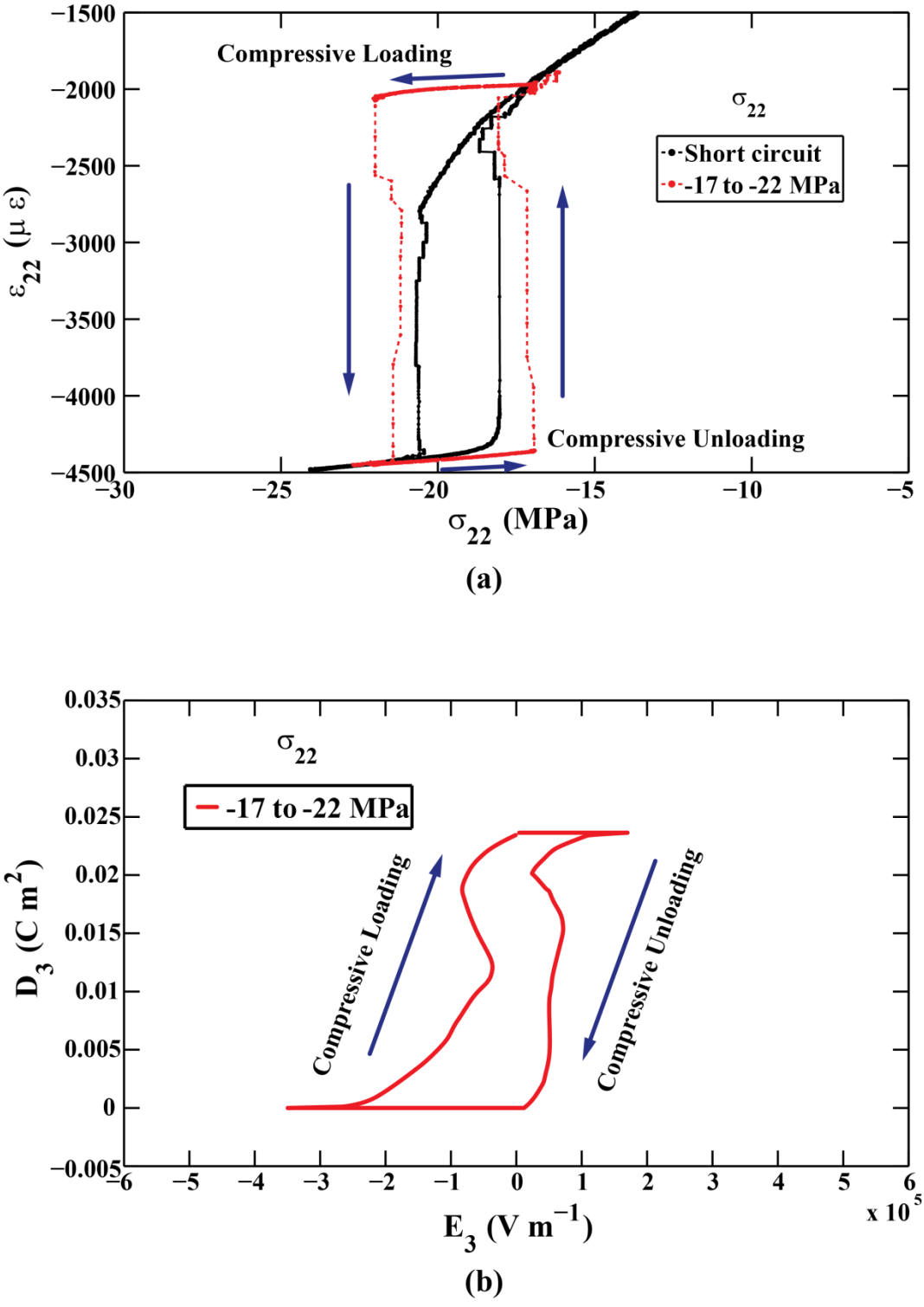

Figure 4-5. a) The stress-strain curves for the short circuit and the idealized energy harvesting cycle under an applied stress interval between -17 and -22MPa. b) The corresponding electric field-electric displacement response for the idealized energy harvesting.

Figure 4-6.a and 4-6.b show the stress-strain and electric field-electric displacement behavior respectively of idealized energy harvesting cycle under various applied stress intervals. Tabulated in Table 4-1 are the W^{Mech} and W^{Elec} calculated using Equations (4.4) and (4.5). In Figure 4-6.a, the open-circuit curves for the much larger stress intervals (i.e. -14 to -25MPa) do not maintain a linear open-circuit stiffness. Instead, the compliance increases as additional open-circuit stress is applied. This implies the internal leakage across the specimen becomes significant when the electric field across the crystal exceeds a certain level. This is seen in the corresponding electric field-electric displacement plot, Figure 4-6.b, where the change in electric displacement is significantly different for the FE_R to FE_O transformation when compared to that of the FE_O to FE_R transformation. In cases where there is leakage, the FE_R to FE_O transformation electric displacement change is less than that of the FE_O to FE_R transformation as the electric fields generated on the FE_R to FE_O open-circuit is greater than that of the return transformation. The leakage of charge across the specimen reduces both the electric field and the change in electric displacement resulting in a reduction in the output electrical energy density relative to the additional input mechanical energy at larger stress intervals. A comparison of the mechanical and electrical hystereses for all stress intervals shown in Table 4-1 is shown in appendix C.1.

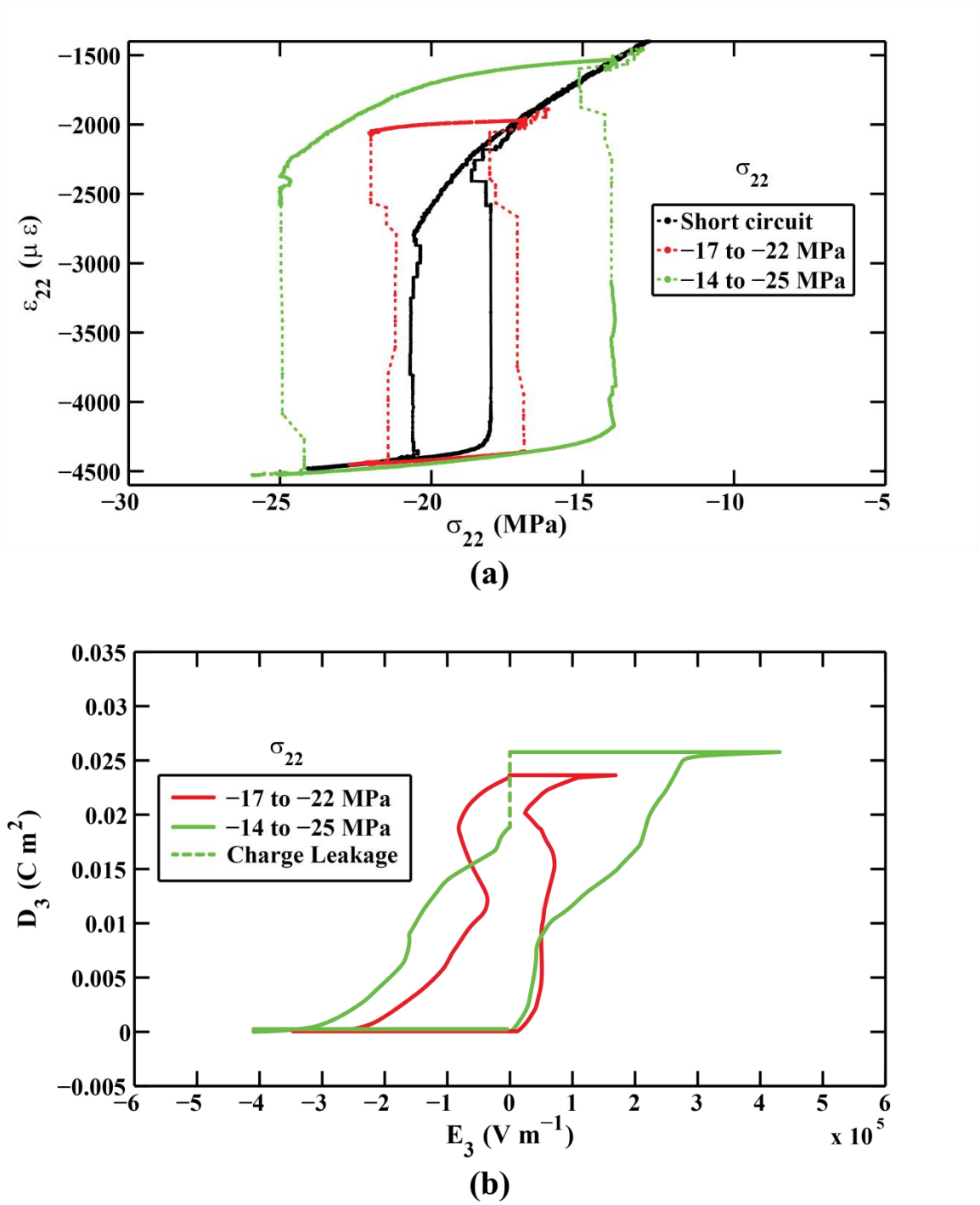

Figure 4-6. a) The stress-strain curves for the short circuit and the idealized energy harvesting cycle under an various applied stress intervals. b) The corresponding electric field-electric displacement response for the idealized energy harvesting cycle.

Table 4-1. Input mechanical energy density and output electrical energy density for various ranges of applied stress intervals.

σ **range (MPa)**	w^{Mech} **(kJ m^{-3} cycle^{-1})**	w^{Elec} **(kJ m^{-3} cycle^{-1})**
Short Circuit Hysteresis	4.99	0
-17.5 to -21.5	8.37	1.86
-17 to -22	10.39	3.34
-16.5 to -22.5	12.71	4.59
-16 to -23	15.39	4.46
-15 to -24	21.80	6.16
-14 to -25	28.69	6.22

4.4 Discussion

Values of w^{Elec} and w^{Mech} from Table 4-1 are plotted in Figure 4-7. At the smaller stress intervals the w^{Elec} scales linearly with the w^{Mech} with an offset that is associated with $w^{irr,R\leftrightarrow O}$ of the phase transformation, in this case 4.99 kJ m^{-3} cycle^{-1}. w^{Mech} in excess of the $w^{irr,R\leftrightarrow O}$ is the surplus mechanical input energy density that is available for energy conversion. The conversion rate between the surplus mechanical input energy density and the w^{Elec} is approximately 60% as can be seen from the slope of the projected conversion rate line in Figure 4-7. The highest w^{Elec} was measured to be 6.22 kJ m^{-3} cycle^{-1} for a stress interval of -14 to -25 MPa. At larger stress intervals, electrical leakage takes place across the specimen. The charge leakage across the specimen causes a roll off in output at higher stress intervals. The efficiency is defined as w^{Elec}

divided by w^{Mech} and peaks at 36% at the -16.5 to -22.5 MPa stress interval. The efficiency is affected by the conversion of the transformation hysteresis to heat and by leakage current across the specimen at high electric field levels.

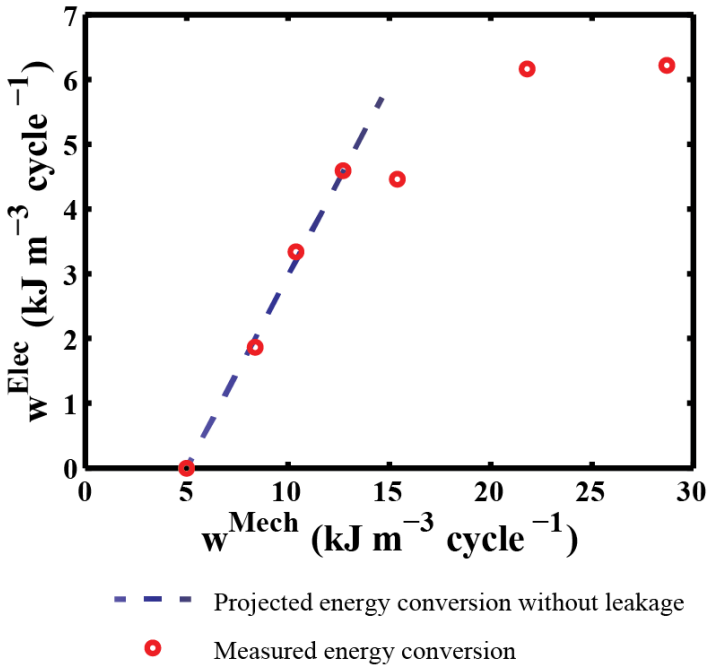

Figure 4-7. Input mechanical energy density compared to output electrical energy density. The blue dotted line signifies the projected mechanical to electrical energy conversion rate in the absence of leakage.

4.5 Conclusions

The experimental results demonstrate the use of an idealized energy harvesting cycle on phase transforming ferroelectric materials for direct mechanical to electrical energy conversion. Under quasi-static conditions the material achieved a peak electrical energy density of 6.22 kJ m^{-3} cycle. The hysteresis in the phase transformations reduced the efficiency for small stress

excitation intervals, and charge leakage across the specimen reduced the efficiency at large stress intervals. The efficiency was found to peak at a point where the charge leakage was not noticeable but the input mechanical energy density was sufficient to offset the hysteresis. The peak efficiency was measured to be 36%. The energy density per cycle from the ideal FE_R-FE_O cycle is much less than that of the Olsen cycles for the same type of materials. This is explained by differences in the electric displacement change associated with the phase transformations. The change in electric displacement of the FE_R-FE_O phase transformation is approximately 0.03 C m^{-2} [61-62] whereas the change in the FE_R-P_C transformation used in the Olsen cycle is approximately 0.3 C m^{-2} [139, 154]. However, FE_R-P_C cycle is a purely thermally driven process and has not been demonstrated for frequencies above 0.1Hz[139]. Although this ideal cycle was performed at quasi-static conditions, the FE_R-FE_O phase transformation can be mechanically driven and has been shown to be sustainable at 100Hz [155]. Theoretically, if the idealized FE_R-FE_O phase transformation energy harvesting cycle is run at several hundred hertz, the power density will far exceed that of the Olsen cycle.

CHAPTER 5

FREQUENCY AND ELECTRIC LOAD IMPEDANCE EFFECTS ON ENERGY HARVESTING USING PHASE TRANSFORMING PIN-PMN-PT SINGLE CRYSTAL

This chapter addresses the effects of excitation frequency and electric load impedance on energy harvesting using a mechanically excited ferroelectric rhombohedral to ferroelectric orthorhombic phase transformation in $[011]$ cut and poled $Pb(In_{1/2}Nb_{1/2})O_3$-$Pb(Mg_{1/3}Nb_{2/3})O_3$-$PbTiO_3$ (PIN-PMN-PT) single crystals. The results have been published in Dong et al. [156]. The motivation of this study was to ascertain the energy harvesting characteristics of the $FE_R - FE_O$ phase transformation in under practical loading environments of energy harvesting devices. Phase transforming specimens were driven through non-idealized energy harvesting cycles with static electric load impedances and cyclic loading. Voltage across the impedance load was measured in order to calculate energy density per cycle and power density.

Over the range of frequencies and electrical impedance loads tested, the crystals behaved as a charge source. The current increased linearly with frequency and the voltage increased linearly with impedance load. Energy density per cycle to scaled linearly with frequency and electrical impedance load and power density to scaled linearly with electrical impedance load and quadratically with frequency. Impedance matching to maximize the energy harvested is discussed. The energy harvested using the phase transformation was on average 27 times, with a peak of 108 times, the energy harvested using the same crystals operating in the linear piezoelectric regime under the same stress excitation amplitude.

5.1 Non-Idealized Energy Harvesting Cycle

The ability of external loads to do work per unit volume is equal to the path integral of the stress with respect to the strain and the path integral of the electric field with respect to the electric displacement. Under electric field (E_m) and stress (σ_{ij}), the availability for the system to do work per unit volume w during the transformation from phase α to phase β is given by Equation (4.1),

$$w = \oint_{\alpha\to\beta} \sigma_{ij} d\varepsilon_{ij} + \oint_{\alpha\to\beta} E_m dD_m \tag{5.1}$$

where D_m and ε_{ij} are respectively the strain and electric displacement during a phase transformation. Indices vary from 1 to 3 and repeated indices imply summation. There is a threshold energy cost to drive the phase transformation, which can be driven through a combination of mechanical or electrical loading. It is this coupling between the electrical and mechanical loading during the phase transformation that is utilized in the energy harvesting cycle. If w exceeds the threshold energy for phase transformation, the electrical work done must be negative. This signifies the electrical energy harvestable by a mechanically driven phase transformation is the difference between w and the phase transformation threshold energy.

Figure 5-1 contrasts the idealized energy harvesting cycle with a non-idealized energy harvesting cycle used in this study. The idealized energy harvesting cycle, shown in Figure 5-1.a and studied in Chapter 4, represents the maximum energy that can be harvested in a cycle operated across an applied stress interval. The energy density that is available for harvesting is the difference between the area within the area within the energy harvesting stress-strain hysteresis loop and the area of the short-circuit stress-strain hysteresis loop. A non-idealized

energy harvesting cycle, shown in Figure 5-1.b, is performed when the specimen is connected to constant electrical impedance load (resistor) and mechanically loaded with a cyclic stress. Instead of controlled isocharge and isostress processes, an electrical impedance load is used to slow the electric displacement change during a mechanically driven phase transformation. This causes a back electric field that opposes the mechanically driven phase transformation and increases the mechanical energy required to drive the phase transformation. Under the same stress excitation, a non-idealized cycle captures only a small fraction of the idealized energy harvesting cycle's electrical energy. Electric displacement and strain change before the maximum pressure is reached because charge is allowed to flow across the electrical impedance load. This decreases both the input mechanical energy density that can be done on the specimen and output electrical energy density that can be done by the system when compared to the ideal cycle. Increases in electrical impedance load slow the change of electric displacement and increases the input mechanical and output electrical energy density. At zero electric impedance, the system operates at short circuit conditions and no energy is harvested; as electrical impedance is increased, the strain – stress and electric displacement – electric field ($D-E$) hystereses swell and approaches that of the ideal case. The $D-E$ behavior is shown in Figure 5-1.b. As stress is ramped the electric field remains constant due to a linear piezoelectric loading region. This is followed by a sharp and quickly decaying spike in the electric field due to the effects of a phase transformation followed by another constant electric field linear piezoelectric loading region. Although the energy harvesting capabilities of the non-idealized cycle is much smaller than the ideal case, this can be still substantially larger than that the energy harvesting capabilities achievable when operating with the same stress amplitude over a linear piezoelectric regime, Figure 5-1.c. The transformation strain and transformation electric displacement greatly

increase the envelope of input mechanical energy density and output electrical energy density. In the linear piezoelectric regime, the input mechanical energy is limited by the increase in the tanδ hysteresis due to the electric load impedance.

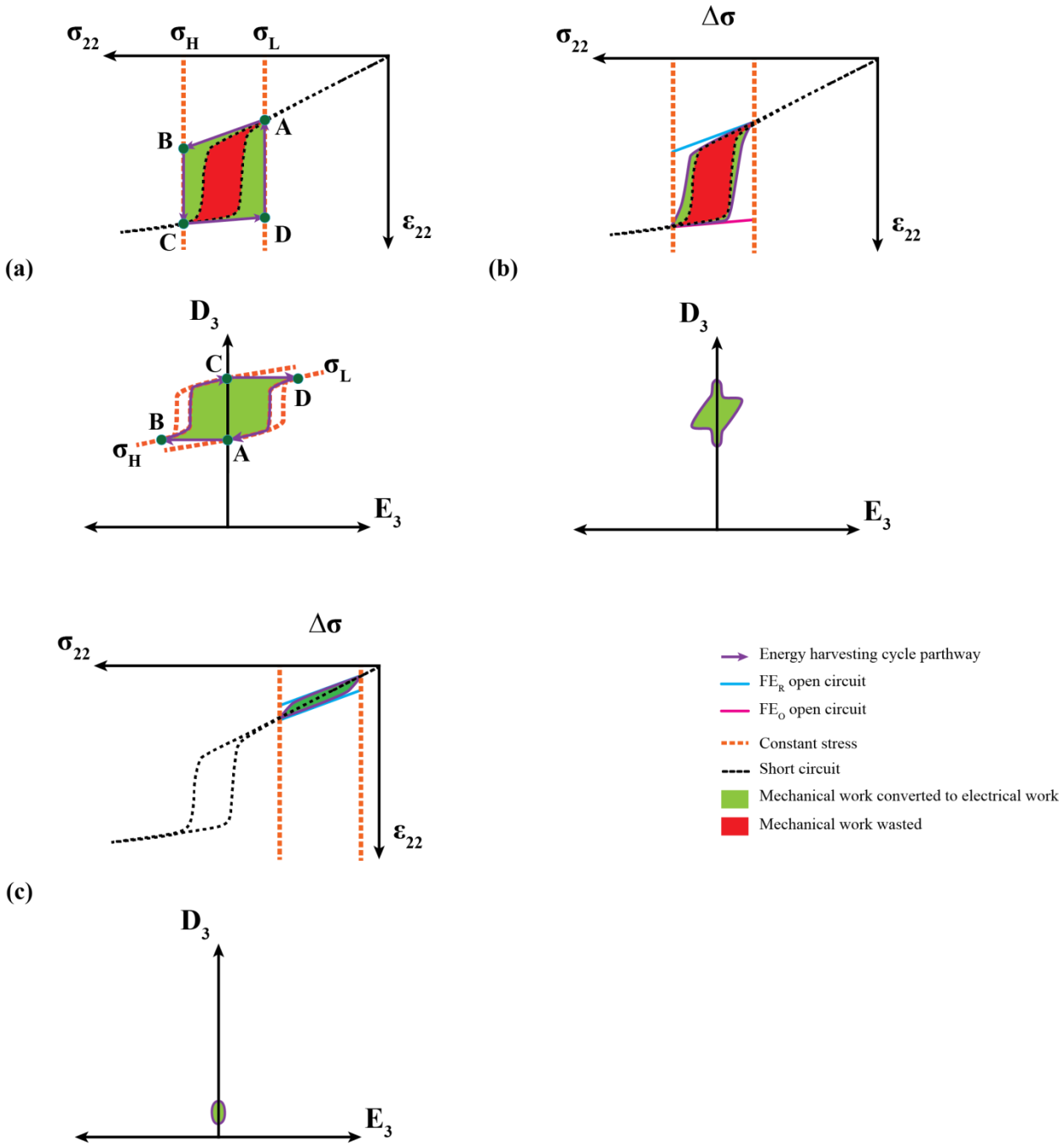

Figure 5-1. a) An idealized energy harvesting cycle over the phase transformation regime. b) Non-idealized energy harvesting cycle over the phase transformation regime. c) non-idealized energy harvesting cycle over a linear piezoelectric regime. σ, ε, E, and D are the stress, strain, electric field and electric displacement respectively.

5.2 Experimental Arrangement

5.2.1 Materials and Specimen Preparation

Two single crystal PIN-PMN-PT compositions were used in this study. Each was cut and poled in the $[011]$ orientation. Composition 1 was provided by HC Materials and composition 2 was provided by TRS Technologies Inc. The two materials were not identical, but were both in the FE_R phase with PT concentrations very close to the MPB. The compositional difference resulted in slightly different phase transformation parameters; however, the overall characteristics of the phase transformations were similar.

Crystal specimens were prepared into $[011]$ cut and poled specifications described in Chapter 3. The crystal cut and the orientation of the applied loads are described in Figure 5-2. Coordinate axes x_1, x_2, and x_3 coincide with the cubic referenced crystallographic directions $[0\bar{1}1]$, $[100]$, and $[011]$. Specimens were cut in the form of bars with dimensions of $4mm \times 4mm \times 12mm$ with $4mm \times 12mm$ faces normal to the x_1 and x_3 axes, and $4mm \times 4mm$ faces normal to the x_2 axis. They were poled in the $[011]$ direction by the manufacturers. Compressive stress was applied in the $[100]$ direction and electric field in the $[011]$ direction. Strain gauges were mounted on the $[0\bar{1}1]$ faces to measure strain ε_{22} in the $[100]$ direction.

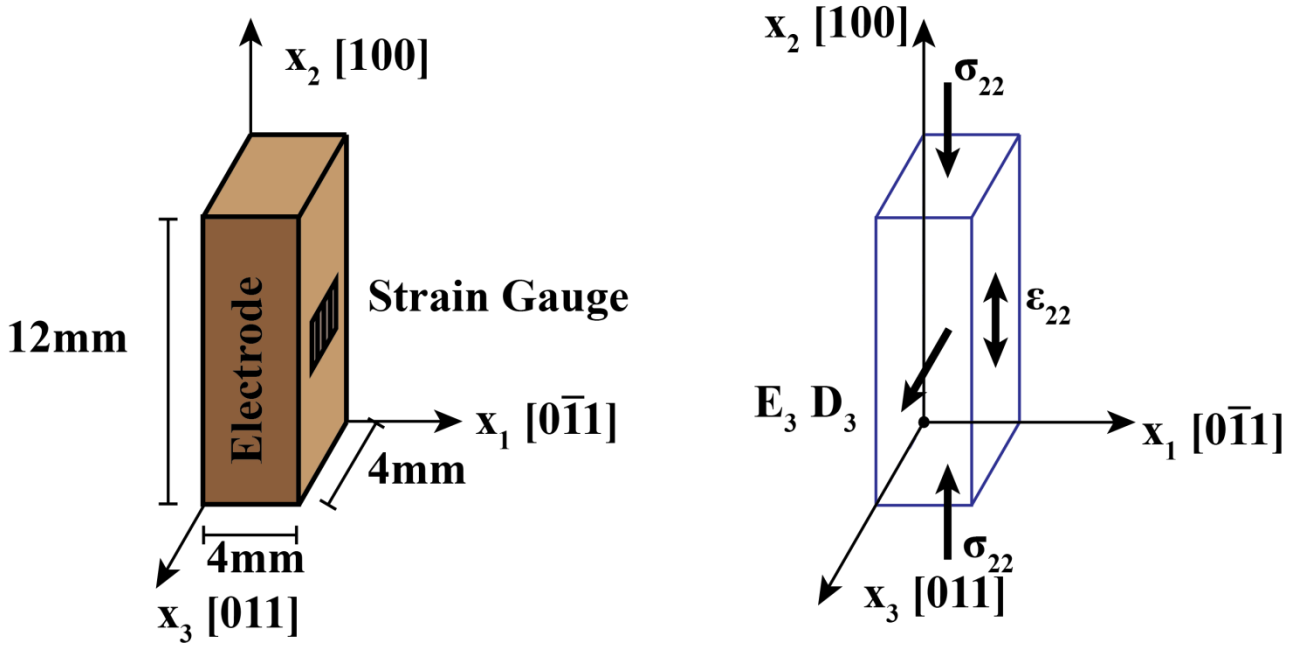

Figure 5-2. Specimen preparation and orientation in the [011] crystal cut and direction of applied loads. The crystal orientation is defined by the cubic referenced Miller indices and the coordinate system shown.

5.2.2 Experimental Arrangement

Two different loading arrangements were used. In the first, a specimen was placed directly in a load frame and the stress was cycled [55-56, 60-63]. The mechanical load consisted of a constant prestress and a superimposed cyclic triangular stress ramp. Load was measured using a load cell, and strain was monitored using a strain gauge. In the second, the specimen was mounted in an X-spring arrangement as shown in Figure 5-3. Shims in the X-spring provided bias stress and an electro-magnetic shaker provided a superimposed sinusoidal stress. The X-spring experimental arrangement provided a means to measure the frequency response, but stress was not measured. Strain was monitored using a strain gauge on the specimen and the voltage drop across the load resistor was monitored. When driving the material through the phase

transformation, sufficient bias stress was introduced such that when the shaker was off, the specimen was in the FE_O phase. As compression was applied to the X-spring the compression on the specimen was decreased. In both cases, the electrical output from the crystal was connected to a bridge rectifier and the rectified signal connected to a resistive load. The voltage drop ϕ across the resistor, R, was measured using a Keithley 6512 electrometer and the electric field E_3 was calculated by $-\phi/d$, where d is the electrode spacing. The crystals were excited for a sufficiently long duration such that ϕ reached steady state and transient effects were negligible.

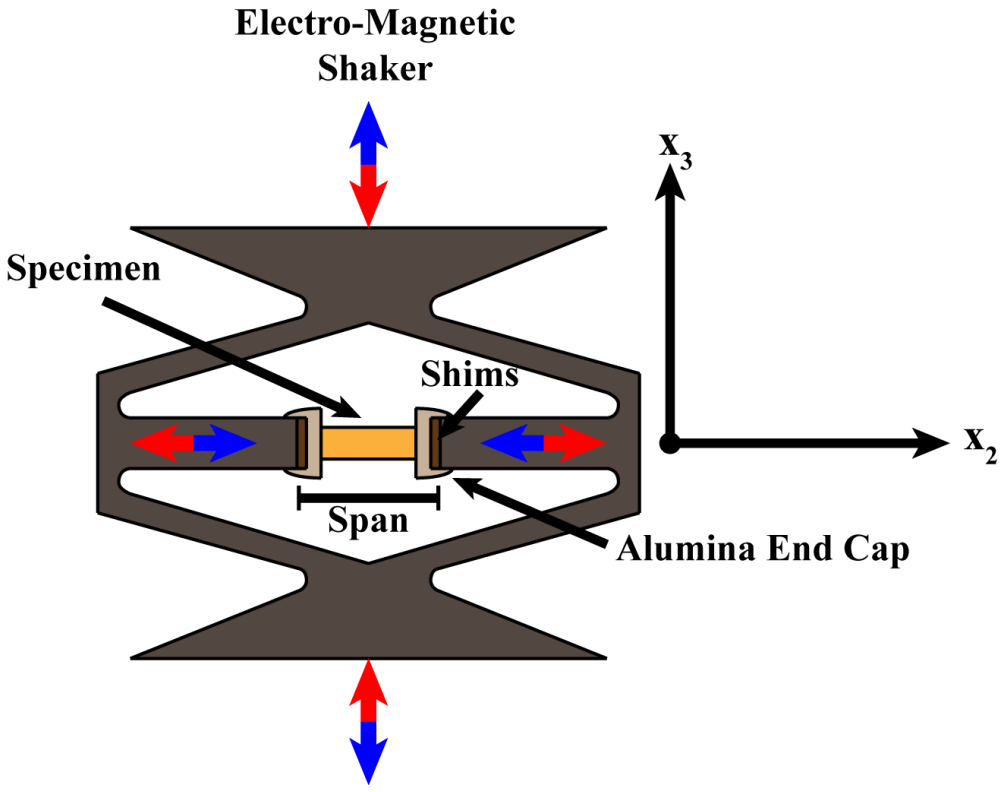

Figure 5-3. The configuration of the X-spring setup with the specimen inserted is shown. Alumina end-caps provide electrical isolation. Shims were inserted to provide a compressive preload.

5.3 Experimental Results

The strain as a function of stress and electric field is shown in Figure 5-4 for material 2. Increasing the electric field reduced the compressive stress required to start the forward and reverse FE_R-FE_O phase transformation as seen in Figures 5.a and 5.b. The load frame was used to mechanically load material 1 across the phase transformation by applying by cycling the stress between -20.5 MPa and -24 MPa; and within the linear response regime by cycling between -6 and -9.5 MPa. The peak-to-peak oscillation was 3.5 MPa in each case. The electrodes were connected to a bridge rectifier with a resistive load and the voltage drop was measured. The stress was cycled at 1 Hz with resistance values of 1 kΩ, 3 kΩ, 6 kΩ, 9 kΩ, 18 kΩ, 91 kΩ, 1 MΩ, and 10 MΩ.

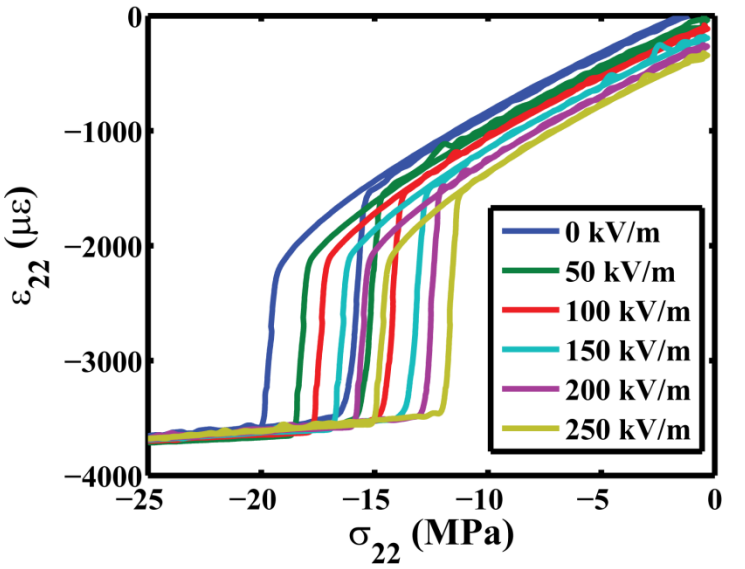

(a)

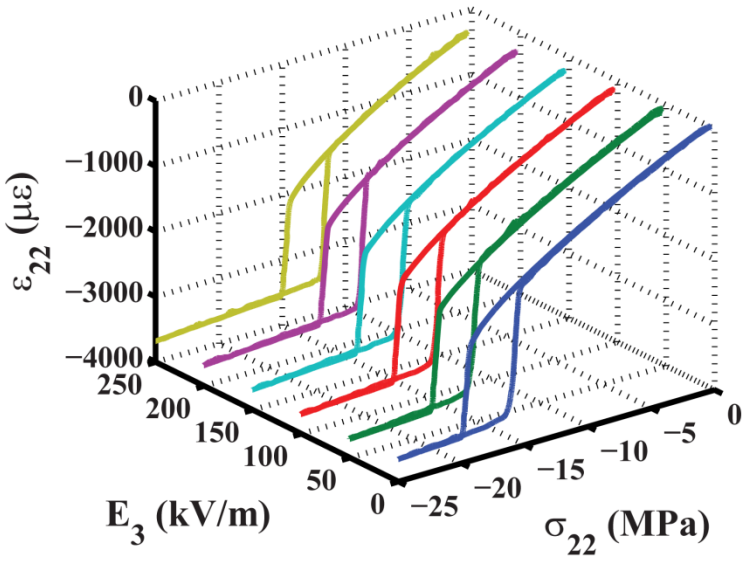

(b)

Figure 5-4. Stress (σ_{22}) versus strain (ε_{22}) for material 2 under bias electric fields (E_3) presented in a) 2D and b) 3D. The electric field is seen to reduce the transformation stress.

Figure 5-5 shows the response of material 1 with the 1kΩ and 10MΩ resistive loads when driven through the phase transformation cycle. Figure 5-5.a details the temporal E_3 and ε_{22} response to a 1 Hz triangular shaped stress cycle with a resistive load of 10 MΩ. The strain response was highly non-linear as the material passed through the phase transformation. Figure 5-5.b shows the resulting strain as a function of stress for the two resistive load values. The material produced a fixed amount of charge during each forward and reverse phase transformation. The largest output voltage was measured across the 10 MΩ resistive load. This back electric field had the effect of hindering the phase transformation; increasing the stress for the forward FE_R-FE_O phase transformation and decreasing the stress for the reverse transformation through the effect of electric fields shown in Figure 5-4. The result is a wider stress-strain hysteresis loop for the 10 MΩ case. The difference between the areas of the stress-strain hysteresis loop at zero field and the stress-strain hysteresis loop in the presence of a back electric field is an indication that additional mechanical work was required to drive the electrical load. Figure 5-5.c shows the strain vs. electric field for the two resistive loads. In each case the maximum and minimum strain values were the same, but with the 10 MΩ load there are significantly greater back electric fields. Figure 5-5.d shows the electric field vs. stress for the 1 kΩ and 10 MΩ resistive loads. The spikes in electric field are associated with the phase transformation. The electric field spikes of the 10 MΩ curve are larger than those of the 1 kΩ curve. Figure 5-5.e shows the strain as a function of stress and electric field. This plot shows that the largest electric field is generated during the transformation, i.e. where the slope of the stress-strain curve is largest. Results for the intermediate resistance values lie between the two cases presented.

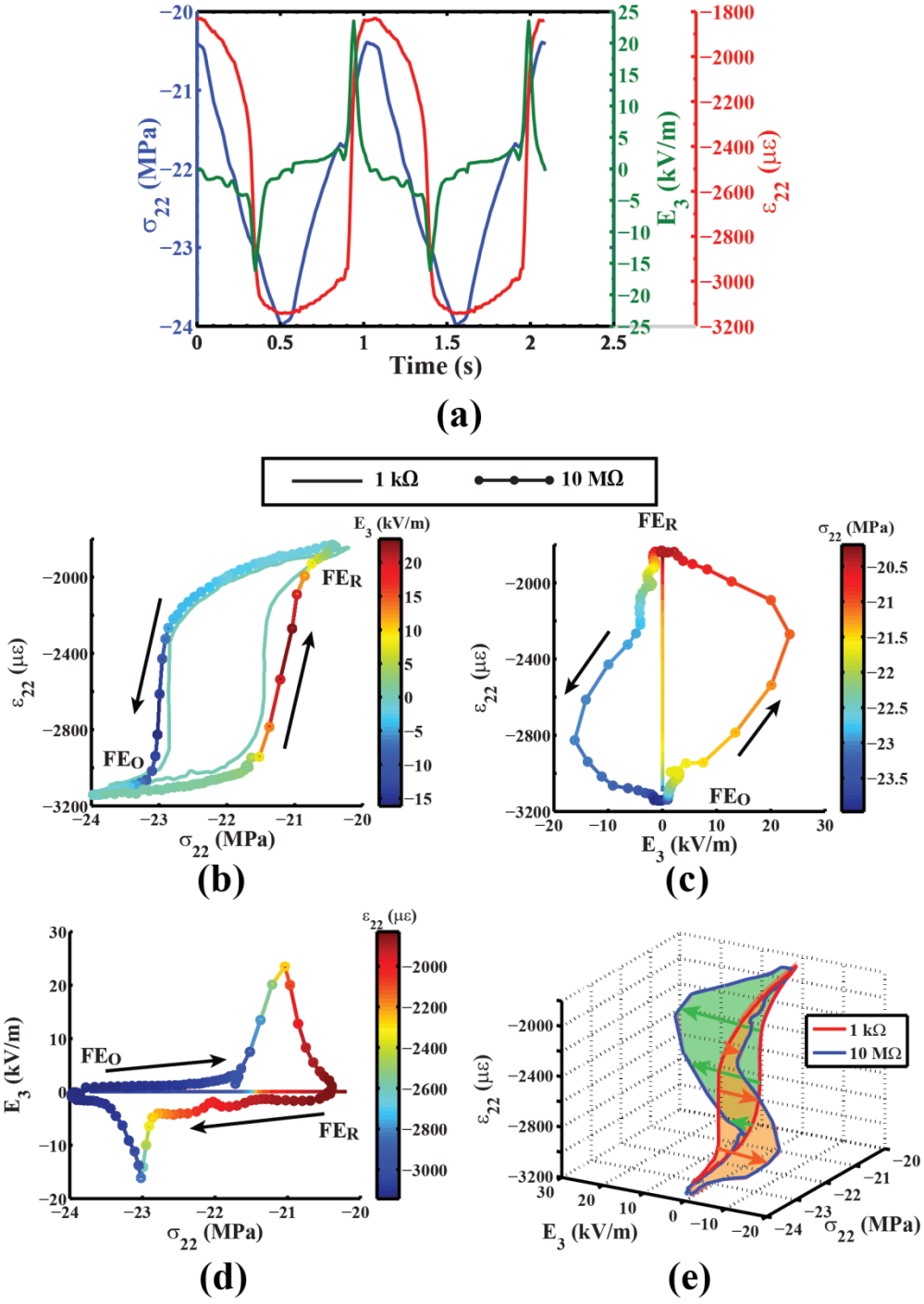

Figure 5-5. a) E_3 and ε_{22} behavior of material 1 under a σ_{22} cycle through the phase transformation with a R of 10MΩ and f of 1 Hz. b) ε_{22} vs. σ_{22} curves, c) ε_{22} vs. E_3 curves d) E_3 vs. σ_{22} curves, and e) 3D ε_{22} vs. E_3 and σ_{22} curves for R values of 1 kΩ and 10 MΩ.

The mechanical work density per cycle when the material was driven through the phase transformation was determined by numerical integration of the stress-strain data over one cycle, Equation (5.2).

$$w^{Mech,PT} = \int_0^{1/f} \sigma(t)\mathrm{d}\varepsilon(t) \tag{5.2}$$

$w^{Mech,PT}$ is the mechanical work density per cycle and f is the frequency of the mechanical excitation. Visually, this is the area within the stress-strain hysteresis loop. Superscripts $Elec$ and $Mech$ are used to distinguish electrical and mechanical work and power densities respectively; superscripts PT and LP are used to distinguish excitation over the phase transformation or the linear piezoelectric regime respectively. The average electrical power density $p^{Elec,PT}$ dissipated through the resistor was calculated using

$$p^{Elec,PT} = \frac{\phi_{RMS}^2}{AdR} \tag{5.3}$$

where ϕ_{RMS} is the root-mean-square voltage, A is the specimen electrode surface area, and d is the electrode-to-electrode spacing. Together Ad gives the specimen volume. The electrical work density dissipated per cycle through the resistor, $w^{Elec,PT}$, was found by dividing average power density by the frequency, Equation (5.4).

$$w^{Elec,PT} = \frac{p^{Elec,PT}}{f} \tag{5.4}$$

The calculated work density for each load value is shown in Figure 5-6 and summarized in Table 5-1. Figure 5-6.a contrasts the mechanical input work density and the electrical output work

density as a function of R. The $w^{Mech,PT}$ curve is closely followed by the $w^{Elec,PT}$ curve with an offset difference of 1400 J cm^{-3}. This offset is the mechanical work required to drive the phase transformation under short circuit conditions, the area within the zero electric field (short-circuit) stress-strain hysteresis loop. Figure 5-6.b shows the efficiency as a function of R. This is defined as the average electrical work per cycle done on the resistor divided by the average input mechanical work per cycle.

The loading cycle was repeated at a lower bias stress to assess energy harvesting in the linear piezoelectric regime using the same R values as the phase transformation cycles. The electrical work per cycle $w^{Elec,LP}$ in the linear regime are listed the last column Table 5-1. Figure 5-7.a presents temporal response of the strain and electric field due to a triangular stress excitation for an R of 10MΩ and shows that the strain closely followed the stress when there was no phase transformation, and the electric field was proportional to the strain rate. This resulted in a constant electric field during the stress ramp. Figure 5-7.b contrasts the difference between the back electric fields produced by the 1k and 10MΩ resistors. Figure 5-7.c gives a visual comparison of the electric field generated in the linear and in the phase transformation regimes. The large increase in electric field generated by the phase transformation is apparent (see the areas within the blue curves).

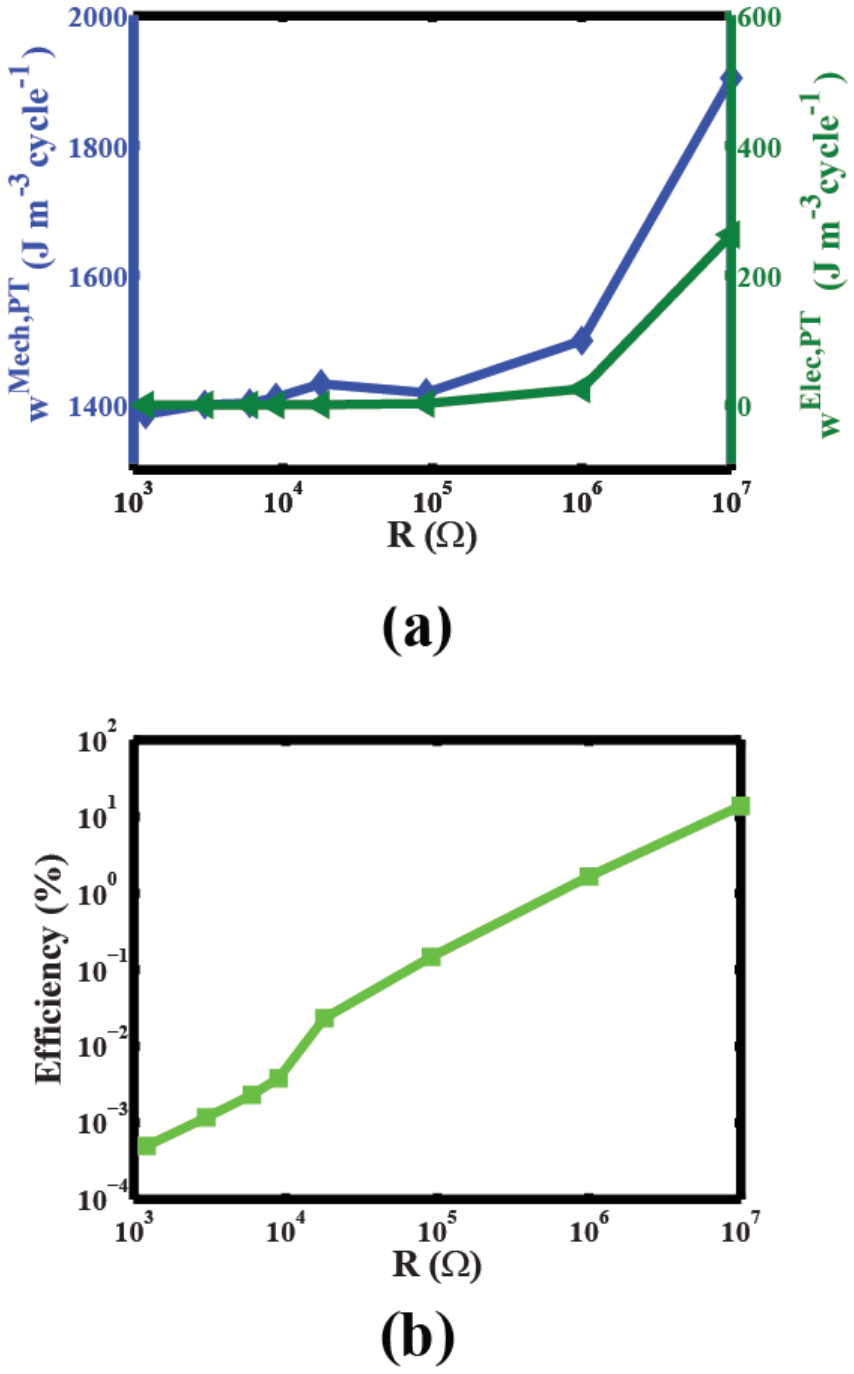

Figure 5-6. a) Comparison of $w^{Mech,PT}$ and $w^{Elec,PT}$ as a function of R. b) Efficiency as a function of R

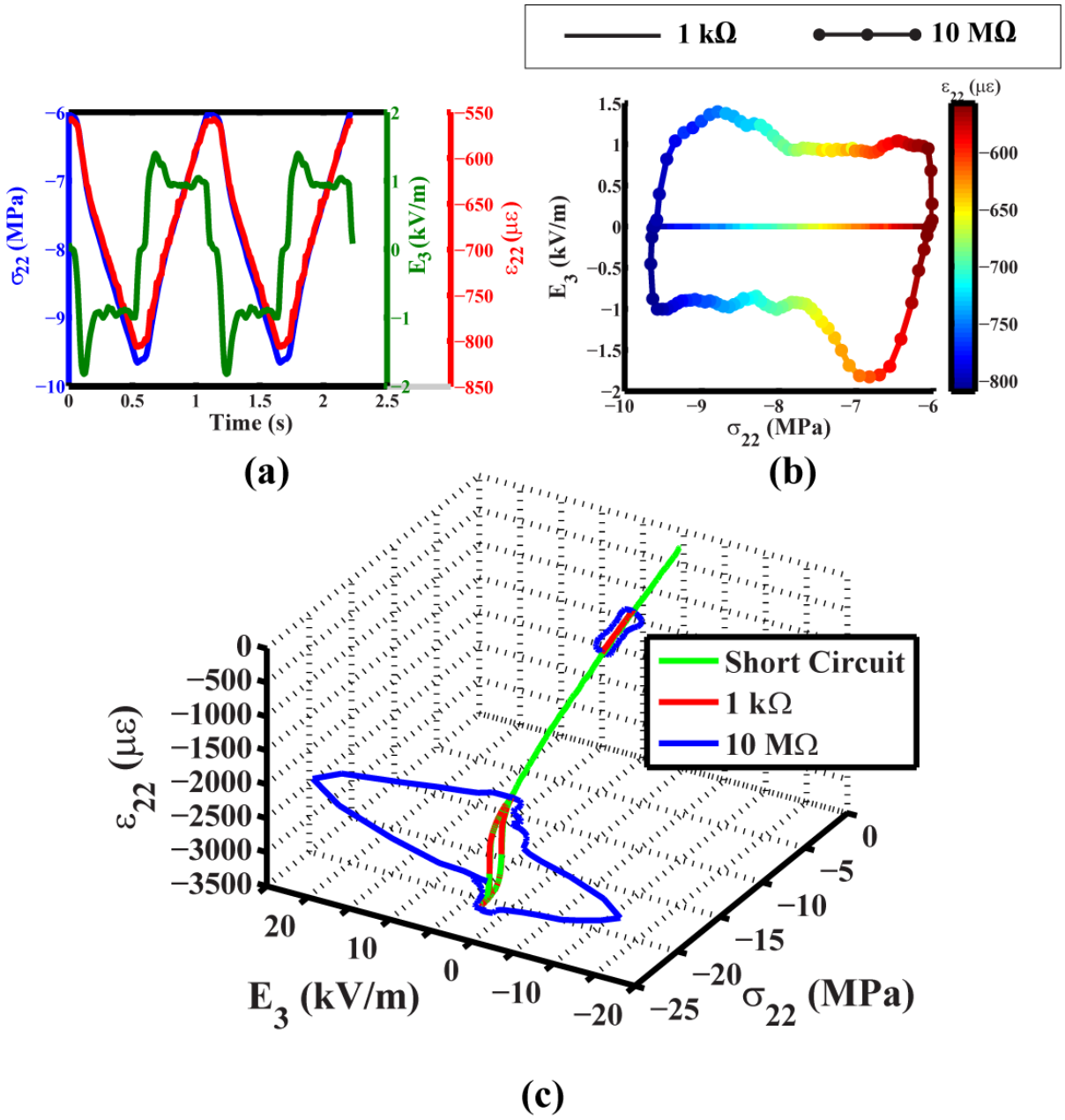

Figure 5-7. a) E_3 and ε_{22} behavior of material 1 under a linear piezoelectric σ_{22} cycle excitation with a R of 10MΩ and f of 1 Hz. b) ε_{22} vs. E_3 parametric curves for R values of 1 kΩ and 10 MΩ under σ_{22} excitation. c) Comparison of 3D ε_{22} vs. E_3 and σ_{22} curves for R values of 1.2 kΩ and 10 MΩ and in the phase transformation and in the linear piezoelectric regimes. The short circuit behavior is presented in green to illustrate the positions of the two cycles on the full ε_{22} vs. σ_{22} curve. The results from loading in the linear regime are summarized in Table 5-1.

The linear results are compared to the phase transformation results in Figure 5-8. Plotted on logarithmic axes, the harvested $w^{Elec,LP}$ and $w^{Elec,PT}$ appear roughly linear and parallel over the range of R values tested and indicate the energy density over the phase transformation region is greater than the linear piezoelectric region by a fairly consistent factor. In the case of material 1, with a σ_{22} peak-to-peak amplitude of 3.5 MPa, $w^{Elec,PT}$ is, on average, approximately 27 times greater than $w^{Elec,LP}$. The ratio of $w^{Elec,PT}$ to $w^{Elec,LP}$ was observed to be largest at 91kΩ with a value of 108.

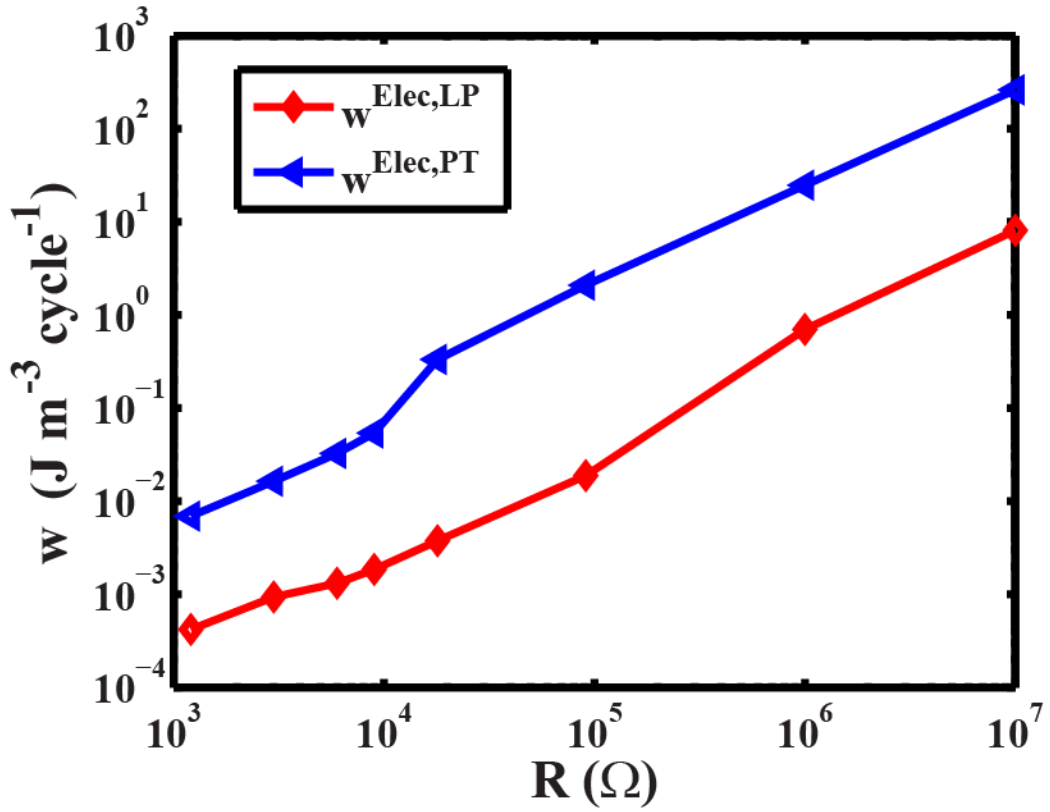

Figure 5-8. Comparison of energy harvesting performance using linear piezoelectric σ_{22} loading cycle and phase transformation σ_{22} loading cycle at various R values.

Table 5-1. Comparison of mechanical $w^{Mech,PT}$ vs. $w^{Elec,PT}$ under a σ_{22} excitation driven over the phase transformation region and $w^{Elec,PT}$ vs. $w^{Elec,LP}$ under a σ_{22} excitation over a linear piezoelectric region with the same stress amplitude at 1 Hz.

Resistor (kΩ)	w^{Mech} (Jcm^{-3})	$w^{Elec-PT}$ (Jcm^{-3})
1.21	1386	0.007
3	1401	0.017
6	1403	0.033
9	1412	0.055
18	1424	0.343
91	1419	2.169
1000	1499	25.774
10000	1904	275.899

Experiments were next performed to determine the effect of frequency on $w^{Elec,PT}$. This was done using the X-spring arrangement with material 2. The ε_{22} profile in the X-spring was sinusoidal with a range from -1500 με to -3500 με. Combinations of R and f ranging from 1k-10MΩ and 1-100Hz respectively were used and $w^{Elec,PT}$ was calculated using Equation (5.4); the results are presented in Table 5-2. The voltage drop across the load resistor is shown for R = 10 MΩ and f = 1, 2, 3, 4, 5, 6, and 7 Hz in Figure 5-9. The charge flow through the resistor per cycle was found to be independent of frequency, therefore, the current through and the voltage across the resistor scale linearly with frequency. This results in the increase of voltage amplitude

with frequency seen in Figure 5-9. $w^{Elec,PT}$ and $p^{Elec,PT}$ from Table 5-2 are plotted against f and R in Appendix C.2.

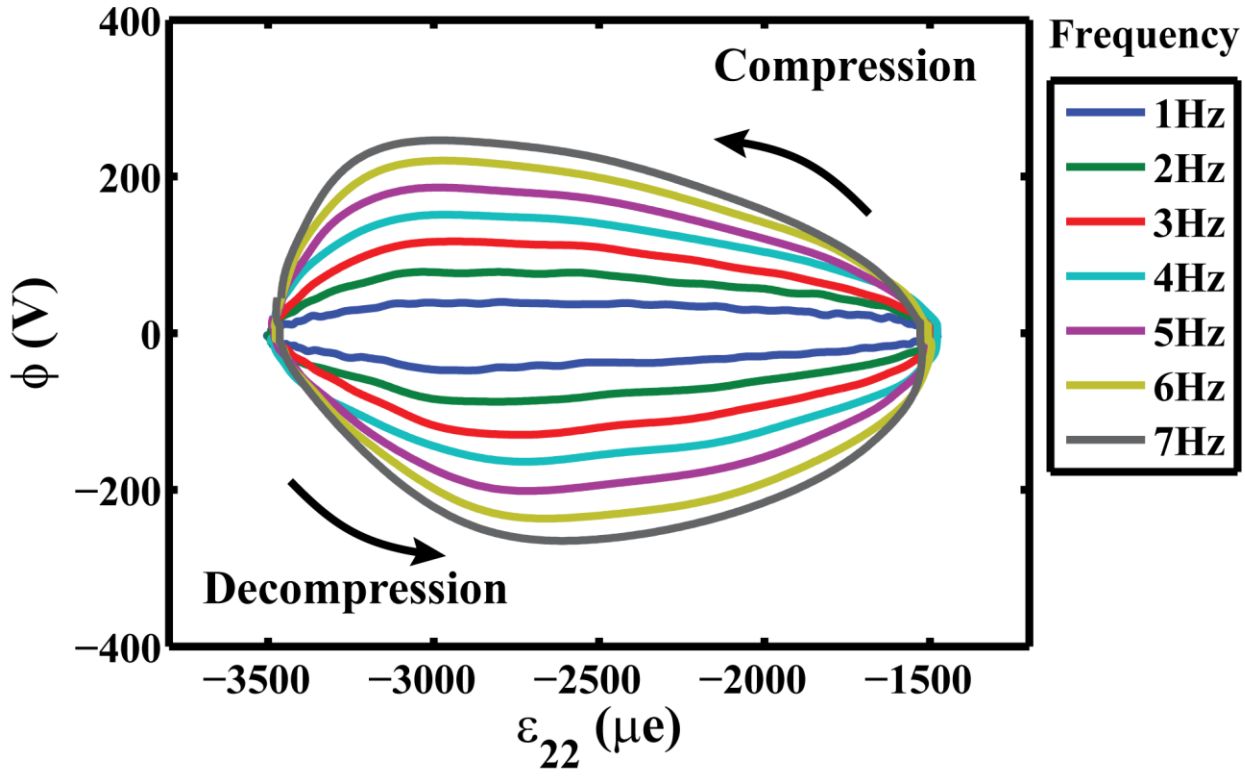

Figure 5-9. Strain vs. voltage as a function of frequency with a resistive load of 10 MΩ.

Table 5-2. $w^{Elec\ PT}$ (J m^{-3} cycle^{-1}) for material 2 in the X-spring fixture under combinations of f and R.

Frequency (Hz) \ Resistance (kΩ)	3	6	9	1000	10000
1	-	-	-	-	384.94
2	-	-	-	-	665.05
3	-	-	-	-	896.12
4	-	-	-	-	1218.70
5	0.34	0.64	0.93	100.89	1389.22
6	-	-	-	-	1614.32
7	-	-	-	-	1828.65
8	-	-	-	-	1963.03
10	0.61	1.15	1.65	217.65	-
15	0.90	1.72	2.58	320.44	-
20	1.16	2.35	3.30	421.77	-
25	1.58	2.89	4.02	520.53	-
30	-	-	-	624.69	-
35	-	-	-	713.56	-
40	-	-	-	806.70	-
45	-	-	-	901.76	-
50	3.31	6.06	8.55	998.70	-
55	-	-	-	1067.61	-
60	-	-	-	1155.39	-
65	-	-	-	1266.67	-
70	-	-	-	1348.12	-
75	4.67	8.34	11.71	-	-
100	6.94	12.20	17.29	-	-

5.4 Discussion

Models for power and work in piezoelectric devices driving a resistive shunt are well developed [122] for linear piezoelectricity. Here a linear analysis was applied to the phase transformation regime and found to model the phase transformation data well over the range of parameters measured. Limitations of this approach are discussed.

The ferroelectric material connected to a resistive shunt was modeled as a current source and capacitor in parallel, connected to a resistor as shown in Figure 5-10. The current was generated by the rate of change of polarization. The charge produced can be either stored by capacitance of the ferroelectric crystal or it can flow through the resistor. In the model presented below, the material was driven back and forth across the phase transformation by a sinusoidal mechanical load with angular frequency ω and the resulting polarization was expressed as a sinusoidal function of time, Equation (5.5),

$$P(t) = \Delta P \sin(\omega t) \tag{5.5}$$

where P is the polarization and ΔP is the peak amplitude of the polarization (half the total polarization change across the phase transformation so that the peak-to-peak amplitude of P was the full phase transformation polarization change).

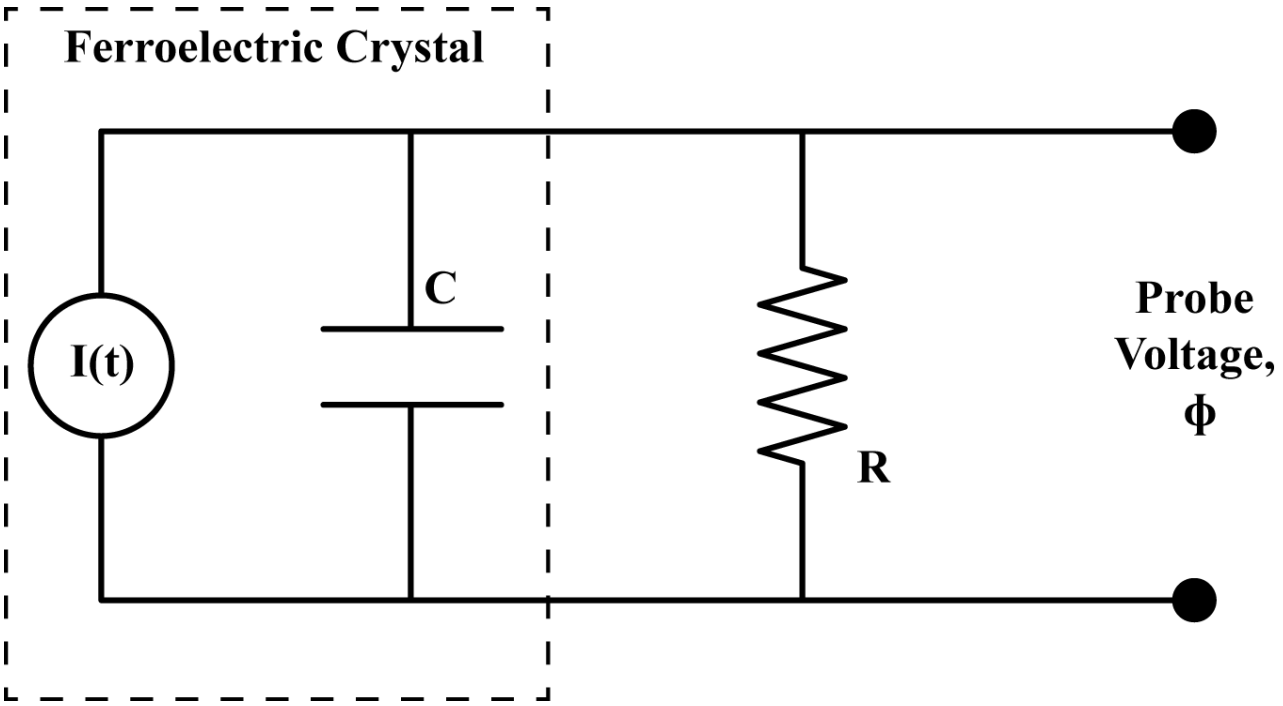

Figure 5-10. Model circuit of strain driven ferroelectric crystal with internal capacitance C attached to a resistive shunt with resistance R.

The experimental results were for monolithic crystals, however, the crystal can be made into a multilayer stacks to increase the electrode area and charge output. The limits on this approach are the ability to build single crystals stacks (practical layer thicknesses are on the order of 0.2 mm), and the energy storage capacity of the specimen that increases with number of layers. Given that d, A, and C are the electrode-to-electrode distance, the electrode area, and the capacitance of the monolithic specimen, a multilayer stack of n layers with the same overall dimensions as the monolithic specimen has electrode-to-electrode spacing d_{stack} of d/n, area A_{stack} of nA, and capacitance C_{stack} of n^2C. The current is found by taking the time derivative of the polarization and multiplying by the electrode surface area, Equation (5.6).

$$I(t) = A_{stack}\Delta P\omega\cos(\omega t) \tag{5.6}$$

Assuming the capacitance remains constant, the circuit in Figure 5-10 is governed by Equation (5.7),

$$C_{stack}\frac{\mathrm{d}\phi(t)}{\mathrm{d}t} + \frac{\phi(t)}{R} = I(t) \tag{5.7}$$

where ϕ is the voltage across the resistor. The solution for ϕ is given by Equation (5.8). For convenience, $A\Delta P$ was replaced by ΔQ, which is the peak amplitude charge change on the surface of the electrode under open circuit conditions for the monolithic material.

$$\phi(t) = n\Delta QR\omega\left[\frac{Rn^2C\omega\sin(\omega t)+\cos(\omega t)}{R^2n^4C^2\omega^2+1}\right]+\left[\phi_0 - \frac{n\Delta QR\omega}{R^2n^4C^2\omega^2+1}\right]e^{\frac{-t}{Rn^2C}} \tag{5.8}$$

After the system has reached steady state, the root-mean-square voltage is given by Equation (5.9).

$$\phi_{RMS} = \sqrt{\frac{1}{2}\frac{n^2\Delta Q^2R^2\omega^2}{\left(n^4R^2C^2\omega^2+1\right)}} \tag{5.9}$$

The average power density p^{Elec} and work density per cycle w^{Elec} are given by Equations (7) and (8),

$$p^{Elec} = \frac{\phi_{RMS}^2}{AdR} = \frac{1}{2Ad}\frac{n^2\Delta Q^2R\omega^2}{\left(n^4R^2C^2\omega^2+1\right)} \tag{5.10}$$

$$w^{Elec} = \frac{p^{Elec}}{f} = \frac{1}{Ad}\frac{\pi n^2 \Delta Q^2 R\omega}{\left(n^4 R^2 C^2 \omega^2 + 1\right)} \tag{5.11}$$

In cases where C_{stack} is small and $n = 1$ so that $RC_{stack}\omega \ll 1$, such as is the case for the monolithic single crystal specimens used in this study, Equations (5.9)-(5.11) simplify to Equations (5.12)-(5.14) where ϕ_{RMS}, p^{Elec}, and w^{Elec} are linear functions of fR, f^2R, and fR respectively.

$$\phi_{RMS} = \frac{\Delta Q R\omega}{\sqrt{2}} = \frac{2\pi\Delta Q}{\sqrt{2}} Rf \tag{5.12}$$

$$p^{Elec} = \frac{\Delta Q^2 R\omega^2}{2Ad} = \frac{2\pi^2 \Delta Q^2}{Ad} Rf^2 \tag{5.13}$$

$$w^{Elec} = \frac{2\pi^2 \Delta Q^2}{Ad} Rf \tag{5.14}$$

Figures 12.a, and 12.b show p^{Elec} vs. Rf^2 and w^{Elec} vs. Rf respectively for all of the data shown in Table 5-2 and compares it against the model. ΔP of 0.01Cm^{-2} was used in the model because the total change in electric displacement across FE_R-FE_O phase transformation was experimentally observed [62] to be of 0.02Cm^{-2}. The p^{Elec} values in Figure 5-11.a and w^{Elec} values in Figure 5-11.b collapse into a single linear curve for the different combinations R and f and correlates extremely well with the model. This suggests a moderately easy design process for energy harvesters using materials that utilize the FE_R-FE_O phase transformation as long as the actuation frequency and capacitance of the design is low.

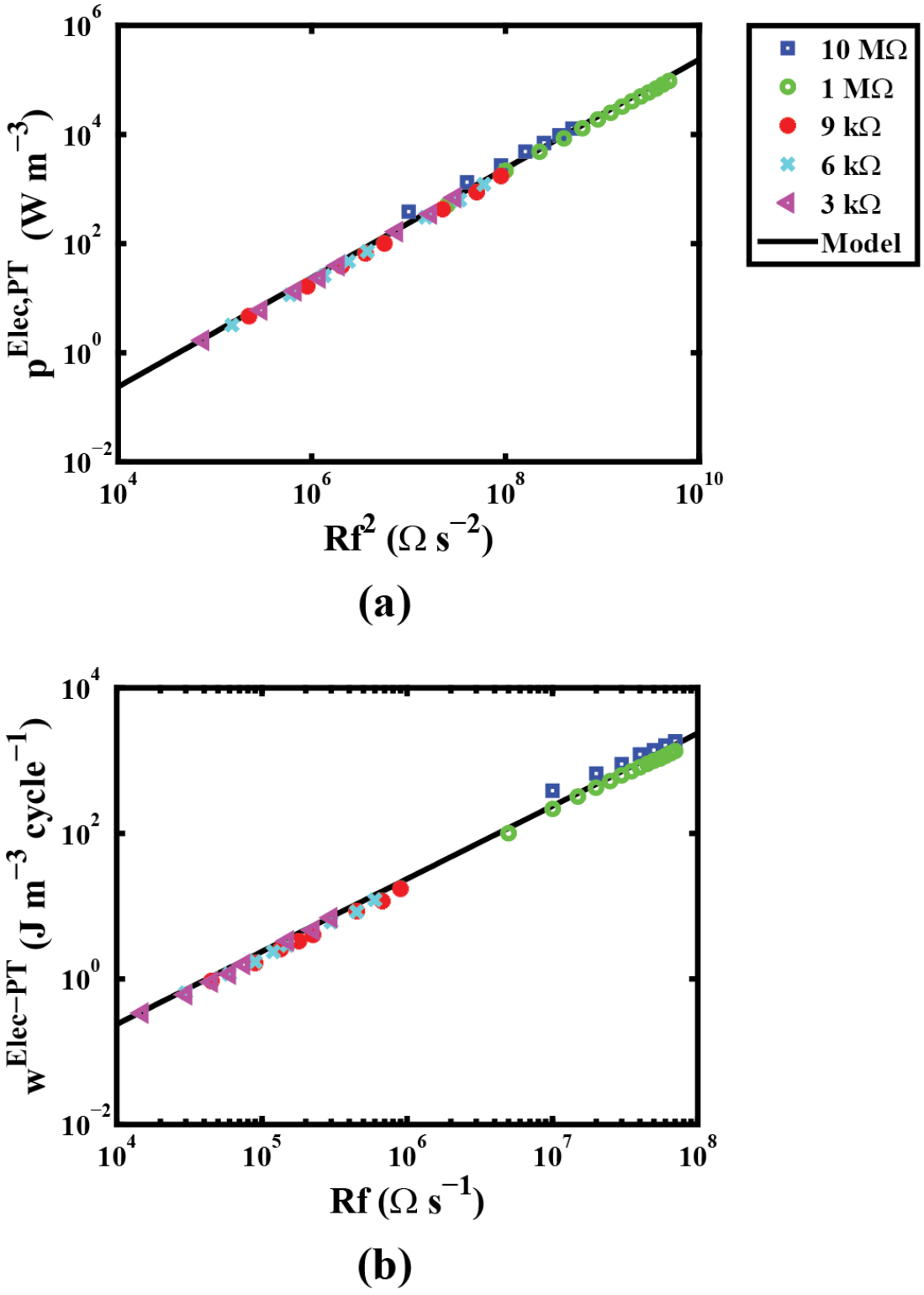

Figure 5-11. a) $w^{Elec-PT}$ as a function of fR and b) $p^{Elec-PT}$ as a function of f^2R for experimental data and model using ΔP of 0.01Cm^{-2}.

If a fixed capacitance assumption is made, the maximum power transfer from a stack into a resistive load is achieved when the resistance of the load is matched to the capacitance of the stack, Equation (5.15).

$$R_{opt}(\omega) = \frac{1}{n^2 C \omega} \tag{5.15}$$

The optimal resistance R_{opt} is not achievable in practice, as it is frequency-dependent; nonetheless, for excitations where the electrical response is pure-tone, Eq. (5.15) provides a basis to "tune" the impedance of the load to extract maximum power from the stack. The max power density p_{max} can be found using R_{opt} in Equation (5.10).

$$p_{max} = \frac{1}{4Ad}\frac{\Delta Q^2 \omega}{C} \tag{5.16}$$

This indicates that with resistive tuning, the maximum power density for a fixed drive frequency is independent of the number of layers. The reduction of R_{opt} due to multilayer stacks is demonstrated in Figure 5-12 where the simulated power is shown for 1, 2, 4, and 8 layer stacks with a C of 0.5pF, ΔP of 0.01Cm^{-2}, and ω of 10 rad s^{-1} for the same specimen dimensions used in this study. The model shows an increase in stack layers reduces R_{opt}, as expected from Equation (5.15), and the peak power remains independent of layer densities at a fixed frequency. Above the optimum frequency the capacitance of the specimen begins to dominate. Charge is stored by the specimen capacitance, which reduces the charge that passes through the resistor and thus reduces the output power density as the load resistance increases. In the extreme case where the crystal is in open circuit and R is infinite, all the charge is stored on the capacitor and no power is discharged across the electrical shunt.

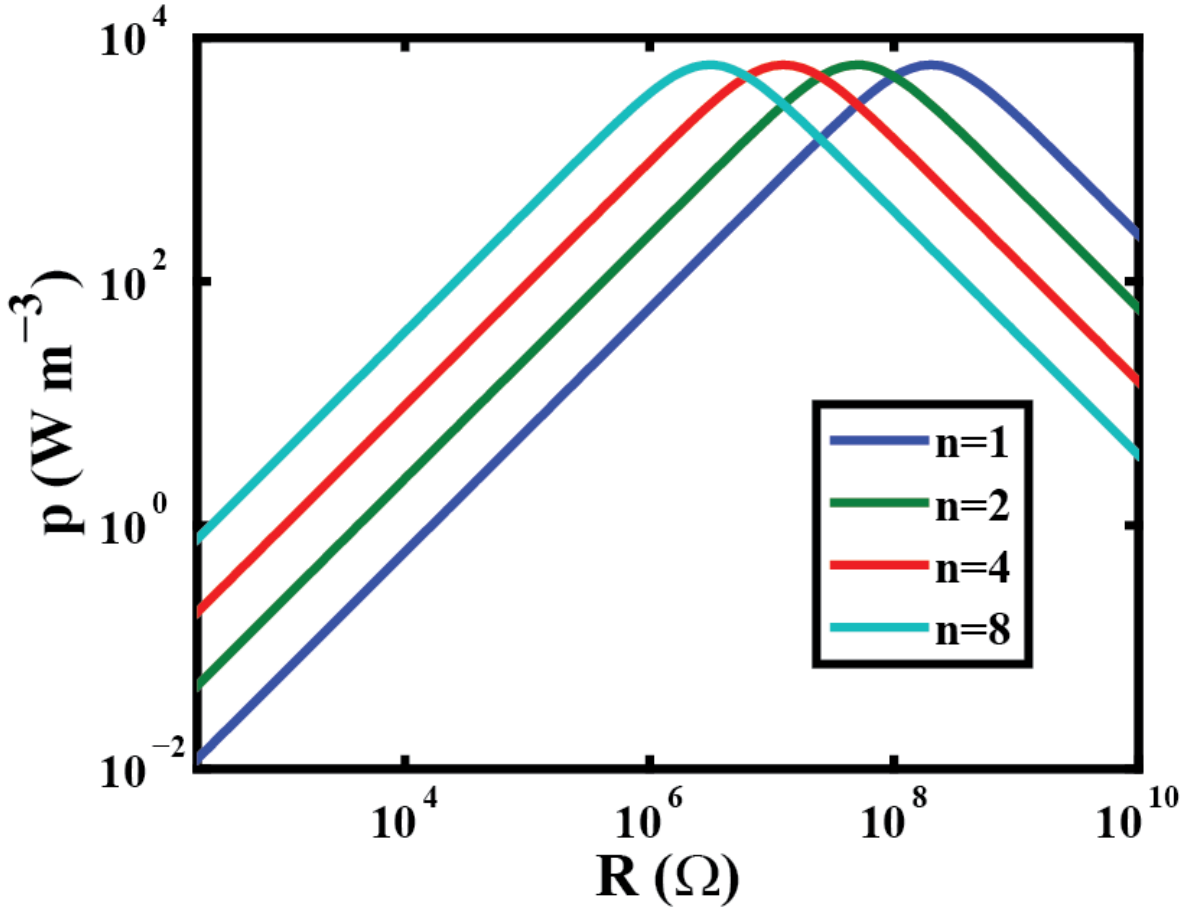

Figure 5-12. Power density as a function of R of a simulated multilayer stack structure with n layers, C of 0.5pF, ΔP of 0.01Cm^{-2}, and ω of 10 rad s^{-1}.

An estimate of R_{opt} and p_{max} of the tested ferroelectric material can be made using Equations (5.15) and (5.16) with linear dielectric assumptions. Although the material permittivity across the phase transformation is difficult to estimate, the FE_R and FE_O capacitances can be used to provide upper and lower bounds for the capacitance of the specimen; FE_R and FE_O capacitances were measured to be 0.5pF and 0.13pF respectively. Using a ΔP of

0.01Cm^{-2}, f of 1Hz, and the FE_R capacitance, the p_{max} is estimated to be 3.8 kWm^{-3} at a R_{opt} of 0.32GΩ; using the FE_O capacitance, the p_{max} is estimated to be 15.8 kWm^{-3} at a R_{opt} of 1.27GMΩ. At 1Hz, p_{max} is potentially 10 to 40 times greater than the 10 MΩ power density of 385 Wm^{-3} shown in Table 5-2. Although the linear dielectric assumption is not accurate for the phase transforming ferroelectric material, this estimate infers that only a small fraction of the maximum possible power density has been demonstrated and further studies are required to verify the maximum power density.

There are a number of limitations to the linear dielectric analysis. For a phase transformations in ferroelectric materials, the fixed capacitance assumption is only valid for $R < R_{opt}$ and $\omega < \omega_{opt}$ where the charge generated by the phase transformation almost entirely passes through the resistive load in each half cycle. The capacitance of the specimen in conjunction with resistor in the circuit forms an RC circuit, but with a highly non-linear capacitance in the case of a phase transforming dielectric. In all cases investigated in this work, the RC time constant was substantially smaller than the period of the applied cyclic load. This resulted in the generated charge passing through the resistive load in each half cycle and negligible charge stored by the capacitance. In this case the material was driven through the full phase transformation as shown in Figure 5-13.a. The nonlinearity in the specimen capacitance becomes an issue at higher frequencies or at higher electrical impedance loads. A failure to pass the entire charge through the resistor during the half cycle will result in a partial phase transformation as illustrated in Figure 5-13.b. A partial phase transformation will reduce the output power. In the extreme case of an open circuit, charge is prevented from flowing through the resistor and no work is dissipated by the resistive load. Instead, the phase transformation is

hindered completely due to the buildup of back electric field; mechanical loading of the material from the FE_R phase towards the FE_O phase will behave as a linear piezoelectric and a linear elastic with FE_R coupling coefficients and open circuit FE_R stiffness.

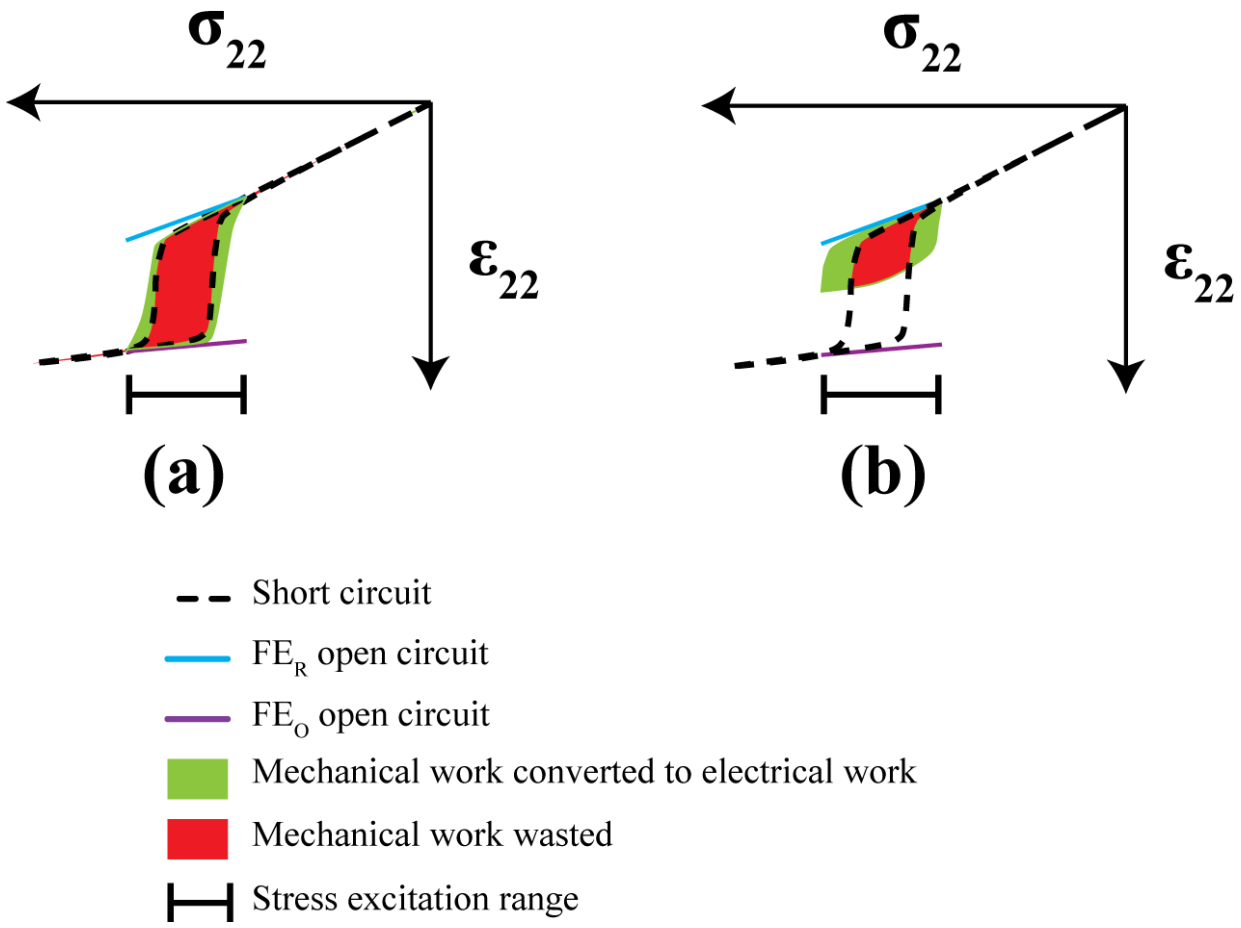

Figure 5-13. Stress-strain transformation behavior of ferroelectric relaxor single crystal for a) a system operating below the cutoff frequency and b) above the cutoff frequency.

5.5 Conclusions

The experimental results demonstrate that σ_{22} excitation over the FE_R-FE_O phase transformation hysteric region is capable of delivering greater harvestable power densities and work densities per cycle than comparable amplitude excitations in σ_{22} in the linear piezoelectric regime of the same material. $w^{Elec,PT}$ was demonstrated to be on average 27 times, with a peak of 108 times, greater than the $w^{Elec,LP}$ when each regime was subjected a stress amplitude of 3.5 MPa. Phase transforming materials require more input mechanical work density but have higher output peak power density than linear piezoelectric materials due to the sizeable jumps in $\Delta\varepsilon_{22}$ and ΔP_3 across the phase transformation. Results also indicate the FE_R-FE_O phase transformation has a fixed overhead cost in w^{Mech} associated with the mechanical energy required to drive the short circuit phase transformation and a large fraction of w^{Mech} beyond that required to drive the short circuit phase transformation is converted to w^{Elec}. Therefore, the efficiency of the energy harvesting cycle increased with R and $\Delta\sigma_{22}$. A linear dielectric model was presented based on the energy harvesting circuit. When used with small specimen capacitance assumptions and low drive frequencies, the model was shown to have good agreement with experimental data and w^{Elec} and p^{Elec} were shown scale be linear to fR and f^2R respectively. This results in a relatively simple design process for energy harvesters that utilize the FE_R-FE_O phase transformation. The model also addresses the effects of multilayered materials and showed that peak power density is independent of the number of layers. Estimates of peak power density using the model at 1 Hz are 10 to 40 times the maximum value experimentally observed.

Limitations to the linear dielectric model were presented for cases of high f and R where the phase transformation is hindered by capacitive charge buildup.

CHAPTER 6

MICROMECHANICS MODELING OF SOLID STATE FERROELECTRIC PHASE TRANSFORMATIONS

This chapter addresses the development of a micromechanics materials model that captures the ferroelectric and ferroelastic phenomena of any jump type variant or phase transformation in ferroelectric materials including ferroelectric – ferroelectric and ferroelectric – antiferroelectric phase transformations. The term phase/variant will be used to describe the ferroelectric phase and variant (polarization orientation) combination. The material constitutive behavior divided into linear and nonlinear components. The nonlinear component used an energy criterion based switching code to determine phase/variant state of the material and the spontaneous polarization and strain that causes ferroelectric and ferroelastic phenomena. Linear constitutive equations were used to describe the elastic, piezoelectric, and dielectric material behavior. A piezoelectric finite element framework, similar to that proposed by Allik and Hughes [66], was used to solve the boundary value problems presented by the mechanical and electrical field equations for materials described by the combined linear and nonlinear constitutive behavior.

While there have been many micromechanics models developed for both relaxor ferroelectrics and PZT ceramics, few have developed a general model that captures both types of phase transformations. Additionally, few works have addressed how to relate experimental quantities and features directly to the switching criterion of a material model. The following work develops a micromechanics material model that captures the nonlinear and hysteretic behavior of all first-order jump type phase transformations. A relation of modeling parameters to experimental quantities is presented. A linear elastic, piezoelectric, and dielectric finite

element framework is presented. Modeling results for FE – AF phase transformations in 95/5-2Nb PZT and FE_R – FE_O phase transformations in PIN-PMN-PT are presented and compared to experimental results.

6.1 Constitutive Relations

In a elastic, piezoelectric, and dielectric material with spontaneous strains and electric polarizations, the total strain (ε) and electric displacement (D) from all sources is,

$$\begin{aligned} \varepsilon &= \varepsilon^{elastic} + \varepsilon^{piezo} + \varepsilon^{0} \\ D &= D^{dielectric} + D^{piezo} + P^{0} \end{aligned} \tag{6.1}$$

where $\varepsilon^{elastic}$, ε^{piezo}, and ε^{0} are the elastic, piezoelectric, and spontaneous contributions to the total strain and $D^{dielectric}$, D^{piezo}, and P^{0} are the dielectric, piezoelectric, and spontaneous polarization contributions to the electric displacement. The constitutive relations for a linear elastic, piezoelectric, and dielectric material in the strain – charge form is,

$$\begin{aligned} \varepsilon_{ij}^{elastic} &= s_{ijkl}^{E}\sigma_{kl} \\ \varepsilon_{ij}^{piezo} & d_{ijn}E_{n} \\ D_{m}^{dielectric} &= \kappa_{mn}^{\sigma}E_{n} \\ D_{m}^{piezo} &= d_{klm}\sigma_{kl} \end{aligned} \tag{6.2}$$

where the parameters σ , and E are the stress, and electric field respectively. The coefficient tensors s^{E} , d , and κ^{σ} are the compliance, strain – charge piezoelectric tensor, and permittivity. Coefficients are valid when superscript loads are held constant. Indices range from 1 to 3, repeated indices imply summation, and commas imply differentiation. Substituting the constitutive relations from equation (6.2) into equation (6.1) yields the strain – charge form for the fully coupled ferroelectric and ferroelastic system.

$$\begin{aligned} \varepsilon_{ij} &= s_{ijkl}^{E}\sigma_{kl} + d_{ijn}E_{n} + \varepsilon_{ij}^{0} \\ D_{m} &= \kappa_{mn}^{\sigma}E_{n} + d_{klm}\sigma_{kl} + P_{m}^{0} \end{aligned} \tag{6.3}$$

In this form, the strain and electric displacement behavior could be described by a combination of load based linear constitutive behavior and nonlinear ferroelectric and ferroelastic behavior. It should be noted that the linear constitutive coefficients are dependent on the polarization direction. The constitutive tensors have symmetries based on the current phase (e.g. tetragonal, rhombohedral, orthorhombic, etc.). Transversely isotropic (hexagonal symmetry) was used as a first order approximation where the number of independent coefficients of a single-crystal single-domain ferroelectric with polarization oriented in the x_3 direction can be reduced to 5 elastic constants, 3 piezoelectric constants, and 2 permittivity constants. For rotation matrices from the local phase/variant coordinate system to the global coordinate system see Appendix A.1.

$$
\begin{aligned}
S^{FE} &= \begin{bmatrix} S_{11} & S_{12} & S_{13} & 0 & 0 & 0 \\ S_{12} & S_{11} & S_{13} & 0 & 0 & 0 \\ S_{13} & S_{13} & S_{33} & 0 & 0 & 0 \\ 0 & 0 & 0 & S_{44} & 0 & 0 \\ 0 & 0 & 0 & 0 & S_{44} & 0 \\ 0 & 0 & 0 & 0 & 0 & 2\left(S_{11}-S_{12}\right) \end{bmatrix}^{FE} \\
d^{FE} &= \begin{bmatrix} 0 & 0 & d_{13} \\ 0 & 0 & d_{13} \\ 0 & 0 & d_{33} \\ 0 & d_{24} & 0 \\ d_{24} & 0 & 0 \\ 0 & 0 & 0 \end{bmatrix}^{FE} \\
\kappa^{FE} &= \begin{bmatrix} \kappa_{11} & 0 & 0 \\ 0 & \kappa_{11} & 0 \\ 0 & 0 & \kappa_{33} \end{bmatrix}^{FE}
\end{aligned}
\tag{6.4}
$$

In the antiferroelectric phase, the piezoelectric behavior is nonexistent as the piezoelectric effect of each polarized unit cell is counteracted by that of a paired unit cell polarized in the opposite direction. There is no net polarization for each antiferroelectric dipole pair; however the orientation of the variant can be determined by the principle strain directions.

$$S^{AF} = \begin{bmatrix} S_{11} & S_{12} & S_{13} & 0 & 0 & 0 \\ S_{12} & S_{11} & S_{13} & 0 & 0 & 0 \\ S_{13} & S_{13} & S_{33} & 0 & 0 & 0 \\ 0 & 0 & 0 & S_{44} & 0 & 0 \\ 0 & 0 & 0 & 0 & S_{44} & 0 \\ 0 & 0 & 0 & 0 & 0 & 2\left(S_{11} - S_{12}\right) \end{bmatrix}^{AF}$$

$$d^{AF} = \begin{bmatrix} 0 & 0 & 0 \\ 0 & 0 & 0 \\ 0 & 0 & 0 \\ 0 & 0 & 0 \\ 0 & 0 & 0 \\ 0 & 0 & 0 \end{bmatrix}^{AF} \tag{6.5}$$

$$\kappa^{AF} = \begin{bmatrix} \kappa_{11} & 0 & 0 \\ 0 & \kappa_{11} & 0 \\ 0 & 0 & \kappa_{33} \end{bmatrix}^{AF}$$

A finite element framework brings together the linear and nonlinear constitutive terms in order to solve the boundary value problems presented by the mechanical and electrical field equations. When formulating the finite element framework, the linear constitutive relations contribute to the final stiffness matrix terms and the nonlinear P^0 and ε^0 are represented as unbalanced forces on the nodes. When a material is loaded, the finite element framework calculates local stresses and electric fields at each of the nodes and an energy based phase/variant

switching model then updates P^0 and ε^0 is used to determine if local loads meet a transformation criterion.

6.2 Boundary Value Problems and Finite Element Formulation

Linear piezoelectric finite element solvers are commonly formulated using the stress – charge form. Equation (6.3) is converted to the stress – charge form can be expressed as:

$$\begin{aligned} \sigma_{ij} &= c^E_{ijkl}\varepsilon_{kl} - e_{ijn}E_n - c^E_{ijkl}\varepsilon^0_{kl} \\ D_m &= \kappa^{\varepsilon}_{mn}E_n + e_{klm}\varepsilon_{kl} + e_{klm}\varepsilon^0_{kl} + P^0_m \end{aligned} \tag{6.6}$$

where the stress – charge piezoelectric coupling coefficient is represented by e.

Using a scalar potential approach to model the dielectric behavior, the electrical boundary value problem over the domain Ω with a scalar potential (ϕ)is as follows:

$$\begin{cases} D_{m,m} - \rho = 0 & \text{in } \Omega \\ E_m = -\phi_{,m} & \text{in } \Omega \\ \phi = \bar{\phi} & \text{on } \Gamma_\phi \\ -D_m \hat{n}_m = \omega & \text{on } \Gamma_\omega \end{cases} \tag{6.7}$$

where ρ is the charge density, $\bar{\phi}$ is scalar potential prescribed on the surface Γ_ϕ, and ω is a surface charge density and $\hat{n}$ is a normal vector on the surface Γ_ω. The elastic boundary value problem with displacement u is likewise defined as:

$$\begin{cases} \sigma_{ij,j} + b_i = 0 & \text{in } \Omega \\ \epsilon_{ij} = \dfrac{1}{2}\left(u_{i,j} + u_{j,i}\right) & \text{in } \Omega \\ u = \bar{u} & \text{on } \Gamma_u \\ \sigma_{ij}\hat{n}_j = t_i & \text{on } \Gamma_t \end{cases} \tag{6.8}$$

where b is the body force, $\bar{u}$ is displacement prescribed on the surface Γ_u, t is the traction on the surface Γ_t.

Multiplying the first relations of equations (6.7) and (6.8) with the virtual displacement δu and virtual potential $\delta\phi$ respectively and integrating by parts yields the weak form formulation in a virtual work framework.

$$\begin{aligned}\int_\Omega \sigma_{ij}\delta\varepsilon_{i,j}d\Omega &= \int_{\Gamma_t} t_i\delta u_i d\Gamma + \int_\Omega b_i\delta u_i d\Omega \\ \int_\Omega D_m\delta E_m d\Omega &= \int_{\Gamma_\omega} \omega\delta\phi d\Gamma + \int_\Omega \rho\delta\phi d\Omega\end{aligned} \tag{6.9}$$

Substituting the constitutive equations in equation (6.6) yields,

$$\begin{aligned}\int_\Omega \left(c^E_{ijkl}\varepsilon_{kl} - e_{ijn}E_n - c^E_{ijkl}\varepsilon^0_{kl}\right)\delta\varepsilon_{i,j}d\Omega &= \int_{\Gamma_t} t_i\delta u_i d\Gamma + \int_\Omega b_i\delta u_i d\Omega \\ \int_\Omega \left(\kappa^\varepsilon_{mn}E_n + e_{klm}\varepsilon_{kl} + e_{klm}\varepsilon^0_{kl} + P^0_m\right)\delta E_m d\Omega &= \int_{\Gamma_\omega} \omega\delta\phi d\Gamma + \int_\Omega \rho\delta\phi d\Omega\end{aligned} \tag{6.10}$$

Moving all constants to the right hand side the final formulation represents the effect of ε^0 and P^0 as unbalanced body force vectors and charge density.

$$\begin{aligned}\int_\Omega \left(c^E_{ijkl}\varepsilon_{kl} - e_{ijn}E_n\right)\delta\varepsilon_{i,j}\,d\Omega &= \int_\Omega \left(b_i\delta u_i + \underbrace{c^E_{ijkl}\varepsilon^0_{kl}\delta\varepsilon_{i,j}}_{\text{Unbalanced Body Force}} \right) d\Omega + \int_{\Gamma_t} t_i\,\delta u_i\,d\Gamma \\ \int_\Omega \left(\kappa^\varepsilon_{mn}E_n + e_{klm}\varepsilon_{kl}\right)\delta E_m\,d\Omega &= \int_\Omega \left(\rho\delta\phi \underbrace{-\left(e_{klm}\varepsilon^0_{kl} + P^0_m\right)\delta E_m}_{\text{Unbalanced Charge Density}} \right) d\Omega + \int_{\Gamma_\omega} \omega\,\delta\phi\,d\Gamma\end{aligned} \tag{6.11}$$

In a finite element formulation, the unknown displacement u and scalar potential ϕ can be approximated by,

$$\begin{aligned}u_i &\approx \hat{u}_i = N^a\tilde{u}^a_i \\ \phi &\approx \hat{\phi} = N^a\tilde{\phi}^a\end{aligned} \tag{6.12}$$

where $\hat{\square}$ denotes an approximation of a function $\square$, N_a is an element's shape function of node a, and $\tilde{\square}^a$ represents a function's nodal value for an element at node a. Similarly the electric field and strain can be represented as,

$$\begin{aligned} \varepsilon_\alpha &\approx \hat{\varepsilon}_\alpha = B^a_{\alpha i}\tilde{u}^a_i \\ E_m &\approx \hat{E}_m = -N^a_{,m}\tilde{\phi}^a \end{aligned} \tag{6.13}$$

where B is the strain – displacement matrix and lower case Greek letter indices imply Mandel-Voigt notation from 1 to 6.

The weak form for an element can be approximated by applying the approximations of equations (6.12) and (6.13) into equation (6.11) integrating over the domain of an element Ω^e.

$$\begin{aligned} \delta\tilde{u}^b_i\left[\int_{\Omega^e}\left(c^E_{\alpha\beta}B^a_{\beta j}\tilde{u}^a_j + e_{\alpha n}N^a_{,n}\tilde{\phi}^a\right)B^b_{\alpha i}\,d\Omega = \int_{\Omega^e}\left(b_i N^b + c^E_{\alpha\beta}\varepsilon^0_\beta B^b_{\alpha i}\right)d\Omega + \int_{\Gamma^e_t} t_i N^b\,d\Gamma\right] \\ \delta\tilde{\phi}^b\left[\int_{\Omega^e}\left(\kappa^\varepsilon_{mn}N^a_{,n}\tilde{\phi}^a - e_{\beta m}B^a_{\beta i}\tilde{u}^a_i\right)N^b_{,m}\,d\Omega = \int_{\Omega^e}\left(\rho N^b + \left(e_{klm}\varepsilon^0_{kl} + P^0_m\right)N^b_{,m}\right)d\Omega + \int_{\Gamma^e_\omega}\omega N^b\,d\Gamma\right] \end{aligned} \tag{6.14}$$

Since $\delta\tilde{u}^b$ and $\delta\tilde{\phi}^b$ are arbitrary values, equation (6.14) can be expressed in the equilibrium equations,

$$\begin{bmatrix} C^{ab}_{ij} & Y^{ab}_i \\ Z^{ab}_i & K^{ab} \end{bmatrix}\begin{Bmatrix} \tilde{u}^a_i \\ \tilde{\phi}^a \end{Bmatrix} = \begin{Bmatrix} F^{a,M}_i \\ F^{a,\mathrm{E}} \end{Bmatrix} \tag{6.15}$$

where C^{ab}, Y^{ab}, Z^{ab}, and K^{ab} form a stiffness matrix for the nodal pair $a-b$ and $F^{a,M}_i$ and $F^{a,E}$ are force vectors shown by the following,

$$
\begin{aligned}
C_{ij}^{ab} &= \int_{\Omega^e} B_{\alpha i}^{b} c_{\alpha\beta}^{E} B_{\beta j}^{a} d\Omega \\
Y_{i}^{ab} &= \int_{\Omega^e} B_{\alpha i}^{b} e_{\alpha n} N_{,n}^{a} d\Omega \\
Z_{i}^{ab} &= \int_{\Omega^e} -N_{,m}^{b} e_{\beta m} B_{\beta i}^{a} d\Omega \\
K^{ab} &= \int_{\Omega^e} N_{,m}^{b} \kappa_{mn}^{\varepsilon} N_{,n}^{a} d\Omega \\
F_{i}^{a,M} &= \int_{\Omega^e} \left(b_i N^b + c_{\alpha\beta}^{E} \varepsilon_{\beta}^{0} B_{\alpha i}^{b} \right) d\Omega + \int_{\Gamma_t^e} t_i N^b d\Gamma \\
F^{a,\mathrm{E}} &= \int_{\Omega^e} \left(\rho N^b + \left(e_{klm} \varepsilon_{kl}^{0} + P_m^0 \right) N_{,m}^{b} \right) d\Omega + \int_{\Gamma_\omega^e} \omega N^b d\Gamma
\end{aligned}
\tag{6.16}
$$

A linear piezoelectric finite element system can be developed by assembling a global stiffness matrix, a global nodal displacement vector, and a global force vectors from element stiffness matrices, nodal displacement vectors, and force vectors.

6.3 Micromechanics Switching Criteria

Below the Curie temperature, each ferroelectric and antiferroelectric phase has specific crystallographic directions along which the P^0 vectors and ε^0 elongation are oriented. Shown in Figure 6-1, the possible ferroelectric tetragonal (FE_T), ferroelectric rhombohedral (FE_R), and ferroelectric orthorhombic (FE_O) phases have possible polarization variants in the 6 $\langle 100 \rangle$, 8 $\langle 111 \rangle$, and 12 $\langle 011 \rangle$ directions respectively. Antiferroelectric phases such as the antiferroelectric tetragonal (AF_T) and antiferroelectric orthorhombic (AF_O) have only 3 and 6 unique variants as each electric dipole is counteracted by an equal and opposite dipole resulting in zero net polarization but non-zero strain unique to each variant. The material phase and variant can thus be described as its phase/variant. Under favorable loading conditions, a material will transform from one phase/variant to the next most energetically favorable phase/variant. If

the material remains in the same phase after a phase/variant transition, then only a polarization reorientation occurs; however, if the phase variant transition causes the material to switch to a variant of a different phase then a phase transformation occurs.

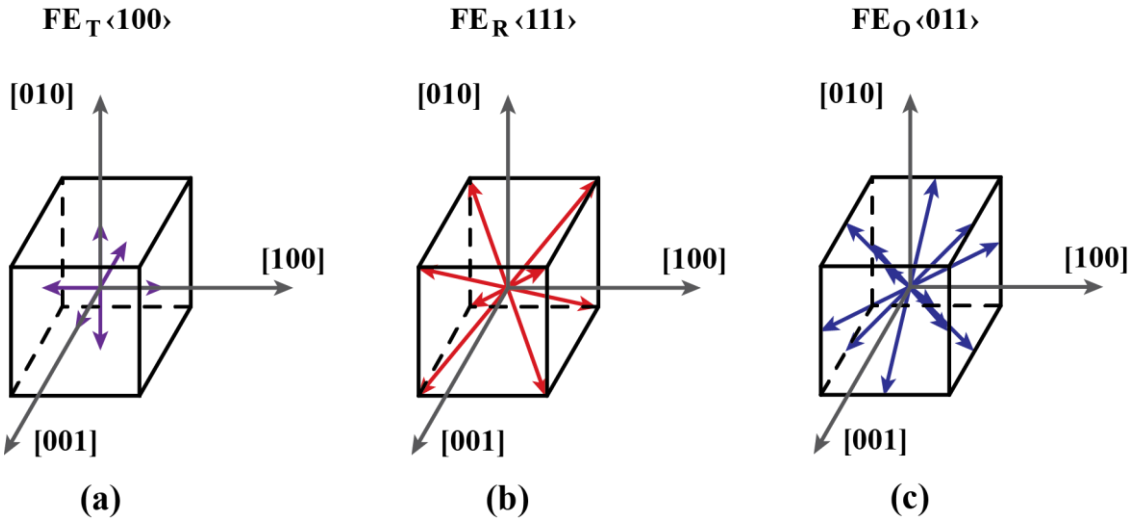

Figure 6-1. Possible spontaneous polarization directions for variants of a) FE_T b) FE_R and c) FE_O phases.

The material model only accounts for the changes in spontaneous strain and polarization, therefore the phase/variant transformation criteria need to be described in terms of changes in P^0 vectors and ε^0 from one phase/variant to another. Given a two phase/variant system of phase/variants A and B with respective spontaneous polarizations $P^{0,A}$ and $P^{0,B}$ and respective spontaneous strains $\varepsilon^{0,A}$ and $\varepsilon^{0,B}$. If the stress and electric field driven hysteresis is centered about the origin, then the availability of the spontaneous strain and polarization of a material to do work (W) when transforming from phase/variant A to phase/variant B is determined by,

$$W^{A\to B} = \sigma_{ij}\Delta\epsilon_{ij}^{0,A\to B} + E_m\Delta P_m^{0,A\to B} \tag{6.17}$$

when subjected to applied loads σ_{ij} and E_m. $\Delta\epsilon_{ij}^{0,A\to B}$ and $\Delta P_m^{0,A\to B}$ are the changes in spontaneous strain and polarization going from phase/variant A to B. The transformation from phase/variant A to phase/variant B occurs if $W^{A\to B}$ exceeds the energy barrier associated with the transformation hysteresis ($U^{h,A\to B}$). $U^{A\to B}$ can be extracted from experimental data using,

$$U^{h,A\to B} = \begin{cases} \sigma_{ij}^{c,A\to B}\Delta\varepsilon_{ij}^{0,A\to B} & \text{Constant } E \\ E_m^{c,A\to B}\Delta P_m^{0,A\to B} & \text{Constant } \sigma \end{cases} \tag{6.18}$$

Assuming energy required to drive the phase transformation is the same for both the electrically driven and mechanically driven phase transformations, $U^{h,A\to B}$ can be calculated using either the electric displacement – electric field hysteresis data or the strain – stress hysteresis data. Shown in Figure 6-2, under constant electric field conditions, $U^{h,A\to B}$ is the product of $\Delta\epsilon_{ij}^{0,A\to B}$ and the coercive stress ($\sigma_{ij}^{c,A\to B}$) or, under constant stress loading conditions, $U^{h,A\to B}$ is the product of $\Delta P_m^{0,A\to B}$ and the coercive field ($E_m^{c,A\to B}$). Visually, $U^{h,A\to B}$ is half the area of either the $\epsilon_{ij}^0 - \sigma_{ij}$ hysteresis or half the $D_m^0 - E_m$ hysteresis.

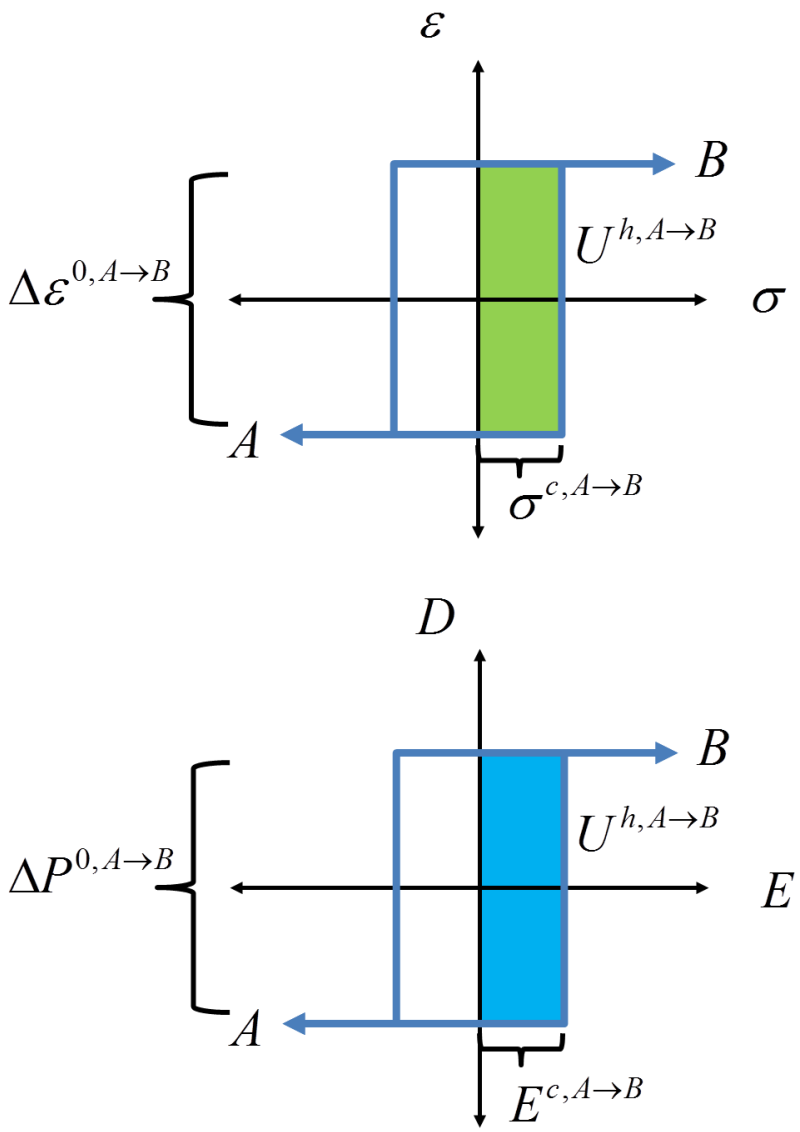

Figure 6-2. Transition energy barrier $U^{A\to B}$ in a two phase variant system with mechanical and electrical hysteresis centered about the origin.

In cases where the transformation hysteresis is not centered about the stress and electric field origins, which is the case for most FE_R – FE_O transformations in relaxor ferroelectrics and FE – AF transformations in 95/5 PZT, a modification is made to equation (6.17) to account for the shift in hysteresis.

$$W^{s,A\to B}=\begin{cases}\left(\sigma_{ij}-\sigma_{ij}^{s,A-B}\right)\Delta\epsilon_{ij}^{0,A\to B}+E_m\Delta P_m^{0,A\to B}\\ \sigma_{ij}\Delta\epsilon_{ij}^{0,A\to B}+\left(E_m-E_m^{s,A-B}\right)\Delta P_m^{0,A\to B}\end{cases} \tag{6.19}$$

where $W^{s,A\to B}$ is the modified work potential, $\sigma_{ij}^{s,A-B}$ is the stress shift of the mechanical hysteresis at zero electric field, and $E_m^{s,A-B}$ is the electric field shift of the electrical hysteresis at zero stress. This is shown graphically in Figure 6-3. Again applying the assumption that the energy required to drive the phase transformation is the same for electrical and mechanical loading, the shift in the phase transformation energy barrier can be described as,

$$U^{s,A\to B}=\begin{cases}\sigma_{ij}^{s,A-B}\Delta\epsilon_{ij}^{0,A\to B}\\ E_m^{s,A-B}\Delta P_m^{0,A\to B}\end{cases} \tag{6.20}$$

changing equation (6.19) to

$$W^{s,A\to B}=\sigma_{ij}\Delta\epsilon_{ij}^{0,A\to B}+E_m\Delta P_m^{0,A\to B}-U^{s,A\to B} \tag{6.21}$$

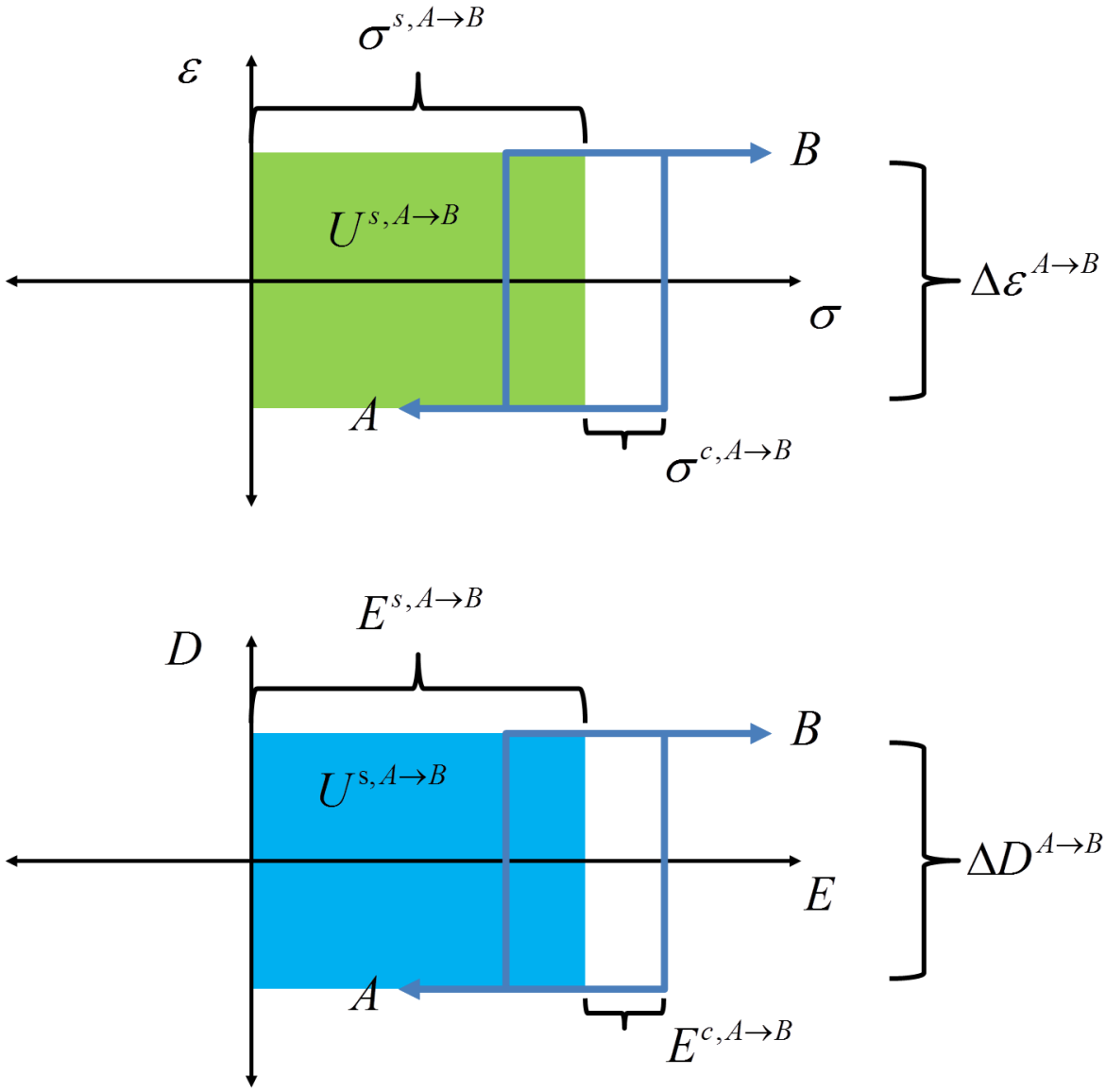

Figure 6-3. Graphical representation of the stress **s**hift in mechanical hysteresis ($\sigma^{s,A\to B}$) at zero electric field and the electric field shift in electrical hysteresis($E^{s,A\to B}$) at zero stress.

The switching criteria $W^{s,A\to B} > U^{h,A\to B}$ for transition from phase/variant A to B becomes,

$$\sigma_{ij}\Delta\epsilon_{ij}^{0,A\to B} + E_m\Delta P_m^{0,A\to B} > U^{h,A\to B} + U^{s,A\to B} \tag{6.22}$$

or,

$$W^{A\to B} > U^{A\to B} \tag{6.23}$$

where $W^{A\to B}$ is given by equation (6.17) and the total transformation energy barrier ($U^{A\to B}$) is,

$$U^{A\to B} = U^{h,A\to B} + U^{s,A\to B} \tag{6.24}$$

From equation (6.23), expressions for the phase transformation surface can be created. The critical phase transformation stress ($\sigma_{ij}^{A\to B}$) under an applied electric field (E_m) and the critical phase transformation electric field ($E_m^{A\to B}$) under an applied stress (σ_{ij}) are,

$$\begin{aligned} \sigma_{ij}^{A\to B} &= \underbrace{-\Delta P_m^{0,A\to B}\left(\Delta \epsilon_{ij}^{0,A\to B}\right)^{-1}}_{\text{Slope}} E_m + \underbrace{\sigma_{ij}^{c,A\to B} + \sigma_{ij}^{s,A-B}}_{\text{Constant}} \\ E_m^{A\to B} &= \underbrace{-\Delta \epsilon_{ij}^{0,A\to B}\left(\Delta P_m^{0,A\to B}\right)^{-1}}_{\text{Slope}} \sigma_{ij} + \underbrace{E_m^{c,A\to B} + E_m^{s,A-B}}_{\text{Constant}} \end{aligned} \tag{6.25}$$

The phase transformation electric fields and stresses shown in equation (6.25) can be used to generate a phase diagram of the phase/variants A and B as a function of the applied loads. Figure 6-4 shows the phase diagram for the phase/variant A – B transformation. Under an applied stress load σ_{ij}, the phase transformation electric fields for the forward and reverse transformations, $E_m^{A\to B}$ and $E_m^{B\to A}$, are shown in red and blue. The slope of $E_m^{A\to B}$ and $E_m^{B\to A}$ are $-\Delta \epsilon_{ij}^{0,A\to B}\left(\Delta P_m^{0,A\to B}\right)^{-1}$ and $-\Delta \epsilon_{ij}^{0,B\to A}\left(\Delta P_m^{0,B\to A}\right)^{-1}$ respectively.

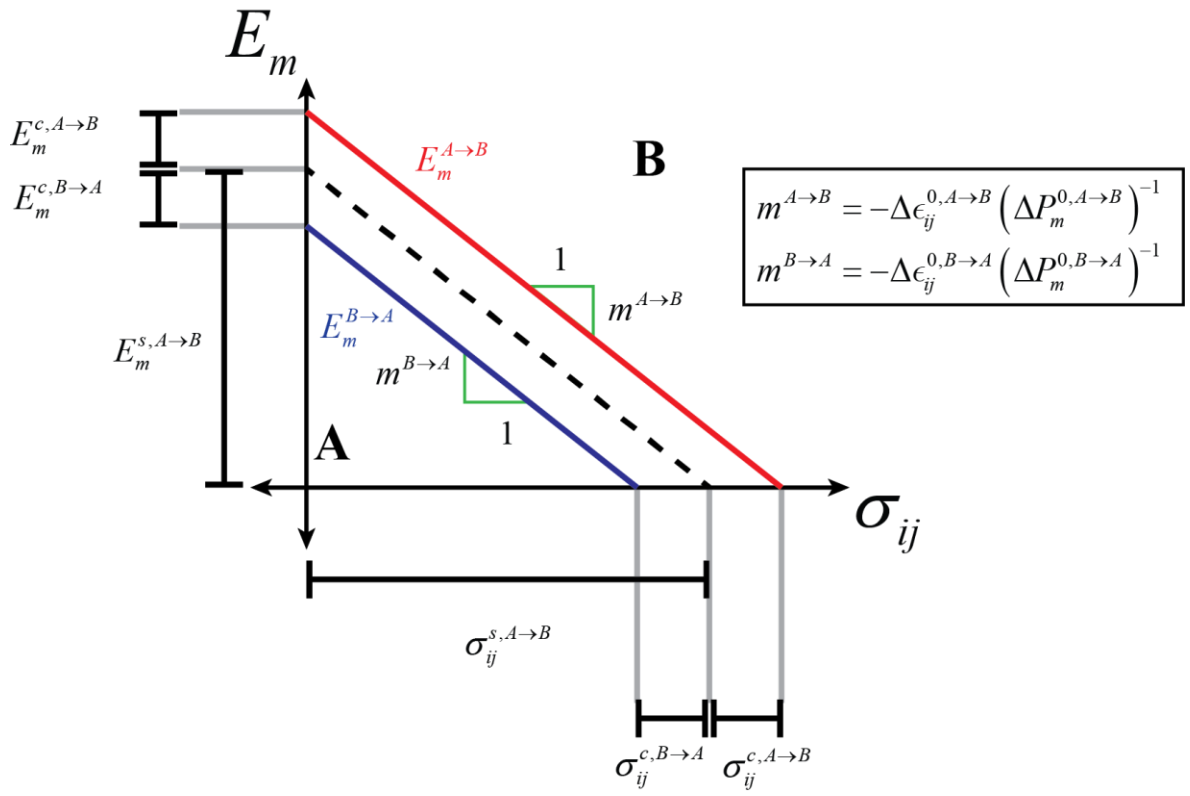

Figure 6-4. Phase diagram of the $A - B$ phase transformation calculated using equation (6.25)

The change in spontaneous strain and polarization between phase/variants A to B can be found from experimental data on the phase transformation. Shown in Figure 6-5.a, $\Delta\epsilon_{ij}^{0,A\to B}$ is determined by analyzing the phase transformation strain – stress behavior and taking the difference between the zero stress ε_{ij}^{A} and the extrapolated zero stress ε_{ij}^{B}. Shown in Figure 6-5.b, $\Delta P_m^{0,A\to B}$ is determined by analyzing the phase transformation electric displacement – electric field behavior and taking the difference between the zero electric field D_m^A and the extrapolated zero electric field D_m^B. Strain – stress, electric displacement – electric field, and phase diagram results from experimental studies can be used determine the coefficients used in the material switching model.

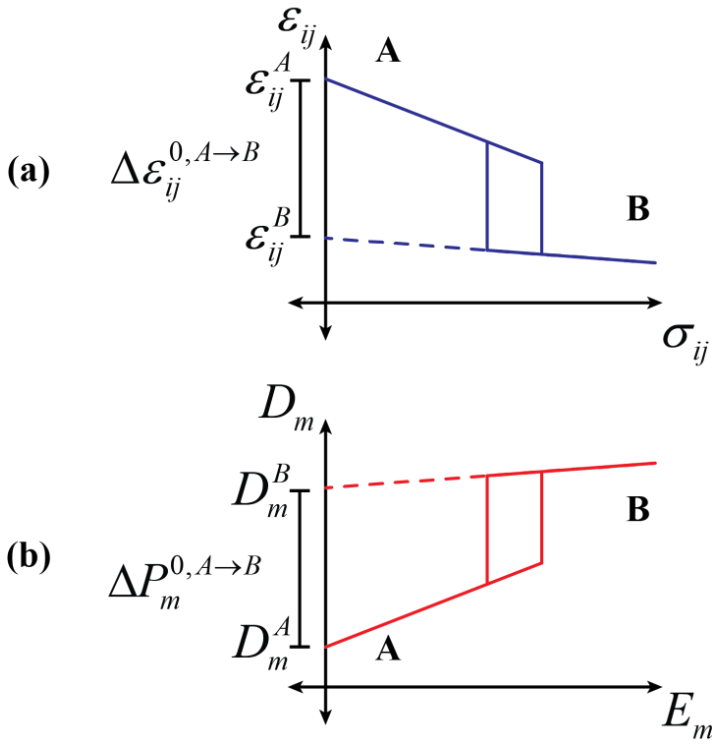

Figure 6-5. Determination of changes in a) spontaneous strain and b) spontaneous polarization during the phase/variant transformation from A to B. $\Delta\epsilon_{ij}^{0,A\to B}$ and $\Delta P_m^{0,A\to B}$ are determined respectively by the difference in strain and electric displacement of the two phases in the unloaded state.

In this work, a look up table was constructed using equation (6.24) for all possible phase/variant transformation permutations applicable to each class of materials. In $[011]$ cut and poled single crystal PIN-PMN-PT, the applicable phases are FE_R and FE_O; in ceramic 95/5 PZT, the applicable phases are FE_R, AF_O, and AF_T. Figure 6-6 shows the look up table for the FE_R to AF_O phase transformation observed at room temperature in 95/5 PZT. The top-left of the look up table (yellow) lists the energy barriers associated with variant only switching between the 8 FE_R (R) phase variants. The bottom-right of the table (blue) lists the energy barrier associated with variant only switching between the 6 AF_O (O) phase variants. The top-right and bottom-left

regions of the look up table (green) are the energy barriers associated with phase/variant switching between AF_O to FE_R variants and FE_R to AF_O variants respectively.

	R1	R2	R3	R4	R5	R6	R7	R8	O1	O2	O3	O4	O5	O6
R1	0	R2→R1	R3→R1	R4→R1	R5→R1	R6→R1	R7→R1	R8→R1	O1→R1	O2→R1	O3→R1	O4→R1	O5→R1	O6→R1
R2	R1→R2	0	R3→R2	R4→R2	R5→R2	R6→R2	R7→R2	R8→R2	O1→R2	O2→R2	O3→R2	O4→R2	O5→R2	O6→R2
R3	R1→R3	R2→R3	0	R4→R3	R5→R3	R6→R3	R7→R3	R8→R3	O1→R3	O2→R3	O3→R3	O4→R3	O5→R3	O6→R3
R4	R1→R4	R2→R4	R3→R4	0	R5→R4	R6→R4	R7→R4	R8→R4	O1→R4	O2→R4	O3→R4	O4→R4	O5→R4	O6→R4
R5	R1→R5	R2→R5	R3→R5	R4→R5	0	R6→R5	R7→R5	R8→R5	O1→R5	O2→R5	O3→R5	O4→R5	O5→R5	O6→R5
R6	R1→R6	R2→R6	R3→R6	R4→R6	R5→R6	0	R7→R6	R8→R6	O1→R6	O2→R6	O3→R6	O4→R6	O5→R6	O6→R6
R7	R1→R7	R2→R7	R3→R7	R4→R7	R5→R7	R6→R7	0	R8→R7	O1→R7	O2→R7	O3→R7	O4→R7	O5→R7	O6→R7
R8	R1→R8	R2→R8	R3→R8	R4→R8	R5→R8	R6→R8	R7→R8	0	O1→R8	O2→R8	O3→R8	O4→R8	O5→R8	O6→R8
O1	R1→O1	R2→O1	R3→O1	R4→O1	R5→O1	R6→O1	R7→O1	R8→O1	0	O2→O1	O3→O1	O4→O1	O5→O1	O6→O1
O2	R1→O2	R2→O2	R3→O2	R4→O2	R5→O2	R6→O2	R7→O2	R8→O2	O1→O2	0	O3→O2	O4→O2	O5→O2	O6→O2
O3	R1→O3	R2→O3	R3→O3	R4→O3	R5→O3	R6→O3	R7→O3	R8→O3	O1→O3	O2→O3	0	O4→O3	O5→O3	O6→O3
O4	R1→O4	R2→O4	R3→O4	R4→O4	R5→O4	R6→O4	R7→O4	R8→O4	O1→O4	O2→O4	O3→O4	0	O5→O4	O6→O4
O5	R1→O5	R2→O5	R3→O5	R4→O5	R5→O5	R6→O5	R7→O5	R8→O5	O1→O5	O2→O5	O3→O5	O4→O5	0	O6→O5
O6	R1→O6	R2→O6	R3→O6	R4→O6	R5→O6	R6→O6	R7→O6	R8→O6	O1→O6	O2→O6	O3→O6	O4→O6	O5→O6	0

Figure 6-6. Look up table for the FE_R – AF_O phase transformation in room temperature 95/5 PZT.

When the micromechanics material model is used in conjunction with a piezoelectric finite element model, the P^0 and ε^0 at any integration point in the material domain is taken to be the averaged behavior a collection of independent single crystal grains where each grain has a phase/variant. The P^0 and ε^0 at the integration point are determined by taking the volume average P^0 and ε^0 of all the grains at that integration point. Each grain is permitted to switch independently based on the switching criteria shown in equation (6.23). If the switching criterion for a grain is satisfied under the applied local loading conditions for at least one type of

phase/variant transformation, the phase/variant transformation of the grain is that where $W^{A\to B} - U_{total}^{A\to B}$ is the greatest. In single crystal material models, all the local axes of each grain are oriented in the same direction; in polycrystalline material models, the local axes of each grain are rotated to random orientations. A method of producing random rotation matrices is discussed in appendix A.2. Under this assumption, each grain reacts to the local loads independently of the other grains and the effects of the domain-walls and phase boundaries are ignored. The model is only accurate when the domain structure scale effects are negligible at the length-scale of interest.

6.4 Results and Discussion

Characterization data from chapters 2 and 3 were used to fit the material models of 95/5-2Nb PZT and PIN-PMN-PT. The following simulations were conducted for a single integration point in the finite element model. Both 95/5-2Nb PZT and PIN-PMN-PT material models were simulated as single crystal.

6.4.1 Model of 95/5-2Nb PZT

Two constant temperature micromechanics material models were created for 95/5-2Nb PZT. Low temperature and high temperature phase transformation models were created to fit the FE_{R1} – AF_O phase transformation at 25°C and the FE_{R2} – AF_T phase transformation at 125°C. Table 6-1 lists parameters required to model the two phase transformations. The constitutive coefficients approximate the material with a transverse isotropic assumption described by equations (6.4) and (6.5). Also listed were the spontaneous polarization and strain values of each phase as well as the phase transformation energy barrier values for each phase transformation

necessary for the phase transformation criterion in equation (6.24). Superscripts represent the corresponding phase of each parameter. The tabulated phase transformation energy barrier corresponds to the smallest energy barrier between transformations between the two phases. Values listed correspond to materials with polarization vector oriented in the x_3 direction and strain state is presented in the Mandel-Voigt notation.

Table 6-1. Constitutive coefficients, spontaneous polarization, spontaneous strain, phase transformation energy barriers for FE_{R1} – AF_O phase transformation and FE_{R2} – AF_T phase transformation.

S_{11}^{FE} (pPa^{-1})	S_{12}^{FE} (pPa^{-1})	S_{13}^{FE} (pPa^{-1})	S_{33}^{FE} (pPa^{-1})	S_{44}^{FE} (pPa^{-1})
23.4	-8.20	-10.31	26.85	67.86
d_{13}^{FE} (nCN^{-1})	d_{33}^{FE} (nCN^{-1})	d_{24}^{FE} (nCN^{-1})	κ_{11}^{FE} (nFm^{-1})	κ_{33}^{FE} (nFm^{-1})
-0.61	1.34	2.09	4.60	4.51
S_{11}^{AF} (pPa^{-1})	S_{12}^{AF} (pPa^{-1})	S_{13}^{AF} (pPa^{-1})	S_{33}^{AF} (pPa^{-1})	S_{44}^{AF} (pPa^{-1})
23.4	-8.20	-10.31	26.85	67.86
d_{13}^{AF} (nCN^{-1})	d_{33}^{AF} (nCN^{-1})	d_{24}^{AF} (nCN^{-1})	κ_{11}^{AF} (nFm^{-1})	κ_{33}^{AF} (nFm^{-1})
0	0	0	4.60	4.51
$\{P^{0,FE_{R1}}\}$ (Cm^{-2})	$\{P^{0,FE_{R2}}\}$ (Cm^{-2})	$\{P^{0,AF_O}\}$ (Cm^{-2})	$\{P^{0,AF_T}\}$ (Cm^{-2})	
{0, 0, 0.35}	{0, 0, 0.30}	{0, 0, 0}	{0, 0, 0}	
$\{\varepsilon^{0,FE_{R1}}\}$ (με)	$\{\varepsilon^{0,FE_{R2}}\}$ (με)	$\{\varepsilon^{0,AF_O}\}$ (με)	$\{\varepsilon^{0,AF_T}\}$ (με)	
{-400, -400, 800, 0, 0, 0}	{-400, -400, 800, 0, 0, 0}	{-2600, -2600, -1400, 0, 0, 0}	{-2600, -2600, -1400, 0, 0, 0}	
$U^{h,FE_{R1}-FE_{R1}}$ (kJm^{-3})	U^{h,AF_O-AF_O} (kJm^{-3})	$U^{h,FE_{R1}-AF_O}$ (kJm^{-3})	$U^{s,FE_{R1}-AF_O}$ (kJm^{-3})	
466.67	329.13	962.50	1396.00	
$U^{h,FE_{R2}-FE_{R2}}$ (kJm^{-3})	U^{h,AF_T-AF_T} (kJm^{-3})	$U^{h,FE_{R2}-AF_T}$ (kJm^{-3})	$U^{s,FE_{R2}-AF_T}$ (kJm^{-3})	
240.00	420.00	630.00	2112.00	

Figure 6-7 presents the electric field and pressure response characteristics of a single-crystal single-domain grain model fitted to the 95/5-2Nb 25°C FE_{R1} – AF_O phase transformation material. The grain was oriented so that the x_1, x_2, and x_3 axes correspond to the $[100]$, $[010]$, and $[001]$ crystallographic directions. Electric field ($E_{[111]}$) and electric displacement ($D_{[111]}$) were applied and measured in the $[111]$ direction. Figure 6-7.a and 6-7.b show the bipolar $E_{[111]}$ response (-10 – 10 MVm^{-1}) of $D_{[111]}$ and volumetric strain (ε_V) respectively at pressures of 0 MPa and 400 MPa. The figures on the left show only the P^0 and ε^0 contributions to $D_{[111]}$ and ε_V; the figures on the right show the combined spontaneous and linear constitutive contributions to $D_{[111]}$ and ε_V. At 0 MPa, the material stays in the FE phase throughout the electric loading cycle and only experiences electric field driven polarization reorientation shown by the single "D" shaped hysteresis in the $D_{[111]}$ – $E_{[111]}$ curve and zero change in ε_V when absent of linear piezoelectric effects. At 400 MPa, the material starts in the AF phase and is driven into the FE phase at high electric fields. This results in double-loop hystereses in $D_{[111]}$ – $E_{[111]}$ and ε_V – $E_{[111]}$ curves. The smallest change in $D_{[111]}$ under FE_{R1} – FE_{R1} and FE_{R1} – AF_O phase/variant transformations are 0.23 Cm^{-2} and 0.35 Cm^{-2} respectively. Therefore, $U^{h,FE_{R1}-FE_{R1}}$ and $U^{h,FE_{R1}-AF_O}$ values listed in Table 6-1 yield $E_{[111]}$ hysteresis widths for the FE_{R1} – FE_{R1} and FE_{R1} – AF_O phase/variant transformations as 4.0 MVm^{-1} and 5.5 MVm^{-1} respectively. Figure 6-7.c and 6.7.d show response of ε_V and $D_{[111]}$ respectively when pressure driven (0 – 500 MPa) through the FE – AF phase transformation. Again, the figures on the left show only the P^0 and ε^0 contributions to $D_{[111]}$ and ε_V; the figures on the right show the combined spontaneous and

linear constitutive contributions to $D_{[111]}$ and ε_V. Under the values of the phase transformation energy barriers $U^{h,FE_{R1}-AF_O}$ and $U^{s,FE_{R1}-AF_O}$ the pressure width and pressure shift at zero electric field of the FE_{R1} – AF_O hysteresis are 291.67 MPa and 221.52 MPa respectively making the critical FE_{R1} to AF_O and AF_O to FE_{R1} transformation pressures and 367.35 MPa and 75.68 MPa. As expected, the AF region display an absence of piezoelectricity in Figure 6-7.b and 6-7.d.

Figure 6-8.a and 6-8.b respectively used the computational model (top) to replicate the experimental (bottom) 25°C FE_{R1} – FE_O and 125°C FE_{R2} – FE_T D – E curves reproduced from Figure 2-2.b . The model again simulated a single grain of the 95/5-2Nb PZT material and used the parameters listed in Table 6-1. A change of the spontaneous polarization magnitude from 0.35 Cm^{-2} in FE_{R1} to 0.3 Cm^{-2} in FE_{R2} accounted for the reduced remnant polarization found in the experimental results. The 125°C FE_{R2} – FE_T phase transformation was fitted for FE_{R2} – FE_{R2} and FE_{R2} – AF_T hysteresis widths in $E_{[111]}$ of 2.4 MVm^{-1} and 4.2 MVm^{-1} respectively. The simulation results show single grain model replicated the critical phase transformation pressures, electric fields, and hysteresis widths with high fidelity. Both types of materials were able to replicate the experimentally demonstrated single "D," "S," AF double-loop, and AF linear-dielectric hysteresis curves at the same pressure and electric field loads.

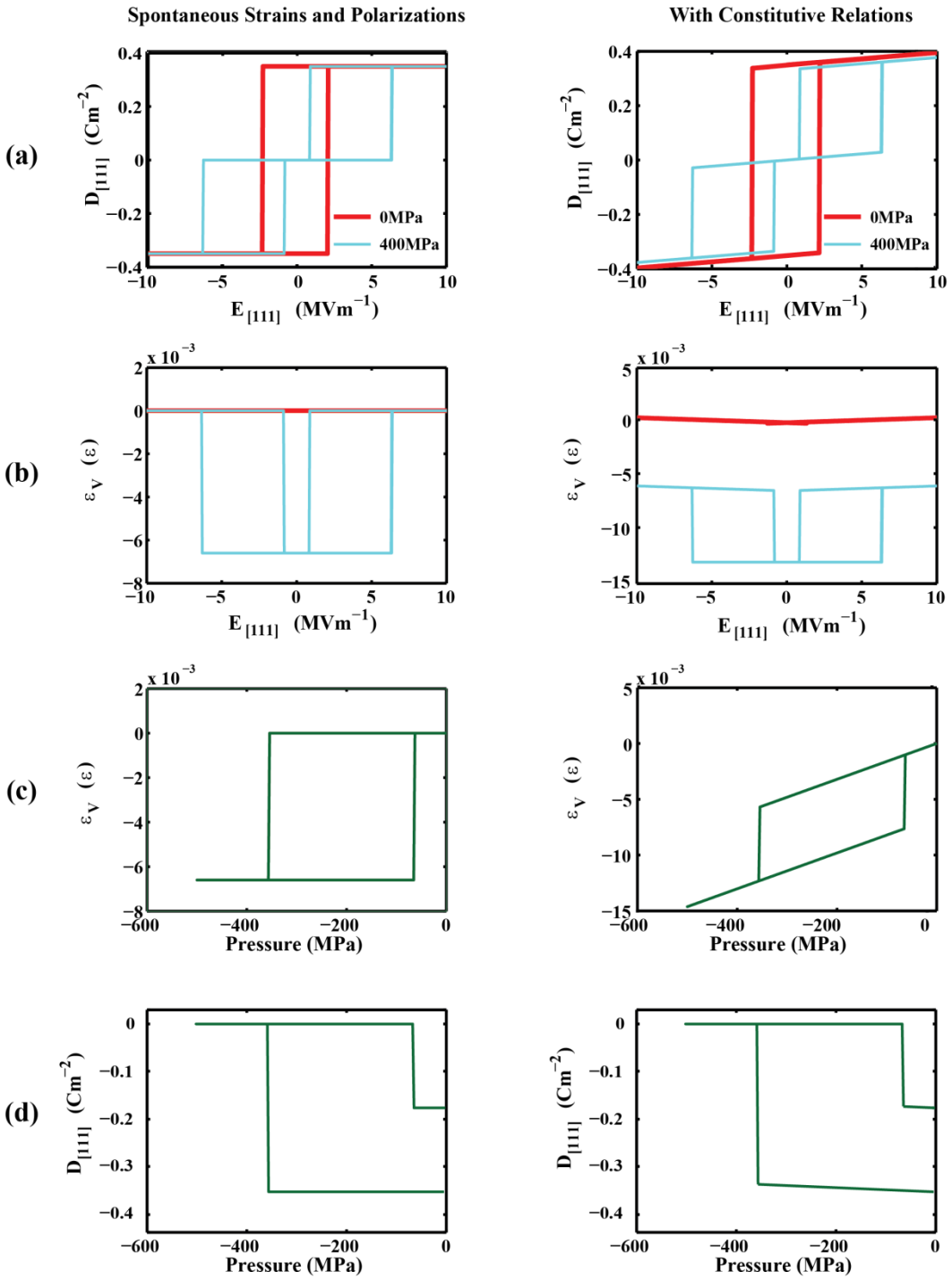

Figure 6-7. Material model fitted for the FE_{R1} to AF_O phase transformation at room 25°C. Bipolar $E_{[111]}$ driven response of a) $D_{[111]}$ and b) ε_V with (right) and without (left) constitutive relations for pressures at 0 MPa (red) and 400MPa (blue). Pressure driven response of c) ε_V and d) $D_{[111]}$ with (right) and without (left) constitutive relations.

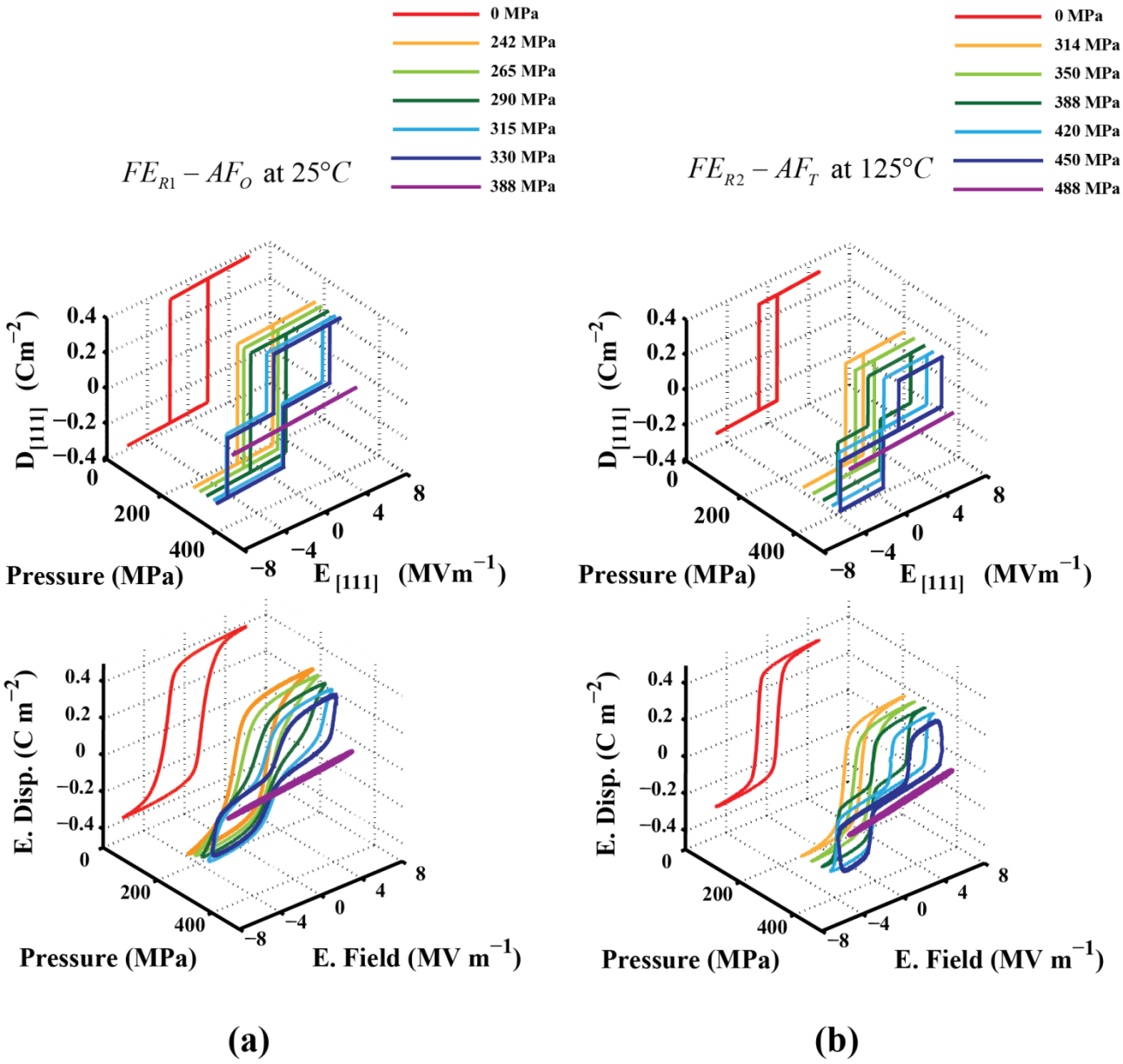

Figure 6-8. Model (top) and experimental results (bottom) of bipolar D – E curves in 95/5 PZT at select pressures for the a) $FE_{R1} - AF_O$ phase transformation at 25°C and b) $FE_{R2} - AF_T$ transformation at 125°C.

6.4.2 Model of Near MPB FE_R PIN-PMN-PT

The near MPB FE_R phase PIN-PMN-PT single crystal with $[011]$ cut and poled configuration was modeled using the micromechanics model using the modeling parameters listed in Table 6-2. The model simulated applied electric field (E_3) and electric displacement (D_3) response in the $[011]$ crystallographic direction in conjunction with applied stress (σ_{22}) and strain (ε_{22}) response in the $[100]$ crystallographic direction.

Table 6-2. Constitutive coefficients, spontaneous polarization, spontaneous strain, phase transformation energy barriers for FE_R – FE_O phase transformation.

$S_{11}^{FE_R}$ (pPa^{-1})	$S_{12}^{FE_R}$ (pPa^{-1})	$S_{13}^{FE_R}$ (pPa^{-1})	$S_{33}^{FE_R}$ (pPa^{-1})	$S_{44}^{FE_R}$ (pPa^{-1})
117.13	-41.00	-51.57	134.27	339.33
$d_{13}^{FE_R}$ (nCN^{-1})	$d_{33}^{FE_R}$ (nCN^{-1})	$d_{24}^{FE_R}$ (nCN^{-1})	$\kappa_{11}^{FE_R}$ (nFm^{-1})	$\kappa_{33}^{FE_R}$ (nFm^{-1})
-0.61	1.34	2.09	15.32	15.05
$S_{11}^{FE_O}$ (pPa^{-1})	$S_{12}^{FE_O}$ (pPa^{-1})	$S_{13}^{FE_O}$ (pPa^{-1})	$S_{33}^{FE_O}$ (pPa^{-1})	$S_{44}^{FE_O}$ (pPa^{-1})
58.57	-20.50	-25.78	67.13	169.66
$d_{13}^{FE_O}$ (nCN^{-1})	$d_{33}^{FE_O}$ (nCN^{-1})	$d_{24}^{FE_O}$ (nCN^{-1})	$\kappa_{11}^{FE_O}$ (nFm^{-1})	$\kappa_{33}^{FE_O}$ (nFm^{-1})
-0.61	1.34	2.09	15.32	15.05
$\{P^{0,FE_R}\}$ (Cm^{-2})	$\{P^{0,FE_O}\}$ (Cm^{-2})	$\{\varepsilon^{0,FE_R}\}$ (με)	$\{\varepsilon^{0,FE_R}\}$ (με)	
{0, 0, 0.3}	{0, 0, 0.3}	{3200, 3200, 6400, 0, 0, 0}	{3200, 3200, 6400, 0, 0, 0}	
U^{h,FE_R-FE_R} (kJm^{-3})	U^{h,FE_O-FE_O} (kJm^{-3})	U^{h,FE_R-FE_O} (kJm^{-3})	U^{s,FE_R-FE_O} (kJm^{-3})	
120.00	93.33	4.95	76.80	

The simulated results of D_3 and ε_{22} from only E_3 at zero stress, unipolar E_3 at zero stress, and uniaxial compressive σ_{22} at zero electric field are shown in Figures 6-9.a, 6-9.b, and

6-9.c respectively. The smallest ΔP^0 contribution D_3 to in the FE_R – FE_R or FE_R – FE_O phase/variant transformations are 0.245 Cm^{-2} and 0.0551 Cm^{-2} respectively. This is consistent with the E_3 width of the FE_R – FE_R phase/variant transformation hysteresis (9.8 MVm^{-1}) shown in Figure 6-9.a given the U^{h,FE_R-FE_R} value in Table 6-2. In Figure 6-9.b, the E_3 width of the FE_R – FE_O phase/variant transformation is 0.18 MVm^{-1} which is consistent with the U^{h,FE_O-FE_R} value reported in Table 6-2. The $\Delta\varepsilon^0$ contribution to a ε_{22} change from the phase transformation in $[011]$ cut and poled PIN-PMN-PT is 3200 με. This agrees with the simulated σ_{22} shift of the hysteresis at zero electric field of -24MPa and the simulated E_3 shift of the FE_R –FE_O hysteresis at zero stress of 1.39MVm^{-1} seen in Figures 6-9.b and 6-9.c. It is important to note that although the change in ε_{22} due to $\Delta\varepsilon^0$ across the FE_R –FE_O hysteresis is 3200 με, the ε_{22} jump seen in Figure 6-9.c is only ~2000 με due to the differences in the compliance of the FE_R and FE_O phases.

The PIN-PMN-PT micromechanics model was used to reproduce the experimental E_3 and σ_{22} driven phase transformation results shown in Figure 3-4. Figure 6-10.a and 6-10.b show the respective simulated D_3 and ε_{22} response to σ_{22} and E_3 loading across the FE_R – FE_O phase transformation. The experimental ε_{22} results under the same loading conditions is shown in Figure 6-10.c. A comparison of the simulated and experimental results in Figure 6-10.b and 6-10.c, shows the model is able to replicate the experimental results with high fidelity. The model shows the FE_R to FE_O and FE_O to FE_R phase transformation occurs at the same critical σ_{22} and E_3 loads as the experimental data with the same ε_{22} jump magnitudes.

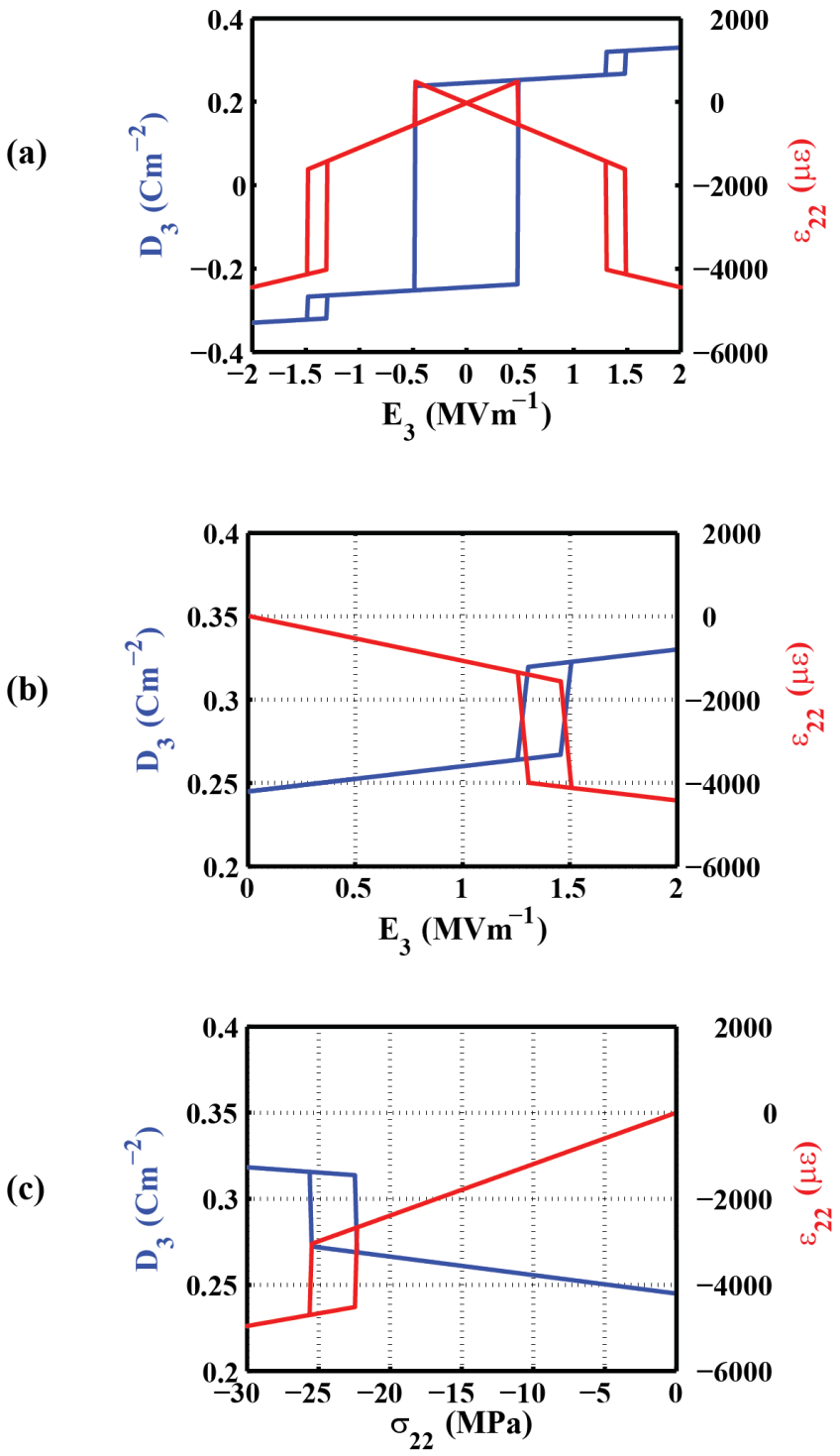

Figure 6-9. Simulated results of D_3 and ε_{22} from only a) bipolar E_3, b) unipolar E_3, and c) uniaxial compressive σ_{22}.

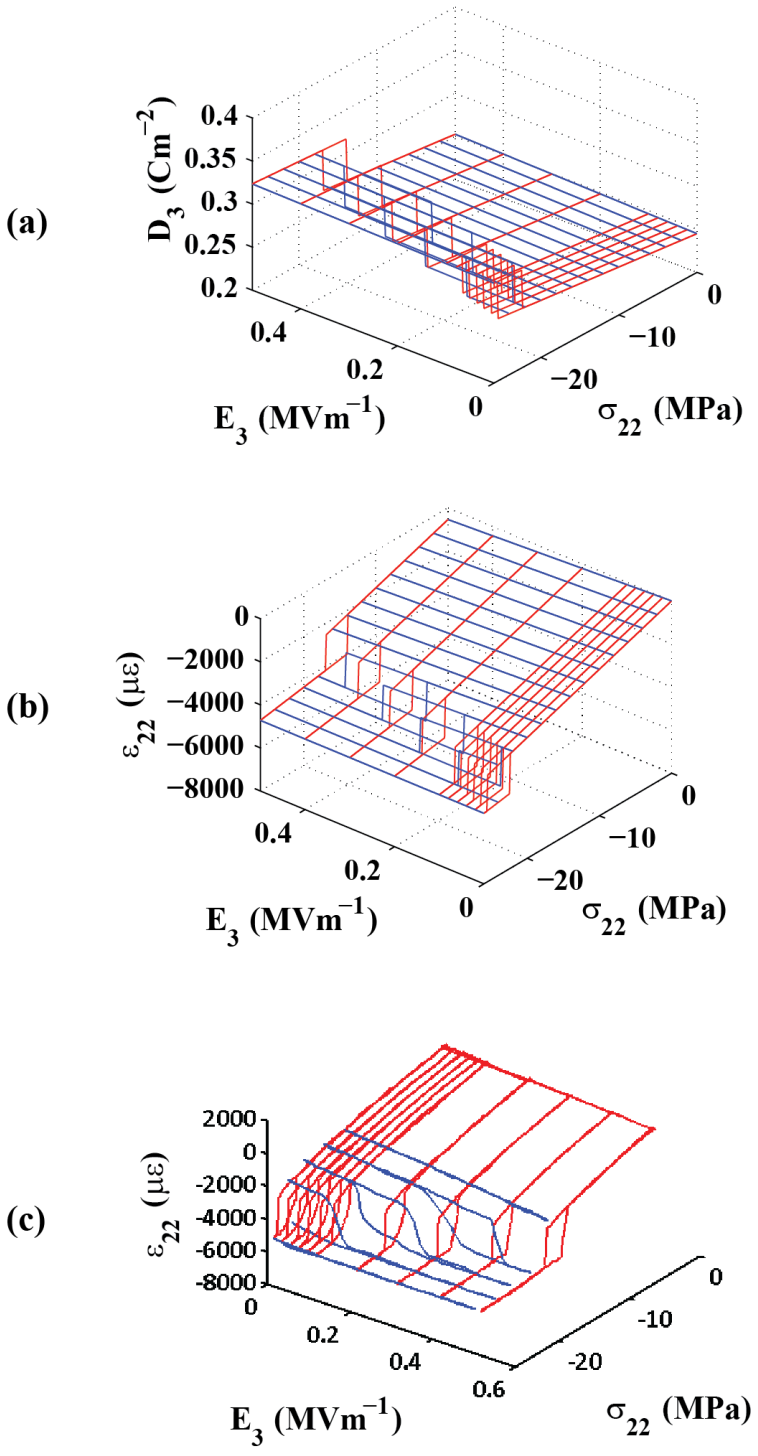

Figure 6-10. Simulated a) D_3 and b) ε_{22} response and c) experimental ε_{22} response to σ_{22} and E_3 loading.

6.5 Conclusions

A micromechanics materials model was developed to simulate stress and electric field driven phase transformations in ferroelectric materials. A formulation of a piezoelectric finite element framework was presented. The finite element framework solves the boundary value problems presented by the electrical and mechanical field equations for a material described by the constitutive relations. The ferroelectric and ferroelastic material behavior was described by a combination of linear and nonlinear constitutive relations. The linear contributions were described by piezoelectric constitutive equations and nonlinear contributions were attributed to spontaneous strains and polarizations with the material. The values of the spontaneous polarization and strain were associated with the phase/variant of the material. An energy based micromechanics phase/variant switching model modifies the material's phase/variant based on local loading conditions and phase/variant history. The phase/variant switching occurs if the ability of external loads to do work positive work on the system exceeds a phase transformation energy barrier. External loads in this case were stress and electric field.

A detailed formulation of the micromechanics phase/variant switching criteria is presented in this chapter along with a discussion of fitting the switching criteria parameters using data from load driven phase transformation experiments. The single crystal computational models were created for both the 95/5 PZT and PIN-PMN-PT ferroelectric materials. The 95/5 PZT was modeled for both the 25°C $FE_{R1} - FE_O$ phase transformation and the 125°C $FE_{R2} - FE_T$ phase transformation. In the PIN-PMN-PT, a $[011]$ cut and poled single crystal was modeled at 25°C. For both models, the computational model demonstrated high fidelity at capturing the ferroelectric and ferroelastic response of the materials. The model holds promise as a tool to simulate future devices that incorporate phase transforming ferroelectric technology. Transverse

isotropic assumption was made for the constitutive relations of the modeled material. Improvements on the accuracy of the model include additional experiments to determine the full anisotropic constitutive tensors.

CHAPTER 7
A FINITE ELEMENT BASED PHASE FIELD MODEL FOR FERROELECTRIC DOMAIN EVOLUTION

This chapter discusses a finite element phase field approach to modeling domain evolution in ferroelectric materials at the unit cell level and discusses the effects of each Landau – Devonshire free energy function term on the domain wall and domain structure of FE_T phase materials. This work was done in collaboration with David M. Pisani and the results have been published in Dong et al. [157]. The approach combines a linear piezoelectric finite element framework, which uses linearly interpolated hexahedral (brick) elements to represent the unit cells of a ferroelectric material, with a material model based on the Landau-Devonshire theory. The Landau-Devonshire approach describes ferroelectric and ferroelastic material behavior using a multi-welled free energy function with polarization as the main order parameter. A time-dependent Ginzburg-Landau theory was applied to calculate polarization evolution. Electrical and mechanical compatibility conditions are enforced by the finite element framework so that the resulting local stress and electric fields can be calculated for each element. A local gradient energy density term is included to approximate the polarization mismatch between neighboring unit cells. The polarization distribution is not modeled as a field. Rather, it is modeled as a discrete distribution of Eigen-strains and Eigen-polarizations subjected to compatibility conditions and boundary conditions through the finite element framework. Results indicate that domain wall orientation and width are a function of a balance between structure driving forces, electrostatic interactions, mechanical interactions, and lattice distortion mismatches.

The work in this chapter investigates the energetic terms that shape domain wall width and domain structures. From literature, the domain wall width is controlled by structure, electrostrictive, electrostatic, and local gradient contributions to the free energy density. Although the physical nature of the local gradient energy is understood to capture the effects of dipole-dipole interaction energy, the effects of lattice distortion on the gradient term are typically neglected. In this work, compatibility conditions between unit cells are enforced when the unit cells are no longer in the symmetric cubic configuration. The effect on the resulting domain wall width of 90º and 180º tetragonal domain walls is discussed and examples are presented.

The result of this work is a finite element based phase field model. The finite element based phase field model is capable of capturing the full range of mechanical and electrical boundary conditions. Future studies on phase transformations are anticipated using this model with utilize Landau – Devonshire single crystal FE – FE phase transformation models, such as that proposed by Zhang [121], or FE – AF phase transformation models, such as that proposed by Kittel [117], Cross [118], and Uchino [119-120].

7.1 Material Model

Ferroelectric materials display spontaneous polarization magnitude and direction. The polarization is coupled to a spontaneous electrostrictive strain that elongates the unit cell along the polarization axis and contracts the unit cell in the plane orthogonal to the polarization axis. The possible polarization orientations are along certain phase dependent crystallographic families of directions. Neighboring dipoles prefer to orient in the same direction to form domains. When two differently oriented domains of the same phase intersect they form an interface referred to as a domain wall. Because the spontaneous polarization directions are limited to certain crystallographic orientations and the domain walls must remain electrically neutral, each phase can only accommodate domain walls of certain angles. The domain walls for tetragonal phased materials occur as 90° and 180° boundaries [158]. Experimental measurements of the domains walls have shown a large difference in the width of the 90º and 180º domain walls in barium titanate. Studies by Zhirnov [159] and Little [160-161] estimated the thickness of the 90° wall to be up to 4 nm and the width of the 180° wall to be around the dimension of a unit cell.

7.1.1 Time-Dependent Ginzburg-Landau

The phase field model used in this investigation incorporates a linear finite element framework with a material model that evolves polarization domain structure. The mechanism for domain-structure evolution is the time-dependent Ginzburg-Landau theory (TDGL) shown in equation (7.1).

$$\frac{\Delta P_i^t\left(x_j\right)}{\Delta t} = -\Gamma \frac{\delta F^t\left(P_i^t\left(x_j\right), \sigma_{ab}^t\left(x_j\right), E_m^t\left(x_j\right)\right)}{\delta P_i^t\left(x_j\right)} + \eta_i^t\left(x_j\right) \tag{7.1}$$

where unless otherwise stated, the indices run from 1 to 3, repeating indices imply summation. The left hand side of Equation (7.1) symbolizes the temporal evolution of the polarization, P_i^t, at time t and at location x_j, is updated by ΔP_i^t in each after a time step Δt. The right hand side shows the polarization evolution is proportional to the negative variational derivative of Landau-Devonshire free energy density (F) with respect to P_i, which is the driving force for a ΔP_i^t that would further minimize the free energy density F. F is a polynomial function of P_i, local stress (σ_{ab}), and local electric field (E_i). Γ is a kinetic coefficient that governs the magnitude of ΔP_i^t and η_i^t is a noise term. After each iteration of the TDGL evolution, the updated polarization is,

$$P_i^{t+1} = P_i^t + \left(-\Gamma \frac{\delta F^t\left(P_i^t\left(x_j\right), \sigma_{ab}^t\left(x_j\right), E_m^t\left(x_j\right)\right)}{\delta P_i^t} + \eta_i^t \right) \Delta t \tag{7.2}$$

and the TDGL is iterated until the F is minimized in P_i.

7.1.2 Finite Elements

The linear piezoelectric finite element framework is the same as that described in Chapter 6. This approach discretizes the domain into individual elements where there is an Eigen-polarization and Eigen-strain in the material model that is mapped to each element in the finite element framework. The finite element framework is used to calculate σ_{ab} and E_i at the

location of each Eigen-polarization and the material model uses TDGL to evolve the Eigen-polarization. The finite element formulation satisfies quasi-static equilibrium and Gauss's law, Equation (7.3). The variables σ, b, D, and ρ are the stress, body force, electric displacement and charge density respectively. The polarization evolution is handled in a TDGL subroutine.

$$\begin{aligned} \sigma_{ij,j} + b_i &= 0 \\ D_{m,m} &= \rho \end{aligned} \tag{7.3}$$

As shown in Figure 7-1, the ABO_3 perovskite structure is represented by a linearly interpolated hexahedron (brick) element where the element nodes represent the A site atoms. Each element retains an Eigen-polarization and Eigen-strain. The Eigen-polarization is expressed as unbalanced charge on each of the brick element's eight nodes. The Eigen-strain of each element is represented by an unbalanced force vector on each of the nodes. The finite element code is used to find the electric potential and mechanical displacement of each of the nodes so that mechanical and electrical compatibility are achieved.

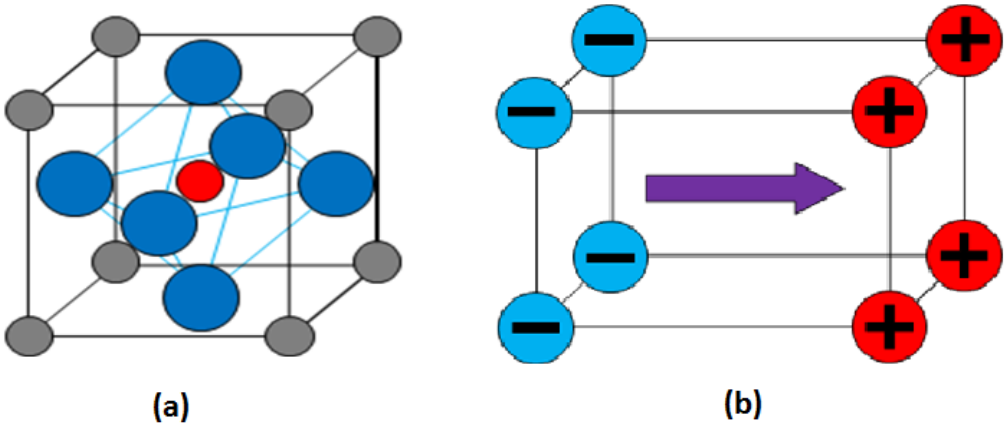

Figure 7-1. (a) Perovskite unit cells. (b) Finite element representation of a poled perovskite unit cell using hexahedron (brick) element showing the unbalanced charges at the nodes.

Figure 7-2 demonstrates how elements with incompatible Eigen-strain are forced to become mechanically compatible. The neighboring elements with incompatible Eigen-strains, shown in Figure 7-2.a, are forced into mechanical compatibility resulting in the local stresses shown in Figure 7-2.b. Similarly, each element is forced into electrical compatibility with its neighbors resulting in local electric fields.

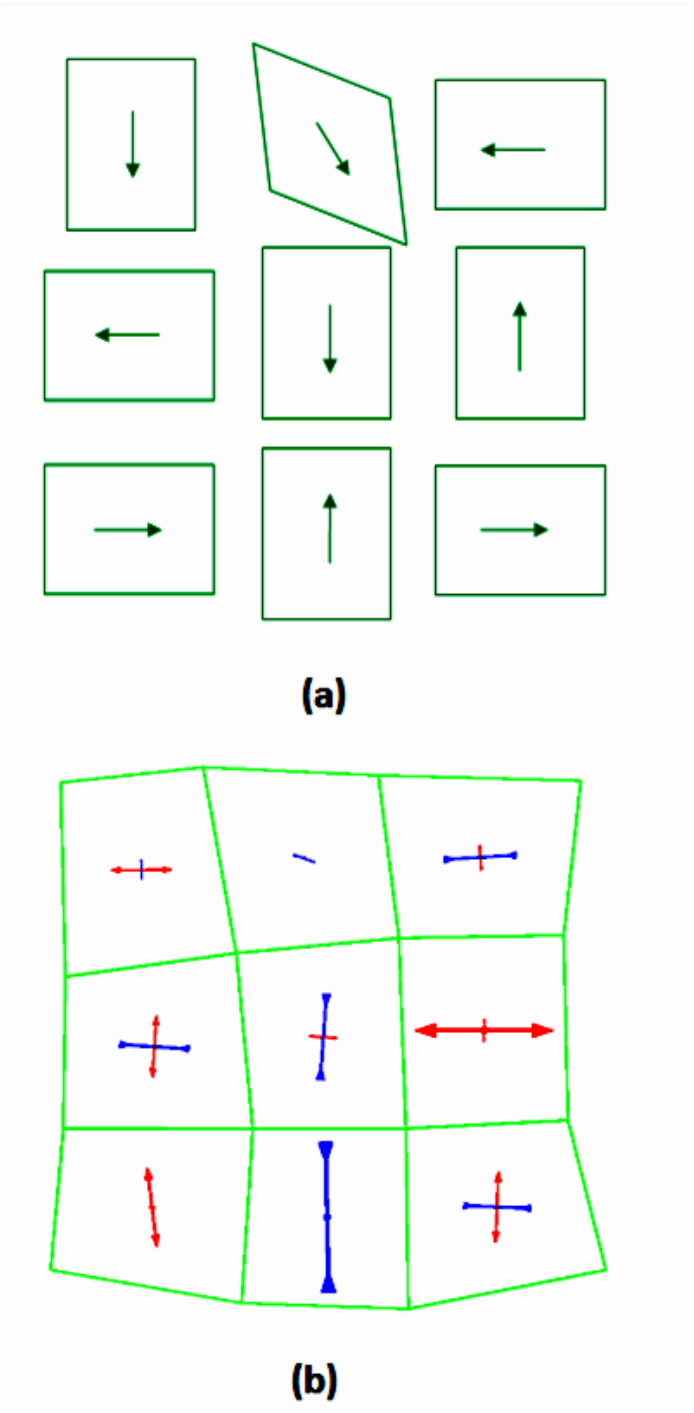

Figure 7-2. a) Polarizations, shown with arrows, gives each unit cell an associated Eigen-strain. b) Displacements due to the total strain after compatibility are satisfied. Arrows indicate the principle stresses with compression in blue and tension in red.

7.1.3. Constitutive Relation

The constitutive behavior of the material is programmed into a material subroutine that uses the TDGL to update the polarization. Devonshire describes the ferroelectric constitutive behavior by taking a series expansion of the Gibbs elastic energy density [100], G_1, shown in Equation (7.4) with respect to its order parameters so that higher order terms can be phenomenologically fitted to describe ferroelectric behavior. In the formulation, polarization can be used to replace electric displacement in the constitutive law since $P \gg \kappa_0 E$.

$$G_1 = \underbrace{\frac{1}{2}a_{ij}P_iP_j + \frac{1}{4}a'_{ijkl}P_iP_jP_kP_l + \frac{1}{6}a''_{ijklmn}P_iP_jP_kP_lP_mP_n}_{f_{structure}} \underbrace{-Q_{abij}\sigma_{ab}^{local}P_iP_j}_{f_{electrostrictive}} \underbrace{-E_m^{local}P_m}_{f_{electrostatic}} \tag{7.4}$$

The expansion of G_1 can be separated into three terms: structure energy density ($f_{structure}$) also known as the Landau energy density, electrostrictive free energy density ($f_{electrostrictive}$), and electrostatic free energy density ($f_{electrostatic}$). $f_{structure}$ represents energy wells along certain crystallographic families of directions that produce the spontaneous polarization orientations of the material. The expression of the structure energy density follows the work of Heitmann and Rossetti who proposed separating the isotropic and anisotropic components [103]. Shown in equation (7.5), the first three terms represent the isotropic terms which greatly influence the magnitude of the polarization. The second three terms with prime coefficients represent the anisotropic terms and control the direction of the energy wells. $f_{electrostrictive}$, describes the effect on the free energy density function when a local stress is applied; here, Q_{ijkl} is an isotropic

electrostrictive tensor. $f_{electrostatic}$, describes the effect on the free energy density when a local electric field is applied. When a local stress, σ_{ab}^{local}, or local electric field, E_m^{local}, is applied to an element, $f_{electrostrictive}$ and $f_{electrostatic}$ distort the entire surface of the total free energy density. The local stress and local electric field are determined by solving equilibrium and Gauss's law in the finite element framework. Equation (7.4) can be rewritten where G_1 is taken as the total Landau-Devonshire free energy density, F, of the material as shown in Equation (7.5).

$$\begin{aligned} F &= f_{structure} + f_{electrostictive} + f_{electrostatic} \\ f_{structure} &= \frac{1}{2}\alpha_2\left(P_1^2+P_2^2+P_3^2\right)+\frac{1}{4}\alpha_4\left(P_1^2+P_2^2+P_3^2\right)^2+\frac{1}{6}\alpha_6\left(P_1^2+P_2^2+P_3^2\right)^3 \\ &\quad +\frac{1}{4}\alpha_4'\left(P_1^4+P_2^4+P_3^4\right)+\frac{1}{6}\left[\alpha_6'\left(P_1^6+P_2^6+P_3^6\right)+\alpha_6''\left(P_1^2P_2^2P_3^2\right)\right] \\ f_{electrostrictive} &= -Q_{abij}\sigma_{ab}^{local}P_iP_j \\ f_{electrostatic} &= -E_m^{local}P_m \end{aligned} \tag{7.5}$$

Figure 7-3 plots the two dimensional total free energy density of a tetragonal phase element. In Figure 7-3.a, no local stress or field are applied to the element and it is possible to see four energy wells representing the four in-plane spontaneous polarization directions. The energy wells have the same depth, thus each of the four polarization directions are equally favorable. In Figure 7-3.b, the element is under a local stress. If a tensile stress is applied, the electromechanical coupling energy density will decrease the total energy density surface along the axis that the stress is applied while increasing the energy density in the orthogonal directions. The converse will occur when a compressive stress is applied. This drives stress induced ferroelectric switching behavior. In Figure 7-3.c, a local electric field has been applied to the element. The local electric field tilts the free energy density surface causing one well to become

deeper than the others. This represents the effect of an external electric field on the polarization direction. The tilting of the energy density surface drives the polarization in the direction of the applied electric field.

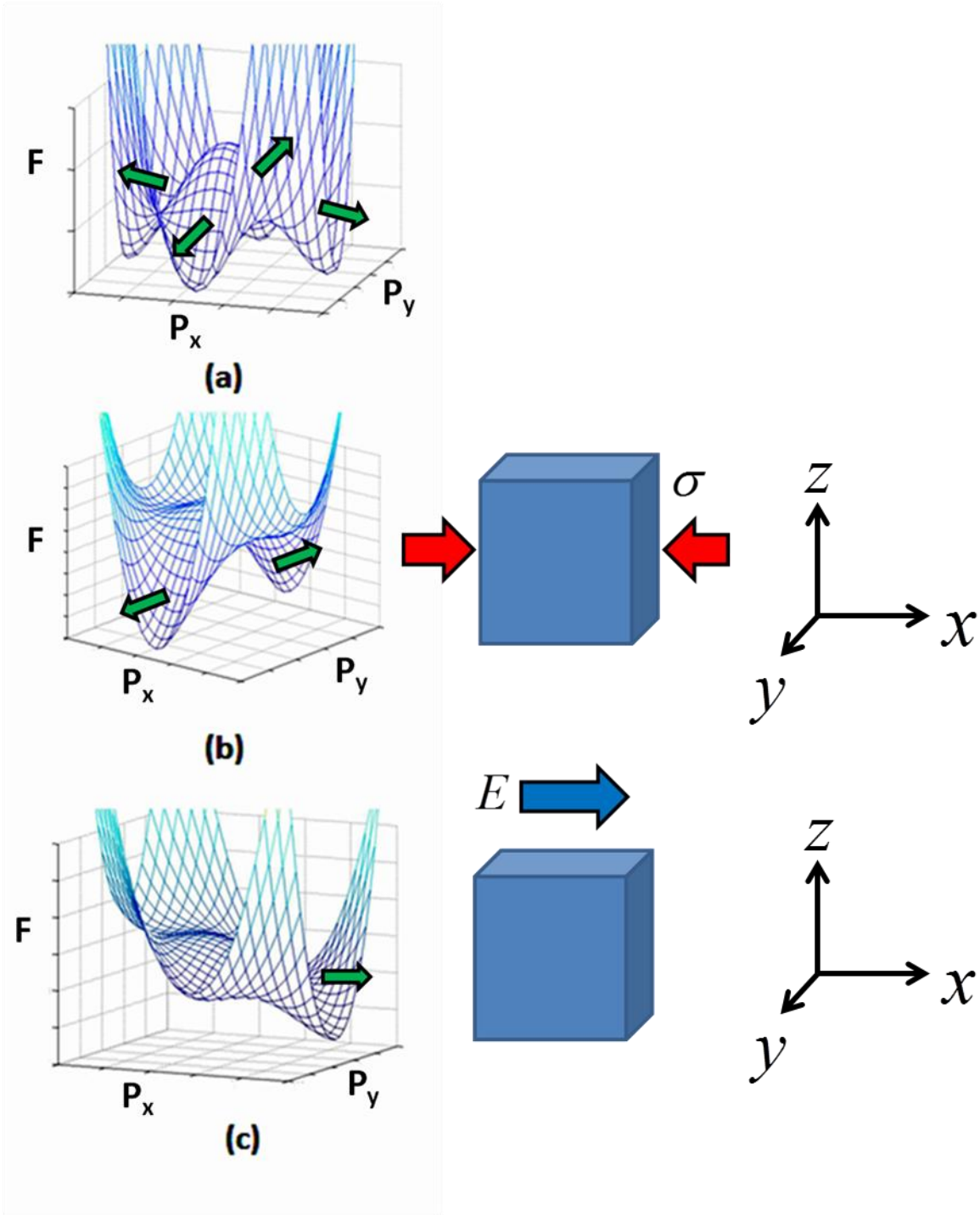

Figure 7-3. Landau-Devonshire free density for a tetragonal material under: (a) no load. (b) externally applied applied stress, (c) externally electric field.

Thus far, the three energy density components used, structure, electrostrictive, and electrostatic, should account for all the possible forces for domain evolution at the unit cell level. The combination of these driving forces determines the spontaneous polarization directions and magnitudes, angle of the domain walls, and the thicknesses of the domain walls. The thickness of a domain wall depends on whether each driving force favors a narrow or wide wall.

Figure 7-4 visualizes the driving force interactions by showing the electrical and mechanical compatibilities for the 90° and 180° domain walls in tetragonal materials under the hexahedron element approximation. When Eigen-polarizations are represented as charges on the nodes of the hexahedron element, Figure 7-4.a, shows that nodes along the domain wall in a 90° tetragonal wall remain neutrally charged. This shows that, within the assumptions and approximations of this model, sharp 90° and 180° domain walls are favored by the electrostatic driving forces. Figure 7-4.b, however, shows that a 90° domain wall in a tetragonal material does not satisfy mechanical compatibility without stress being present. Therefore the mechanical driving force will try to evolve the domain wall to be as wide as possible in order to reduce energy penalty caused by the local stress. The structure energy density will favor polarization directions in any of the spontaneous polarization directions and therefore will always favor a narrow wall. The driving force toward a narrow wall contributed by the structure energy density is a function of the depth of the energy wells with deeper wells giving narrower walls. The width of the 90° domain wall in tetragonal materials depends on a driving force balance between these driving forces. In a piezoelectric finite element framework with hexahedron elements, the electrostatic and structure driving forces push for the wall to be narrow and mechanical driving forces push for the wall to be wide. Figures 4.c and 4.d, depict the electrical and mechanical compatibilities of 180° domain walls. In the case of the 180° domain wall, nodes remain neutral

along the domain wall as seen in Figure 7-4.c, but the system is also mechanically compatible. Therefore, in this case, all three driving forces favor a narrow wall.

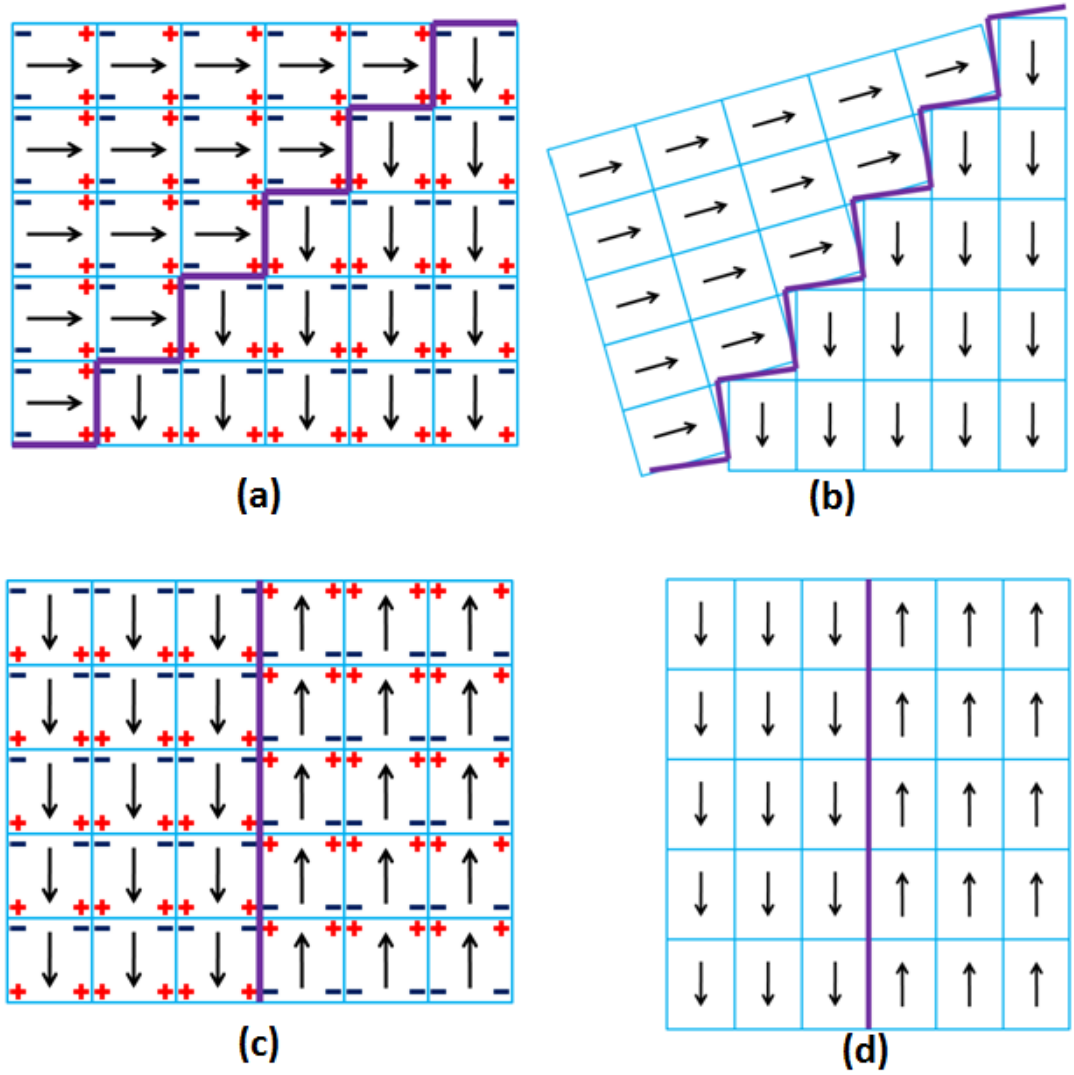

Figure 7-4. (a) Electrical compatibility along 90° domain wall in Tetragonal material. (b) Mechanical compatibility along 90° domain wall in Tetragonal material. (c) Electrical compatibility along 180° domain wall in Tetragonal material. (d) Mechanical compatibility along 180° domain wall in Tetragonal material

As seen in Figure 7-5, enforcing only the mechanical and electrical compatibility of the Eigen-strain and Eigen-polarization of each element presents a problem with domain formation in the current material model forumlation. The mechanical and electrical compatibility at the nodes are shown for the single domain configuration in Figure 7-5.a and the anti-parallel head-to-tail configuration in Figure 7-5.b and in both cases the mechanical and electrical compatibility at the nodes are satisfied. In both configurations, the charges at the nodes are zero and there is no mismatch of the Eigen-strains between neighboring elements. This implies that anti-parallel head-to-tail (antiferroelectric) and single domain (ferroelectric) configurations are equally energetically favorable and likely to form. From experimental observations, it is known that single domains are favored in ferroelectric materials. Therefore, there has to be another energetic term not currently captured in the material model that favors the formation of single domains and penalizes the anti-parallel configuration.

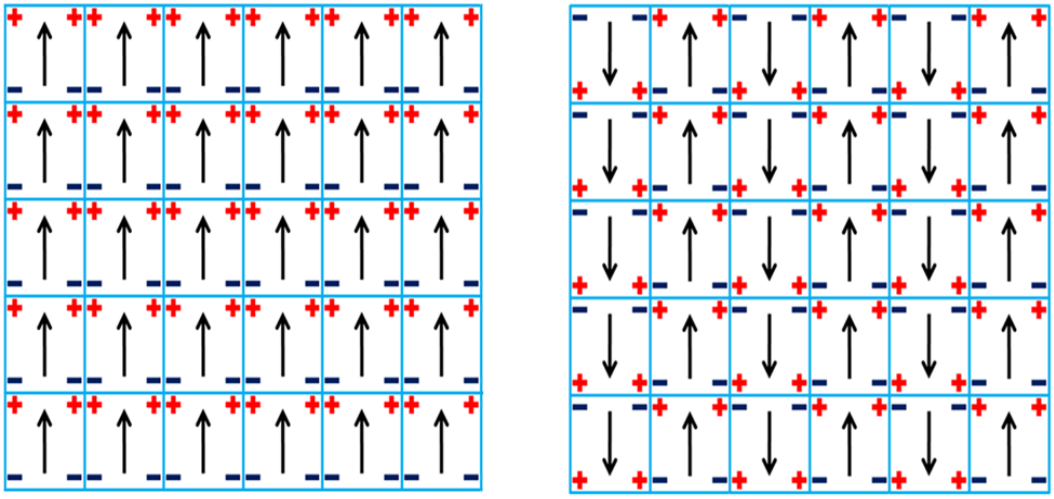

Figure 7-5. Mechanical and electrical compatibility for the a) single domain and b) anti-parallel head-to-tail configurations.

The driving force that favors the formation of domains originates at the unit cell. Representing the perovskite unit cell with a linearly interpolated hexahedron element does not account for the shifting of ions in the perovskite unit cell structure. The Eigen-strain of the each unit cell only accounts for the distortion of the A site atoms, which have been used to define the eight corners of the hexahedron element. The Eigen-strain does not account for the shifts of the B site or Oxygen atoms, which do not necessarily elongate proportionally to the distortion of the element. Figure 7-6.a shows the findings by Shirane et al. [162] for lead titanate where the oxygen and titanium atoms are disproportionately shifted with respect to the lead atom.

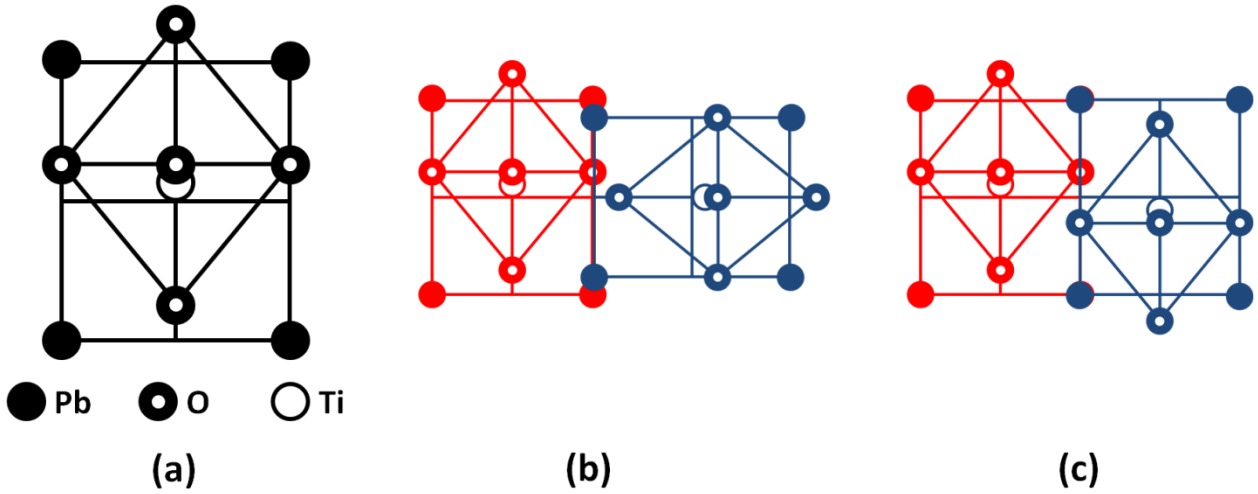

Figure 7-6. a) The atomic distortions for poled PbTiO3 unit cell modified from Shirane 1956 [162]. b) Neighboring PbTiO3 unit cells with 90° change in polarization direction. c) Neighboring PbTiO3 unit cells with 180° change in polarization direction.

The source of the driving force that favors domain formation can be seen in Figures 6.b and 6.c. Figure 7-6.b the shows the atomic mismatch associated with a 90° change in the polarization direction of neighboring unit cells. There is a clear mismatch of the lead (A site) atoms as wells as the oxygen atoms. The atomic mismatch of the A site atoms are accounted for already by the difference of the Eigen-strain between the two unit cells; however, the atomic

mismatch of the oxygen atoms are not. Figure 7-6.c shows the atomic mismatch between two neighboring perovskite unit cells that have a polarization change of 180°. There is a matching of the lead (A site) atoms indicating the Eigen-strains are compatible, but there is a clear atomic mismatch of the shared oxygen atom. Ferroelectrics favor single domain configuration rather than the anti-parallel head-to-tail configuration due to the need for neighboring unit cells to have matching Eigen-strains and oxygen distortions.

An energy penalty must be given to neighboring unit cells of different polarization directions and magnitudes. The mismatch energy can be approximated by a polarization gradient squared term shown in Equation (7.6).

$$f_{gradient} = g_{ijkl} P_{i,j} P_{k,l} \tag{7.6}$$

Where $f_{gradient}$ is the local gradient energy density term and $P_{i,j}$ is the polarization gradient across adjacent unit cells. The tensor g_{ijkl} needs to have the symmetry of the underlying crystal structure. For a cubic system, the tensor g_{ijkl} can be simplified in notation and reduced to four constants [106-108, 111] and is shown below where the values of g_{11}, g_{12}, g_{44}, and g'_{44} depend on the atomic distortions of the particular perovskite unit cell when at its spontaneous polarization.

$$\begin{aligned} f_{gradient} = & \frac{1}{2} g_{11} \left(P_{1,1}^2 + P_{2,2}^2 + P_{3,3}^2 \right) + g_{12} \left(P_{1,1} P_{2,2} + P_{1,1} P_{3,3} + P_{2,2} P_{3,3} \right) \\ & + \frac{1}{2} g_{44} \left[\left(P_{1,2} + P_{2,1} \right)^2 + \left(P_{1,3} + P_{3,1} \right)^2 + \left(P_{2,3} + P_{3,2} \right)^2 \right] \\ & + \frac{1}{2} g'_{44} \left[\left(P_{1,2} - P_{2,1} \right)^2 + \left(P_{1,3} - P_{3,1} \right)^2 + \left(P_{2,3} - P_{3,2} \right)^2 \right] \end{aligned} \tag{7.7}$$

7.2 Implementation

Simulations were conducted using coefficients shown in Table 7-1. The simulation was conducted using a modified form of the time-dependent Ginzburg-Landau method such that the maximum change in polarization for each time step did not exceed 10% of the spontaneous polarization magnitude. The structure, electrostrictive, and electrostatic driving forces are independent of element dimensions. The local gradient term was dependent on element dimensions as due to the discretization of the polarization such that each element has a fixed polarization. The g coefficients were scaled such that $g_{ij} = \gamma_{ij} a^2$ where $a \times a \times a$ is the dimension of an undistorted element. The electrostrictive coefficients are given for the material coordinate space of each element where the 1 direction is parallel to the polarization orientation of the element. The simulations were performed in pseudo-2D where each simulation was 5 elements thick and uniform through the thickness with polarization restricted to in-plane directions. Each simulation also has a 5 element thick border of vacuum (near 0 stiffness, $\varepsilon = \varepsilon_0$, and no polarization) on each side to enforce open circuit unclamped boundary conditions. The open circuit boundary conditions prevent the formation of a single domain since components of polarization normal to surfaces incur a high energy penalty due to Gauss's law.

Table 7-1. Values of coefficients used in the simulations for tetragonal ferroelectric material.

$f_{structure}$ coefficients

$\alpha_2\ (\mathrm{J\,m^{-3}})$	$\alpha_4\ (\mathrm{J\,m^{-3}})$	$\alpha_6\ (\mathrm{J\,m^{-3}})$	$\alpha_4'\ (\mathrm{J\,m^{-3}})$	$\alpha_6'\ (\mathrm{J\,m^{-3}})$	$\alpha_6''\ (\mathrm{J\,m^{-3}})$
-0.312×10^{6}	-1.056×10^{6}	2.676×10^{6}	-1.305×10^{6}	0	0

$f_{gradient}$ coefficients

$\gamma_{11}\ (\mathrm{m\,V\,C^{-1}})$	$\gamma_{12}\ (\mathrm{m\,V\,C^{-1}})$	$\gamma_{44}\ (\mathrm{m\,V\,C^{-1}})$	$\gamma_{44}'\ (\mathrm{m\,V\,C^{-1}})$
282	0	138.4	138.4

$f_{electrostrictive}$ and finite element coefficients

$Q_{11}^0\ (\mathrm{m^4C^{-2}})$	$Q_{22}^0\ (\mathrm{m^4C^{-2}})$	$c_{11}\ (\mathrm{MPa})$	$c_{12}\ (\mathrm{MPa})$	$c_{44}\ (\mathrm{MPa})$	$\varepsilon\ (\varepsilon_0)$
0.015	–0.0075	120	80	20	200

7.3 Results and Discussion

Two simulations were conducted using different aspect ratios to explore the effect on domain patterns. Figure 7-7 depicts a 20 × 20 element simulation with a vacuum border of 5 elements to impose open circuit boundary conditions. The open circuit boundary conditions, along with an aspect ratio of 1, promote the development of four domains arranged in a vortex pattern separated by 90° domain walls. The influence of each of the energetic driving forces can be seen. The enforcement of Gauss's law through the electrostatic term can be seen by the lack of polarization normal to the surfaces and the head-to-tail behavior of the polarization pattern. Domain formation is due to the local gradient term as it is minimized when the polarizations of neighboring elements are identical. The lack of sharpness in the 90° domain wall is due energy penalties assigned to the electrostrictive and local gradient terms at a sharp 90° polarization transition. The preference for polarizations to lie in the vertical or horizontal directions is due to the influence of the structure term, which is minimized when the polarization rests at an energy well.

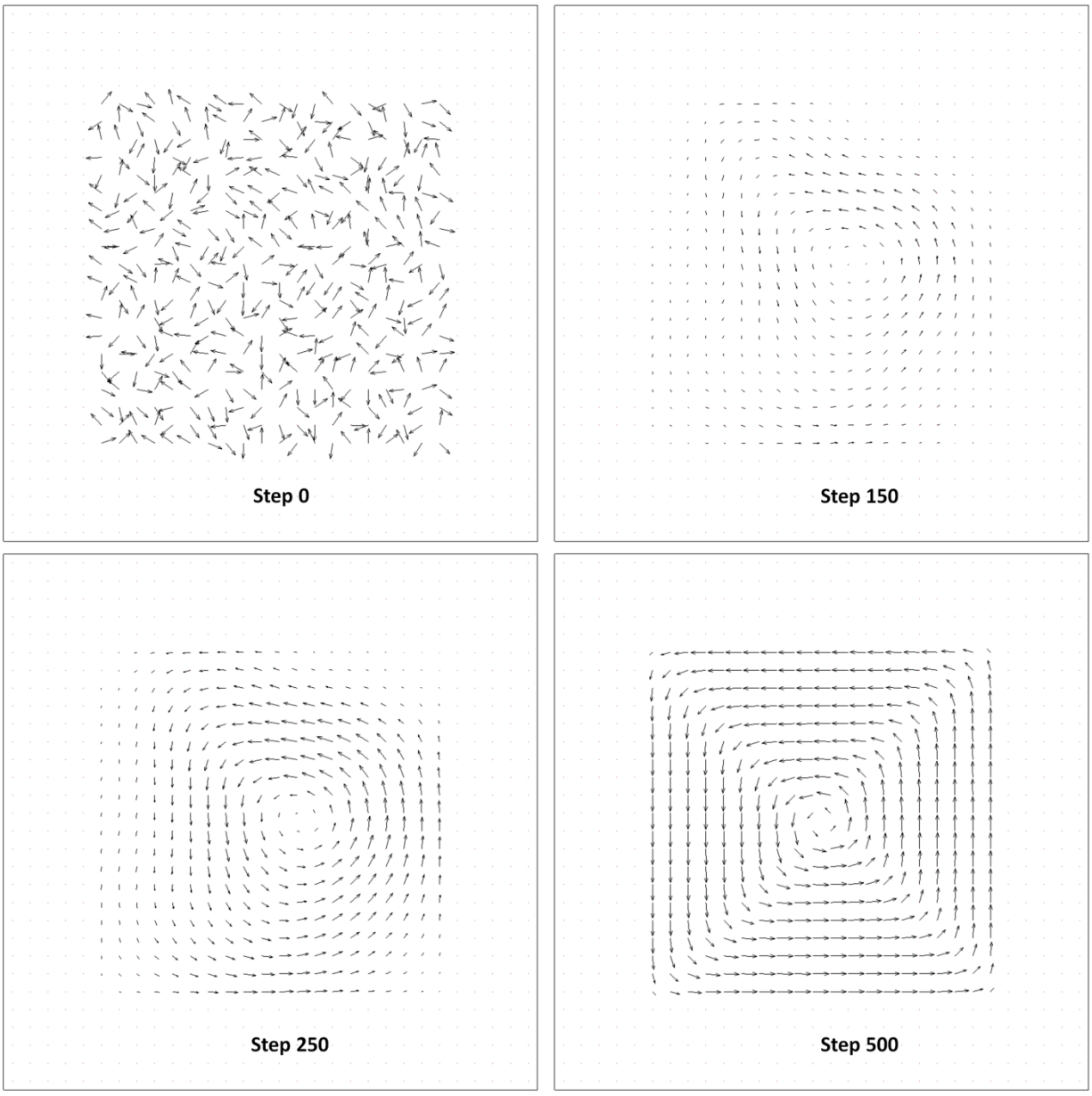

Figure 7-7. 20 × 20 element simulation of tetragonal ferroelectric material with unconstrained open circuit boundary conditions.

The effect of higher aspect ratio on domain patterns can be seen in Figure 7-8.a, which shows a simulation of 50 × 20 elements with the same boundary conditions. The higher aspect ratio forces a 180° domain wall in order to maintain electrical compatibility with the boundary conditions. A comparison of the width of the 90° and 180° domain walls in Figure 7-8.b further highlights the behavior of the energetic driving forces. A measurement of the domain walls finds the 180° domain wall width to be $3a$ where as the 90° domain wall has width of $5.4a$. An explanation of the discrepancy of the domain walls can be found by looking back at Figure 7-4. Figures 7-4.c and 7-4.d show a sharp 180° domain wall minimizes the structure, electrostatic, and electrostrictive energy density terms and penalizes the local gradient energy density term. Figures 4a and 4b show a sharp 90° domain wall minimizes the structure and electrostatic terms and penalizes electrostrictive and local gradient terms. The difference between the length of the 180° and 90° walls in tetragonal ferroelectric material is therefore due to whether the electrostrictive energy density term is minimized by a wider or narrower wall. Table 7-2 compiles the influence on the domain wall widths due to each energy density term for tetragonal ferroelectric materials modeled using discretized polarization on hexahedron elements.

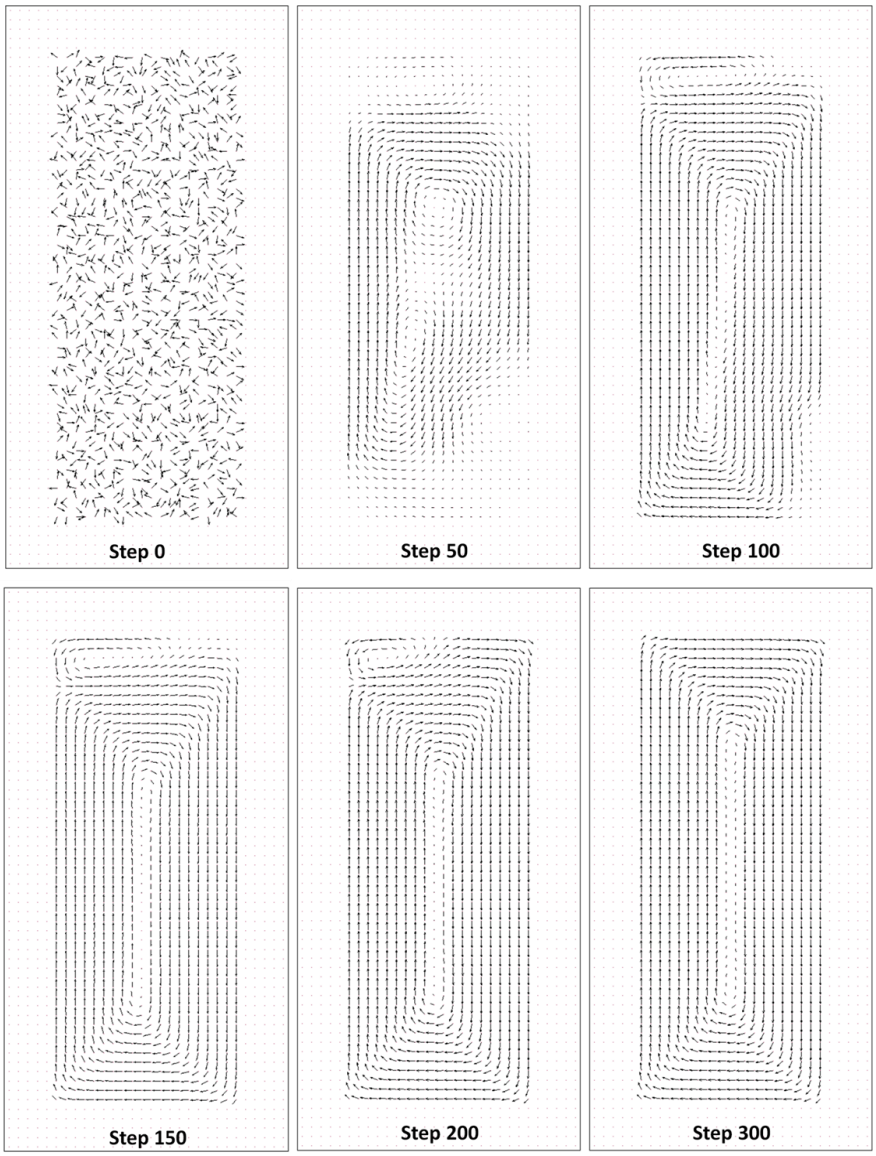

(a)

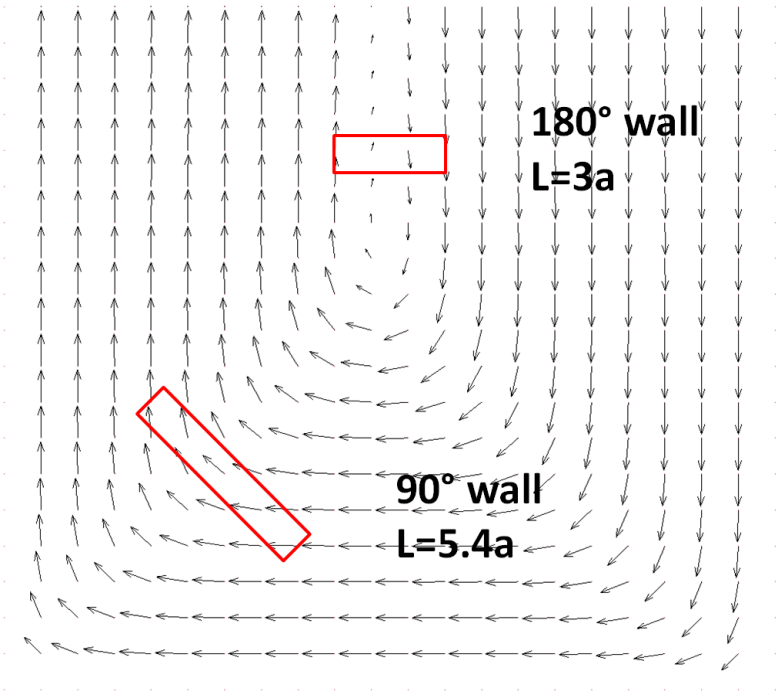

Figure 7-8. a) 50 × 20 element simulation of tetragonal ferroelectric material with unconstrained open circuit boundary conditions. b) Enlarged portion of the simulation shown in 8a that highlights the difference in width between the 180° and 90° domain walls.

Table 7-2. Characteristic of domain wall width that minimizes each energy density term.

Energy Density Term	90º Domain Wall	180º Domain Wall
$f_{structure}$	Narrow	Narrow
$f_{electrostatic}$	Narrow	Narrow
$f_{electrostrictive}$	Wide	Narrow
$f_{gradient}$	Wide	Wide

7.4 Conclusions

The finite element based phase field method uses local stresses and electric fields calculated by satisfying mechanical equilibrium and Gauss's law to simulate domain formation for ferroelectric materials at the perovskite unit cell level. The method shows that the domain patterns and domain wall widths are determined by a balance of the electrostatic, electrostrictive, structure, and local gradient energy densities. The effect on domain formation and domain wall widths due to each of the energy density terms has been described. The driving force due to each of the energy densities is the negative variational derivative of each free energy density term with respect to P_i and contributes an energetic driving force on the polarization that minimizes that energy density term. When the polarization magnitude and direction coincide with an energy well whose location in the energy landscape is dictated by the crystal structure, the structure energy term is minimized. The electrostrictive energy density term is minimized when the Eigen-strains of neighboring elements are compatible. The electrostatic energy density term is minimized when Gauss's law is satisfied. The local gradient term is minimized when neighboring cells have identical polarization. The model shows a minimization of the sum of these four free energy densities determines the characteristics of domain patterns and domain walls in ferroelectric materials.

The development of a phase field solver where the effects of each Landau-Devonshire energetic term are understood paves the way for future work on the study of phase transformations and phase boundaries within domain structures. The FE_R – FE_O phase transformation could be modeled using phase field methods by adopting the anisotropic free structural free energy density function for $[011]$ cut single crystal PIN-PMN-PT developed by

Zhang [121]. The evolutionary pathways for polarization orientation using Zhang's anisotropic structural free energy density is reproduced Figure 7-9. This anisotropic structural free energy density could be readily adapted into the Heitmann and Rossetti form of the structural free energy density.

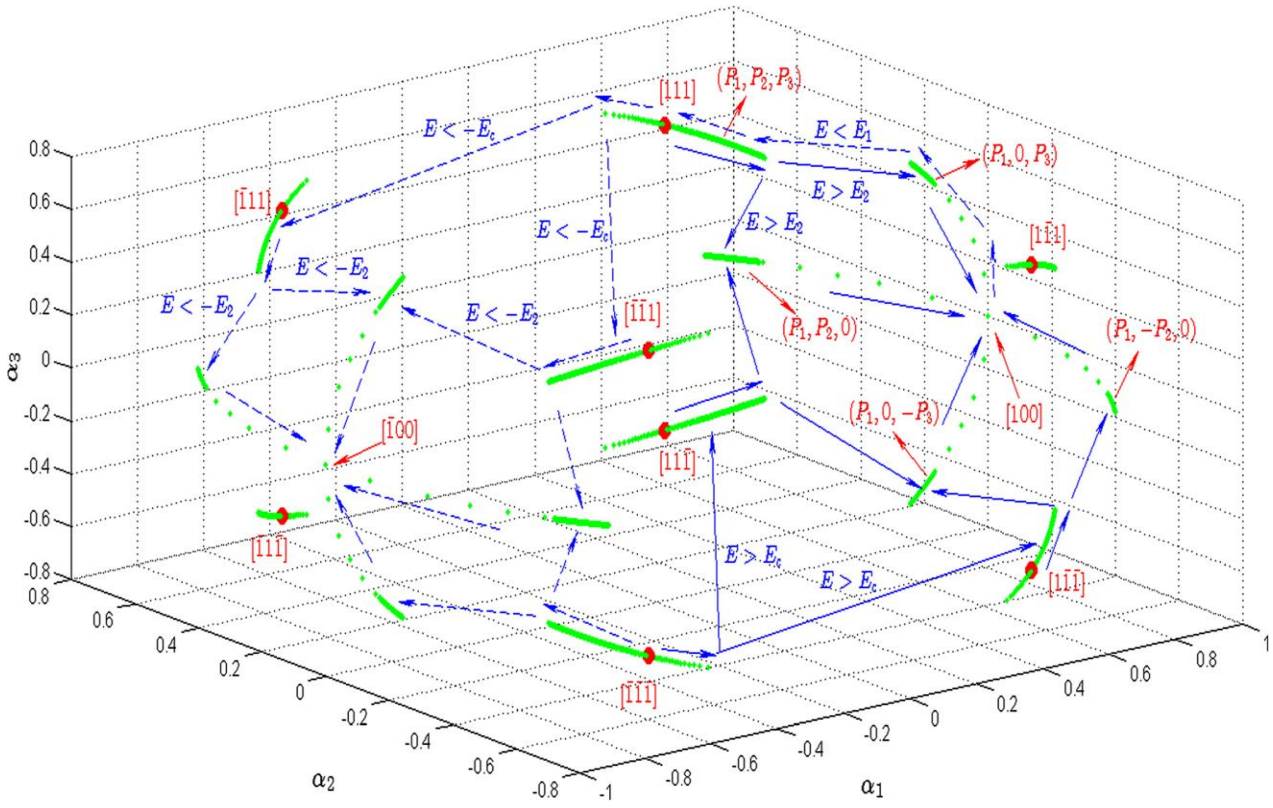

Figure 7-9. The evolutionary pathways for polarization orientation using Zhang's anisotropic structural free energy density for $[011]$ cut relaxor ferroelectric single crystals. Reproduced from Zhang [121].

Similarly, the FE – AF phase transformation models could be modeled in phase field by using structural free energy density functions proposed by Kittel [117], Cross [118], and Uchino [119-120]. These formulations propose splitting the Eigen-polarization lattice into two separate sub-

lattices with temperature and pressure dependent coefficients that force the sub-lattices to be copular in the FE phase or contrapolar in the AF phase. Another method would be to modify the gradient energy term such that antiferroelectric domains are favored over ferroelectric domains.

CHAPTER 8

CONCLUSIONS

Solid state phase transformations in ferroelectric materials (driven through thermodynamic cycles of temperature, electric field, and stress) offer exceptional electrical-mechanical coupling properties. These significantly exceed the results that can be obtained over linear piezoelectric regimes due to the large strain and polarization jumps across the phase transformation. The phase transformation leads to significant increases in compliance, permittivity, and electrical-mechanical coupling which are of interest for energy harvesting, transduction, and sensing applications.

The development of devices utilizing ferroelectric phase transformation technology requires a detailed understanding of phase transformation energetics and physics, streamlined material characterization techniques, the development of phase transformation modeling capabilities, and the design and demonstration of phase transformation energy harvesting cycles. Prior to this work, the combined electrical, mechanical, and thermal responses and phase stabilities of FE_R – FE_O phase transformations in single crystal PIN-PMN-PT and FE – AF phase transformations in 95/5-2Nb PZT were largely unexplored. Phase transformation computational models where modeling parameters could be related to experimental values and features did not exist. And demonstration of thermodynamically viable energy harvesting cycles using FE_R – FE_O phase transformations in single crystal PIN-PMN-PT had not been investigated. This dissertation has addressed these issues and sets the foundation for future developments in the area of ferroelectric phase transformation technology.

8.1 Summary of Results

Characteristics of the FE – AF phase transformation in 95/5-2Nb PZT ceramic ferroelectric material were explored under combined pressure, bipolar electric field, and temperature loads. At fixed combinations of pressure and temperature, specimens were electrically loaded with a large biaxial electric field and the corresponding electric displacement was captured. Large jumps in the polarization were used as indicators of phase transformation with a depolarization of the remnant polarization as an indication of the AF phase. Lower pressure, larger electric field magnitude, and higher temperature were shown to stabilize the FE phase and destabilize AF phase. At fixed temperature, phase boundaries were shown to be linear functions of pressure and electric field. Electric field – pressure – temperature 3-dimensional phase diagrams were created. Differences in electric field – pressure phase diagrams indicated three types of FE – AF phase transformations occurring over the temperature range tested. The linear dependence of the phase transformation criterion allowed for simplified phase diagram mapping.

Characteristics of the FE_R – FE_O phase transformation in near MPB FE_R composition PIN-PMN-PT single crystal relaxor ferroelectric material were explored under combined stress, electric field, and temperature loading. Electric field was applied and electric displacement was measured in the $[011]$ direction and compressive stress was applied and strain was measured in the $[100]$ direction. Stress, electric field, and temperature were shown to contribute towards the stabilization of the FE_O phase over the FE_R phase. Phase transformations were accompanied by a large increase in measured electric displacement and decrease in measured strain. Stress, electric field, and temperature phase diagrams were created for the FE_R – FE_O phase transformation. The phase transformation surfaces for FE_R to FE_O and FE_O to FE_R were shown

to be linear functions of stress, electric field, and temperature and the two transformation surfaces were shown to be parallel over the range of applied loads. Phase stability mapping of PIN-PMN-PT could be simplified to a few measurements.

An idealized energy harvesting thermodynamic cycle was developed for the $FE_R - FE_O$ phase transformation in PIN-PMN-PT. This idealized energy harvesting thermodynamic cycle was modeled after the reverse-Brayton cycle. The idealized ferroelectric cycle consists of four steps: 1) Isocharge (constant electric displacement) compression. 2) Isostress electric displacement change to minimize electric field. 3) Isocharge decompression. 4) Isostress electric displacement change to minimize electric field. When perfectly executed, the ideal cycle generates the greatest electrical energy density per cycle per over a given operating stress range independent of excitation frequency or electric load impedance values. The cycle was implemented over various stress excitation amplitudes across the mechanical phase transformation hysteresis. A fixed overhead cost associated with hysteresis was required to drive the phase transformation, but beyond the overhead cost mechanical energy was converted to electrical energy with 66% efficiency. Internal electrical leakage across the specimen reduced efficiencies and energy harvested at large stress amplitudes when electric fields exceeded a threshold value.

Non-idealized energy harvesting cycles were tested on PIN-PMN-PT to determine electric load impedance and frequency effects on energy harvesting characteristics. Cyclic uniaxial stress of ~5MPa in amplitude was applied across the phase transformation hysteresis. Increases in electric load impedance and frequency increased the size of the mechanical hysteresis (input mechanical energy). The additional input mechanical energy was converted to

electrical energy with 66% efficiency. Compared to a FE_R phase linear piezoelectric regime, the phase transformation regime had an energy density per cycle that was on average 27 times, with a maximum of 108 times, greater. Frequency studies showed the energy density per cycle scaled linearly with electric load impedance and linearly with frequency. The power density scaled linearly with electric load impedance and quadratically with frequency. An electrical model of the specimen and electric circuit verified the experimental result.

On length scales beyond domain structures, a non-linear ferroelectric material model was developed to simulate both the PIN-PMN-PT FE_R – FE_O phase transformation and the 95/5-2Nb PZT FE – AF phase transformation. The ferroelectric material model improved upon linear piezoelectric models by incorporating ferroelectric and ferroelastic phenomena. Ferroelectric and ferroeleastic phenomena were described using a set of linear constitutive equations and spontaneous strains and polarizations within the material. The spontaneous strains and polarizations were determined using energy based phase/variant switching criterion. A linear piezoelectric finite element framework was used to solve the boundary value problems presented by the mechanical and electrical field equations for materials described by the constitutive relations. Modeling parameters were fit to materials using experimental data and the models reproduced both the PIN-PMN-PT and a single grain of the 95/5-2Nb PZT with high fidelity.

The development of a finite element based phase field model was presented. Local spontaneous polarization and associated spontaneous strain was calculated using the time – dependent Landau – Ginzburg theory and Landau –Devonshire type multi-well potential energy functions. A linear piezoelectric finite element model was used to solve for local stresses and electric fields that affect the Landau – Devonshire free energy landscape. TDGL was used to

evolve domain structures until the Landau – Devonshire free energy was minimized. The impact of geometry and free energy function terms on the domain structure and 90 and 180 domain wall behavior is discussed. A physical description of the gradient energy term in Landau-Devonshire theory was presented. Methods to implement FE – FE and FE – AF phase transformations in the finite element based phase field model were presented.

8.2 Contributions

Prior to this research the use of mechanically driven phase transformations in ferroelectric materials was unexplored. The work of this dissertation has focused on the characterization and computational modeling of two types of ferroelectric phase transforming materials: $F_{ER} - F_{EO}$ phase transformation in domain engineered cut and poled PIN-PMN-PT and FE – AF phase transformation in ceramic 95/5-2Nb PZT. Additionally, an energy harvesting cycle with high performance capabilities was demonstrated for PIN-PMN-PT. It is the hope of the author that this research can pave the way for the development of ferroelectric phase transforming technologies in actuation, sensing, and energy harvesting. A list of contributions is shown below.

- FE – AF phase transformation in ceramic 95/5-2Nb PZT was characterized and shown to have phase transformation criterion that is linearly dependent on pressure and electric field. The electric field – pressure phase diagram at each temperature can be characterized with as few as two independent measurements.
- A 3-dimensional phase diagram is created for the FE – AF phase diagram in pressure (0 to 500MPa), temperature (25 to 125°C), and electric field (0 to $\pm 6 MVm^{-1}$

- $F_{ER} - F_{EO}$ phase transformation in domain engineered cut and poled PIN-PMN-PT was characterized and shown to have phase transformation criterion that is linearly dependent on stress, electric field, and temperature. The phase diagram in stress, electric field, and temperature can thus be characterized using as few as three independent measurements.
- A generalized micromechanics material model was developed to model variant switching and phase transformation. The material model was developed using a generalized approach that is capable of modeling both the AF – FE and FE_R – FE_O phase transformations. The model tracks the spontaneous polarization and strain changes within the material and is designed to work with a linear piezoelectric solver. A discussion on how experimental values relate to model parameters is presented.
- The energy harvesting characteristics of single crystal relaxor ferroelectric PIN-PMN-PT was assessed. First, specimens were loaded under an ideal energy harvesting cycle, similar to the reverse-Brayton cycle, to assess the maximum possible energy harvesting characteristics of the material. Second, specimens were loaded under sinusoidal stress loading cycles and the energy harvesting characteristics of PIN-PMN-PT was assessed under changes of load frequency and electric load impedance.

8.3 Future work

The findings of this dissertation have opened up many more interesting questions and future areas for investigation. The streamlined phase diagram mapping techniques described in Chapter 2 for PZT and Chapter 3 for PIN-PMN-T allow for the rapid characterization of new phase transformation material compositions. This eases the labor intensive characterization techniques previously required to identify the load-driven phase response of new material compositions and

paves the way for developments compositions that better suit phase transformation based applications. In FE – AF materials, desired qualities include lower FE to AF transformation pressures, higher spontaneous polarizations in the FE phase, sharper phase transformations, and smaller phase transformation hysteresis. Future work on improved FE – AF compositions involves detailed studies on the effect of dopants such as niobium, tin, lanthanum, barium, and strontium. In FE_R – FE_O materials, desired material properties include decreased phase transformation stresses, larger phase transformation strain and polarization changes, reduced phase transformation hysteresis, and sharper phase transformations. Future composition studies in PIN-PMN-PT could involve variations indium and titanium concentrations as well as the development of other ternary solid state solutions.

Future modeling work involves the development of a ceramic code for the FE – AF phase transforming 95/5-2Nb PZT. The modeling code in this work simulated the 95/5-2Nb PZT for a single crystal grain. The ceramic model would involve taking volume average response of numerous randomly oriented single-domain single crystal grains that are superimposed at each integration point. Preliminary work indicates there is significant domain-structure scale interaction in the FE – AF phase transformation of 95/5 PZT. Future work would look into finding ways to incorporate the domain-structure scale interactions into the micromechanics model. A method to understand the domain-structure scale interactions of phase transforming materials is to use the phase field model to simulate domain structure behavior during phase transformations. This can be achieved by using Landau-Devonshire crystalline anisotropy energy density terms developed for phase transforming materials as described in Chapter 7.

Future work on energy harvesting involves creating prototype energy harvesting devices that are capable of powering small devices such as sensors. The work in Chapters 4 and 5 demonstrated the $FE_R - FE_O$ phase transformation is thermodynamically a viable phenomenon for energy harvesting which offers significantly increased energy and power density over linear piezoelectric materials. Creating a prototype device for energy harvesting using the non-idealized cycle would require a pre-stressing fixture for the specimen and an oscillatory load that is sufficient to traverse the span of the phase transformation. Implementing the idealized energy harvesting cycle would require a controlled set of switches that open and close once target stress loads are achieved.

APPENDIX A

VARIANT TRANSFORMATION EQUATIONS

A.1 Phase/Variants Transformation Matrices

The material properties described in equations (6.4) and (6.5) and listed in tables 6-1 and 6-2 are for polarizations with orientations in the x_3 coordinate axis. A list of transformation matrices $[T]$ are provided below to describe the transformation between the material and global coordinates of each phase-variant.

A.1.1 Tetragonal

T1 Polarization orientation: $[100]$

$$[T] = \begin{bmatrix} 0 & 0 & 1 \\ 0 & -1 & 0 \\ 1 & 0 & 0 \end{bmatrix} \tag{A.1}$$

T2 Polarization orientation: $[010]$

$$[T] = \begin{bmatrix} 0 & 1 & 0 \\ 0 & 0 & 1 \\ 1 & 0 & 0 \end{bmatrix} \tag{A.2}$$

T3 Polarization orientation: $[\bar{1}00]$

$$[T] = \begin{bmatrix} 0 & 0 & -1 \\ 0 & 1 & 0 \\ 1 & 0 & 0 \end{bmatrix} \tag{A.3}$$

T4 Polarization orientation: $\left[0\,\bar{1}0\right]$

$$[T]=\begin{bmatrix}0 & -1 & 0\\ 0 & 0 & -1\\ 1 & 0 & 0\end{bmatrix} \tag{A.4}$$

T5 Polarization orientation: $\left[00\,\bar{1}\right]$

$$[T]=\begin{bmatrix}0 & 1 & 0\\ 1 & 0 & 0\\ 0 & 0 & -1\end{bmatrix} \tag{A.5}$$

T6 Polarization orientation: $\left[001\right]$

$$[T]=\begin{bmatrix}1 & 0 & 0\\ 0 & 1 & 0\\ 0 & 0 & 1\end{bmatrix} \tag{A.6}$$

A.1.2 Rhombohedral

R1 Polarization orientation: $\left[\bar{1}\,\bar{1}\,\bar{1}\right]$

$$[T]=\begin{bmatrix}\frac{-1}{\sqrt{2}} & \frac{1}{\sqrt{6}} & \frac{-1}{\sqrt{3}}\\ \frac{1}{\sqrt{2}} & \frac{1}{\sqrt{6}} & \frac{-1}{\sqrt{3}}\\ 0 & \frac{-\sqrt{2}}{\sqrt{3}} & \frac{-1}{\sqrt{3}}\end{bmatrix} \tag{A.7}$$

R2 Polarization orientation: $\left[1\,\bar{1}\,\bar{1}\right]$

$$[T]=\begin{bmatrix} \frac{-1}{\sqrt{2}} & \frac{-1}{\sqrt{6}} & \frac{1}{\sqrt{3}} \\ \frac{-1}{\sqrt{2}} & \frac{1}{\sqrt{6}} & \frac{-1}{\sqrt{3}} \\ 0 & \frac{-\sqrt{2}}{\sqrt{3}} & \frac{-1}{\sqrt{3}} \end{bmatrix} \tag{A.8}$$

R3 Polarization orientation: $\left[11\bar{1}\right]$

$$[T]=\begin{bmatrix} \frac{1}{\sqrt{2}} & \frac{-1}{\sqrt{6}} & \frac{1}{\sqrt{3}} \\ \frac{-1}{\sqrt{2}} & \frac{-1}{\sqrt{6}} & \frac{1}{\sqrt{3}} \\ 0 & \frac{-\sqrt{2}}{\sqrt{3}} & \frac{-1}{\sqrt{3}} \end{bmatrix} \tag{A.9}$$

R4 Polarization orientation: $\left[\bar{1}1\bar{1}\right]$

$$[T]=\begin{bmatrix} \frac{1}{\sqrt{2}} & \frac{1}{\sqrt{6}} & \frac{-1}{\sqrt{3}} \\ \frac{1}{\sqrt{2}} & \frac{-1}{\sqrt{6}} & \frac{1}{\sqrt{3}} \\ 0 & \frac{-\sqrt{2}}{\sqrt{3}} & \frac{-1}{\sqrt{3}} \end{bmatrix} \tag{A.10}$$

R5 Polarization orientation: $\left[\bar{1}\bar{1}1\right]$

$$[T]=\begin{bmatrix} \frac{-1}{\sqrt{2}} & \frac{-1}{\sqrt{6}} & \frac{-1}{\sqrt{3}} \\ \frac{1}{\sqrt{2}} & \frac{-1}{\sqrt{6}} & \frac{-1}{\sqrt{3}} \\ 0 & \frac{-\sqrt{2}}{\sqrt{3}} & \frac{1}{\sqrt{3}} \end{bmatrix} \tag{A.11}$$

R6 Polarization orientation: $\left[1\,\bar{1}1\right]$

$$\left[T\right]=\begin{bmatrix}\frac{-1}{\sqrt{2}} & \frac{1}{\sqrt{6}} & \frac{1}{\sqrt{3}}\\ \frac{-1}{\sqrt{2}} & \frac{-1}{\sqrt{6}} & \frac{-1}{\sqrt{3}}\\ 0 & \frac{-\sqrt{2}}{\sqrt{3}} & \frac{1}{\sqrt{3}}\end{bmatrix} \tag{A.12}$$

R7 Polarization orientation: $\left[111\right]$

$$\left[T\right]=\begin{bmatrix}\frac{1}{\sqrt{2}} & \frac{1}{\sqrt{6}} & \frac{1}{\sqrt{3}}\\ \frac{-1}{\sqrt{2}} & \frac{1}{\sqrt{6}} & \frac{1}{\sqrt{3}}\\ 0 & \frac{-\sqrt{2}}{\sqrt{3}} & \frac{1}{\sqrt{3}}\end{bmatrix} \tag{A.13}$$

R8 Polarization orientation: $\left[\bar{1}11\right]$

$$\left[T\right]=\begin{bmatrix}\frac{1}{\sqrt{2}} & \frac{-1}{\sqrt{6}} & \frac{-1}{\sqrt{3}}\\ \frac{1}{\sqrt{2}} & \frac{1}{\sqrt{6}} & \frac{1}{\sqrt{3}}\\ 0 & \frac{-\sqrt{2}}{\sqrt{3}} & \frac{1}{\sqrt{3}}\end{bmatrix} \tag{A.14}$$

A.1.3 Orthorhombic

O1 Polarization orientation: $\left[\bar{1}0\,\bar{1}\right]$

$$[T]=\begin{bmatrix} \frac{\sqrt{2}}{2} & 0 & \frac{-\sqrt{2}}{2} \\ 0 & -1 & 0 \\ \frac{-\sqrt{2}}{2} & 0 & \frac{-\sqrt{2}}{2} \end{bmatrix} \quad \text{(A.15)}$$

O2 Polarization orientation: $\left[0\,\bar{1}\,\bar{1}\right]$

$$[T]=\begin{bmatrix} 0 & 1 & 0 \\ \frac{\sqrt{2}}{2} & 0 & \frac{-\sqrt{2}}{2} \\ \frac{-\sqrt{2}}{2} & 0 & \frac{-\sqrt{2}}{2} \end{bmatrix} \quad \text{(A.16)}$$

O3 Polarization orientation: $\left[10\bar{1}\right]$

$$[T]=\begin{bmatrix} \frac{\sqrt{2}}{2} & 0 & \frac{\sqrt{2}}{2} \\ 0 & -1 & 0 \\ \frac{\sqrt{2}}{2} & 0 & \frac{-\sqrt{2}}{2} \end{bmatrix} \quad \text{(A.17)}$$

O4 Polarization orientation: $\left[01\bar{1}\right]$

$$[T]=\begin{bmatrix} 0 & 1 & 0 \\ \frac{\sqrt{2}}{2} & 0 & \frac{\sqrt{2}}{2} \\ \frac{\sqrt{2}}{2} & 0 & \frac{-\sqrt{2}}{2} \end{bmatrix} \quad \text{(A.18)}$$

O5 Polarization orientation: $\left[\bar{1}\,\bar{1}0\right]$

$$[T]=\begin{bmatrix} 0 & \frac{-\sqrt{2}}{2} & \frac{-\sqrt{2}}{2} \\ 0 & \frac{\sqrt{2}}{2} & \frac{-\sqrt{2}}{2} \\ 1 & 0 & 0 \end{bmatrix} \quad \text{(A.19)}$$

O6 Polarization orientation: $[1\bar{1}0]$

$$[T]=\begin{bmatrix} 0 & \frac{-\sqrt{2}}{2} & \frac{\sqrt{2}}{2} \\ 0 & \frac{-\sqrt{2}}{2} & \frac{-\sqrt{2}}{2} \\ 1 & 0 & 0 \end{bmatrix} \quad \text{(A.20)}$$

O7 Polarization orientation: $[110]$

$$[T]=\begin{bmatrix} 0 & \frac{\sqrt{2}}{2} & \frac{\sqrt{2}}{2} \\ 0 & \frac{-\sqrt{2}}{2} & \frac{\sqrt{2}}{2} \\ 1 & 0 & 0 \end{bmatrix} \quad \text{(A.21)}$$

O8 Polarization orientation: $[\bar{1}10]$

$$[T]=\begin{bmatrix} 0 & \frac{\sqrt{2}}{2} & \frac{-\sqrt{2}}{2} \\ 0 & \frac{\sqrt{2}}{2} & \frac{\sqrt{2}}{2} \\ 1 & 0 & 0 \end{bmatrix} \quad \text{(A.22)}$$

O9 Polarization orientation: $\left[\bar{1}01\right]$

$$\left[T\right]=\begin{bmatrix}\frac{\sqrt{2}}{2} & 0 & \frac{-\sqrt{2}}{2}\\ 0 & 1 & 0\\ \frac{\sqrt{2}}{2} & 0 & \frac{\sqrt{2}}{2}\end{bmatrix} \tag{A.23}$$

O10 Polarization orientation: $\left[0\bar{1}1\right]$

$$\left[T\right]=\begin{bmatrix}0 & -1 & 0\\ \frac{\sqrt{2}}{2} & 0 & \frac{-\sqrt{2}}{2}\\ \frac{\sqrt{2}}{2} & 0 & \frac{\sqrt{2}}{2}\end{bmatrix} \tag{A.24}$$

O11 Polarization orientation: $\left[101\right]$

$$\left[T\right]=\begin{bmatrix}\frac{\sqrt{2}}{2} & 0 & \frac{\sqrt{2}}{2}\\ 0 & 1 & 0\\ \frac{-\sqrt{2}}{2} & 0 & \frac{\sqrt{2}}{2}\end{bmatrix} \tag{A.25}$$

O12 Polarization orientation: $\left[011\right]$

$$\left[T\right]=\begin{bmatrix}0 & -1 & 0\\ \frac{\sqrt{2}}{2} & 0 & \frac{\sqrt{2}}{2}\\ \frac{-\sqrt{2}}{2} & 0 & \frac{\sqrt{2}}{2}\end{bmatrix} \tag{A.26}$$

A.2 Grain Randomization in Ceramic Materials

Implementing a material model to simulate ceramics requires the random rotation of each grain at an integration point. The creation of a series of randomized rotation matrices $[T]$ for each grain first requires establishing a spherical coordinate system with colatitudes ϕ and longitude θ. ϕ is the angle from the angle from the x_3 coordinate axis and θ is the positive angle from the x_1 axis in the $x_1 - x_2$ plane. Although the range of ϕ is $\{0, \pi\}$ and the range of θ is $\{0, 2\pi\}$. A distribution of ϕ and θ as,

$$\begin{aligned} \theta &= \mathcal{U}[0, 2\pi] \\ \phi &= \mathcal{U}[0, \pi] \end{aligned} \tag{A.27}$$

where $\mathcal{U}$ is a random uniform distribution function results in concentrations at the poles. The polar concentration is due to the fact that ϕ should be sparse at the poles if θ is a uniform distribution in order to maintain uniform projection onto the poles. If the transformation from x_1, x_2, x_3 to r, θ, ϕ is,

$$\begin{aligned} x_1 &= r \sin\phi \cos\theta \\ x_2 &= r \sin\phi \sin\theta \\ x_3 &= r \cos\phi \end{aligned} \tag{A.28}$$

Then the Jacobian for the transformation is,

$$J = \begin{bmatrix} \sin\phi\cos\theta & r\cos\phi\cos\theta & -r\sin\phi\sin\theta \\ \sin\phi\sin\theta & r\cos\phi\sin\theta & r\sin\phi\cos\theta \\ \cos\phi & -r\sin\phi & 0 \end{bmatrix} \tag{A.29}$$

And the determinant of the Jacobian for a unit circle is,

$$D = \sin\phi \tag{A.30}$$

Because the determinant for a unit circle varies due to changes in ϕ, the probability density function (f_ϕ) and cumulative density function (F_ϕ) of ϕ must take on the form,

$$f_\phi = \sin\left(x_2\right)$$
$$F_\phi = \int_0^{x_2} \sin\left(t\right) dt \tag{A.31}$$

Using the inverse cumulative density function method, the randomized distribution function for ϕ (p_ϕ) is given by

$$\mathcal{U}\left[0,1\right] = \frac{\int_0^{p_\phi} \sin\left(t\right) dt}{\int_0^{\pi} \sin\left(t\right) dt} \tag{A.32}$$

with the solution,

$$p_\phi = \pm 2\sin^{-1}\left(\sqrt{\mathcal{U}\left[0,1\right]}\right) \tag{A.33}$$

Taking the positive solution, the correct distribution for ϕ and θ to ensure fully randomized Jacobians is:

$$\theta = \mathcal{U}\left[0, 2\pi\right]$$
$$\phi = 2\sin^{-1}\left(\sqrt{\mathcal{U}\left[0,1\right]}\right) \tag{A.34}$$

The Jacobian listed in equation (A.29) is for vectors and tensors oriented in the x_1 direction. For vectors and tensors oriented in the x_3 direction the following Jacobian or transformation matrix is used,

$$\left[T\right] = J = \begin{bmatrix} \cos\phi\cos\theta & -\sin\phi\sin\theta & \sin\phi\cos\theta \\ \cos\phi\sin\theta & \sin\phi\cos\theta & \sin\phi\sin\theta \\ -\sin\phi & 0 & \cos\phi \end{bmatrix} \tag{A.35}$$

APPENDIX B

95/5-2NB PZT PHASE TRANSFORMATION SUPPLEMENTARY DATA

This section of the appendix contains supplementary data that was not included in the study on FE – AF phase transformation characterization in 95/5-2Nb PZT in Chapter 2. Figure B-1 presents the raw data for the electric displacement contour lines used to generate the load-driven phase diagrams. At each stress and temperature value, electric field values corresponding to electric displacement values of $0.3Cm^{-2}$, $0.2Cm^{-2}$, and $0.1Cm^{-2}$ on the D – E curve were determined.

(a)

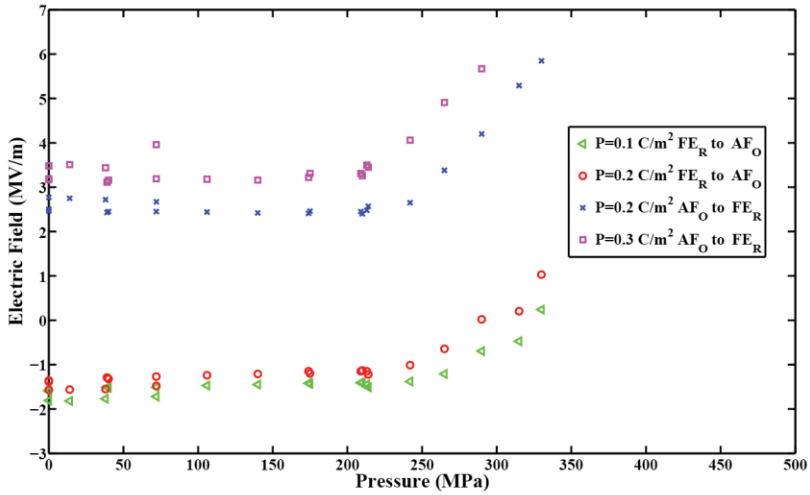
Electric Field (MV/m)
Pressure (MPa)
P=0.1 C/m² FE_R to AF_O
P=0.2 C/m² FE_R to AF_O
P=0.2 C/m² AF_O to FE_R
P=0.3 C/m² AF_O to FE_R

(b)

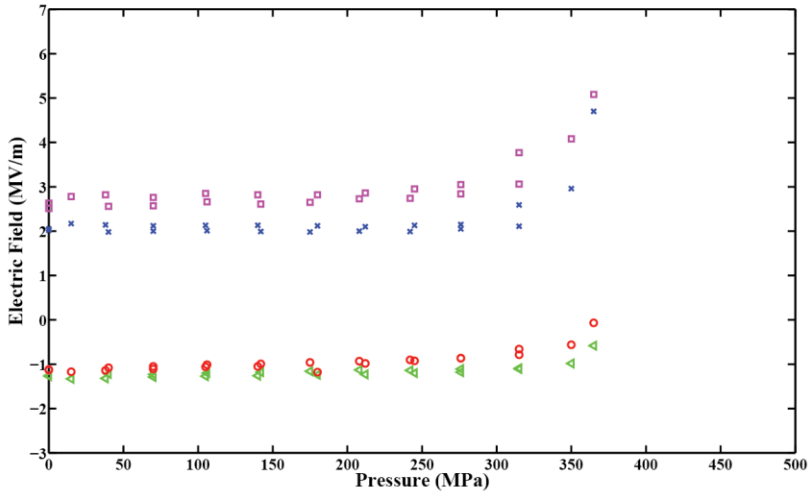
Electric Field (MV/m)
Pressure (MPa)

(c)

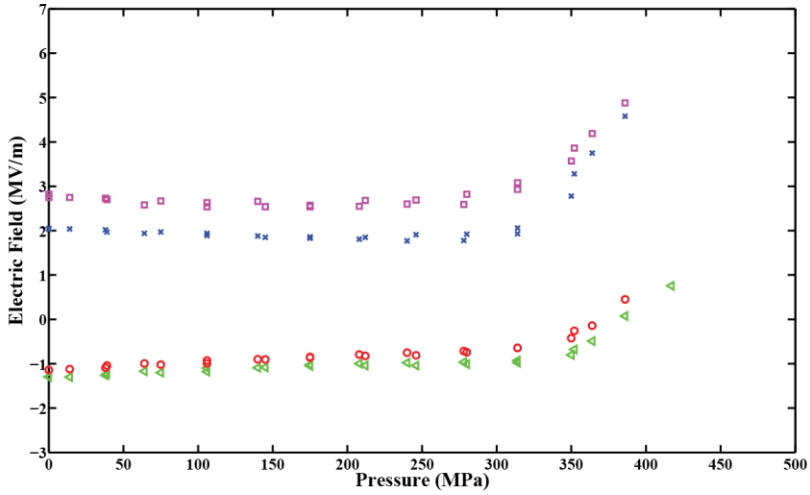
Electric Field (MV/m)
Pressure (MPa)

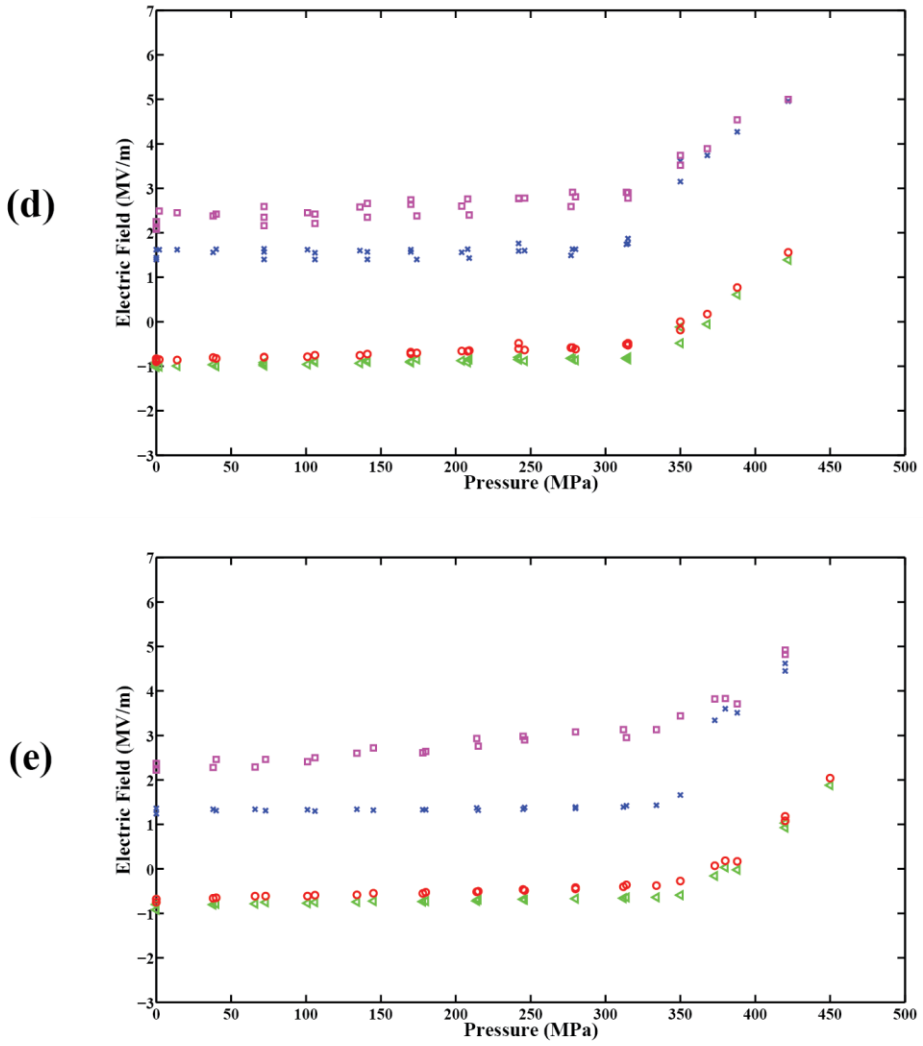

Figure B-1. Electric field values corresponding to electric displacement values of 0.3Cm^{-2} , 0.2Cm^{-2}, and 0.1Cm^{-2} on the D – E curve at fixed stress intervals and temperatures of a) 25°C, b) 50°C, c) 75°C, d) 100°C, e) 125°C.

APPENDIX C

PIN-PMN-PT PHASE TRANSFORMATION ENERGY HARVESTING SUPPLEMENTARY DATA

This section of the appendix contains supplementary data that was not included in the energy harvesting discussions of Chapters 5 and 6.

C.1 Idealized Energy Harvesting Cycle.

Figure D-1 shows the strain, electric field, and electric displacement data from the closing of the switch after isocharge loading. Initial peaks in electric field quickly decay, allowing for large changes in electric displacement and strain.

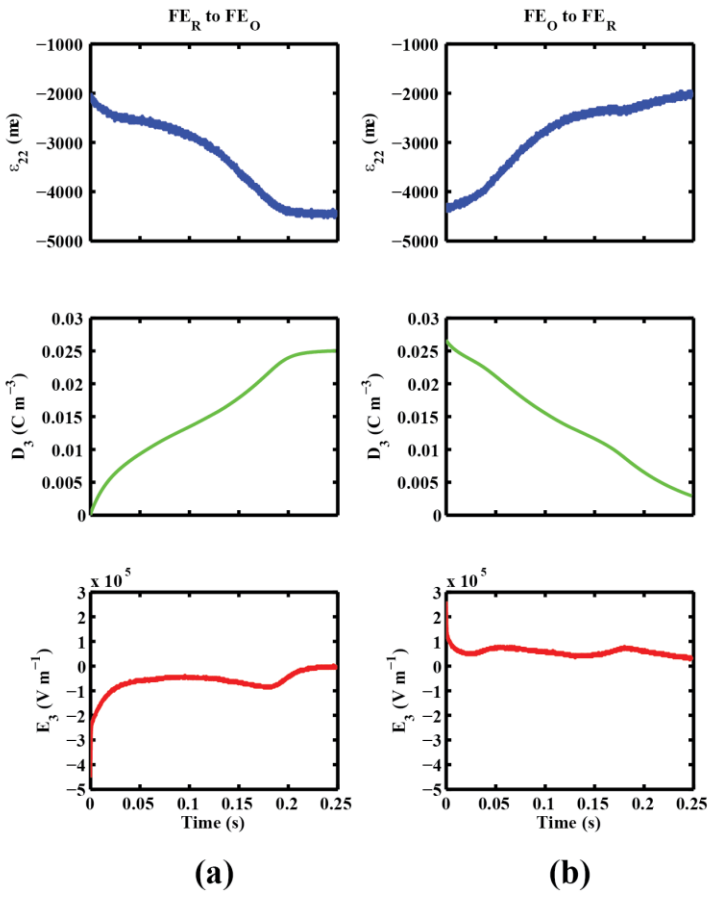

Figure C-1. Time dependent strain, electric displacement, and electric field behavior after compressive a) loading and b) unloading

Figure C-2 shows the strain – stress loops and electric displacement – electric field loops for the idealized energy harvesting cycle at all load intervals. Difference in electric displacement change are due to leakage.

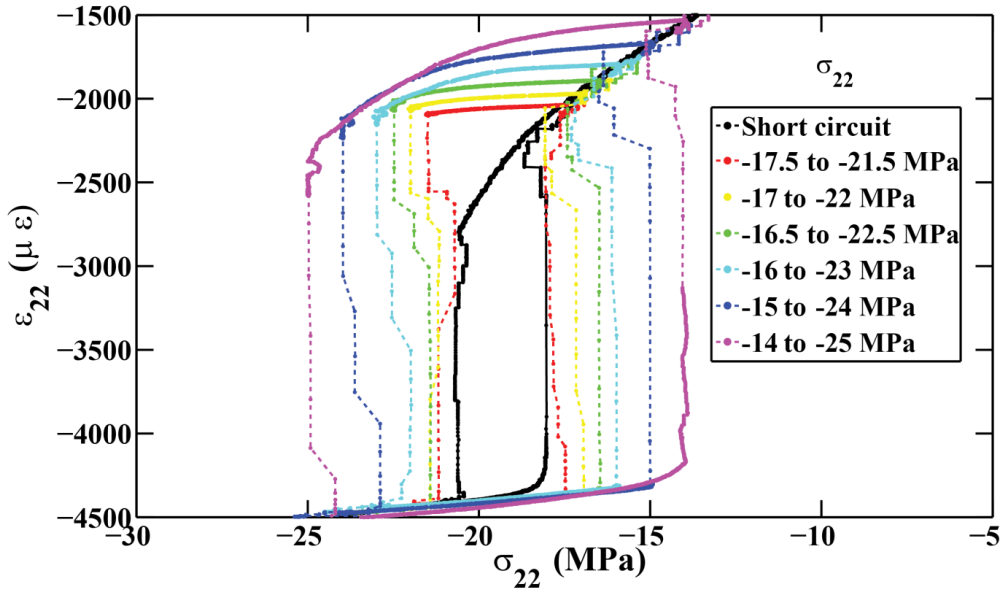

(a)

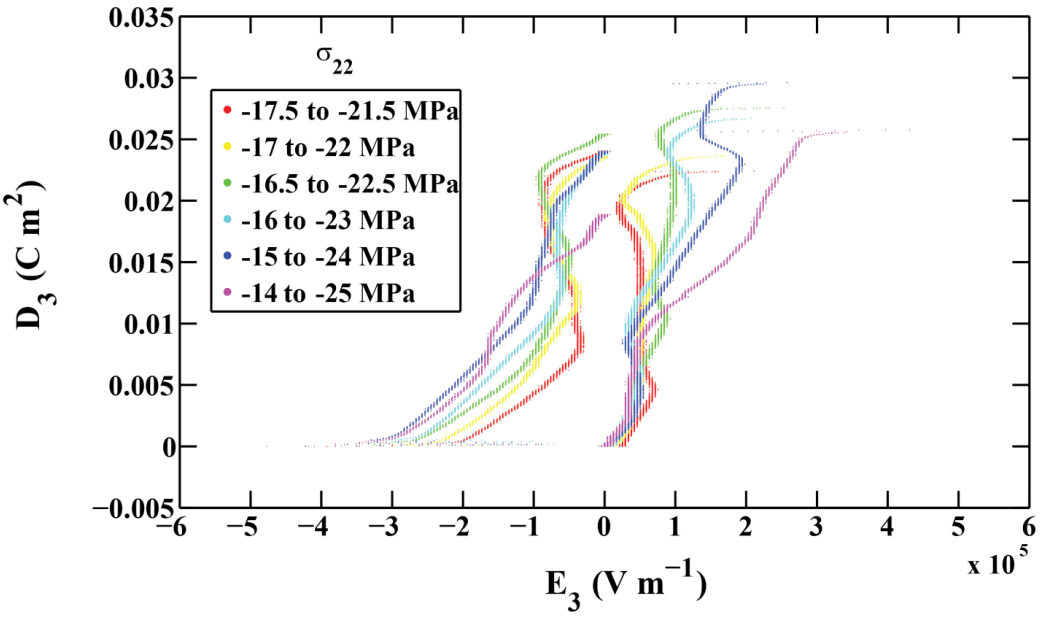

(b)

Figure C-2. a) strain – stress loops and b) electric displacement – electric field loops for the idealized energy harvesting cycle at all load intervals.

C.2 Non-Idealized Energy Harvesting Cycle

Figures C-3, C-4, C-5, C-6, show the energy density per cycle and power density properties as a function of mechanical excitation frequency and electric load impedance.

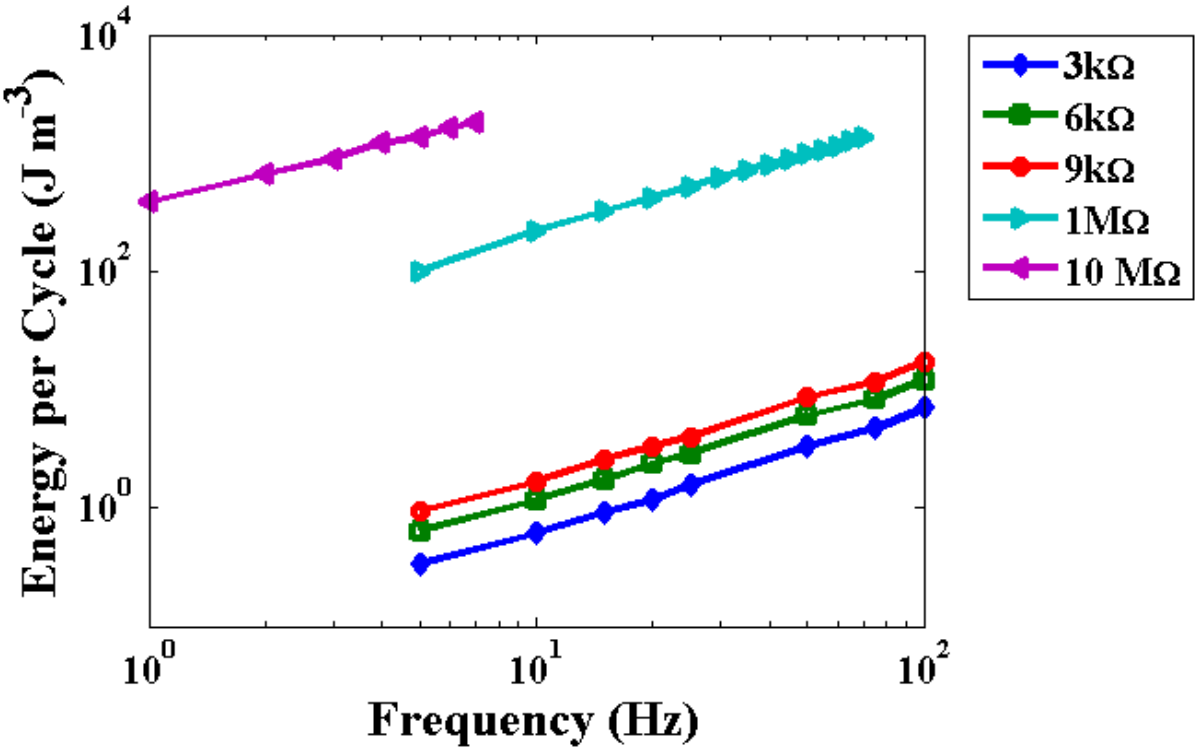

Figure C-3. Energy density per cycle as a function of frequency.

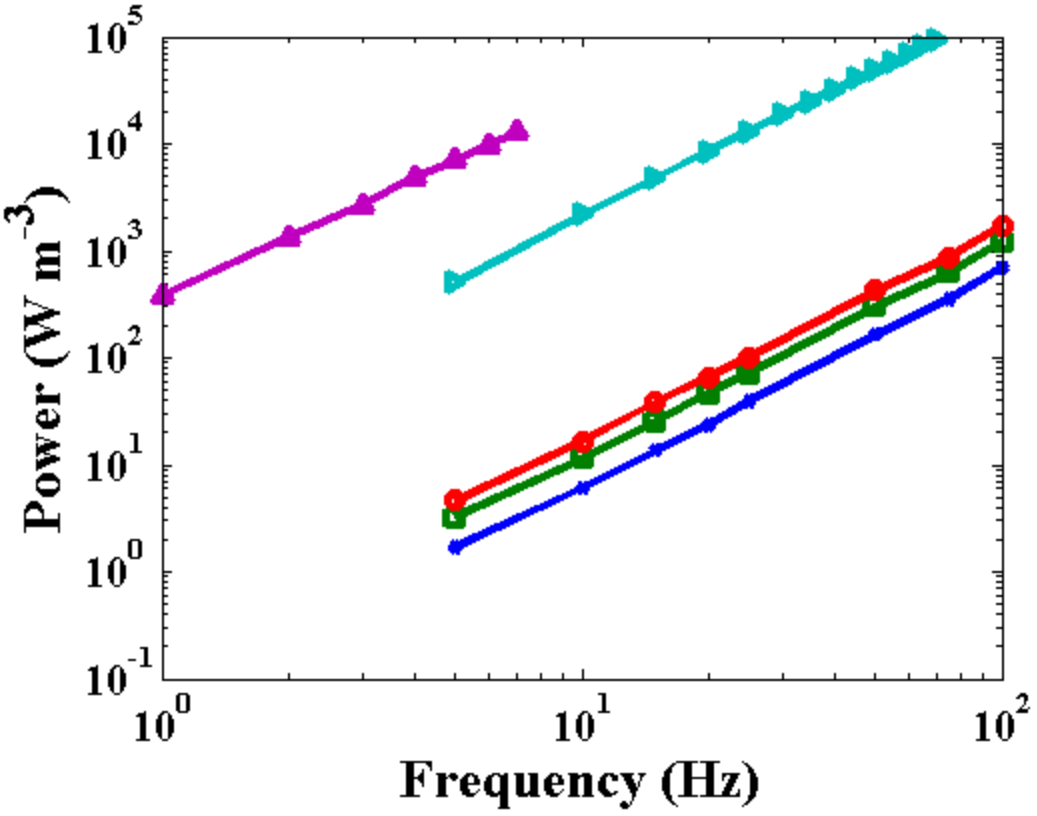

Figure C-4. Power density as a function of frequency.

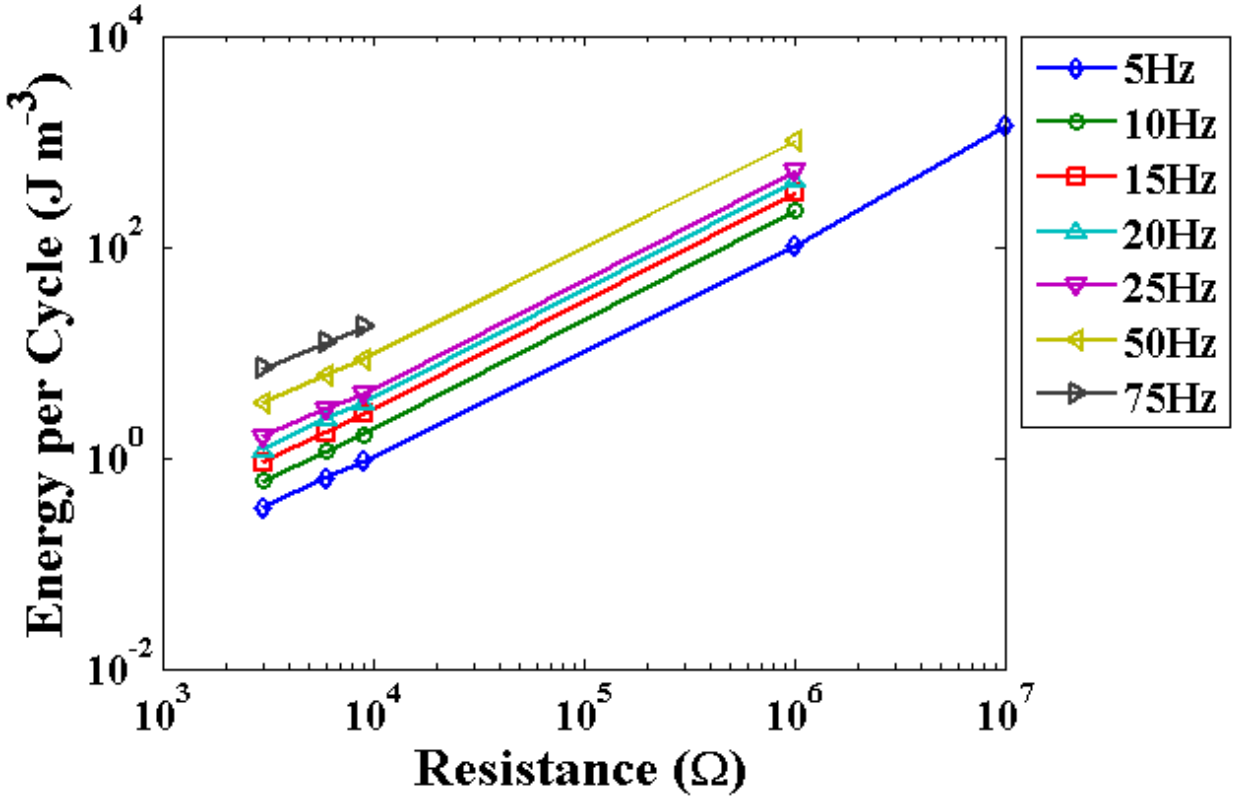

Figure C-5. Energy density per cycle as a function of electric load impedance

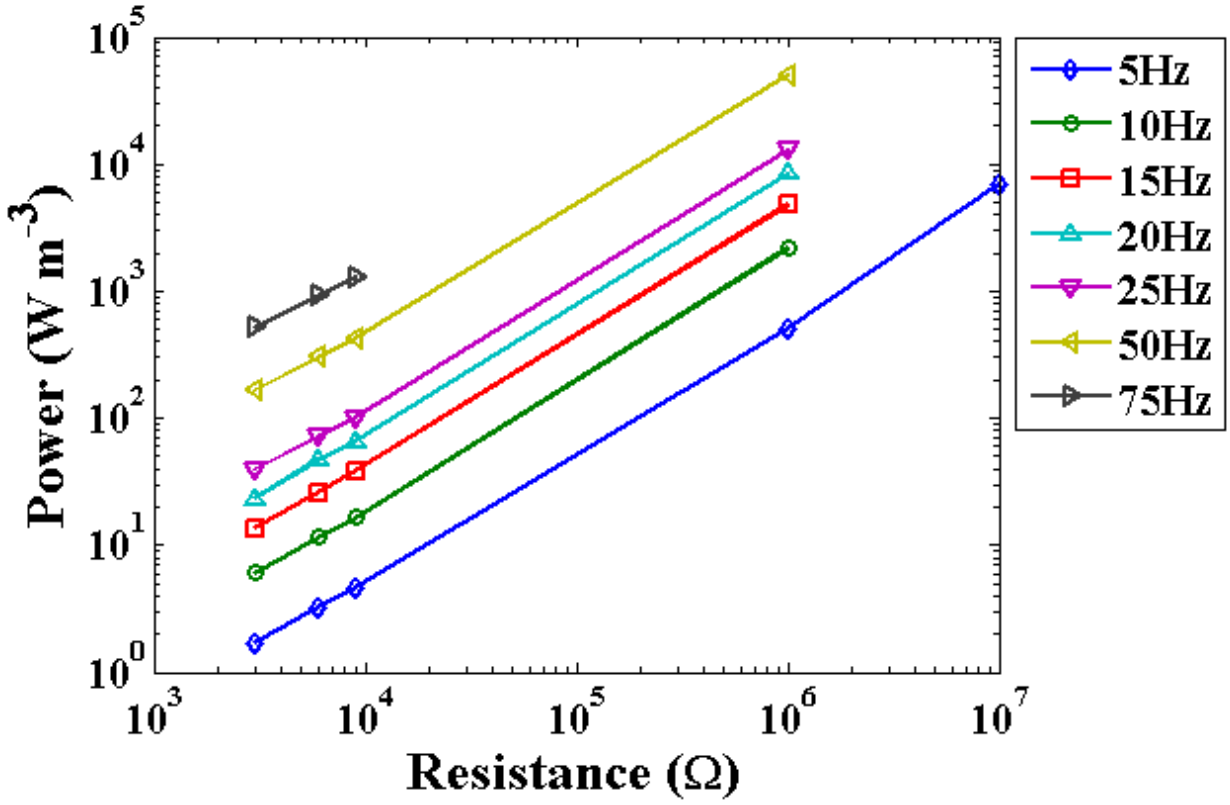

Figure C-6. Power density as a function of electric load impedance

REFERENCES

[1] D. J.J., *et al.*, "A Self-Sensing Piezoelectric Actuator for Collocated Control," *Journal of Intelligent Material Systems and Structures,* vol. 3, pp. 166-185, 1992.

[2] G. G., *Piezoelectric Sensorics: Force, Strain, Pressure, Acceleration and Accoustic Emission Sensors, Materials and Amplifiers*: Springer, 2002.

[3] E. Aksel and J. L. Jones, "Advances in Lead-Free Piezoelectric Materials for Sensors and Actuators," *Sensors,* vol. 10, pp. 1935-1954, Mar 2010.

[4] E. Sawaguchi, "Ferroelectricity versus Antiferroelectricity in the Solid Solutions of PbZrO 3 and PbTiO 3," *Journal of the Physical Society of Japan,* vol. 8, pp. 615-629, 1953.

[5] B. Jaffe, *et al.*, "Properties of piezoelectric ceramics in the solid-solution series lead titanate-lead zirconate-lead oxide: Tin oxide and lead titanate-lead hafnate," *Journal of Research of the National Bureau of Standards,* vol. 55, p. 239, 1955.

[6] B. Jaffe, *et al.*, "Piezoelectric Properties of Lead Zirconate-Lead Titanate Solid-Solution Ceramics," *Journal of Applied Physics,* vol. 25, pp. 809-810, 1954.

[7] G. H. Haertling, "Ferroelectric ceramics: History and technology," *Journal of the American Ceramic Society,* vol. 82, pp. 797-818, Apr 1999.

[8] C. B. Fleddermann and J. A. Nation, "Ferroelectric sources and their application to pulsed power: A review," *Ieee Transactions on Plasma Science,* vol. 25, pp. 212-220, 1997.

[9] H. W. Gundel, *et al.*, "Pulse polarization inversion and phase transition in ferroelectric and antiferroelectric thick films," *Journal of the European Ceramic Society,* vol. 21, pp. 1619-1623, 2001.

[10] D. G. Doran, "Shock-Wave Compression of Barium Titanate and 95⁄5 Lead Zirconate Titanate," *Journal of Applied Physics,* vol. 39, p. 40, 1968.

[11] W. J. Halpin, "Current from a Shock-Loaded Short-Circuited Ferroelectric Ceramic Disk," *Journal of Applied Physics,* vol. 37, p. 153, 1966.

[12] D. Jinmei, *et al.*, "Effects of lateral rarefaction wave on phase transition of PZT-95/5 ceramics under shock wave," *Ferroelectrics,* vol. 254, pp. 329-335, 2001.

[13] R. E. Setchell, "Shock wave compression of the ferroelectric ceramic Pb[sub 0.99](Zr[sub 0.95]Ti[sub 0.05])[sub 0.98]Nb[sub 0.02]O[sub 3]: Depoling currents," *Journal of Applied Physics,* vol. 97, p. 013507, 2005.

[14] R. Seveno, *et al.*, "Pulse characterization of antiferroelectric PbZrTiO3 thin films," *Journal of the European Ceramic Society,* vol. 25, pp. 2263-2267, 2005.

[15] P. C. Lysne, "Dielectric Properties of Shock-Wave-Compressed Pzt-95-5," *Journal of Applied Physics,* vol. 48, pp. 1020-1023, 1977.

[16] P. C. Lysne and C. M. Percival, "Electric Energy Generation by Shock Compression of Ferroelectric Ceramics - Normal-Mode Response of Pzt 95-5," *Journal of Applied Physics,* vol. 46, pp. 1519-1525, 1975.

[17] W. Mock and W. H. Holt, "Pulse Charging of Nanofarad Capacitors from the Shock Depoling of Pzt 56-44 and Pzt 95-5 Ferroelectric Ceramics," *Journal of Applied Physics,* vol. 49, pp. 5846-5854, 1978.
[18] G. Shirane and K. Suzuki, "Crystal Structure of Pb(Zr-Ti)O 3," *Journal of the Physical Society of Japan,* vol. 7, pp. 333-333, 1952.
[19] G. Shirane, *et al.*, "Phase Transitions in Solid Solutions of PbZrO 3 and PbTiO 3 (II) X-ray Study," *Journal of the Physical Society of Japan,* vol. 7, pp. 12-18, 1952.
[20] H. Barnett, "Evidence for a New Phase Boundary in the Ferroelectric Lead Zirconate-Lead Titanate System," *Journal of Applied Physics,* vol. 33, p. 1606, 1962.
[21] C. Michel, *et al.*, "Atomic structures of two rhombohedral ferroelectric phases in the Pb(Zr, Ti)O3 solid solution series," *Solid State Communications,* vol. 7, pp. 865-868, 1969.
[22] D. Berlincourt, *et al.*, "Stability of phases in modified lead zirconate with variation in pressure, electric field, temperature and composition," *Journal of Physics and Chemistry of Solids,* vol. 25, pp. 659-674, 1964.
[23] R. H. DUNGAN, *et al.*, "Phase Relations and Electrical Parameters in the Ferroelectric-Antiferroelectric Region of the System PbZrO3-PbTiO3-PbNbO2O6," *Journal of the American Ceramic Society,* vol. 45, pp. 382-388, 1962.
[24] I. J. Fritz and J. D. Keck, "Pressure-temperature phase diagrams for several modified lead zirconate ceramics," *Journal of Physics and Chemistry of Solids,* vol. 39, pp. 1163-1167, 1978.
[25] B. Jaffe, *et al.*, "Piezoelectric Ceramics," *Journal of the American Ceramic Society,* vol. 41, pp. 494-498, 1971.
[26] B. Jaffe, "Antiferroelectric Ceramics with Field-Enforced Transitions: A New Nonlinear Circuit Element," *Proceedings of the IRE,* vol. 49, pp. 1264-1267, 1961.
[27] Y. Xu, *et al.*, "Phenomenological theory of electric-field-induced phase transition behavior of antiferroelectric ceramic (Pb,Ba,La)(Zr,Sn,Ti)O3 under uniaxial compressive pre-stress," *Journal of Applied Physics,* vol. 112, p. 034112, 2012.
[28] A. Peláiz-Barranco, *et al.* (1999). *Advances in Ferroelectrics*. Available: http://www.intechopen.com/books/advances-in-ferroelectrics/relaxor-behavior-in-ferroelectric-ceramics
[29] J. Kuwata, *et al.*, "Phase-Transitions in the Pb(Zn1/3nb2/3)O3-Pbtio3 System," *Ferroelectrics,* vol. 37, pp. 579-582, 1981.
[30] J. Kuwata, *et al.*, "Dielectric and Piezoelectric Properties of 0.91pb(Zn1/3nb2/3)O3-0.09pbtio3 Single-Crystals," *Japanese Journal of Applied Physics Part 1-Regular Papers Short Notes & Review Papers,* vol. 21, pp. 1298-1302, 1982.
[31] T. R. Shrout, *et al.*, "Dielectric Behavior of Single-Crystals near the (1-X) Pb(Mg1/3nb2/3)O3-(X) Pbtio3 Morphotropic Phase-Boundary," *Ferroelectrics Letters Section,* vol. 12, pp. 63-69, 1990.
[32] Y. Yamashita and S. Shimanuki, "Synthesis of lead scandium niobate-lead titanate pseudo binary system single crystals," *Materials Research Bulletin,* vol. 31, pp. 887-895, Jul 1996.
[33] Y. P. Guo, *et al.*, "The phase transition sequence and the location of the morphotropic phase boundary region in (1-x)[Pb(Mg1/3Nb2/3)O-3]-xPbTiO(3) single crystal," *Journal of Physics-Condensed Matter,* vol. 15, pp. L77-L82, Jan 22 2003.

[34] J. M. Kiat, *et al.*, "Monoclinic structure of unpoled morphotropic high piezoelectric PMN-PT and PZN-PT compounds," *Physical Review B*, vol. 65, Feb 1 2002.
[35] Y. Lu, *et al.*, "Phase transitional behavior and piezoelectric properties of the orthorhombic phase of Pb(Mg(1/3)Nb(2/3))O(3)-PbTiO(3) single crystals," *Applied Physics Letters*, vol. 78, pp. 3109-3111, May 14 2001.
[36] S. Priya, *et al.*, "Investigation of the ferroelectric orthorhombic phase in the Pb(Zn1/3N2/3)O-3-PbTiO3 system," *Ferroelectrics*, vol. 274, pp. 121-126, 2002.
[37] A. K. Singh and D. Pandey, "Evidence for M-B and M-C phases in the morphotropic phase boundary region of (1-x)[Pb(Mg1/3Nb2/3)O-3]-xPbTiO(3): A Rietveld study," *Physical Review B*, vol. 67, Feb 1 2003.
[38] D. Viehland, *et al.*, "Piezoelectric instability in < 011 >-oriented Pb((B1/3B2/3II)-B-I)O-3-PbTiO3 crystals," *Applied Physics Letters*, vol. 79, pp. 1006-1008, Aug 13 2001.
[39] D. S. Paik, *et al.*, "E-field induced phase transition in < 001 >-oriented rhombohedral 0.92Pb(Zn1/3Nb2/3)O-3-0.08PbTiO(3) crystals," *Journal of Applied Physics*, vol. 85, pp. 1080-1083, Jan 15 1999.
[40] S. F. Liu, *et al.*, "E-field dependence of piezoelectric properties of rhombohedral PZN-PT single crystal," *Ferroelectrics*, vol. 221, pp. 169-174, 1999.
[41] W. Ren, *et al.*, "Piezoelectric properties and phase transitions of < 001 >-oriented Pb(Zn1/3Nb2/3)O-3-PbTiO3 single crystals," *Applied Physics Letters*, vol. 80, pp. 3174-3176, Apr 29 2002.
[42] S. E. E. Park and W. Hackenberger, "High performance single crystal piezoelectrics: applications and issues," *Current Opinion in Solid State & Materials Science*, vol. 6, pp. 11-18, Feb 2002.
[43] D. Viehland, "Symmetry-adaptive ferroelectric mesostates in oriented Pb(BI1/3BII2/3)O-3-PbTiO3 crystals," *Journal of Applied Physics*, vol. 88, pp. 4794-4806, Oct 15 2000.
[44] K. G. Webber, *et al.*, "Ceramic and single-crystal (1-x)PMN-xPT constitutive behavior under combined stress and electric field loading," *Acta Materialia*, vol. 56, pp. 1219-1227, Apr 2008.
[45] Y. Hosono, *et al.*, "Growth of single crystals of high-Curie-temperature Pb(In1/2Nb1/2)O-3-Pb(Mg1/3Nb2/3)O-3-PbTiO3 ternary systems near morphotropic phase boundary," *Japanese Journal of Applied Physics Part 1-Regular Papers Short Notes & Review Papers*, vol. 42, pp. 5681-5686, Sep 2003.
[46] Y. Hosono, *et al.*, "Crystal growth of Pb(In1/2Nb1/2)O-3-Pb(Mg1/3Nb2/3)O-3-PbTiO3 and Pb(SC1/2Nb1/2)O-3-Pb(Mg1/3Nb2/3)O-3-PbTiO3 piezoelectric single crystals using the solution Bridgman method," *Japanese Journal of Applied Physics Part 1-Regular Papers Short Notes & Review Papers*, vol. 42, pp. 6062-6067, Sep 2003.
[47] T. Karaki, *et al.*, "Top-seeded solution growth of Pb[(In1/2Nb1/2),(Mg1/3Nb2/3),Ti]O-3 single crystals," *Japanese Journal of Applied Physics Part 1-Regular Papers Short Notes & Review Papers*, vol. 42, pp. 6059-6061, Sep 2003.
[48] J. Tian, *et al.*, "Improved stability for piezoelectric crystals grown in the lead indium niobate-lead magnesium niobate-lead titanate system," *Applied Physics Letters*, vol. 91, Nov 26 2007.
[49] G. S. Xu, *et al.*, "Growth and electrical properties of large size Pb(In1/2Nb1/2)O-3-Pb(Mg1/3Nb2/3)O-3-PbTiO3 crystals prepared by the vertical Bridgman technique," *Applied Physics Letters*, vol. 90, Jan 15 2007.

[50] G. A. Samara, *et al.*, "Pressure-induced crossover from long-to-short-range order in [Pb(Zn1/3Nb2/3)O-3](0.905)(PbTiO3)(0.095) single crystal," *Applied Physics Letters,* vol. 76, pp. 1327-1329, Mar 6 2000.
[51] D. Viehland and J. Powers, "Electromechanical coupling coefficient of < 001 >-oriented Pb(Mg1/3Nb2/3)O-3-PbTiO3 cystals: Stress and temperature independence," *Applied Physics Letters,* vol. 78, pp. 3112-3114, May 14 2001.
[52] D. Viehland and J. Powers, "Effect of uniaxial stress on the electromechanical properties of 0.7Pb(Mg1/3Nb2/3)O-3-0.3PbTiO(3) crystals and ceramics," *Journal of Applied Physics,* vol. 89, pp. 1820-1825, Feb 1 2001.
[53] D. Viehland, *et al.*, "Electroacoustic properties of < 110 >-oriented Pb-(Mg1/3Nb2/3)O-3-PbTiO3 crystals under uniaxial stress," *Applied Physics Letters,* vol. 83, pp. 132-134, Jul 7 2003.
[54] T. Q. Liu, *et al.*, "Thermodynamics of stress and electric field induced phase transition in relaxor ferroelectric crystals," *Journal of Intelligent Material Systems and Structures,* vol. 18, pp. 409-415, Apr 2007.
[55] E. A. McLaughlin, *et al.*, "Relaxor ferroelectric PMN-32%PT crystals under stress and electric field loading: I-32 mode measurements," *Acta Materialia,* vol. 52, pp. 3849-3857, Aug 2 2004.
[56] E. A. McLaughlin, *et al.*, "Relaxor ferroelectric PMN-32%PT crystals under stress, electric field and temperature loading: II-33-mode measurements," *Acta Materialia,* vol. 53, pp. 4001-4008, Aug 2005.
[57] M. Davis, *et al.*, "Electric-field-, temperature-, and stress-induced phase transitions in relaxor ferroelectric single crystals," *Physical Review B,* vol. 73, Jan 2006.
[58] A. Amin, *et al.*, "Stability of domain engineered lead zinc niobate-lead titanate single crystals for 32-mode sound projectors (vol 97, 062903, 2010)," *Applied Physics Letters,* vol. 97, Sep 20 2010.
[59] C. Okawara and A. Amin, "dc field effect on stability of piezoelectric PZN-0.06PT single crystals under compressive stress (vol 95, 072902, 2009)," *Applied Physics Letters,* vol. 95, Nov 9 2009.
[60] P. Finkel, *et al.*, "Study of phase transitions in ternary lead indium niobate-lead magnesium niobate-lead titanate relaxor ferroelectric morphotropic single crystals," *Applied Physics Letters,* vol. 97, Sep 20 2010.
[61] W. D. Dong, *et al.*, "Stress dependence of thermally driven pyroelectric charge release during FER-FEO phase transformations in [011] cut relaxor ferroelectric crystals," *Applied Physics Letters,* vol. 100, Jun 25 2012.
[62] W. D. Dong, *et al.*, "Giant electro-mechanical energy conversion in [011] cut ferroelectric single crystals," *Applied Physics Letters,* vol. 100, Jan 23 2012.
[63] P. Finkel, *et al.*, "Large strain transduction utilizing phase transition in relaxor-ferroelectric Pb(In1/2Nb1/2)O-3-Pb(Mg1/3Nb2/3)O-3-PbTiO3 single crystals," *Applied Physics Letters,* vol. 98, May 9 2011.
[64] M. Shanthi and L. C. Lim, "Electric-field- and stress-induced R-O phase transformation in [011]-poled Pb(Mg1/3Nb2/3)O-3-(28-32)%PbTiO3 single crystals of [100]-length cut," *Journal of Applied Physics,* vol. 106, Dec 1 2009.

[65] M. Shanthi, *et al.*, "Stress and electric field induced phase transformation phenomena in [0 1 1]-poled PZN-PT single crystals of [1 0 0]-length cut," *Sensors and Actuators a-Physical*, vol. 168, pp. 112-116, Jul 2011.
[66] H. Allik and H. J.R., "Finite element method for piezoelectric vibration," *International Journal for Numerical Methods in Engineering*, vol. 2, pp. 151-157, 1970.
[67] A. Benjeddou, "Advances in piezoelectric finite element modeling of adaptive structural elements: a survey," *Computers & Structures*, vol. 76, pp. 347-363, Jun 2000.
[68] C. L. Hom and N. Shankar, "A finite element method for electrostrictive ceramic devices," *International Journal of Solids and Structures*, vol. 33, pp. 1757-1779, May 1996.
[69] S. C. Hwang, *et al.*, "Ferroelectric/ferroelastic interactions and a polarization switching model," *Acta Metallurgica et Materialia*, vol. 43, pp. 2073-2084, 1995.
[70] W. Chen and C. S. Lynch, "Finite element analysis of cracks in ferroelectric ceramic materials," *Engineering Fracture Mechanics*, vol. 64, pp. 539-562, Nov 1999.
[71] D. Fang and A. K. Soh, "Finite element modeling of electro-mechanically coupled analysis for ferroelectric ceramic materials with defects," *Computer Methods in Applied Mechanics and Engineering*, vol. 190, pp. 2771-2787, 2001.
[72] F. X. Li and D. N. Fang, "Simulations of domain switching in ferroelectrics by a three-dimensional finite element model," 2004, pp. 959-973.
[73] D. N. Fang, *et al.*, "Analysis of the electromechanical behavior of ferroelectric ceramics based on a nonlinear finite element model," *Acta Mechanica Sinica*, vol. 21, pp. 294-304, Jun 2005.
[74] H. Kessler, *et al.*, "Constitutive and finite element modeling of ferroelectric repolarization," San Diego, CA, United States, pp. 21-30.
[75] M. Kamlah and C. Tsakmakis, "Phenomenological modeling of the non-linear electro-mechanical coupling in ferroelectrics," *International Journal of Solids and Structures*, vol. 36, pp. 669-695, 1999.
[76] M. Kamlah and U. Bohle, "Finite element analysis of piezoceramic components taking into account ferroelectric hysteresis behavior," *International Journal of Solids and Structures*, vol. 38, pp. 605-633, Jan 2001.
[77] C. M. Landis, "A new finite-element formulation for electromechanical boundary value problems," *International Journal for Numerical Methods in Engineering*, vol. 55, pp. 613-628, Oct 20 2002.
[78] A. C. F. Cocks and R. M. McMeeking, "A phenomenological constitutive law for the behaviour of ferroelectric ceramics," *Ferroelectrics*, vol. 228, pp. 219-228, 1999.
[79] S. C. Hwang, *et al.*, "The simulation of switching in polycrystalline ferroelectric ceramics," *Journal of Applied Physics*, vol. 84, p. 1530, 1998.
[80] J. Li and G. J. Weng, "A micromechanics-based hysteresis model for ferroelectric ceramics," *Journal of Intelligent Material Systems and Structures*, vol. 12, pp. 79-91, Feb 2001.
[81] T. Liu, *et al.*, "Finite Element Analysis With a Ferroelectric and Ferroelastic Material Model," *Integrated Ferroelectrics*, vol. 101, pp. 164-173, 2008.
[82] T. LIU and C. S. LYNCH, "CHARACTERIZATION AND MODELING OF RELAXOR SINGLE CRYSTALS," *Integrated Ferroelectrics*, vol. 71, pp. 173-179, 2005.

[83] T. Liu and C. S. Lynch, "Domain Engineered Relaxor Ferroelectric Single Crystals," *Continuum Mechanics and Thermodynamics,* vol. 18, pp. 119-135, 2006.
[84] T. Liu and C. S. Lynch, "Ferroelectric properties of [110], [001] and [111] poled relaxor single crystals: measurements and modeling," *Acta Materialia,* vol. 51, pp. 407-416, 2003.
[85] K. G. Webber, *et al.*, "Micromechanical modeling of PMN-32%PT ceramic based on single crystal properties - art. no. 617005," *Smart Structures and Materials 2006: Active Materials: Behavior and Mechanics,* vol. 6170, pp. 17005-17005, 2006.
[86] K. G. Webber, *et al.*, "A distributed step-like switching model of the continuous field-driven phase transformations observed in PMN-xPT relaxor ferroelectric single crystals," *Acta Materialia,* vol. 56, pp. 2744-2749, Jul 2008.
[87] K. G. Webber and C. S. Lynch, "Micromechanical model of nonlinear relaxor ferroelectric phase transformation," *Behavior and Mechanics of Multifunctional and Composite Materials 2008,* vol. 6929, 2008.
[88] K. Jayabal, *et al.*, "Multiaxial behavior of ferroelectric single and polycrystals with pressure dependent boundary effects," *Computational Materials Science,* vol. 44, pp. 1222-1230, Feb 2009.
[89] J. A. Gallagher and C. S. Lynch, "Characterization of ferroelectric single crystals with field induced phase transformations," *Smart Materials and Structures,* vol. 22, Sep 2013.
[90] J. Robbins, *et al.*, "Microstructural modeling of ferroic switching and phase transitions in PZT," in *Proc. SPIE* vol. 6526, M. J. Dapino, Ed., ed, 2007, pp. 652607-652607-12.
[91] S. Lange and A. Ricoeur, "A condensed microelectromechanical approach for modeling tetragonal ferroelectrics," *International Journal of Solids and Structures,* vol. 54, pp. 100-110, Feb 2015.
[92] K. Ghandi and N. W. Hagood, "Nonlinear finite element modeling of phase transitions in electro-mechanically coupled material," *Mathematics and Control in Smart Structures,* vol. 2715, pp. 121-140, 1996.
[93] S. T. Montgomery and D. H. Zeuch, "A Model for the Bulk Mechanical Response of Porous Ceramics Exhibiting a Ferroelectric-to-Antiferroelectric Phase Transition During Hydrostatic Compression," *Ceramic Engineering and Science Proceedings,* vol. 25, pp. 313-18, 2004.
[94] X. Tan, *et al.*, "Electric-field-induced antiferroelectric to ferroelectric phase transition in mechanically confined Pb_{0.99}Nb_{0.02}[(Zr_{0.57}Sn_{0.43})_{0.94}Ti_{0.06}]_{0.98}O_{3}," *Physical Review B,* vol. 81, p. 014103, 2010.
[95] A. Fasano, *Free boundary problems : theory and applications*. Boston: Pitman Advanced Pub. Program, 1983.
[96] J. S. Langer, "Instabilities and Pattern-Formation in Crystal-Growth," *Reviews of Modern Physics,* vol. 52, pp. 1-28, 1980.
[97] S.-k. Ma, *et al.*, *Directions in condensed matter physics : memorial volume in honor of Prof. S.K. Ma*. Singapore ; Philadelphia, PA: World Scientific, 1986.
[98] S. Nambu and D. A. Sagala, "Domain Formation and Elastic Long-Range Interaction in Ferroelectric Perovskites," *Physical Review B,* vol. 50, pp. 5838-5847, Sep 1 1994.
[99] A. Onuki, "Ginzburg-Landau Approach to Elastic Effects in the Phase-Separation of Solids," *Journal of the Physical Society of Japan,* vol. 58, pp. 3065-3068, Sep 1989.

[100] A. F. Devonshire, "Theory of Ferroelectrics," *Advances in Physics,* vol. 3, pp. 85-130, 1954.
[101] G. R. Barsch, *et al.*, "Landau-Devonshire theory with rotationally invariant expansion coefficients," *Ferroelectrics,* vol. 35, pp. 187-190, 1981.
[102] G. A. Rossetti and N. Maffei, "Specific heat study and Landau analysis of the phase transition in PbTiO3 single crystals," *Journal of Physics-Condensed Matter,* vol. 17, pp. 3953-3963, Jun 29 2005.
[103] A. A. Heitmann and G. A. Rossetti, "Thermodynamics of polar anisotropy in morphotropic ferroelectric solid solutions," *Philosophical Magazine,* vol. 90, pp. 71-87, 2010.
[104] G. A. Rossetti, *et al.*, "Ferroelectric solid solutions with morphotropic boundaries: Vanishing polarization anisotropy, adaptive, polar glass, and two-phase states," *Journal of Applied Physics,* vol. 103, pp. -, Jun 1 2008.
[105] A. Kumar and U. V. Waghmare, "First-principles free energies and Ginzburg-Landau theory of domains and ferroelectric phase transitions in BaTiO3," *Physical Review B,* vol. 82, pp. -, Aug 25 2010.
[106] W. W. Cao and L. E. Cross, "Theory of Tetragonal Twin Structures in Ferroelectric Perovskites with a 1st-Order Phase-Transition," *Physical Review B,* vol. 44, pp. 5-12, Jul 1 1991.
[107] H. L. Hu and L. Q. Chen, "Computer simulation of 90 degrees ferroelectric domain formation in two-dimensions," *Materials Science and Engineering a-Structural Materials Properties Microstructure and Processing,* vol. 238, pp. 182-191, Oct 30 1997.
[108] H. L. Hu and L. Q. Chen, "Three-dimensional computer simulation of ferroelectric domain formation," *Journal of the American Ceramic Society,* vol. 81, pp. 492-500, Mar 1998.
[109] L. Q. Chen and J. Shen, "Applications of semi-implicit Fourier-spectral method to phase field equations," *Computer Physics Communications,* vol. 108, pp. 147-158, Feb 1998.
[110] Y. L. Li, *et al.*, "Effect of substrate constraint on the stability and evolution of ferroelectric domain structures in thin films," *Acta Materialia,* vol. 50, pp. 395-411, Jan 22 2002.
[111] J. Wang, *et al.*, "Phase field simulations of ferroelectric/ferroelastic polarization switching," *Acta Materialia,* vol. 52, pp. 749-764, Feb 9 2004.
[112] Y. Su and C. M. Landis, "Continuum thermodynamics of ferroelectric domain evolution: Theory, finite element implementation, and application to domain wall pinning," *Journal of the Mechanics and Physics of Solids,* vol. 55, pp. 280-305, Feb 2007.
[113] J. Wang, *et al.*, "Phase field simulations of ferroelectric nanoparticles with different long-range-electrostatic and -elastic interactions," *Journal of Applied Physics,* vol. 105, pp. -, Jan 1 2009.
[114] J. Wang and M. Kamlah, "Three-dimensional finite element modeling of polarization switching in a ferroelectric single domain with an impermeable notch," *Smart Materials & Structures,* vol. 18, Oct 2009.
[115] J. Wang and M. Kamlah, "Effect of electrical boundary conditions on the polarization distribution around a crack embedded in a ferroelectric single domain," *Engineering Fracture Mechanics,* vol. 77, pp. 3658-3669, 2010.

[116] S. E. Young, *et al.*, "Mechanical self-confinement to enhance energy storage density of antiferroelectric capacitors," *Journal of Applied Physics*, vol. 113, p. 054101, 2013.
[117] C. Kittel, "Theory of Antiferroelectric Crystals," *Physical Review*, vol. 82, pp. 729-732, 1951.
[118] L. E. Cross, "Antiferroelectric-Ferroelectric Switching in a Simple Kittel Antiferroelectric," *Journal of the Physical Society of Japan*, vol. 23, pp. 77-&, 1967.
[119] K. Uchino, *et al.*, "Electrostrictive Effects in Paraelectric-Ferroelectric-Antiferroelectric Phase-Transitions," *Japanese Journal of Applied Physics*, vol. 19, pp. L425-L428, 1980.
[120] K. Uchino, *et al.*, "Electrostrictive effects in antiferroelectric perovskites," *Journal of Applied Physics*, vol. 52, pp. 1455-1459, 1981.
[121] H. Zhang, "Polarization rotation and field induced phase transition in PZN-4.5% PT single crystal," *Journal of Applied Physics*, vol. 114, Aug 28 2013.
[122] A. Erturk and D. J. Inman, *Piezoelectric energy harvesting*. Chichester: Wiley, 2011.
[123] A. Erturk and D. J. Inman, "Broadband piezoelectric power generation on high-energy orbits of the bistable Duffing oscillator with electromechanical coupling," *Journal of Sound and Vibration*, vol. 330, pp. 2339-2353, May 9 2011.
[124] J. Dayou, *et al.*, "The effects of width reduction on the damping of a cantilever beam and its application in increasing the harvesting power of piezoelectric energy harvester," *Smart Materials and Structures*, vol. 24, 2015.
[125] J. C. Han, *et al.*, "A novel cylindrical torsional magnetoelectric composite based on d(15) shear-mode response," *Journal of Physics D-Applied Physics*, vol. 48, Feb 4 2015.
[126] E. S. Nour, *et al.*, "A flexible anisotropic self-powered piezoelectric direction sensor based on double sided ZnO nanowires configuration," *Nanotechnology*, vol. 26, 2015.
[127] H. Nguyen, *et al.*, "Pyroelectric energy converter using co-polymer P(VDF-TrFE) and Olsen cycle for waste heat energy harvesting," *Applied Thermal Engineering*, vol. 30, pp. 2127-2137, 2010.
[128] R. B. Olsen, "Ferroelectric Conversion of Heat to Electrical Energy - a Demonstration," *Journal of Energy*, vol. 6, pp. 91-95, 1982.
[129] R. B. Olsen, *et al.*, "Pyroelectric Conversion Cycle of Vinylidene Fluoride Trifluoroethylene Copolymer," *Journal of Applied Physics*, vol. 57, pp. 5036-5042, 1985.
[130] R. B. Olsen, *et al.*, "Pyroelectric Conversion Cycles," *Journal of Applied Physics*, vol. 58, pp. 4709-4716, 1985.
[131] L. Kouchachvili and M. Ikura, "High performance pyroelectric converter," *Proceedings of the Sixth IASTED International Conference on European Power and Energy Systems*, pp. 366-371, 2006.
[132] L. Kouchachvili and M. Ikura, "Improving the efficiency of pyroelectric conversion," *International Journal of Energy Research*, vol. 32, pp. 328-335, Mar 25 2008.
[133] M. Ikura, "Conversion of low-grade heat to electricity using pyroelectric copolymer," *Ferroelectrics*, vol. 267, pp. 403-408, 2002.
[134] A. Navid and L. Pilon, "Pyroelectric energy harvesting using Olsen cycles in purified and porous poly(vinylidene fluoride-trifluoroethylene) [P(VDF-TrFE)] thin films," *Smart Materials & Structures*, vol. 20, Feb 2011.
[135] G. Sebald, *et al.*, "Electrocaloric and pyroelectric properties of 0.75Pb(Mg1/3Nb2/3)O-3-0.25PbTiO(3) single crystals," *Journal of Applied Physics*, vol. 100, Dec 15 2006.

[136] G. Sebald, *et al.*, "Electrocaloric Effect In Relaxor Ferroelectric Ceramics and Single Crystals," *2006 15th Ieee International Symposium on Applications of Ferroelectrics*, pp. 190-193, 2007.
[137] G. Sebald, *et al.*, "Electrocaloric properties of high dielectric constant ferroelectric ceramics," *Journal of the European Ceramic Society*, vol. 27, pp. 4021-4024, 2007.
[138] G. Sebald, *et al.*, "On thermoelectric and pyroelectric energy harvesting," *Smart Materials and Structures*, vol. 18, p. 125006, 2009.
[139] R. Kandilian, *et al.*, "The pyroelectric energy harvesting capabilities of PMN-PT near the morphotropic phase boundary," *Smart Materials & Structures*, vol. 20, May 2011.
[140] I. M. McKinley, *et al.*, "A novel thermomechanical energy conversion cycle," *Applied Energy*, vol. 126, pp. 78-89, Aug 1 2014.
[141] I. M. McKinley, *et al.*, "A novel thermally biased mechanical energy conversion cycle," *Journal of Applied Physics*, vol. 114, Dec 14 2013.
[142] I. M. McKinley, *et al.*, "Waste heat energy harvesting using the Olsen cycle on 0.945Pb(Zn1/3Nb2/3)O-3-0.055PbTiO(3) single crystals," *Smart Materials and Structures*, vol. 21, Mar 2012.
[143] D. Guyomar, *et al.*, "Energy harvesting based on FE-FE transition in ferroelectric single crystals," *Ieee Transactions on Ultrasonics Ferroelectrics and Frequency Control*, vol. 55, pp. 279-285, Feb 2008.
[144] H. Zhu, *et al.*, "Thermal energy harvesting from Pb(Zn[sub 1/3]Nb[sub 2/3])[sub 0.955]Ti[sub 0.045]O[sub 3] single crystals phase transitions," *Journal of Applied Physics*, vol. 106, p. 124102, 2009.
[145] A. Khodayari, *et al.*, "Nonlinear pyroelectric energy harvesting from relaxor single crystals.," *IEEE transactions on ultrasonics, ferroelectrics, and frequency control*, vol. 56, pp. 693-9, 2009.
[146] S. Patel, *et al.*, "A technique for giant mechanical energy harvesting using ferroelectric/antiferroelectric materials," *Journal of Applied Physics*, vol. 115, Feb 28 2014.
[147] Y. X. Jiang, *et al.*, "Breakdown and critical field evaluation for porous PZT 95/5 ferroelectric ceramics under shock wave compression," *Smart Materials and Structures*, vol. 23, Aug 2014.
[148] G. Xu, *et al.*, "Growth and electrical properties of large size Pb(In[sub 1⁄2]Nb[sub 1⁄2])O[sub 3]–Pb(Mg[sub 1⁄3]Nb[sub 2⁄3])O[sub 3]–PbTiO[sub 3] crystals prepared by the vertical Bridgman technique," *Applied Physics Letters*, vol. 90, p. 032901, 2007.
[149] J. Tian, *et al.*, "Improved stability for piezoelectric crystals grown in the lead indium niobate–lead magnesium niobate–lead titanate system," *Applied Physics Letters*, vol. 91, p. 222903, 2007.
[150] P. Finkel, *et al.*, "Large strain transduction utilizing phase transition in relaxor-ferroelectric Pb(In(1/2)Nb(1/2))O(3)-Pb(Mg(1/3)Nb(2/3))O(3)-PbTiO(3) single crystals," *Applied Physics Letters*, vol. 98, May 9 2011.
[151] C. B. Sawyer and C. H. Tower, "Rochelle salt as a dielectric," *Physical Review*, vol. 35, pp. 0269-0273, Feb 1930.
[152] W. D. Dong, *et al.*, "Ideal energy harvesting cycle using a phase transformation in ferroelectric crystals," *Smart Materials and Structures*, vol. 23, Dec 2014.

[153] P. Finkel, *et al.*, "Phase switching at low field and large sustainable strain output in domain engineered ferroic crystals," *physica status solidi (a)*, vol. 209, pp. 2108-2113, 2012.
[154] I. M. McKinley and L. Pilon, "Phase transitions and thermal expansion in pyroelectric energy conversion," *Applied Physics Letters*, vol. 102, Jan 14 2013.
[155] W. D. Dong, *et al.* (2014). *Energy harvesting using the FER–FEO phase transformation in [011] cut single crystal PIN-PMN-PT (March 10, 2014 ed.)*.
[156] W. D. Dong, *et al.*, "Energy harvesting using the FER-FEO phase transformation in [011] cut single crystal PIN-PMN-PT," *Journal of Intelligent Material Systems and Structures*, vol. 25, pp. 1786-1799, Sep 2014.
[157] W. D. Dong, *et al.*, "A finite element based phase field model for ferroelectric domain evolution," *Smart Materials and Structures*, vol. 21, Sep 2012.
[158] P. Marton, *et al.*, "Domain walls of ferroelectric BaTiO3 within the Ginzburg-Landau-Devonshire phenomenological model," *Physical Review B*, vol. 81, pp. -, Apr 1 2010.
[159] B. Meyer and D. Vanderbilt, "Ab initio study of ferroelectric domain walls in PbTiO(3)," *Physical Review B*, vol. 65, Mar 1 2002.
[160] E. A. Little, "Dynamic Behavior of Domain Walls in Barium Titanate," *Physical Review*, vol. 98, pp. 978-984, 1955.
[161] C. Kittel, "Thickness of Domain Walls in Ferroelectric and Ferroelastic Crystals," *Solid State Communications*, vol. 10, pp. 119-&, 1972.
[162] G. Shirane, *et al.*, "X-Ray and Neutron Diffraction Study of Ferroelectric Pbtio3," *Acta Crystallographica*, vol. 9, pp. 131-140, 1956.